universität wien

DISSERTATION / DOCTORAL THESIS

Titel der Dissertation / Title of the Doctoral Thesis

"Mathematical Models of Speciation and Polygenic Adaptation"

verfasst von / submitted by

Mag. Ilse Höllinger BSc.

angestrebter akademischer Grad / in partial fulfillment of the requirements for the degree of

Doktorin der Naturwissenschaften (Dr.rer.nat.)

Wien 2018 / Vienna 2018

Studienkennzahl lt. Studienblatt / degree program code as it appears on the student record sheet:	A 796 605 405
Dissertationsgebiet lt. Studienblatt / field of study as it appears on the student record sheet:	Mathematik
Betreut von / Supervisor:	Univ.-Prof. Dr. Joachim Hermisson ao. Univ.-Prof. Dr. Reinhard Bürger

Acknowledgements/ Danksagung

First, I want to thank Joachim Hermisson, for providing me with the opportunity to work on very different and interesting projects during the course of my PhD. He has been a very patient and helpful supervisor, and I am very grateful for this experience, including my research stay in Berkley, California and several international conferences and workshops!

I am also very thankful to Reinhard Bürger, Andrea Betancourt and Ovidiu Paun, who have served as co-supervisors and PhD committee members, and have been helpful in improving my work with their thoughtful comments and criticisms. In this context, I also want to extend my thanks to the members of the SAB committee, who have given me a lot of good ideas and pointed to open questions during the external review process every year.

I also want to say thank you to all of my dear (MaBS) colleagues, especially Sylvain Mousset, Alexandre Blanckaert, Derek Setter for the good vibes and delightful lunches, but also for fruitful discussions and many hours of exchanging ideas. Special thanks of course also goes to our good soul Michael Dorninger, who has always been most helpful in administrative issues and with the coffee, without which we would all just be doomed!

I am also very grateful to all the people who have worked very hard to setup and keep the Graduate School of Population Genetics, Vienna, up and running, enabling me to attend fascinating talks, speak to world-renown scientist on a regular basis and attend our yearly retreat, as well as of course for paying most of my salary, which has made this entire endeavor possible.

Special thanks also goes to Sam Yeaman and Claus Vogl, who have kindly agreed to review this thesis at the most busy time of the year! I hope you still have a merry Christmas and a good start into the new year!

Finally, I want to say thank you to the most important people in my life, my partner Christoph and our son Erik. Thanks for being there for me – and to our number 2, who

has set up the ultimate deadline for this PhD to come to an end! I also want to thank my family, especially my mother Ingrid, for helping out so much and being the most amazing and engaged grandmother! Finally, my thanks also go to my dear friend Agnes, who has always had an open ear for my problems over the last 20 years!

... and now, let's get to business...

Abstract

Adaptation to new environmental challenges is ubiquitous in natural populations, such that organisms have come to live in almost every possible niche. While such phenotypic adaptations have been observed and documented for a long time, the underlying genetic and genomic mechanisms have long been elusive. For many processes, evolutionary biology relied entirely on theoretical inferences. Only the recent advent of high trough put, genome-wide sequencing techniques has opened up the possibility of cross-validation of some of the long standing theoretical paradigms by empirical observations, as well as the influence of empiricism back towards the development of new analytical frameworks. In this new era the genome is more and more understood as an entity, responding jointly to new selective challenges. In the current thesis different genomic architectures, including aspects of genomic position (autosomes, sex-chromosomes, cytoplasmic genome), number of contributing loci, or strength of selection and epistatic interactions are vetted for their individual and cumulative impact on adaptation and parapatric speciation. The theoretical and numerical predictions presented all rely on models in the tradition of population genetics, following dynamics of individual alleles. The first project deals with the process of incipient, parapatric speciation, based on a two locus Dobzhansky-Muller hybrid incompatibility in a continent island model. It turns out that the genomic positioning of the involved loci, e.g. X-linkage or sex-biased selection and epistasis can strongly increase the sustainability of incipient divergence against swamping due to immigrating alleles, showing the importance of the genomic architecture of the DMI for its evolution and maintenance. The second and third project focus on evolutionary dynamics of polygenic adaptation of a complex trait within a single, panmictic population, based on a binary trait and a quantitative trait model. In both cases the strength of genetic redundancy within the trait basis proves to be the main, composite predictor for the resulting adaptive architecture of a polygenic trait.

Zusammenfassung

Anpassung an verschiedenste Lebensräume und Umweltbedingungen hat dazu geführt, dass natürliche Organismen so gut wie jede ökologische Nische unseres Planeten besiedeln konnten. Während dabei die phänotypischen Veränderungen offensichtlich sind, waren und sind die genetischen Mechanismen die zu diesen Anpassungen führten oft unbekannt und boten ein weites Feld für Spekulationen. Dadurch spielten theoretische Vorhersagen eine große Rolle, sodass über lange Zeit weite Felder der Evolutionsbiologie gänzlich auf diesen beruhten. Inzwischen hat die Entwicklung moderner, genomweiter Sequenzierungsmethoden eine neue wissenschaftliche Ära eingeläutet. Es ist nun möglich langfristig etablierte Paradigmen der theoretischen Evolutionsbiologie eingehender, empirischer Verifikation zu unterziehen. Umgekehrt führen die neuen Methoden auch zur Inspiration und Entwicklung neuer evolutionsbiologischer Theorien und Ansätze. Heutzutage wird das Genom zunehmend als Einheit verstanden, die in ihrer Gesamtheit auf neue, selektive Einflüsse reagiert. In der vorliegenden Arbeit untersuche ich den Einfluss verschiedener genetische Architekturen, das heißt Genomposition, Anzahl der involvierten Loci oder der Stärke Selektion und epistatischer Interaktionen, auf den daraus resultierenden adaptiven Prozess und auf die beginnende Artbildung. Der Fokus liegt hierbei auf populationsgenetischen Modellen, die Allelefrequenztrajektorien und -dynamiken beschreiben. Das erste Kapitel widmet sich dem Prozess beginnender Artbildung durch eine zwei-lokus Dobzhansky-Muller Hybridinkompatibilität. Es zeigt sich sich, dass genomische Architekturen die Sexchromosomen enthalten stärkere Resistenz gegen Genfluss zeigen, als rein autosomale oder mitochondriale Inkompatibilitäten. Das zweite und dritte Kapitel beschreiben verschiedene Modelle zur Dynamik der Anpassung eines komplexen, phänotypischen Merkmals mit einer polygenen Basis in einer panmiktischen Population. Dabei stellt sich heraus, dass die Stärke der genetischen Redundanz der polygenen Basis immer der Schlüsselfaktor für die resultierende adaptive Architektur ist.

Contents

List of authors and contributions

- **Introduction**

  Author: Ilse Höllinger

- **Chapter I: *Bounds to Parapatric Speciation***

  Authors: Ilse Höllinger, Joachim Hermisson

  Reference: Höllinger, I., & Hermisson, J. (2017). Bounds to parapatric speciation: A Dobzhansky–Muller incompatibility model involving autosomes, X chromosomes, and mitochondria. Evolution, 71(5), 1366-1380.

  Author contributions:

  - JH designed the study concept.
  - IH wrote the first draft of the manuscript.
  - IH prepared the figures.
  - JH revised the manuscript with comments by IH.
  - IH derived the analytical results.
  - IH wrote the simulations code.
  - IH prepared the numerical results.

- **Chapter II: *Polygenic Adaptation: from Sweeps to Subtle Frequency Shifts***

  Authors: Ilse Höllinger, Pleuni Pennings, Joachim Hermisson

  Reference: Höllinger, I., Pennings, P., & Hermisson, J. (2018). Polygenic Adaptation: From sweeps to subtle frequency shifts. bioRxiv, 450759.

  Author contributions:

  - JH, PSP and IH designed the study concept.

- IH wrote the first version of the manuscript.
- IH prepared the figures.
- JH revised the manuscript with comments by PSP and IH.
- JH derived the analytical results with input from PSP and IH.
- IH wrote the simulations code with input from JH and PSP.
- IH prepared the numerical results.

- **Chapter III:** ***Polygenic Adaptation II: Sweeps and Shifts for a quantitative trait model with stabilizing selection***

  Authors: Ilse Höllinger, Joachim Hermisson

  Author contributions:

  - JH and IH designed the study concept.
  - IH wrote the current version of the manuscript.
  - IH prepared the figures.
  - JH derived the analytical results with input from IH.
  - IH wrote the simulations code.
  - IH prepared the numerical results.

1 Introduction

In this thesis I present, on the influence of genetic architectures of a trait on its response to selection within and between diverging populations. Thereby I cover scenarios of polygenic adaptation to a new optimum, as well as incipient speciation with gene flow. In summary, I find that different genetic architectures, in particular epistatic interactions (all Chapters), genomic position, such as *e.g.* autosomal, X-linked or cytoplasmic genes in incipient speciation (Chapter 2) and genetic redundancy of the trait (Chapter 3-4) substantially impact how genomes react to selective pressure.

1.1 Defining *genetic* and *adaptive* architecture of a trait

The *genetic architecture of a phenotypic trait* is constituted by the entity of its genetic basis and thus it fully defines the *genotype-phenotype map* (Hansen, 2006). In detail, it comprises the number of loci involved in governing a trait, their linkage pattern and more general their genomic position, *i.e.* being situated on an autosome, linkage to sex-chromosomes or genes in extra nuclear genomes such as organelle *e.g.* mitochondria. For each of these loci, the genetic architecture also covers the number of different alleles. Furthermore, it contains functional information, such as the effect size of each allele, which includes the individual, allelic effect together with its dominance and epistatic interactions with other alleles within the trait basis, *i.e.* intra- and inter-locus interactions. Next, pleiotropy, that is the influence of individual alleles or loci on several unrelated phenotypic traits (reviewed in Paaby and Rockman, 2013), can also be summarized within the functional properties. Finally, effects of new mutations can also be included and affect function and variation, especially concerning the response of the trait to a selective pressure (defined in Wagner, 2000; Hansen, 2006). Hence the "genetic architecture" of a trait is independent of allele frequencies (following Wagner, 2000). It describes the *potential for change* (due to single- and multiple locus substitutions) and is defined for a given reference genotype (could be the ancestral genotype). It includes

the entire genetic basis of a trait, but does not refer to fitness in any way.

The concept of the "genetic architecture" needs to be carefully distinguished from the concept of the "adaptive architecture" of the trait. While, as described above, the former comprises all genomic loci that affect a trait, the latter only refers to a subset. In particular, I describe the adaptive architecture by the *effective changes* in allele frequencies in the context of phenotypic adaptation (again relative to a reference genotype). This includes the impact of all evolutionary forces such as selection, genetic drift, mutation and migration. Across many replicate runs of evolution, this is given by a joint distribution of allele frequencies. The realized change for a single run is obtained by sampling from this distribution.

Information about the genetic architecture of a trait is of special interest for predictions concerning its evolutionary dynamics. Following the *Neodarwinian paradigm*, evolution is usually defined as the change in allele frequencies (reviewed in Kutschera and Niklas, 2004), so the genetic architecture coupled with the composite allele frequency distribution of a trait basis provides the substrate for the possible adaptive response of a trait to selection. While here I follow the definition of genetic architecture excluding allele frequency informations (Wagner, 2000; Hansen, 2006), there exist alternative concepts (*e.g.* Visscher et al., 2017), which additionally include allele frequency distributions into their definition. Yet, I abide by the former definition for the following reasons: The genetic architecture (*e.g.* in the two fly populations, one big population living in the wild and one much smaller population maintained in the lab, constituted of sampled descendants from the wild population) can be the same, while the adaptive architecture (that I assess through replicate runs) is still different. In each single replicate I obtain a realized architecture, strongly depending on factors such as the available genetic variation, the effective population size or the effect on trait wide population mutation rates *etc*.

In conclusion this means that under selection with a given genetic architecture, different adaptive architectures should be expected. (Alternatively, one could call the single realized architecture the "adaptive architecture" and the joint distribution a "distribution

of architectures".)

1.1.1 The search for genome wide footprints of speciation and adaptation

In the current *post-genomic era* of evolutionary biology (Perbal, 2015) (since the decoding of the human genome), newly developed high-throughput sequencing methods allow scientists to study entire genomes and large numbers of individuals at once. Together with functional information evolution is now understood more and more as a process affecting the genome as an entity and reaching the statistically necessary sample sizes now allow us to unravel complex genetic architectures and detect weak adaptive footprints. This development also has a huge impact on theoretical evolutionary biology. While theoretical predictions of evolutionary processes often have lacked empirical confirmation, this new era enables comprehensive validations and corrections of long-standing theoretical paradigms. Additionally, empirical observations also start to have a strong impact on evolutionary modeling.

One example for the application of such scans to look for genome-wide patterns in speciation research is the concept of *islands of genomic divergence* or sometimes also called *islands of speciation* (Wu, 2001; Turner et al., 2005; Butlin et al., 2012; Nosil, 2012; Nosil and Feder, 2012; Via, 2012). The idea being that some loci, putatively due to local adaptation, might reduce effective gene flow in their immediate genomic proximity. This leads to increased divergence levels within these linkage groups, *i.e.* the islands of divergence. These islands could in turn serve as nuclei of incipient barriers to gene flow, which upon expansion might lead to a severe reduction or even to the complete block of gene flow over the entire genome and thus result in speciation. There are genome scans for such islands in *e.g.* plants (Strasburg et al., 2012) or in host races of pea aphids (Via and West, 2008), yet in general the empirical results on the abundance and size of such island are mixed (Nosil, 2012; Cruickshank and Hahn, 2014; Pennisi, 2014). The ongoing debate about whether these islands are real, has also inspired theoreticians to provide some predictions on if and how such barrier could build up and how that would

depend on the respective genetic architecture of the causal loci within the island (see Feder et al., 2012; Yeaman, 2013; Aeschbacher and Bürger, 2014; Yeaman et al., 2016; Blanckaert and Hermisson, 2018).

Another instance of genome wide scans are genome-wide-association-studies (GWAS) searching for candidate loci potentially contributing to differentiation in various (model-) organisms, such as humans (Visscher et al., 2012, 2017), *Arabidopsis thaliana* (see Tognalli et al., 2017, for an overview) or *Drosophila* (Wangler et al., 2017). Instead of clear genomic footprints of adaptation, empirical data however often yield footprints of selection, which do not agree with complete sweep patterns, in the tradition of (*e.g.* Maynard-Smith and Haigh, 1974). Instead adaptive haplotypes might be found to segregate at intermediate frequencies in natural or experimental populations, a pattern usually called *partial sweeps*. For example, in evolution experiments in *Drosophila*, putatively beneficial variants rise but do not sweep to fixation, but eventually segregate as stable polymorphisms in the population (Burke et al., 2010; Tobler et al., 2014; Franssen et al., 2015). Alternatively, the detected loci might only explain a tiny fraction of the trait heritability (Manolio et al., 2008, 2009), such that the majority of causal factors remains unknown. Among others *polygenic adaptation* has been put forward as putative underlying cause of these phenomena (Pritchard et al., 2010; Pritchard and Di Rienzo, 2010). These studies suggest, that the genomic adaptive architecture of the traits itself might obscure the signal. The idea being that for a complex trait under selection many loci could potentially react in parallel via subtle, concerted allele frequency shifts, an expectation in the tradition of quantitative genetics. While such a genomic signal would be feeble, such that the detection of significant signals would be strongly limited, yielding probably only a few loci, phenotypic adaptation could still be substantial. This pattern of *polygenic adaptation* stands in stark contrast to the pattern of selective sweeps, where single loci experience a significant frequency increase and are the main contributors responsible for adaptation – a signal that is much easier to detect (reviewed in Hermisson and Pennings, 2017). Following the influential work of Pritchard et al. (2010), the em-

phasize of molecular geneticists shifted from searching for sweep patterns to trying to identify weak patterns of polygenic adaptation in data (*e.g.* Hancock et al., 2010; Daub et al., 2013; Berg and Coop, 2014). To do so, new methodology to identify concerted frequency shifts despite their small, individual size were developed, usually relying on the common trends of frequency changes of allele cohorts (Field et al., 2016) or on linkage disequilibria (LD) (Berg and Coop, 2014), leaving the study of single significant SNPs behind. Human height quickly emerged as the standard example of a quantitative trait (QT), but signals of polygenic adaptation were also found for many other traits, showing pervasive selection shaping the human genome (*e.g.* Daub et al., 2013; Berg and Coop, 2014; Field et al., 2016; Boyle et al., 2017). These results even lead to the postulate of the *omnigenic model* (Boyle et al., 2017), where basically every gene could potentially contribute to adaptation of many traits. The shock to the field followed a few years later, when it was discovered that the original strongest signal of polygenic scores on height was heavily inflated by remaining population stratification in the data (Berg et al., 2018; Sohail et al., 2018). To this date, the abundance of polygenic adaption via subtle frequency shifts remains unclear.

1.1.2 The role of epistasis in genetic architectures

One common key aspect of all investigated genetic architectures in this thesis is epistasis, that is the differential effect of an allele on the phenotype or fitness conditional on its respective genetic background. There is ongoing discussion about the importance of epistasis for evolution, yet this predominantly stems from inexact differentiation between functional/physiological and statistical epistasis (Hansen, 2013, and detailed below) .

First, in the (Bateson-)Dobzhansky-Muller hybrid incompatibility (DMI) model (Bateson, 1909; Dobzhansky, 1936; Muller, 1942) (presented in Chapter 2) for incipient parapatric speciation, epistasis is of course essential and its role remains fairly undoubted. Thereby a 2-locus DMI is constituted by two, usually biallelic loci ($\mathcal{A}$ and $\mathcal{B}$). While 3 pairs of alleles are compatible, one pair of variants at the two loci, that emerged on

different backgrounds, is incompatible. One classic and illustrating evolutionary trajectory for such a scenario is *secondary contact*: A population splits into two, allopatric sister populations, and a new, derived variants arise and fix at each of the two loci in the two populations (*e.g.* $a \rightarrow A$ in population 1 and $b \rightarrow B$ in population 2). While these new alleles work well in their native, separate backgrounds, they cause hybrids, carrying both derived alleles A and B, to be less fit (instances are reduced hybrid fitness or even hybrid sterility or lethality), once these variants interact statistically within the same individual. As there is abundant empirical evidence for the occurrence of DMIs in natural population (Barnard-Kubow et al., 2016; Fishman and Sweigart, 2018, to cite but a few) (extensively reviewed in Coyne and Orr, 2004; Maheshwari and Barbash, 2011), epistasis in this context is probably least contested. In Chapter 2 I show that genomic position and effect sizes, especially the strength of epistatic interactions in the DMI strongly influence its evolution and stability in the face of gene flow.

However, despite the polygenic nature of quantitative genetics, epistasis there is often neglected in favor of pure additive effects on the trait and fitness or it is modeled as a non-directional variance component *e.g.* in the infinitesimal model (see Fisher (1918) and its extensions by Barton et al. (2017)). This results in part from the fact, that with QT the phenotypic variation that can be attributed to epistatic variance in data is low, despite abundant empirical evidence for physiological epistatic interactions of QT-loci (QTL) (Malmberg and Mauricio, 2005; Hill et al., 2008; Crow, 2010). Nevertheless, this does not mean that generally epistasis is irrelevant, as the non-directional implementation of epistasis does not capture the nature of functional or physiological epistasis. Furthermore physiological epistasis can largely contribute to additive genetic variance (Hansen, 2013). Indeed, in the current work I show that the directionality of epistatic interactions, in this case *diminishing-returns epistasis* (often found in data *e.g.* Kryazhimskiy et al., 2014), can have a decisive impact, strongly shaping the adaptive footprint selection leaves within genomes. In detail, I show that the strength of negative epistasis is directly related to the expected adaptive architecture of a complex trait, as it is the key determinant for

the functional redundancy of the involved loci. For this I compare different models of complex traits, such as a binary trait with a (completely) redundant polygenic basis (Chapter 3) and a QT-model with additive phenotypic effects and stabilizing selection, yielding negative epistasis on fitness (Chapter 4).

1.2 Parapatric speciation with a DMI model (Chapter 2)

1.2.1 Background and motivation

For a long time speciation research has primarily focused on the two endpoints of the continuum of different migration rates, constituted by either allopatric (*i.e.* complete isolation of incipient sister species) or sympatric (*i.e.* common habitat of the diverging subpopulations) speciation scenarios (Coyne and Orr, 2004; Orr and Turelli, 2001; Via and West, 2008). In allopatry the classical approach for postzygotic isolation barriers is the (Bateson-)Dobzhansky-Muller model (DMM) (Bateson, 1909; Dobzhansky, 1936; Muller, 1942).

Here, however I aim for a comprehensive treatment of the entire spectrum of variable gene flow rates, known as *parapatric speciation*, because it is still unclear how the homogenizing effect of gene flow and recombination can be counteracted (Felsenstein, 1981; Slatkin, 1987). Yet, recent estimates of non-negligible hybridization rates between "good species" with still viable and not completely sterile offspring (potential back-crossing) in nature provide legitimate ground to assume ongoing gene flow in many naturally diverging populations (see Coyne and Orr, 2004; Mallet, 2008, for a review). Also there is widespread empirical evidence for the occurrence of DMIs (Coyne and Orr, 2004; Presgraves, 2010; Maheshwari and Barbash, 2011) even within species boundaries (Corbett-Detig et al., 2013). Together with these empirical findings, a several theoretical studies (Agrawal et al., 2011; Feder and Nosil, 2009; Gavrilets, 1997; Bank et al., 2012) also support the hypothesis that the DMM might be a potential evolutionary route to parapatric speciation. In detail, Bank et al. (2012) showed that autosome-autosome 2-

191 locus DMIs allow for the evolution of postzygotic isolation in early phases of parapatric
192 speciation, given that migration rates do not exceed a critical value.

193 Concerning speciation, two other prominent mechanisms come to mind, *i.e.* Hal-
194 dane's rule and the large X-effect. The former states that within species with sex
195 specific reduced hybrid fitness usually the heterogametic sex is affected (first described
196 by Haldane, 1922), (and reviewed in Coyne and Orr, 2004). The latter describes the
197 finding that a disproportional number of genes involved in postzygotic isolation maps to
198 the X-chromosome (reviewed in Presgraves, 2008). Both phenomena point to a major
199 role of sex-chromosomes in speciation. Furthermore, various cases of cytoplasmic in-
200 compatibilities between nuclear and mitochondrial genomes (Burton and Barreto, 2012;
201 Ellison and Burton, 2008), as well as plastids in plants (for biological examples *e.g.* see
202 Snijder et al., 2007) and incompatibilities due to infection with the cytoplasmic bac-
203 terium Wolbachia (reviewed *e.g.* in Coyne and Orr, 2004; O'Neill et al., 1992; Werren,
204 1997) have been documented.

205 Given the large body of empirical and theoretical evidence concerning the variable
206 genetic architecture of a DMIs, the necessity to extend investigations in this direction
207 is apparent. I investigate the effects of including non-autosomal loci, such as X-linked
208 alleles, *e.g.* like the mammalian Xy-system. Nevertheless, the model readily extend to
209 heterogametic females (WZ-system in birds). Additionally I include extra-nuclear alleles,
210 *e.g.* mitochondrial genes into the analysis. As sex-chromosomes and mitochondria both
211 experience sex-biased inheritance, I analyses the influence of sex-biased migration rates
212 on parapatric DMI evolution and sex-biased allelic and epistatic effects, especially due
213 to dosage compensation of the hemizygous X in males.

214 ### 1.2.2 Model

215 Based on (Bank et al., 2012), I focus on the initial phase of the speciation process and
216 setup a deterministic, minimal model of a two locus DMI in a continent-island frame-
217 work (a monomorphic continent with unidirectional gene flow to the island). I assume

linkage equilibrium (LE) among both loci and Hardy-Weinberg-proportions, due to weak evolutionary forces. Using a pair of differential equations in continuous time (see **Box 1** in Section 2.2) I follow the allele frequencies of the incompatible alleles on the island and study the maximum tolerated migration rates, where a two locus polymorphism, a DMI, can persist stably against swamping or even invade. Mathematically a DMI hence corresponds to a stable, internal equilibrium in the frequency space. In detail I look at eight different genomic architecture (combinations of autosomal, X-linked and mitochondrial genes, see Table 2.1 and Fig. 2.1, B.1 for illustrations), where I refer to the incompatible allele immigrating from the continent as the *continental allele* and the incompatible allele residing on the island as the *island allele*. I investigate codominant DMIs (additive by additive epistasis), where the strength of the hybrid incompatibility is directly proportional to the number of incompatible pairs of alleles, recessive DMIs (respecting Haldane's rule, such that F1-females are not affected) and a general model comprising these two fitness schemes, where I study the effect of sex-biased migration rates and sex-biased X-linked locus effects (dosage compensation), respectively. Only the codominant model lends itself to comprehensive analytical treatment, while I have to resort to numerical investigations for most of the other fitness schemes.

1.2.3 Results

Like Bank et al. (2012), I find three potential boundary equilibria for the general model. A monomorphic fixed point, where the continental genotype fixes on the island. This is always permissible and will be reached for strong migration rates. Additionally, there can be up to two single locus polymorphisms (SLP), at each of the DMI loci, where either only one allele is polymorphic and the other locus has been swamped. Only codominance allows for complete analytical description, where I find further find at most one, locally or globally stable internal fixed point, a DMI.

Depending on local or global stability of the DMI, I distinguish two different migration limits, as in (Bank et al., 2012). First, for migration rates $0 \leq m \leq m^{-}_{max}$

(Section 2.3.1), the internal equilibrium is globally stable and will be reached from all starting conditions. These can be mapped to different evolutionary histories of the DMI, *i.e.* where which incompatible alleles arose together with the migration history of the two populations (see Fig. B.4). Second, for migration rate $m^-_{max} < m < m^+_{max}$ I obtain a locally stable equilibrium, which can only be reached from favorable evolutionary histories. Finally for strong migration rates exceeding $m \geq m^+_{max}$ I do not find any permissible DMI.

In accordance with results for autosomal DMIs in (Bank et al., 2012), I find that also non-exclusively autosomal DMIs require local adaptation due to ecological differentiation, *i.e.* the island allele needs to be adaptive, such that its sex-averaged advantage exceeds the immigration. In general the dynamics are governed by two evolutionary forces, namely by *selection against immigrants*, due to maladapted continental alleles or by *selection against hybrids*, or by a combination of both. With maladapted gene flow, and weak to moderate selection against hybrids, the DMI is most often globally stable, if it exists. However, if selection against hybrids is dominant or the immigrating allele is beneficial on the island, it will act against immigrating alleles, only when they are rare, such that the DMI is predominantly locally stable, if it exists.

If I start to disentangle the effects of different genetic architectures I find that X-linked architectures are by trend among the most stable architectures. For example in nuclear DMIs, where the X is dosage compensated and male migration is non-zero, models with X-linked alleles are always more stable than autosomal DMIs, see Fig. 2.2. Only in the case of female biased migration and without dosage compensation all models with autosomal island alleles result in more migration-resistant DMIs, as shown in Fig. 2.3. Similarly in cyto-X, DMIs with X-dosage compensation are more stable than cyto-autosome-DMIs (Fig. 2.4). In general sex-biased migration rates have a strong impact on DMI stability. X-linked DMIs with immigrating X alleles are noticeably weakened/strengthened with female/male migration bias. As mitochondria are only maternally inherited the impact of male male-biased migration is especially pronounced in that

case and almost always enhances the stability of all X-linked architectures.

I round up the investigations by challenging the assumption of LE using numerical simulations, where I observe no differences for weak to moderate levels of epistasis and LD. However, strong epistasis (hybrid inviability or infertility), causes qualitatively different behavior for some of the investigated architectures (autosome-autosome and X-X-DMIs, see Fig. A.2). Second, I find that the deterministic migration bounds provide a strict upper bound to the results with drift (obtained by simulations), see subsection A.3. Finally, I find that X-linked alleles experience stronger barriers against introgression, when compared to autosomes.

1.2.4 Discussion

In conclusion, I find that parapatric differentiation might act as a potential contributor towards the large X-effect, as I find that X-linked parapatric DMIs together with dosage compensation or male-biased migration are amongst the most stable DMIs to migration. Additionally, in the codominant model with dosage compensation and unbiased or male biased migration I find that X-linked substitution rates exceed the rates on autosomes. (Charlesworth et al., 1987) observed this effect only for recessive alleles in a model without migration, where it was termed the *faster X-effect*. As a faster evolution of X-linked substitutions also favors a larger X contribution to isolation, this could be an additional factor of how parapatric speciation could add to the large X-effect. On the contrary, concerning Haldane's rule, I do not obtain any predictions, as I find that recessive DMIs, following Haldane's rule do not show qualitative differences compared to codominant DMIs, see Fig. A.1.

As such the model provides a mechanistic route towards an initial step to speciation in parapatry. Of course the results only capture the evolution of a first DMI, corresponding to a stable polymorphic state of the population, but this does not yet lead to complete reproductive isolation. Nevertheless, such an incompatibility might serve as a seed for further accumulation of barrier genes, following the idea of islands of divergence

discussed above. In this context however it is necessary to note that while in allopatric speciation scenarios DMIs are expected to accumulate increasingly rapidly (Coyne and Orr, 2004), this "snow ball effect" of DMI accumulation can be effectively disrupted in parapatric scenarios with unfavorable DMI architectures (Blanckaert and Hermisson, 2018). This further highlights the impact of the genetic architecture for DMI stability during speciation. In detail, the authors show that linkage patterns of DMI loci are essential for more complex DMI evolution and growth of the isolation barrier from an initial seed additional to the prerequisite that gene flow is sufficiently weak. The impact of linkage is also underlined by related results in hybrid speciation, where linkage patterns of DMI loci make or break the potential for the formation of a hybrid species, that is separate of both of its parental populations (Blanckaert and Bank, 2018).

Finally, concerning the results of easier autosomal introgression compared to X-introgression, I find that the observation agrees with empirical data, where often autosomal introgression is pervasive, while X-linked divergence is much more pronounced, with examples from the complex of *Anopheles gambia* sister clade (Fontaine et al., 2015), hybrid zones in mice (Macholán et al., 2007; Liu et al., 2015) and different bird species (Sætre et al., 2003; Hooper and Price, 2015)

1.3 Polygenic adaptation (Chapter 3 and 4)

Below I introduce my work on polygenic adaptation of a complex trait, which consists of two projects. However, as they are conceptually tightly linked, I have chosen to present the results and conclusions together.

1.3.1 Background and motivation

While Darwin originally thought, that phenotypic adaptation was a rather slow process (Darwin, 1859), recent empirical examples show that adaptation can be so rapid, that it can easily be observed within a human life time (Hairston Jr et al., 2005; Hendry et al., 2008; Gingerich, 2009; Losos, 2014). There are many well documented examples

from natural populations, ranging from pigmentation changes in the peppered moth (Cook et al., 2012), apple maggot flies adapting to specific food sources (apple races) (reviewed in Reznick, 2011) or beak size alterations in Darwin's finches (Grant and Grant, 2008, 2011), as well as results from evolutionary experiments (Burke et al., 2010; Kolbe et al., 2012; Franssen et al., 2017; Zan et al., 2017; Barghi et al., 2018, to cite but a few examples in *Drosophila*, lizards or chickens). These high rates of adaptation are of particular interest, as they nourish hope, that the recent accelerated climate change still might leave limited possibilities for some organisms to adapt and evade extinction (Gingerich, 2009; Kopp and Matuszewski, 2014; Losos, 2014).

In Chapter 3 and 4, I investigate the initial phase of rapid phenotypic adaptation of a complex trait to a new phenotypic optimum. Interestingly, it is still unclear, how rapid adaptation generally proceeds on the genomic level and different models have focused on variable aspects of the process. However, the sparsity of comprehensive treatments including all possible evolutionary trajectories is surprising. On the one side quantitative genetics rests on the infinitesimal model by Fisher (1918) (see also Barton et al., 2017) or on one dimensional summary statistics, *e.g.* means and variance, yet it does not disentangle individual allele frequency dynamics (*e.g.* Turelli and Barton, 1990, 1994; Bürger and Lynch, 1995; Bürger, 2000; Rice, 2004)) In contrast, models covering selective sweeps (in the tradition of Maynard-Smith and Haigh, 1974), or adaptive walks (consecutive fixations) (Geritz et al., 1998; Orr, 2005; Matuszewski et al., 2015) concentrate on adaptive substitutions. In this context, (Chevin and Hospital, 2008) constituted a novel starting point. Based on (Lande, 1983), these authors studied adaptation at a single QTL on an "infinitesimal background". Subsequently, (Pavlidis et al., 2012; Wollstein and Stephan, 2014) also focused on allele frequency changes at 2-8 QTL. Nevertheless, patterns of comprehensive polygenic adaptation are largely neglected as these studies do not consider the collective adaptive dynamics at *many* individual loci within the trait basis without a background. In the current study, I base my models on recent work by (de Vladar and Barton, 2014; Jain and Stephan, 2015, 2017), who have

studied rapid adaptation of a QT under stabilizing selection in a deterministic framework.

Here I study two models of adaptation of a trait with a polygenic basis consisting of a discrete number of loci, following individual allele frequency dynamics under the influence of selection, mutation and genetic drift. I resolve the adaptive architecture, upon phenotypical adaptation for a binary trait with a polygenic, functionally redundant basis (Chapter 3) and I extend the investigations to a QT under stabilizing selection (Chapter 4). Our model choice allows for a comprehensive analysis of all adaptive architectures, from selective sweeps to subtle frequency shifts, or any intermediate patterns. I emphasize that to obtain concerted, small frequency shifts as adaptive pattern, when following a trait governed by a finite number of loci, I require negative epistasis within the polygenic basis. Alternatively, strict additivity for fitness results in parallel and/or consecutive sweeps, while individual alleles cannot dampen the rise of alleles at other loci. Adaptation via concerted frequency shifts therefore constitutes a collective adaptation pattern of the entire genetic trait basis.

For the binary trait model in Chapter 3, strong negative epistasis between all loci is a natural consequence of complete redundancy (fixation of a single derived allele results in complete phenotypic adaptation of the population). Later I relax this stringent condition to include diminishing returns epistasis. Alternatively, in Chapter 4 individual genotypic effects are additive, yet the curvature of the fitness function (genotype-phenotype map) results again in diminishing returns epistasis, enabling all adaptive architectures from sweeps to shifts. Yet the distance to the new optimum determines the strength of the redundancy and thereby also influences the strength of negative epistasis in the QT-model.

I find a striking uniformity of mainly three different adaptive patterns for different trait basis sizes, that are determined by a single compound parameter, the background population mutation rate Θ_{bg}. This parameter effectively measures the degree of functional redundancy within the trait basis and delimits whether I mostly obtain completed, single sweeps, a combination of completed and partial sweeps, or small, concerted fre-

quency shifts at many loci. Additionally, I find that selection strength and standing genetic variation (SGV) do not affect the adaptive architecture (Chapter 3 and 4) and that my results readily extend to linked loci and diploids (Chapter 3). Finally, I also include alternative starting conditions deviating from mutation-selection-drift equilibrium (Chapter 3). I complement the extensive numerical investigations with the introduction of a comprehensive, analytical framework and derive well fitting, complex analytical predictions for the adaptive architectures of a complex trait.

1.3.2 Models

To study the adaptive architectures of a complex trait governed by a polygenic basis, I study two different models: First I study adaptation of binary trait with a strongly redundant, genetic basis ("redundant" or "binary trait model") and second I follow adaptation of a QT ("QT-model") under stabilizing selection to a new optimum. Each time I focus on a haploid, panmictic population of size N_e and track individual allele frequencies. The polygenic basis consists of L biallelic loci (ancestral/derived: a_i, A_i), with allelic mutation rate μ_l.

From the single locus equations at time t

$$\dot{p}_{A_i} = \Big(\omega^*_{A_i}(t) - \bar{\omega}(t)\Big)p_{A_i} \tag{1}$$

with marginal and mean fitness $\omega^*_{A_i}$ and $\bar{\omega}$, I obtain very similar frequency dynamics for the two models. In the case of the redundant trait model, I derive

$$\dot{p}_{A_i} = s(t)p_{A_i}\bigg(Z_{opt} - \bar{Z}(t)\bigg), \tag{2}$$

with the optimum and the mean phenotype $Z_{opt}(t)$ and $\bar{Z}(t)$ and selection strength $s(t)$.

In the QT-model I obtain two "sub-models", one emphasizing directional selection, *i.e.* the "directional selection model"

$$\dot{p}_{A_i} = \sigma \gamma_{A_i} p_{A_i}(1 - p_{A_i}) \left(Z_{\text{opt}} - \bar{Z} \right) \tag{3}$$

and a more complex QT-model also capturing the decrease of genetic variance by allele sorting, *i.e.* the "full model"

$$\dot{p}_{A_i} = \sigma \gamma_{A_i} p_{A_i}(1 - p_{A_i}) \left(Z_{\text{opt}} - \bar{Z} - \frac{\gamma_{A_i}}{2}(1 - 2p_{A_i}) \right) \tag{4}$$

with selection strength in the QT-model , corresponding to selection in the binary trait model, $\sigma \cdot \gamma_{A_i} = s$

The dynamical equations obtained for the QT-model also coincide with models studied in previous papers (de Vladar and Barton, 2014; Jain and Stephan, 2015, 2017).

In both cases, the redundant model and the QT-model, I study rapid adaptation either from the ancestral state via de novo mutations or evolving from standing genetic variation (SGV) built up under mutation, selection and drift. This entails that my results capture the adaptive architecture, once the population has reached the new phenotypic optimum, while they neglect long-term dynamics after selection has ceased.

For both approaches, I derive a comprehensive analytical framework to predict the expected adaptive architecture. This is based on partitioning the rapid adaptive phase into an early stochastic phase, governed by mutation, drift and selection, and a subsequent deterministic phase, governed mainly by epistasis and selection. I describe the early phase via the stochastic *Yule process* and prove that the results transmit through to the end of the deterministic phase. Upon some transformations, accounting for different stopping conditions (when I sample the population, usually conditioned on mean fitness reaching a certain threshold) and assuming linkage equilibrium, I finally obtain a joint distribution of derived allele frequencies, a family of inverted *Dirichlet distributions* describing the adaptive architecture of the polygenic trait. From that, I obtain the marginal distribution of the loci contributing most significantly to adaptation. Interestingly all these predictions are independent of selection strength, before or after the

change in the environment, conditioned on equal effects of each locus. I contrast the analytical results with extensive Wright-Fisher simulations.

1.3.3 Results

In my investigations I discern the "major" locus as the locus with the highest frequency change and hence the locus which contributed most to adaptation, from all other $L-1$ loci. I refer to the latter as "minor" loci, called first, second, third, *etc.* minor, according to their (smaller) contributions. This is in good agreement with empirical practice, as in a case control GWAS study a major locus with the strongest frequency change compared to an out-group, would also give the highest signal (*e.g.* Visscher et al., 2012, 2017). Keep in mind, that as the effect size of all major and minor loci are all equivalent. With adaptation from de novo mutations (in Chapter 3 & 4) or SGV built up under negative selection (only valid in Chapter 3), the major locus is equal to the locus with highest frequency at the end of the adaptive phase. However, the definition based on *effective frequency change* is more general, as it always described the locus that contributed the most to adaptation as the "major" locus.

Using a small trait basis of $L = 2$ in the redundant trait model the ratio of the first minor allele over the major allele, serves as as a initial, one-dimensional estimator, $E[x]$, Eq. (3.9) in dependence of the population mutation rate. It yields a crude distinction of "homogeneous"($E[x] \approx 1$) and "heterogeneous" adaptive architectures ($E[x] \approx 0$), where the major and the first minor locus show qualitatively similar/different behavior (different $=$ it acts as a sole main contributor to adaptation). I show that this ratio stays constant over the entire adaptive phase (Section 3.3.4 and D.1), and is hence independent of the time of sampling. $E[x]$ is also independent of selection strength and SGV (Fig. 3.3), as predicted, as well as unaltered by linkage (Fig. C.1).

Similarly, with the QT-directional selection model, as predicted, selection strength and time of sampling do not impact the resulting adaptive architecture (Fig. 4.1), irrespective of the L. In contrast, for the full model I only obtain independence of selection,

as long I sample the population far away from the optimum, while at complete adaptation, weaker selection results in more polygenic architectures with 2 loci.

As I cannot obtain predictions for marginal distributions for basis $L \gtrsim 5$, I aim to extend the two or few loci ($k << L$) formalisms to larger basis. To do so I need to account for the aberrant waiting times between the arrival of a successive mutation and its predecessor, (assuming that with low enough mutation rates the order of appearance of mutations reflects the their contribution to final adaptation). From the waiting time between the first minor and the major I recuperate the *cumulative background mutation rate*

$$\Theta_{bg} := 2(L-1)N_e\mu_l = \Theta_l(L-1) \tag{5}$$

as the parameter of interest (effective population size N_e, locus mutation rate per individual and generation mu_l, trait basis size L). It turns out, that Θ_{bg} acts as the single, decisive compound parameter for the resulting adaptive architecture (see Section 3.4.1). Effectively, it is a measure of redundancy within the trait basis, as it describes the mutational pressure a single, rising focal locus has to compete against in a completely redundant trait basis. With reduced redundancy this generalizes to the rescaled rate

$$\Theta'_{bg} := \Theta_l(L'-1), \tag{6}$$

with $L' \leq L$, the number of effectively equivalent/redundant loci in the basis. Using the appropriate Θ'_{bg} $k-$locus based approximations easily extend to larger trait basis and arbitrary redundancy, as long as mutation rates are not too high.

Based on the principal factor, Θ_{bg} I differentiate three main adaptive patterns (Fig. 3.4, 4.2 and 4.3) which are strikingly uniform for the different models and increasing L : For very small Θ_{bg} single sweeps predominate. For large Θ_{bg} I find small concerted allele frequency shifts, the common expectation for polygenic adaptation. Finally, for intermediate Θ_{bg} I observe an intermediate pattern, characterized by a combination of complete and partial sweeps at several loci. While these three main adaptive architectures occur

in both model, the exact bounds of transition between them vary. Tendentiously, the QT-model (especially the directional selection model) yields more polygenic architectures, such that I transition from single sweeps to several sweeps at $\Theta_{bg} \geq 0.1$ and obtain shifts at $\Theta_{bg} \geq 10$. In the redundant trait model, these bounds based on Θ_{bg} are approximately one magnitude larger, such that I obtain the intermediate, multiple (complete and partial) sweep pattern for $1 \leq \Theta_{bg} \leq 10$, and single sweeps and frequency shifts below and above, respectively.

These qualitative patterns are conserved with relaxed redundancy (two mutational steps to the new optimum: Fig. 3.5, 4.4 and 4.5). Especially, the abundance of small frequency shifts is completely unchanged.

It is remarkable that by the single, required rescaling of Θ'_{bg}, I am able predict the observed patterns perfectly. I cannot only predict the behavior of major and minor loci with reduced redundancy in the redundant trait model (Fig. 3.5), but also the adaptive dynamics of successive contribution of several major loci during the course of adaptation in the QT-model (see Fig. 4.12 and 4.13). For the QT-model I also include adaptation from SGV at a phenotypic optimum in the phenotypic range, to a new optimum, and recuperate the same qualitative, adaptive patterns, which I can also predict with a good fit based on Θ'_{bg}.

Next, in the redundant trait model, I investigate the impact of linkage (Fig. C.2) and diploids (Fig. C.4) in LE. The qualitative pattern and the threefold classification remains unchanged in both cases. I also provide analytical predictions for diploids and for completely linked loci. Finally, studying alternative starting conditions I find that the adaptive architecture is crucially depending on them at selection onset. While starting from mutation-selection-drift equilibrium, shift patterns require a relatively high Θ_{bg}, deviations can result in frequency shifts at much lower mutation rates. This is also one of the main explanations for the diverging results in preceding studies of polygenic adaptation (de Vladar and Barton, 2014; Jain and Stephan, 2015, 2017) which all ignore genetic drift.

1.3.4 Discussion

It is quite striking that despite the complexity of the different models of rapid adaptation of complex traits, I am able to provide a uniform, threefold classification of different adaptive architectures, all based on a single, compound parameter, $\Theta_{bg} = 2N_e\mu(L - 1)$ (in haploids, $= 4N_e\mu(L - 1)$ in diploids), a measure of within trait redundancy. Namely, *single sweeps* dominate the adaptive pattern for low Θ_{bg}, while for large Θ_{bg} small, concerted *frequency shifts* prevail. I point out, that while the implemented strong negative epistasis, together with the equal locus effects (supporting redundancy) should be most favorable to shifts, I require relatively large Θ_{bg} to obtain them. For intermediate Θ_{bg}, the adaptive architecture is best characterized by a combination of completed and partial sweeps. Concerning the exact bounds of Θ_{bg} between the different architectures, I find that the QT-directional selection model yields the a more polygenic response, than the redundant trait model. With the full QT-model results are variable, where earlier sampling and larger basis by trend result in more polygenic response similar to the directional QT-model. Below I want to disentangle the different parameter influencing Θ_{bg}.

Trait basis size

The span of how many loci actually contribute to rapid adaptation of a complex trait is huge, ranging from a single or a few to a myriad of loci (*e.g.* Mackay, 2009; Lamichhaney et al., 2015; van't Hof et al., 2016; Barghi et al., 2018). However, the general parameter $\Theta'_{bg} = 2N_e\mu(L' - 1)$, describes only the subset of truly redundant loci L'. Therefore, the resulting adaptive architecture for a given complex trait could very well be a composition of my results for redundant submodules of the trait.

Population size N_e and genetic drift

Also effective population sizes are an elusive measure and are a hotly debated concept (Hermisson and Pennings, 2017). In the case of adaptation, N_e relying on neutral

diversity constitute a massive underestimate. *E.g* in humans $N_e = 10\,000$ is often reported, driven by the out of Africa bottle neck, yet strong selective pressures might operate on a much small time scales, which requires taking the more recent population expansion into account.

The effective population size is also the decisive factor for the strength of genetic drift. Previous analytical work in deterministic models predicted a prevalence of more polygenic, shift-like architectures (de Vladar and Barton, 2014; Jain and Stephan, 2015, 2017). I mainly attribute the deviating outcomes to the effect of genetic drift, affecting the standing genetic variation: First, drift strongly affects the early phase of adaptation. While deterministic frameworks start from homogeneous intermediate allele frequencies, mutation-selection-drift equilibrium results in a strongly skewed SGV distribution. My result thus reflects the effects of genetic drift during the early phase of adaptation.

Second, genetic drift also plays another role, after phenotypic adaptation has been accomplished, which is not captured by my results. Hence they do not represent a *stationary* distribution, but are transient by nature. Yeaman (2015) showed that if a quantitative trait under selection is governed by large number of redundant alleles of small effects size, which by themselves are prone to swamping, there is still considerable, rapid phenotypic adaptation possible. Yet, the underlying adaptive architecture, and with that the particular alleles, is transient due to constant allelic turnover. Yeaman and Whitlock (2011) further demonstrate that with stabilizing selection, migration and drift, genetic architectures will evolve towards fewer large effect loci. So a given adaptive architecture for a phenotypically adapted trait still might change substantially, such that small effect alleles will eventually be out-competed by few newly evolved, large effect alleles, probably under less pleiotropic constraints. Thus it is possible that the original adaptive architecture underlying the rapid phenotypic change might be hard to detect due to its ephemeral nature, while the long lasting genomic footprint of adaptation is clearer. As a consequence, time scales partition into the initial rapid adaptation and a long-term stabilization phase marked by larger effect substitution. This decoupling

is also observed in evolution experiments, such as Franssen et al. (2017), who show that rapid adaptation precedes the phase of allele sorting and final manifestation of the long-lasting adaptive architecture.

Mutation rate

The allelic mutation rate μ highly depends on the genomic architecture of a given allele. While for single nucleotide polymorphisms (SNP) the mutation rates are mostly fixed, adaptive loss of function mutations might be much easier to attain due to a larger target size for functional disruption of a trait.

Population structure

Finally, population structure or gene flow before the start of the selective phase can have a strong effect on the available genetic variation in a population. In particular, if for example the population is admixed, mutant alleles might segregate far from selection-mutation-drift equilibrium at intermediate frequencies, which would results in small, concerted frequency shifts. This might be on causal factor for the lack of sweep patterns underlying adaptation in modern human populations (Pritchard et al., 2010), as modern European human populations have experienced major admixture events in their history (Lazaridis et al., 2016; Pickrell and Reich, 2014).

Conclusion and outlook

To answer which adaptive architecture to expect for a given trait, I hence need to predict the appropriate Θ_{bg}. Two current examples of estimates of Θ_l are $\lesssim 0.1$ for *Drosophila*, and $\lesssim 0.01$ for humans (Hermisson and Pennings, 2017). From these estimates, I still would need a rough idea about the number of redundant loci within a trait basis and the starting allele frequency distribution of segregating alleles, to predict the prevalence of shifts over sweeps. For example (Barghi et al., 2018) find approximately 100 putative targets of artificial selection for temperature adaptation in *Drosophila* in separate repli-

cates. With humans, currents estimates for the number of loci involved in human height go into the hundreds or thousands (Field et al., 2016; Berg et al., 2018; Sohail et al., 2018), so subtle frequency shifts are very well within or close to the scope of potential adaptive responses for both organisms.

One clear limitation of the presented models, is the assumption of uniformity of effects, concerning equal selection coefficients. These extensions are currently work in progress. Yet, I predict that different locus effects, cause more heterogeneous starting conditions, which in turn have proven to be most favorable of sweeps, while they do not boost the abundance of polygenic frequency shifts. Yet, I am uncertain if I will be able to include strong deviations from uniform selection coefficients in the analytical approximations.

A second limitation concerns population structure, as I only treat panmictic populations with constant size. Changes in these parameters will most certainly influence the resulting adaptive architectures. These interesting investigations are left for future explorations.

2 Bounds to parapatric speciation: A Dobzhansky-Muller incompatibility model involving autosomes, X chromosomes and mitochondria

Reference:

Hoellinger, Ilse, and Joachim Hermisson. "Bounds to parapatric speciation: A Dobzhansky–Muller incompatibility model involving autosomes, X chromosomes, and mitochondria." Evolution 71.5 (2017): 1366-1380.

Abstract

We investigate the conditions for the origin and maintenance of postzygotic isolation barriers, so called (Bateson-)Dobzhansky-Muller incompatibilities or DMIs, among populations that are connected by gene flow. Specifically, we compare the relative stability of pairwise DMIs among autosomes, X chromosomes, and mitochondrial genes. In an analytical approach based on a continent-island framework, we determine how the maximum permissible migration rates depend on the genomic architecture of the DMI, on sex bias in migration rates, and on sex-dependence of allelic and epistatic effects, such as dosage compensation. Our results show that X-linkage of DMIs can enlarge the migration bounds relative to autosomal DMIs or autosome-mitochondrial DMIs, in particular in the presence of dosage compensation. The effect is further strengthened with male-biased migration. This mechanism might contribute to a higher density of DMIs on the X chromosome (large X-effect) that has been observed in several species clades. Furthermore, our results agree with empirical findings of higher introgression rates of autosomal compared to X-linked loci.

2.1 Introduction

Historically, speciation research has mostly focused on two idealized scenarios: allopatric speciation (complete geographic isolation of incipient species) and sympatric speciation (divergence of subpopulations in a common habitat) (Orr and Turelli, 2001; Coyne and Orr, 2004; Via and West, 2008). Both scenarios are simplifications of biological reality. While strict sympatry of incipient species seems to be an exception, there is abundant evidence for hybridization even among "good species" with viable and not completely sterile hybrid offspring (reviewed *e.g.* in Coyne and Orr, 2004; Mallet, 2008). Population genetic theory shows that even low levels of gene flow can strongly interfere with population differentiation (Felsenstein, 1981; Slatkin, 1987). This makes it inevitable to assess the impact of limited gene flow at various stages of the speciation process, a scenario commonly referred to as parapatric speciation.

The classical model for the evolution of postzygotic isolation barriers in allopatry is the (Bateson-)Dobzhansky-Muller model (DMM) (Bateson, 1909; Dobzhansky, 1936; Muller, 1942). The DMM assumes that new substitutions occur on different genetic backgrounds. When brought into secondary contact, these previously untested alleles might be mutually incompatible and form Dobzhansky-Muller incompatibilities (DMIs), thus reducing hybrid fitness and decreasing gene flow at linked sites. The emergence of species boundaries due to accumulation of DMIs in allopatry is well understood (Coyne and Orr, 1989; Orr and Turelli, 2001; Coyne and Orr, 2004). More recently, several studies have considered this process in parapatry (Gavrilets, 1997; Feder and Nosil, 2009; Agrawal et al., 2011; Bank et al., 2012; Wang, 2013; Lindtke and Buerkle, 2015). All support that the DMM provides a viable mechanism for the evolution of postzygotic isolation even in the presence of gene flow, although the bounds for maximum permissible migration rates can be quite stringent.

Empirically, there is widespread evidence for DMIs not only among recently diverged sister species (Maheshwari and Barbash, 2011; Presgraves, 2010; Sweigart and Flagel,

2014), but also segregating within species (Corbett-Detig et al., 2013). Hence, these authors argue that the genetic basis of reproductive isolation is continuously present within natural populations, rendering the independent allopatric evolution of newly incompatible substitutions obsolete.

While most theoretical studies focus on autosomal DMIs, empirical evidence points to a major role of sex chromosomes in speciation. Haldane's rule (Haldane, 1922, reviewed in Coyne and Orr, 2004), states that in species with sex specific reduced hybrid fitness the affected sex is generally heterogametic. The *large X-effect* (Coyne and Orr, 1989, reviewed in Presgraves, 2008) expresses the disproportional density of X-linked incompatibility genes in postzygotic isolation. For example Masly and Presgraves (2007) report a higher density of incompatibilities causing hybrid male sterility on the X chromosome relative to autosomes in *Drosophila*. Equivalent findings exist of a *large Z-effect* in WZ-systems, such as birds, where WZ-females are heterogametic (Ellegren, 2009). Also cytoplasmic incompatibilities have been described (Ellison and Burton, 2008; Lee et al., 2008; Burton and Barreto, 2012; Barnard-Kubow et al., 2016).

A recent study by Bank et al. (2012) determined stability conditions and maximum permissible migration rates of autosomal two-locus DMIs in a continent-island framework. They distinguished two main mechanisms shaping the evolution of DMIs: selection against (maladapted) immigrants and selection against (unfit) hybrids, which lead to different dependence of maximum migration rates on the model parameters.

Prompted by the empirical observations described above, we extend the model by Bank et al. (2012) to general two-locus DMIs in diploids involving X chromosomes, autosomes, or mitochondria. We include sex-specific fitness effects, in particular, to account for the effect of dosage compensation of hemizygous X-linked genes in males. We also allow for sex-specific migration, as many species display differences in migration patterns for males and females Greenwood (1980).

Following Bank et al. (2012) we derive maximum migration bounds where DMIs can still originate in parapatry, or resist continental gene flow. In contrast to the autosomal

case, we find that sex specific fitness- and sex-biased migration cause substantial differences in the maximum permissible rates and hence influence the prevalence of autosomal DMIs relative to X-linked and mitochondrial DMIs. Especially, we find that X-linkage of (nuclear or cytonuclear) DMIs together with dosage compensation and/or male-biased migration boosts migration bounds and thus enhances the evolution of X-linked DMIs, possibly contributing to a *large X-effect* and to reduced introgression probabilities of X-linked DMI loci.

2.2 Model and Methods

We consider a diploid, dioecious population with separate sexes (at 1:1 ratio) that is divided into two panmictic subpopulations, continent and island. (See Fig. 2.1 and Fig. B.1 in the Supporting Information (SI)). Both demes are sufficiently large that drift can be ignored (drift effects are discussed in SI Section A.3). They are connected by unidirectional sex-dependent migration at rate $m^{\female}$ and $m^{\male}$ from the continent to the island. We fix the average migration rate per individual, $m = \frac{m^{\female}+m^{\male}}{2}$, and define

$$R := \frac{m^{\female} - m^{\male}}{m^{\female} + m^{\male}} \in [-1, 1] \tag{2.1}$$

as a measure of sex-bias in migration. Sex-specific migration gives rise to distinct migration rates per allele for autosomes, X chromosomes, and mitochondria, $m_{\mathcal{A}}$, $m_{\mathcal{X}}$, and $m_{\mathcal{O}}$ (Eqs. (B.5)-(B.7)). For $-1 \leq R < 0$ migration is male-biased and we obtain $m_{\mathcal{A}} > m_{\mathcal{X}} > m_{\mathcal{O}}$. In contrast, for $0 < R \leq 1$ migration is female-biased, resulting in $m_{\mathcal{A}} < m_{\mathcal{X}} < m_{\mathcal{O}}$.

The DMI

The incompatibility is formed by two unlinked biallelic loci, situated on autosomes $\mathcal{A}$, X chromosomes $\mathcal{X}$, or in the mitochondrial genome (cytoplasmic organelle) $\mathcal{O}$, (cf. Table 2.1). Both sexes are diploid for autosomes and haploid for the mitochondrial

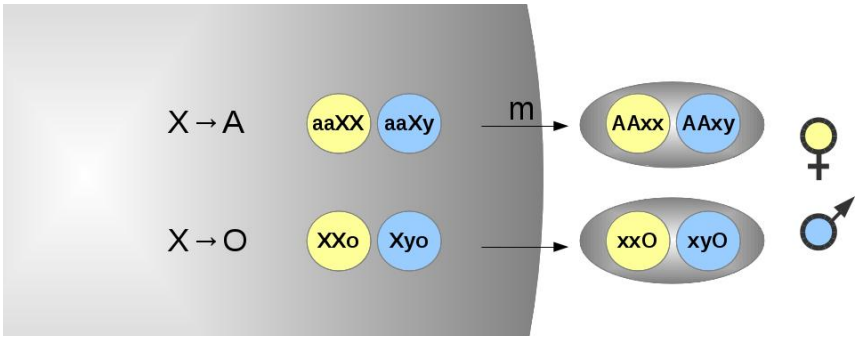

Figure 2.1: **Schematic model.** The population inhabits a continent (left) and an island (right), which are connected by unidirectional migration at rate m. The figure shows two out of eight genomic architectures investigated: an X-autosome DMI (upper line) and a cytoplasmic DMI between X and mitochondrion (lower line). Genotypes of female residents are depicted by yellow circles and males by blue circles, respectively. The capital letters denote incompatible alleles, which reduce hybrid fitness.

locus. Males are hemizygous for the X chromosomes, whereas females are diploid. The continent is monomorphic for the continental (geno-)type and only acts as source of migrants for the island. Our analysis focuses on the evolutionary dynamics on the island. A stable DMI corresponds to a stable equilibrium on the island where all four alleles are maintained (a two-locus polymorphism), including the pair of incompatible alleles (indicated by capital letters in Table 2.1).

We model genotypic fitness as the sum of direct allelic fitness and epistasis. Hence any given allele contributes directly to genotype fitness, where it can be locally or globally adapted. Additionally it can contribute via epistasis if it is incompatible with other alleles in the same genotype. We set the (Malthusian) fitness of genotypes containing no incompatible alleles (only lower case letters) in both sexes to 0. For simplicity, we assume no dominance of the single-locus effects, but we allow for dominance or recessitivity of the incompatibility.

We define the fitness of an arbitrary female genotype as

$$\omega(G^{\female}) = \underbrace{n_{\mathsf{C}} \cdot \sigma_{\mathsf{C}}^{\female} + n_{\mathsf{I}} \cdot \sigma_{\mathsf{I}}^{\female}}_{\text{allelic fitness}} - \underbrace{\Gamma_*(G^{\female})}_{\text{epistasis}} \tag{2.2}$$

Different genomic architectures of DMIs.

Model	DMI	continental type (♀,♂)	island type (♀,♂)
A→A	$\mathcal{A}$-$\mathcal{A}$	aaBB	AAbb
X→A	$\mathcal{A}$-$\mathcal{X}$	aaXX, aaXy	AAxx, AAxy
A→X	$\mathcal{A}$-$\mathcal{X}$	AAxx, AAxy	aaXX, aaXy
X→X	$\mathcal{X}$-$\mathcal{X}$	$X_1X_1x_2x_2$, X_1x_2y	$x_1x_1X_2X_2$, x_1X_2y
A→O	$\mathcal{A}$-$\mathcal{O}$	AAo	aaO
O→A	$\mathcal{A}$-$\mathcal{O}$	aaO	AAo
X→O	$\mathcal{X}$-$\mathcal{O}$	XXo,Xyo	xxO,xyO
O→X	$\mathcal{X}$-$\mathcal{O}$	xxO,xyO	XXo,Xyo

Table 2.1: Each genomic architecture is defined by a continental (geno-)type (third column) and an island (geno-)type (fourth column). Mutually incompatible pairs of DMI-alleles are denoted by capital letters. We call the immigrating DMI-allele *continental allele* and its resident incompatible partner *island allele*. The name of each model in the first column is constituted by "the continental allele → the island allele". The A→A-model corresponds to the model by Bank et al. (2012).

or for a male genotype as

$$\omega(G^{\male}) = n_{\mathsf{C}} \cdot \sigma_{\mathsf{C}}^{\male} + n_{\mathsf{I}} \cdot \sigma_{\mathsf{I}}^{\male} - \Gamma_*(G^{\male}). \tag{2.3}$$

The allelic fitness is captured by the selection coefficient $\sigma^{\female}, \sigma^{\male}$ (for females and males) and weighted with the respective number of incompatible alleles, $n_{\mathsf{C,I}} \in \{0, 1, 2\}$ in a given genotype. To match the locus effects of haploid mitochondrial genes to autosomes, we set $n_{\mathsf{C,I}} \in \{0, 2\}$ for the absence or presence of the single incompatible allele in this case.

We assume $\sigma^{\male} = \sigma^{\female}$ for autosomes and organelles, but for X-linked alleles the fitness effect may be enhanced in males, $\sigma^{\male} = (1+D)\sigma^{\female}$, where $D \in \{0, 1\}$ measures dosage compensation (see below). The contribution of epistasis to hybrid genotype fitness can be summarized by an epistasis vector Γ_*, for each model ($_*$), detailed in Table 2.2

Strength of the incompatibility: The epistasis vector

DMI	hybrids: ♀,♂	epistasis vector Γ_*
$\mathcal{A}$-$\mathcal{A}$	♀: AaBb, AaBB, AABb, AABB ♂ AaBb, AaBB, AABb, AABB	$\Gamma_{\mathcal{AA}} = (\underbrace{\gamma_1, \gamma, \gamma, 2\gamma}_{♀}, \underbrace{\gamma_1, \gamma, \gamma, 2\gamma}_{♂})$
$\mathcal{A}$-$\mathcal{X}$	♀ : AaXx, AaXX, AAXx, AAXX, ♂: AaXy, AAXy	$\Gamma_{\mathcal{AX}} = (\gamma_1, \gamma, \gamma, 2\gamma, (1+D)\frac{\gamma}{2}, (1+D)\gamma)$
$\mathcal{X}$-$\mathcal{X}$	♀: $X_1x_1X_2x_2$, $X_1x_1X_2X_2$ $X_1X_1X_2x_2$, $X_1X_1X_2X_2$, ♂: X_1X_2y	$\Gamma_{\mathcal{XX}} = (\gamma_1, \gamma, \gamma, 2\gamma, (1+3D)\frac{\gamma}{2})$
$\mathcal{A}$-$\mathcal{O}$	♀: AaO, AAO, ♂: AaO, AAO	$\Gamma_{\mathcal{AO}} = (\gamma, 2\gamma, \gamma, 2\gamma)$
$\mathcal{X}$-$\mathcal{O}$	♀: XxO, XXO, ♂: XyO	$\Gamma_{\mathcal{XO}} = (\gamma, 2\gamma, (1+D)\gamma)$

Table 2.2: The table shows all possible hybrid genotypes with DMIs (second column) and corresponding fitness cost, parametrized by the entries of the epistasis vector (third column). The strength of the incompatibility depends on the number of incompatible alleles in the genotype. Plausibly, the strength increases with the number of incompatible pairs, which can be 1, 2, or 4 (Turelli and Orr, 2000). We focus on two particular epistasis schemes, one with a codominant DMI ($\gamma_1 = \frac{\gamma}{2}$) with fitness cost proportional to the number of incompatible pairs and one with a recessive DMI ($\gamma_1 = 0$) where the fitness cost is zero if there is still a pair of compatible alleles in the genotype. The strength of X-linked incompatibilities in males depends on dosage compensation, captured by $D \in \{0, 1\}$.

Dosage compensation

Dosage compensation can be related to different mechanisms. For example, in the model organism *Drosophila melanogaster* the expression of the X chromosome is doubled in males. An alternative mechanism has evolved in mammals, where one X chromosome is randomly inactivated in females (Payer and Lee, 2008). Finally, in birds dosage compensation seems to be incomplete, as some genes show elevated expression levels in homogametic ZZ-males compared to heterogametic females, whereas other genes are dosage compensated (Ellegren et al., 2007; Graves et al., 2007).

Our model allows for arbitrary sex-dependence of allelic and epistatic effects, but we focus on dosage compensation of the hemizygous X chromosome in males as a key biological mechanism. We model fitness for any X-linked allele in hemizygous males in two ways (Charlesworth et al., 1987):

- *No dosage compensation,* $D = 0$: A single copy of an X-linked allele has the same

allelic ($\sigma^{\male} = \sigma^{\female}$) and epistatic effects in hemizygous males as in females.

- *Full dosage compensation,* $D = 1$: Hemizygosity of the X chromosome is compensated in males, and a single X-linked allele has the same effect as a homozygous pair of X chromosomes in females (allelic selection coefficient: $\sigma^{\male} = 2\sigma^{\female}$).

With random deactivation of X in females we naturally obtain a codominant DMI in our model since (average) heterozygous fitness is equal to the mean of the homozygous fitnesses in this case.

Dynamics of the general model

For our analytical treatment, we assume weak evolutionary forces, such that linkage equilibrium among both loci and Hardy-Weinberg-proportions can be assumed. It is then sufficient to track the frequencies of the continental allele p_{C} and the island allele p_{I} on the island. We test this approximation for stronger selection by numerical simulations in SI Section A.2.

For each genomic architecture (Table 2.1) we derive a pair of differential equations in continuous time (see **Box 1**). For the case of an X→A DMI, in particular, p_{C} measures the frequency of the incompatible X allele that immigrates from the continent and p_{I} the frequency of the incompatible autosomal allele on the island. We obtain:

$$\begin{aligned}
\dot{p}_{\mathsf{C}} &= p_{\mathsf{C}}(1-p_{\mathsf{C}})\left(\tfrac{3+D}{3}\sigma_{\mathsf{C}}^{\female} + \tfrac{2}{3}p_{\mathsf{I}}\Big((2p_{\mathsf{C}}(1-p_{\mathsf{I}})+p_{\mathsf{I}})(2\gamma_1-\gamma) - 2\gamma_1 - \tfrac{\gamma}{2}(1+D)\Big)\right) \\
&\quad +(1-p_{\mathsf{C}})(1+\tfrac{R}{3})m \\
\dot{p}_{\mathsf{I}} &= p_{\mathsf{I}}(1-p_{\mathsf{I}})\left(\sigma_{\mathsf{I}}^{\female} + \tfrac{1}{2}p_{\mathsf{C}}\Big((2p_{\mathsf{I}}(1-p_{\mathsf{C}})+p_{\mathsf{C}})(2\gamma_1-\gamma) - 2\gamma_1 - \tfrac{\gamma}{2}(1+D)\Big)\right) \\
&\quad -p_{\mathsf{I}}m
\end{aligned} \tag{2.4}$$

We see that with dosage compensation ($D = 1$), the X-linked allelic fitness is increased ($\frac{4}{3}\sigma_{\mathsf{C}}^{\female}$), because a single X-allele in males now acts as strongly as two X-alleles in females. Similarly, dosage compensation increases the term due to epistasis in males ($\frac{\gamma}{2}(1+$

D)) affecting both the X-linked allele and the autosomal allele. Sex-biased migration, quantified by R (see Eq. 2.1), affects only the X-linked allele, as males are hemizygous X carriers. Parameterizations for all other cases are provided in the SI Section B.1.

Box 1:

Dynamics of the continental allele frequencies p_{C}:

$$\dot{p}_{\mathsf{C}} = \begin{cases} \text{for } \mathcal{A}: & p_{\mathsf{C}}\Big(\frac{\omega_{\mathsf{C}}^{*\mathsf{Q}}+\omega_{\mathsf{C}}^{*\mathsf{O}}}{2} - \frac{\bar{\omega}^{\mathsf{Q}}+\bar{\omega}^{\mathsf{O}}}{2}\Big) & +(1-p_{\mathsf{C}})m \\ \text{for } \mathcal{X}: & p_{\mathsf{C}}\Big(\frac{2\omega_{\mathsf{C}}^{*\mathsf{Q}}+\omega_{\mathsf{C}}^{*\mathsf{O}}}{3} - \frac{2\bar{\omega}^{\mathsf{Q}}+\bar{\omega}^{\mathsf{O}}}{3}\Big) & +(1-p_{\mathsf{C}})(1+\frac{R}{3})\cdot m \\ \text{for } \mathcal{O}: & p_{\mathsf{C}}\Big(\omega_{\mathsf{C}}^{*\mathsf{Q}} - \bar{\omega}^{\mathsf{Q}}\Big) & +(1-p_{\mathsf{C}})(1+R)\cdot m \end{cases}$$

Dynamics of the island allele p_{I}:

$$\dot{p}_{\mathsf{I}} = \begin{cases} \text{for } \mathcal{A}: & p_{\mathsf{I}}\Big(\frac{\omega_{\mathsf{I}}^{*\mathsf{Q}}+\omega_{\mathsf{I}}^{*\mathsf{O}}}{2} - \frac{\bar{\omega}^{\mathsf{Q}}+\bar{\omega}^{\mathsf{O}}}{2}\Big) & -p_{\mathsf{I}}m \\ \text{for } \mathcal{X}: & p_{\mathsf{I}}\Big(\frac{2\omega_{\mathsf{I}}^{*\mathsf{Q}}+\omega_{\mathsf{I}}^{*\mathsf{O}}}{3} - \frac{2\bar{\omega}^{\mathsf{Q}}+\bar{\omega}^{\mathsf{O}}}{3}\Big) & -p_{\mathsf{I}}(1+\frac{R}{3})\cdot m \\ \text{for } \mathcal{O}: & p_{\mathsf{I}}\Big(\omega_{\mathsf{I}}^{*\mathsf{Q}} - \bar{\omega}^{\mathsf{Q}}\Big) & -p_{\mathsf{I}}(1+R)\cdot m \end{cases}$$

Marginal fitness $\omega_{\mathsf{C/I}}^{*\mathsf{Q}/\mathsf{O}}$ and mean fitness $\bar{\omega}^{\mathsf{Q}/\mathsf{O}}$ for each sex are functions of genotype fitness (consult SI Eqs. (B.1), (B.2) for explicit expressions). Sex-bias in migration m is measured by R (Eq. (2.1)).

The codominant model

If the effect of the incompatibility is additive, such that it is proportional to the number of incompatible pairs in a genotype ($\gamma_1 = \frac{\gamma}{2}$ in Table 2.2), the model simplifies greatly.

For the X→A model, in particular,

$$\begin{aligned} \dot{p}_{\mathsf{C}} &= (1-p_{\mathsf{C}})(\tfrac{3+D}{3}p_{\mathsf{C}}(\sigma_{\mathsf{C}}^{\mathsf{Q}} - \gamma p_{\mathsf{I}}) + (1+\tfrac{R}{3})m) \\ \dot{p}_{\mathsf{I}} &= p_{\mathsf{I}}((1-p_{\mathsf{I}})(\sigma_{\mathsf{I}}^{\mathsf{Q}} - \tfrac{(3+D)}{4}\gamma p_{\mathsf{C}}) - m) \end{aligned} \tag{2.5}$$

see SI Eqs. (B.26) for the other models.

Evolutionary histories

A parapatric DMI can evolve via different routes, depending on the timing and geographic location of the origin of the two mutations. Following Bank et al. (2012), we distinguish five histories: For *secondary contact*, both substitutions occur during an allopatric phase and can originate in any order. In contrast, if the substitutions originate in the presence of gene flow, the timing matters and we obtain four further scenarios: for a *continent-island* DMI we have the first substitution originating on the continent and the second on the island. Analogously, there are *island-continent*, *island-island*, and *continent-continent* scenarios. Note that the first two scenarios lead to *derived-derived DMIs*, with one substitution in each deme, whereas the last two lead to *derived-ancestral DMIs*, where both substitutions occur in the same deme. In all cases we refer to the immigrating incompatible allele as the *continental allele* and to the resident, incompatible allele as the *island allele*. All five evolutionary histories lead to the same dynamics (as given in **Box 1**) upon appropriate relabeling of genotypes, where different histories correspond to different initial conditions (see SI Section B.2 and "Mapping of evolutionary histories" below).

2.3 Results

Our analytical analysis of the dynamical system in **Box 1** is presented in comprehensive form in SI B.. It comprises the following steps. For the general model ($0 \leq \gamma_1 < \gamma$), we determine all boundary equilibria and conditions for their stability. Instability of all

boundary equilibria implies a protected polymorphism at both loci. Excluding cycling behavior, this is a sufficient condition for a globally stable DMI that will be reached from all starting conditions (all evolutionary histories). An internal stable equilibrium (DMI) can also coexist with a stable boundary equilibrium. In this case, the DMI is only locally stable and will only be reached from favorable starting conditions. Necessary and sufficient conditions for the existence of (locally or globally) stable DMIs can be derived for weak migration by means of perturbation analysis: A stable DMI results if the monomorphic boundary equilibrium ($p_{\mathsf{I}} = 1,\ p_{\mathsf{C}} = 0$) is stable for $m = 0$ and is dragged inside the state space for small $m > 0$. For codominant DMIs, also the internal equilibria can be assessed analytically and conditions for stable DMIs follow from a bifurcation analysis. For the recessive DMIs, we complement our analytical results by numerical work to derive stability conditions for locally stable DMIs under stronger migration.

Below, we summarize the key results for the general model. This is followed by a detailed analysis of the codominant model. In the supplement we added continuative results, first for the recessive model in SI Section A.1. Second, SI Section A.2 contains simulation results to assess the effects of linkage disequilibrium (LD), which is relevant for very strong incompatibilities. Third, we present simulations for finite populations and analyze how migration limits are affected by genetic drift in SI Section A.3. Finally, in SI Section A.4 we calculate adaptive substitution rates for autosomes and X chromosomes with gene flow and derive conditions on dominance favoring the *faster X-effect*, described by Charlesworth et al. (1987).

2.3.1 Evolution and maintenance of DMIs

Stable equilibria: global and local stability of DMIs

The model has three boundary equilibria: A monomorphic state, where the continental genotype swamps the island, which is always reached for strong migration. Furthermore, two single locus polymorphisms (SLPs) where one locus is swamped, but the other is

maintained polymorphic. There is at most one stable internal equilibrium, corresponding to a DMI. It can either be globally or locally stable. In the latter case, one of the boundary equilibria is also locally stable and it depends on the evolutionary history which equilibrium is reached. We therefore obtain two migration thresholds $0 \leq m^-_{\mathsf{max}} \leq m^+_{\mathsf{max}}$:

- For migration rates $0 \leq m < m^-_{\mathsf{max}}$, a globally stable DMI, that is reached for all evolutionary histories.
- For migration rates $0 \leq m^-_{\mathsf{max}} \leq m < m^+_{\mathsf{max}}$, the dynamics are bistable and yield a locally stable DMI. Hence, only certain evolutionary histories permit its evolution, but any existing DMI will be maintained.
- For migration rate $m^+_{\mathsf{max}} \leq m$ no stable DMI exists.

Mapping of evolutionary histories

Every evolutionary history maps to a distinct initial condition (SI Section B.2 for results and proofs). As in Bank et al. (2012), we find three permissive histories that always result in the evolution of a stable DMI for $m < m^+_{\mathsf{max}}$: *secondary contact*, *island-continent*, and *continent-continent*. In all these cases, the second substitution occurs in a deme where the incompatible first substitution is not (yet) present. In contrast, the evolution of a stable DMI in parapatry is more difficult for an *island-island* or *continent-island* substitution history. Here, the second substitution needs to invade on the island despite competition of the incompatible allele. We need $m < m^-_{\mathsf{max}}$ for a DMI to originate under these circumstances.

Necessary conditions for the existence of a stable DMI

Based on previous results for the model without migration (Rutschman, 1994) or without epistasis (Bürger and Akerman, 2011), and in accordance to Bank et al. (2012), we find that with epistasis and increasing migration a stable DMI can only exist if the island allele is beneficial and its sex-averaged selection coefficient exceeds migration.

Furthermore, any averaged selective advantage of the continental allele must be outweighed by averaged epistasis. For example for X→A, we obtain $m < \sigma_{\mathsf{I}}^{\varphi}$ and $\frac{\sigma_{\mathsf{C}}^{\varphi}}{3} < \frac{\gamma}{2}$. Consult Eqs. B.21, B.23 and Table B.3 for different terms for each model and the SI Sections B.1, B.1 for proofs.

2.3.2 Nuclear codominant DMIs

We obtain full analytical solutions for the maximum migration bounds $m_{\mathsf{max}}^{\pm}$ (B.2). Below, we discuss how these rates depend on the various genetic architectures, sex dependence of fitness and migration, and on dosage compensation. Figures 2.2 and 2.3 compare the $m_{\mathsf{max}}^{\pm}$ for the different types incompatibilities among nuclear genes: DMIs among autosomal genes (A→A), DMIs among X and autosomes, with either the incompatible X allele immigrating from the continent (X→A) or the autosomal locus (A→X), and DMIs among two X-linked loci (X→X). Fig. 2.2 assumes full dosage compensation of X-linked alleles in males, Fig. 2.3 treats the case without dosage compensation.

Selection against hybrids and against immigrants

Following Bank et al. (2012), we can distinguish two main selective forces maintaining a DMI in the face of gene flow. If the continental allele is beneficial on the island (first column of Fig. 2.2 and 2.3), a polymorphism at the respective locus can only be maintained by hybrid formation and selection against the immigrating allele is due to hybrid inferiority ("selection against hybrids"). This type of selection will only be effective as long as the immigrating allele is rare. Once the migration pressure is so high that the immigrating continental allele is in a majority, incompatibility selection rather works against the resident allele on the island. Consequently, we expect a large bistable regime with $m_{\mathsf{max}}^{+} >> m_{\mathsf{max}}^{-}$ and a small region with global stability, as can indeed be seen for all types of DMIs with a beneficial continental allele. Note also that m_{max}^{+} increases with γ, as should be expected if hybrid incompatibility, i.e. epistasis, is the sole cause of (local) stability.

In contrast, with a deleterious immigrating allele (third column of Fig. 2.2 and 2.3), a DMI can also be maintained by "selection against immigrants" for small values of epistasis, or via a combination of the two selective forces (selection against hybrids and immigrants) with stronger epistasis. If selection against immigrants predominates, maintenance of the DMI is driven by local adaptation. The fitness advantage of the resident allele depends on its direct effect and the dynamics will usually be frequency independent. Therefore we obtain no or only a small bistable regime, with $m^{+}_{\mathsf{max}} \approx m^{-}_{\mathsf{max}}$. For stronger epistasis, selection against hybrids becomes more important, leading to a relative increase of the bistable regime. The main effect of epistasis now is that it promotes swamping of the island allele: $m^{+/-}_{\mathsf{max}}$ decreases with epistasis. In the case of a neutral immigrating allele, the observed migration bounds exhibit an intermediate pattern.

Sex-biased migration

To understand the differences among the DMI architectures, we take the case of full dosage compensation and strict female-biased migration ($R = 1$) as a starting point (Fig. 2.2(a)-(c)). In this case, all curves for $m^{\pm}_{\mathsf{max}}$ for the different models collapse onto a single one. Indeed, if only females migrate, the number of migrating X chromosomes and autosomes is equal. Full dosage compensation balances any direct and epistatic effects of loci with different ploidy levels. Consequently, the corresponding Eqs. (B.26) differ only by a constant factor.

If also males migrate (Fig. 2.2(d)-(i)) genomic architectures involving an X chromosomes experience effectively lower migration rates of the X and hence increasing $m^{\pm}_{\mathsf{max}}$. Male-biased migration boosts $m^{\pm}_{\mathsf{max}}$ most effectively for X→X, as both loci experience reduced migration pressure. For unbiased migration, m^{+}_{max} of X→X relative to A→A DMIs increases by $\frac{4}{3}$ (the autosome-X ratio), and doubles for pure male migration (corresponding to the 1:2 X-autosome ratio among migrants in this case).

The migration bounds $m^{\pm}_{\mathsf{max}}$ for the A→X and X→A DMIs are intermediate between

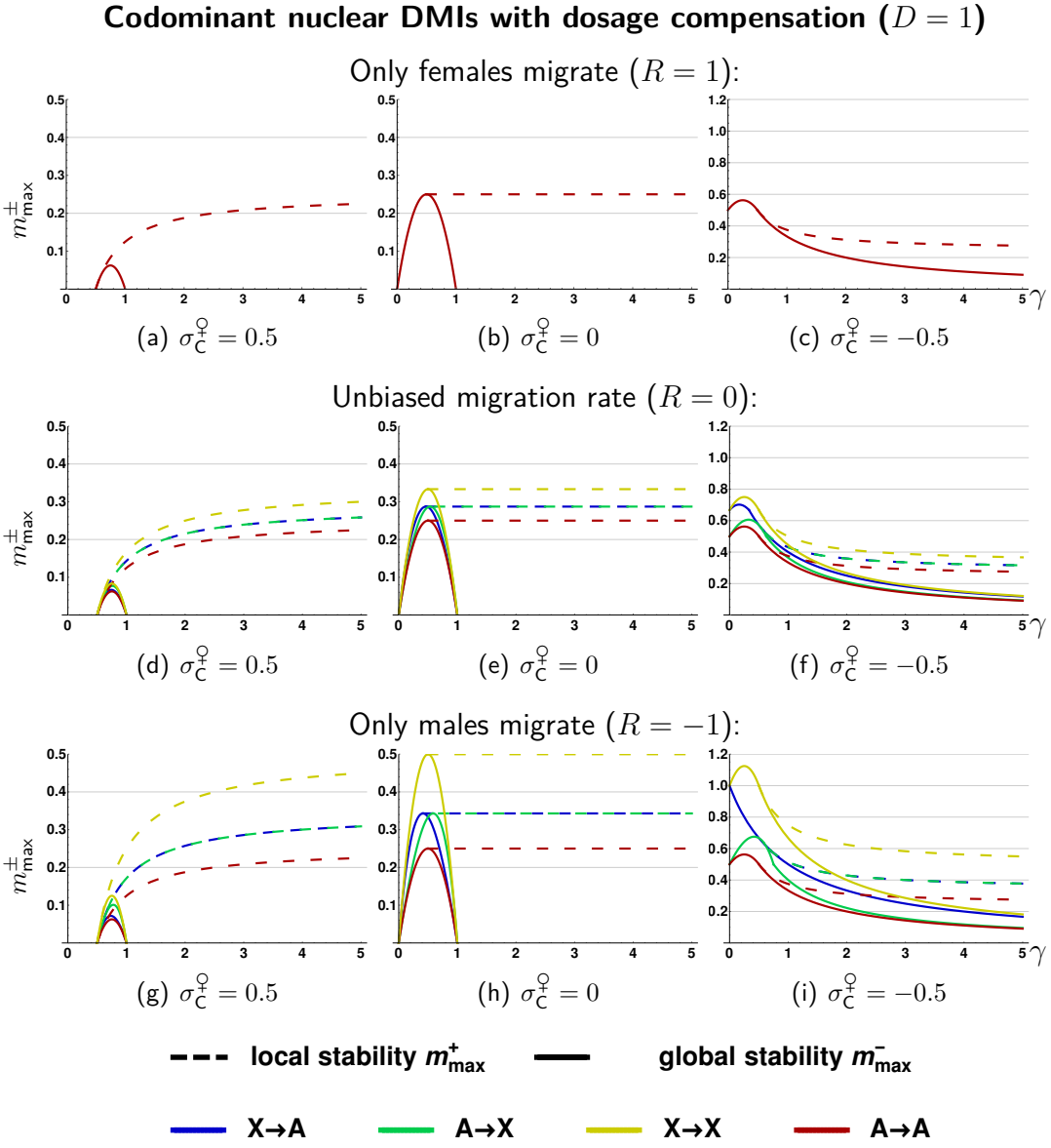

Figure 2.2: **Codominant nuclear DMIs with dosage compensation,** $D = 1$**.** The columns show $m^{\pm}_{\max}$ as a function of the strength of epistasis γ for beneficial ($\sigma_C^{\varphi} = 0.5$), neutral ($\sigma_C^{\varphi} = 0$), and deleterious ($\sigma_C^{\varphi} = -0.5$) effect of the immigrating allele. All quantities in the figure ($\sigma_C^{\varphi}, \gamma, m^{\pm}_{\max}$) are measured relative to the fitness effect of the island allele, which is normalized to $\sigma_I^{\varphi} = 1$. Note the different scaling of the y-axis in the third column. Strong differences between $m^{\pm}_{\max}$ in the various models occur if migration rates are sex-biased. For female-biased migration $m^{\pm}_{\max}$ coincide for all four models. With increasing proportion of male migrants (top to bottom), migration pressure on the X chromosome is reduced and differences among the models appear. All bounds $m^{\pm}_{\max}$ are derived analytically, see Eqs. (B.32),(B.34).

the A→A and X→X DMIs. Our analytical results (see B.2) show that the upper limit of the bistable regime (i.e., the value of $m^{+}_{\max}$) is identical for the A→X and the X→A

models with dosage compensation. However, the limits for global stability, m^{-}_{max}, can differ, which can be understood as follows:

For pure selection against migrants (no epistasis $\gamma \to 0$, and $\sigma_{\mathsf{C}} < 0$, right column in Fig. 2.2), increased male migration reduces the effective migration pressure on the X chromosome. This leads to a corresponding increase in the migration bound m^{-}_{max} ($= m^{+}_{\mathsf{max}}$ in this case) for all DMIs that are lost for $m > m^{\pm}_{\mathsf{max}}$ because of swamping at an X-locus. This is clearly always the case for X→X DMIs, but also for the X→A model, as long as $|\sigma_{\mathsf{C}}| < |\sigma_{\mathsf{I}}|$ (as in our example: X fixes before A is lost). In contrast, for the A→A and the A→X model (if $|\sigma_{\mathsf{C}}| < |\sigma_{\mathsf{I}}|$) the DMI is lost due to swamping at the autosomal locus (continental locus in these cases). Increased male bias in migration therefore does not change the migration bound $m^{\pm}_{\mathsf{max}}$ in these cases.

For strong epistasis (with a deleterious immigrating allele), where the direct locus effects are less important, it is always the incompatible island allele that cannot invade on the island for migration rates $m > m^{-}_{\mathsf{max}}$. Here, any incompatible island allele that interacts with an X allele has an advantage from male-biased migration since it feels less gene flow from the competing X. This can be seen for the m^{-}_{max} lines in Fig. 2.2(f),(i): While the migration bound is increased for the X→A model (and the X→X model) over the whole range of epistasis, it converges to the value of the autosomal DMI for the A→X model.

No dosage compensation

In Fig. 2.3 we investigate migration bounds without dosage compensation, such that the differences in ploidy between autosomes and X chromosomes are no longer masked. Relative to the model with dosage compensation, we have weaker allelic and epistatic effects of the X chromosome. Hence, incompatible island X alleles are easier go get swamped and also have a more difficult time to keep incompatible continental (A or X) alleles from swamping.

The consequences can most easily be seen in the first row of Fig. 2.3(a)-(c) with

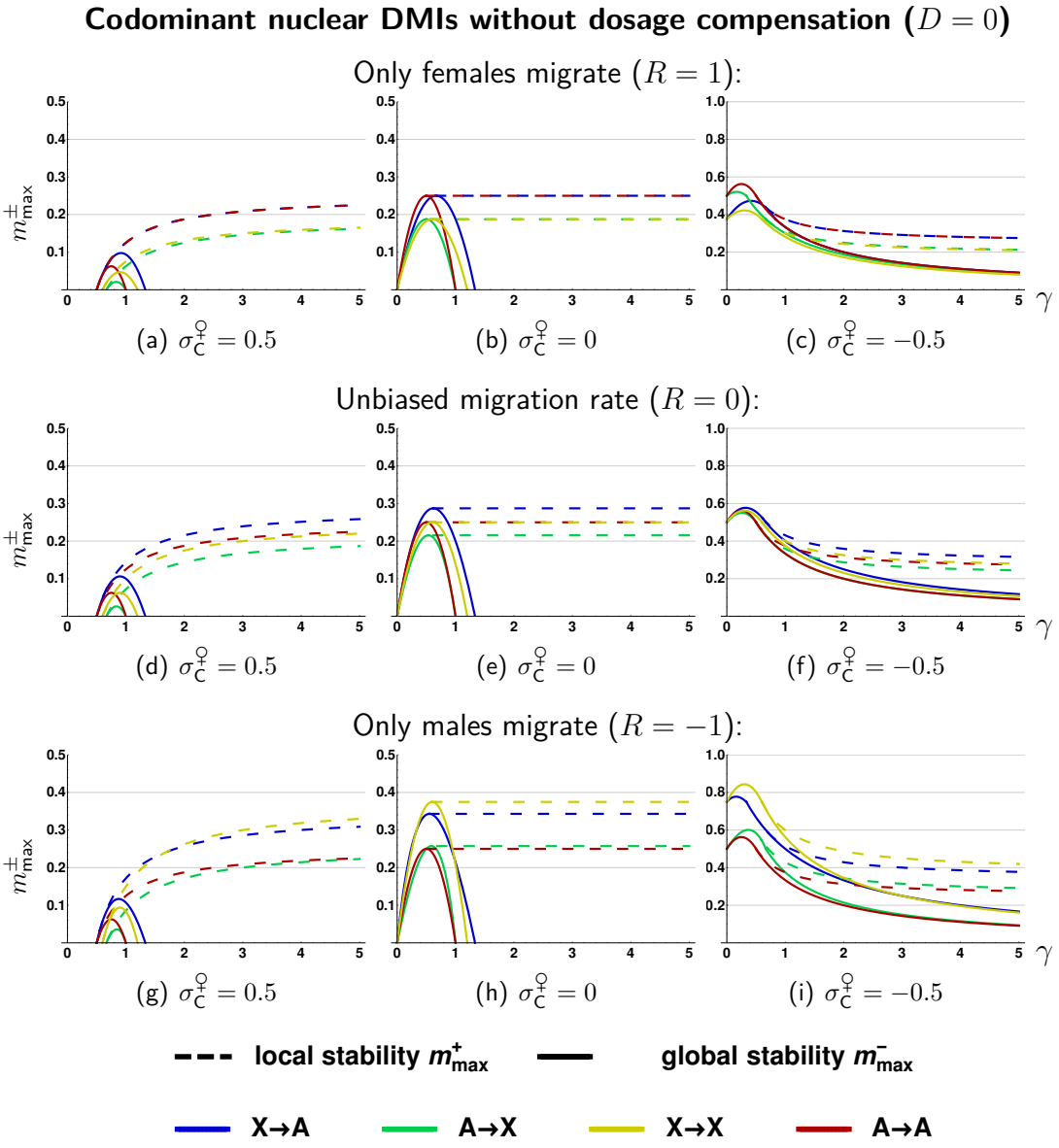

Figure 2.3: **Codominant nuclear DMIs without dosage compensation,** $D = 0$**.** Without dosage compensation the ploidy differences between the autosomes and the X chromosome are unmasked, inducing strong asymmetry between the $\mathcal{A}$-$\mathcal{X}$-models. this leads to a larger effect per allele. All bounds $m^{\pm}_{\max}$ are derived analytically, see Eqs. (B.32),(B.34). See also Fig. 2.2 for further explanations. Note the different scaling of the y-axis in the third column.

pure female migration, where, in contrast to dosage compensation, differences between the various genomic architectures are not compensated anymore. We observe a strong asymmetry between $m^{\pm}_{\max}$ of X→A and A→X-models for all levels of male migration relative to the corresponding results with dosage compensation. Here migration bounds

for X→A always exceed those obtained for A→X-models. Intuitively, one can understand this as follows: In the X→A model, three immigrating X chromosomes "fight" against four resident autosomes, whereas in A→X the odds are in favor of the immigrating autosomes. Thus the island is swamped more easily in the latter case.

As seen for dosage compensation before, for weak epistasis ($\gamma \approx 0$, pure "selection against immigrants"), it is always the locus with weaker direct effect that is swamped first. In our example this is always the "continental" locus, because we have stronger selection on the island locus. For unbiased migration (Fig. 2.3(f)) all models converge to the same bound. However, introducing sex-biased migration leads to relative higher gene flow on the X for a female bias (and therefore lower bounds for models with immigrating X), as can be seen in Fig. 2.3(c). Similarly, male-biased migration leads to weaker X-linked gene flow and a higher bounds in these models, i.e. X→A and X→X, (Fig. 2.3(i)).

If we compare migration bounds of Fig. 2.2 and 2.3, we can see that dosage compensation outbalances most of the differences in $m^{\pm}_{\mathsf{max}}$ between A→X and X→A, especially for local stability. While dosage compensation strengthens the fitness effect of the island allele in A→X, the increased epistatic pressure on the continental allele in X→A is outbalanced by its increased fitness effect.

2.3.3 Cytonuclear (mitochondrial) codominant DMIs

Finally, we investigate cytonuclear DMIs in Fig. 2.4, where a gene in the haploid mitochondrial genome (termed o/O for organelle) is incompatible with a nuclear locus. Dosage compensation of the X chromosome again means that the male XyO-hybrids suffer as much as the female XXO-hybrids while they suffer only as much as XxO hybrids without dosage compensation. Relative to nuclear DMIs, three main effects lead to changes in $m^{\pm}_{\mathsf{max}}$:

First, the cytoplasmic locus experiences effectively stronger direct and epistatic selection (factor two in Eqs. (B.26c)), because we maintain the per locus effect identical

to nuclear loci. Since a single allele already accounts for the full mitochondrial locus effect this leads to a larger effect per allele. As a consequence, $m^{\pm}_{\mathsf{max}}$ without sex-bias in migration is elevated relative to A→A model (gray lines in Fig. 2.4(a)-(c)).

Second, sex-biased migration has an even stronger effect in cytonuclear DMIs than in the X-linked nuclear DMIs: Since mitochondria are maternally inherited, the effective gene flow for mitochondrial loci is reduced to zero with pure male migration. Consequently, all migration bounds with immigrating incompatible mitochondrial genes diverge to infinity. In Fig. 2.4 (last two rows), we study the case of strong, but not complete male bias ($R = -0.9$). Since the migration pressure on the mitochondrial locus and the X chromosome is reduced, migration bounds $m^{\pm}_{\mathsf{max}}$ increase for all cytonuclear DMIs, especially for those also involving X chromosomes. This increase in $m^{\pm}_{\mathsf{max}}$ is even further promoted by dosage compensation, strengthening the effect of X.

Finally, because of strict maternal inheritance, the dynamics of the mitochondrial locus is not influenced by any fitness effects in males. In $\mathcal{X}$-$\mathcal{O}$ models this also entails that dosage compensation only affects the dynamics of the X-locus - in contrast to nuclear DMIs, where also autosomal loci are affected if they interact with a hemizygous X locus. As a consequence, the boosting effect of dosage compensation on $m^{\pm}_{\mathsf{max}}$ is symmetric for O→X and X→O, in stark contrast to nuclear DMIs, where dosage compensation does not change much for X→A while it strongly increases A→X.

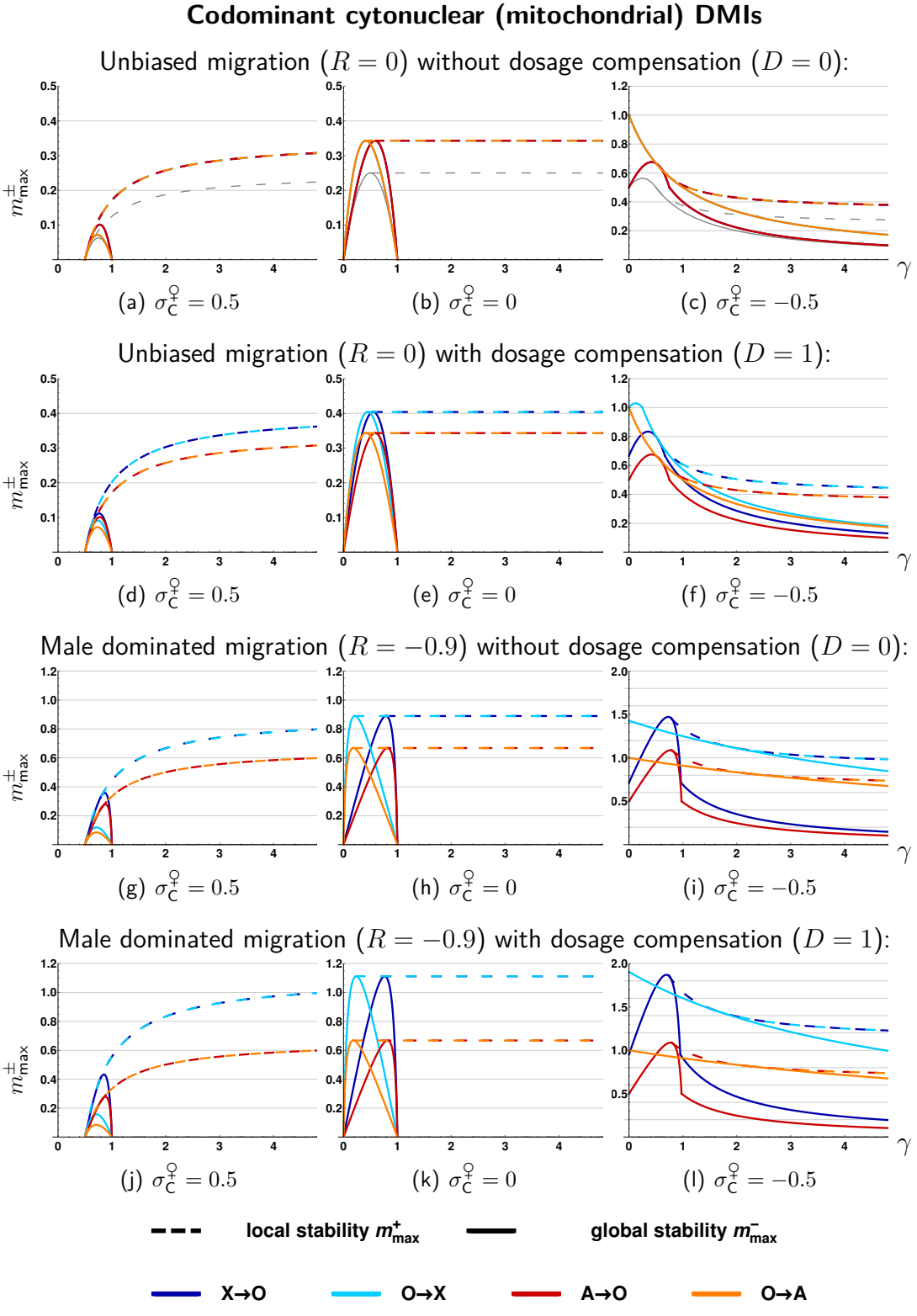

Figure 2.4: **Codominant cytonuclear DMIs.** Maximum permissible migration rates for local stability either coincide for all models (a)-(c), or just for X→O and O→X as well as for O→A and A→O in all other cases. Migration bounds for global stability only coincide without dosage compensation or sex-biased migration between O→X and O→A, as well as for X→O and A→O. The A→A model is given in panel (a)-(c) in gray as a reference. All bounds $m_{max}^{\pm}$ are derived analytically, see Eqs. (B.32),(B.34). See Fig. 2.2 for further explanations. Note the different scaling of the y-axis in third column.

2.4 Discussion

If barriers to gene flow build up among populations in primary or secondary contact, this can have important consequences for their genetic architecture. A lot of recent interest has focused on *islands of speciation (or divergence)* (Wu, 2001; Turner et al., 2005; Butlin et al., 2012; Nosil, 2012; Nosil and Feder, 2012; Via, 2012), yet corresponding empirical findings are equivocal on that matter (Cruickshank and Hahn, 2014; Pennisi, 2014). There are, however, several clear and undisputed genomic patterns of speciation, on which we concentrate here. The most widely known ones are Haldane's rule, (Haldane, 1922), which has motivated much previous speciation research (see reviews and examples in Coyne and Orr (2004); Presgraves (2008); Lachance and True (2010); Presgraves (2010); Oka and Shiroishi (2013) and the *large X-effect* (reviewed in Presgraves, 2008), which both highlight an important role of the X chromosome (or the Z chromosome in birds) in speciation. In addition, hybrid incompatibilities are frequently observed also between nuclear and cytoplasmic markers. Plants show incompatibilities with plastid genomes (Greiner et al., 2011; Snijder et al., 2007) and mitochondria have been reported to be incompatible with nuclear genes across a wide range of species (Ellison and Burton, 2008; Lee et al., 2008; Burton and Barreto, 2012). In insects, cytoplasmic incompatibilities can also be caused by infections with the intracellular bacterium Wolbachia (O'Neill et al., 1992; Werren, 1997; Coyne and Orr, 2004).

In the current study we investigate how the genetic architecture of an inital hybrid incompatibility between incipient sister species can maintain divergence in the presence of ongoing gene flow. Can (primary or secondary) gene flow favor X-linked or cytonuclear DMIs over autosomal ones, and if so under which conditions? We studied this question about a possible first step towards speciation using a minimal model of a two-locus DMI in a continent-island population that allows for analytical treatment. We derive maxium permissible migration bounds which still permit maintenance of a DMI in the face of gene flow. Conditions that yield increased migration limits facilitate speciation, as they

are lost less easily and can subsequently provide more persistent seeds for further ongoing differentiation.

2.4.1 Conditions for parapatric DMIs

Like in the autosomal case (Bank et al., 2012), the origin and maintenance of a two-locus X-linked or cytonuclear DMI requires that at least one of the DMI substitutions (namely: the incompatible variant on the island) is adaptive. If multi-locus barriers to gene flow build up gradually from initial two-locus incompatibilities, this confirms that postzygotic parapatric speciation requires at least some degree of ecological differentiation and local adaptation. Empirically, there is widespread evidence for positive selection on genes involved in DMIs (Macnair and Christie, 1983; Ting et al., 1998; Presgraves et al., 2003; Barbash et al., 2004; Dettman et al., 2007).

For all types of DMIs, we observe two basic selective forces driving their evolution. Selection against immigrants implies that the new migrants have a fitness deficit relative to island residents, resulting in *ecological speciation* scenarios (Schluter and Conte, 2009; Nosil, 2012). A characteristic of this regime is that evolution of a stable DMI is independent of its evolutionary history.

Alternatively, a stable DMI is caused by selection against hybrids, where migrants can even have a positive fitness. If hybrids are unfit, immigrants still suffer an indirect disadvantage as long as they are rare and their genotypes are readily broken down by sex and recombination. This scenario typically leads to a bistable dynamics, where a stable DMI will only evolve from favorable starting conditions or permissive evolutionary histories (such as secondary contact). The scenario has also been referred to as *mutation-order-speciation* (Mani and Clarke, 1990).

We measure the strength of a parapatric DMI by means of two migration bounds. The higher one, m^{+}_{max}, is the limit beyond which a DMI can neither evolve nor an existing one can be maintained. The lower bound, m^{-}_{max}, is the limit up to which a DMI will always evolve in the face of gene flow, irrespective of the evolutionary history

(globally stable DMI). For migration rates between both bounds, a DMI is maintained, but will evolve only under favorable histories, such as secondary contact, or if the second incompatible substitution occurs on the continent.

2.4.2 Contrasting different DMI architectures

We find that the genetic architecture of a DMI (with incompatible genes on autosomes, X chromosomes, or in the mitochondrial genome) can have a strong effect on its stability. However, this effect also crucially depends on other factors, such as, in particular, the level of dosage compensation and the sex-bias in the migration rates.

First, without dosage compensation and without sex-biased gene flow, the hemizygosity of the X chromosome in males leads to shifts of $m^{\pm}_{\mathsf{max}}$ in the presence of epistasis compared to autosome-autosome DMIs. This is due to ploidy differences: "3 X chromosomes fight 4 autosomes". Therefore, the A→X scenario (where a resident X-linked allele competes with an immigrating incompatible autosomal gene) constitutes a weaker barrier to gene flow than the X→A model. Note that this effect depends crucially on the (negative) epistasis of the DMI and is not observed in a single-locus model of local adaptation. Second, dosage compensation strengthens the X alleles, which leads to higher migration bounds in all X-linked DMIs. In particular, it increases stability of DMIs with an incompatible X locus on the island, compensating the A→X versus X→A asymmetry. Third, sex-biased migration leads to lower/higher limits for DMIs with immigrating X for female/male bias. Fourth, our results in the SI Section A.1 show no large difference between codominant and recessive nuclear DMIs (which lead to Haldane's rule) concerning the migration bounds. In fact, the difference for X-linked DMIs are even smaller than for autosome-autosome DMIs. Fifth, for cytonuclear DMIs we often observe stronger barriers to gene flow since the haploid cytoplasmic alleles experience the full locus effect. Furthermore, sex-bias in migration yields an especially strong effect, as for pure male migration effective gene flow at the mitochondrial locus ceases completely.

Our numerical simulations for the effect of LD in the SI Section A.2 agree with

the approximate analytical results for weak and moderately strong DMIs. For very strong DMIs, stronger deviations occur for codominant A→A and X→X DMIs, which maintain very strong LD once all (male and female) hybrids with incompatible alleles are almost inviable/infertile. As a consequence, gene flow among the continent and island haplotypes is blocked and we obtain higher migration bounds relative to X→A and A→X DMIs. For the latter two, F1 hybrid males carrying the compatible x allele (genotype Aaxy) are viable and can produce ax gametes for the F2 generation. This effect of extreme LD and blocked gene flow does not exist for recessive DMIs (see SI Section A.1 for details). Our numerical simulations also show that the effect of drift is usually small and does not lead to qualitative changes (SI Section A.3). Since DMI alleles can be lost by drift, stochastic migration bounds m_{max}^{N} are generally smaller than their deterministic counterparts. In SI Section A.3, we present an analytical approximation to estimate this reduction due to drift.

2.4.3 The *large X-effect*

Summarizing all different cases described above, we find that the most stable DMIs are almost always X-linked, where migration bounds are typically enhanced by a factor of $4/3$ to 2 relative to autosomal DMIs (unless migration is strongly female biased). Although this is not a very strong effect, it is very general and applies whenever gene flow plays a role at any stage of the speciation process. This includes, in particular, scenarios of secondary contact and also later stages of the speciation process where additional barriers to gene flow exist in the genomic background. In this latter case, the gene flow at the focal DMI loci needs to be replaced by appropriate effective migration rates (Barton and Bengtsson, 1986). The pattern that follows from a more stable X barrier is consistent with a higher density of X-linked hybrid incompatibilities, the *large X-effect*.

Our results show a clear boost of X migration bounds, in particular, if there is dosage compensation and if migration is male biased. Empirical studies show that sex-biased

migration is common in nature and report a prevalence for migration of the heterogametic sex in both mammals, where dispersal is on average male biased, (Lawson Handley and Perrin, 2007) and in birds, where female dispersal dominates (Greenwood, 1980). In the context of our results, these trends strengthen the predicted pattern of a *large X-effect* or *large Z-effect*, respectively.

One example stems from the house mouse, *Mus musculus*. There is strong empirical evidence for a *large X-effect* in this species (Tucker et al., 1992; Good et al., 2008; White et al., 2012), such as the major involvement of the X chromosome in hybrid sterility (Oka et al., 2004; Storchova et al., 2004). Mice exhibit rather complete dosage compensation due to X-inactivation in females (Payer and Lee, 2008). Furthermore, the house mouse displays male-biased dispersal at breeding age (Greenwood, 1980; Gerlach, 1990).

Several alternative mechanisms as potential underlying causes for a *large X-effect* have been discussed in the literature, such as sex ratio meiotic drive, regulation of the X chromosome in the male germ line (Coyne and Orr, 2004; Presgraves, 2008), or faster evolution of the X chromosome (termed *faster-X-effect* Charlesworth et al., 1987). In the panmictic population model by Charlesworth et al. (1987), faster evolution on the X chromosome results if adaptations are, on average, recessive and are thus exposed to stronger selection on the hemizygous X. We note that our model with gene flow predicts an advantage of X-linked genes for island adaptations even if they are not recessive, but codominant (or even slightly dominant, see SI Section A.4 for details and proofs). Since the *faster X-effect* (more adaptations on the X) also favors a *larger X-effect* (more incompatibilities involving the X), this is another way how speciation with gene-flow can contribute to this pattern. In summary a mono-causal explanation for the *large X-effect* seems unlikely, and it remains an open question, to which extent each factor contributes. Our study adds differentiation under gene flow as another element to this mix.

Our results relate to Haldane's rule only in so far as this pattern partially overlaps with the *large X-effect*. Beyond that, we do not obtain a prediction. In particular, the migration bounds for codominant and recessive DMIs are similar (while only the latter

lead to Haldane's rule).

2.4.4 Introgression patterns

A second conclusion from our results that can be related to data is that X-linked alleles in an incompatibility face stronger barriers to introgression than the corresponding autosomal alleles. This effect rests on two basic observations: the tendency for higher migration bounds of all X-linked DMIs with dosage compensation (which also contributes to a large X-effect), and the asymmetry promoting A$\rightarrow$X over X$\rightarrow$A introgression that we observe for the incompatible allele if dosage compensation is incomplete or absent (the 3 versus 4 chromosomes effect). Our findings agree with the result of a recent simulation study for DMIs on a cline by Wang (2013), who showed that, for an X-autosome DMIs, the incompatible X allele flows less easily across a cline than the autosomal allele.

A pattern of reduced X-introgression relative to autosomal introgression has been recognized in many sister-species in nature. In the complex of *Anopheles gambiae* sister clades Fontaine et al. (2015) found "pervasive autosomal introgression" between different species, in contrast to the X chromosome, which contains disproportionately more factors in reproductive isolation.

Liu et al. (2015) report three interspecies hybridization events in mice (*Mus musculus domesticus* and *M. spretus*), leading to exclusively autosomal, partially adaptive introgression. Similarly, Macholán et al. (2007) showed weaker introgression patterns and lower selection pressure on the X chromosomes compared to the autosomes in the central European mouse hybrid zone of *Mus musculus musculus* and *M. m. domesticus*. The authors suppose that the X is shielded more effectively from introgression due to the *large X-effect*.

Further examples exist for birds. Sætre et al. (2003) report "rather extensive hybridization and backcrossing in sympatry" between two populations of flycatchers hybridizing in secondary contact. Nevertheless, gene flow was again predominantly found on the autosome. Hooper and Price (2015) report that derived cross-species inversions

among sister species of Estrilid finches are strongly enriched on the Z chromosome. The pattern is strongest in continental clades with high level of sympatry and (plausibly) higher levels of gene-flow during the speciation process. If inversions harbor DMIs, this is consistent with our finding that derived incompatibilities on the Z chromosome are more stable to gene flow than autosomal incompatibilities.

Also other factors, such as recombination, can influence differential introgression on X chromosomes and autosomes. Indeed, there is empirical evidence that recombination can structure autocorrelation patterns among introgressed loci. However, available data also show that recombination cannot be the the sole explanation for differential introgression among genomic regions, *e.g.* in mice (Payseur et al., 2004) or finches (Hooper and Price, 2015). As for the *large X-effect* our mechanism is one of several possible ones.

2.4.5 Biological assumptions and limitations of the model

Our study has been intended as a minimal model approach that allows for analytical treatment. As such, it rests on several simplifying assumptions concerning the genetics of the DMI and the ecological setting. These limitations suggest possible model extensions for future work.

All our results assume a simple DMI between just two loci. This is in line with most previous theoretical work and known empirical cases (Coyne and Orr, 2004; Maheshwari and Barbash, 2011). Nevertheless, complex DMIs involving multiple loci are clearly relevant at later stages of a speciation process and could lead to new effects that are not captured here (*e.g.* Lindtke and Buerkle, 2015).

Our fitness scheme for two-locus DMIs comprises codominant and recessive cases. Empirically, the functional form depends on the underlying mechanisms causing hybrid fitness loss, which is still debated. Hybrid incompatibilities can be due to loss-of-function or gain-of-function mutations (reviewed by Maheshwari and Barbash, 2011)). While the former tend to act recessively, the latter will likely affect heterozygotes, and may be better captured by a partially dominant DMI.

Recessive DMIs, in turn, occur in a number of different types, (*e.g.* Presgraves, 2010; Cattani and Presgraves, 2012; Matsubara et al., 2015), which lead to slightly different models. We have briefly studied some of these alternatives analytically, such as a *recessive-A codominant-X*-DMI or a *codominant-A recessive-X*-DMI (data not shown). We did not detect any noteworthy difference in their evolutionary dynamics or for the migration bounds relative to the results reported here. Still, more relevant changes are clearly possible, for example if the single locus effects can lead to over- or underdominance.

For the results presented, we assume that dosage compensation enhances not only the single-locus effect, but also the incompatibility. Empirically, hybrid incompatibilities are frequently dosage-sensitive, *e.g.* in a *Arabidopsis thaliana*/ *A. arenosa* cross, where a DMI results due to failure in gene silencing (Josefsson et al., 2006), or in a *Mus musculus musculus*/ *M. m. domesticus* cross, where X-linked hybrid male sterility results from over-expression of X-linked genes in spermatogenesis (Good et al., 2010). Furthermore, in haplo-diploid Nasonian wasps genetically engineered diploid males were less affected by hybrid sterility than haploid male hybrids, pointing to a strong effect of ploidy on hybrid fertility (Beukeboom et al., 2015).

Nevertheless, we also investigated the effect of dosage compensation only on the single locus effect or only on the incompatibility (results not shown). As expected, we obtain intermediate patterns between no and full dosage compensation.

Concerning the ecological assumptions, our model assumes unidirectional gene flow between two panmictic demes. While our results readily extend to weak back migration (which leads only to slight shifts of the equilibria), strong bidirectional migration can lead to qualitatively new effects that are not captured by our framework. For example, polymorphisms at single loci can be maintained for arbitrarily strong gene flow if heterogeneous soft selection leads to a rare-type advantage (Levene, 1953). Furthermore, generalist genotypes that are inferior in both demes, but do well on average, can be maintained if (and only if) bidirectional migration is sufficiently strong (see Akerman

and Bürger, 2014, for results in a two-locus model without epistasis).

Alternative models for the population structure can also lead to substantial differences. In particular, our two-deme model ignores isolation by distance, which can be captured either in a discrete cline model with a chain of demes, or in a continuous-space framework. It is expected that polymorphisms (and DMIs) can be maintained with much larger gene flow (or weaker selection) in these settings (Barton, 2013). Still, several of our key results, such as reduced introgression of X-linked incompatibility alleles, should still hold under these conditions (see Wang, 2013, for a discrete cline model).

A. Supporting Information: Results

A.1 Recessive model for nuclear DMIs

One of the most widely observed patterns in speciation genomics is Haldane's rule (Haldane, 1922). It predicts that sex-biased hybrid break down in the F1 generation is more likely to affect the heterogametic sex- in our case the hemizygous F1 hybrid male. Since recessive DMIs involving sex chromosomes is the most widely accepted explanation for this effect (reviewed in Coyne and Orr (2004)), we extend our investigations to this case.

We set up our recessive fitness scheme such that in all X-linked DMI the F1-female hybrids are not affected by the incompatibility, see Table A.1. The fitness of F1 hybrid males depends on the genetic architecture of the DMI. For $\mathcal{X}$-$\mathcal{A}$ DMIs, male F1 hybrids with genotype AaXy, are affected by the DMI, in accordance with Haldane's rule. In contrast, neither recessive $\mathcal{A}$-$\mathcal{A}$ nor $\mathcal{X}$-$\mathcal{X}$ DMIs exhibit a fitness deficit of F1 males. Neither scheme therefore agrees with Haldane's rule.

Due to the departure from strict additivity of the DMI, the recessive dynamics are much more complicated. Therefore, only a part of the results can be obtained analytically (the limits for global stability m^{-}_{max}). We therefore complement our investigations with numerical results for local stability, m^{+}_{max}.

DMI	**hybrids:**♂, ♀	**epistasis vector** Γ
$\mathcal{A}$-$\mathcal{A}$	♀: AaBb, AaBB, AABb, AABB ♂: AaBb, AaBB, AABb, AABB	$\Gamma_{\mathcal{A}\mathcal{A}} = (0, \gamma, \gamma, 2\gamma, 0, \gamma, \gamma, 2\gamma)$
$\mathcal{A}$-$\mathcal{X}$	♀: AaXx, AaXX, AAXx, AAXX, ♂: AaXy, AAXy	$\Gamma_{\mathcal{A}\mathcal{X}} = (0, \gamma, \gamma, 2\gamma, (1+D)\frac{\gamma}{2}, (1+D)\gamma)$
$\mathcal{X}$-$\mathcal{X}$	♀: $X_1x_1X_2x_2$, $X_1x_1X_2X_2$, $X_1X_1X_2x_2$, $X_1X_1X_2X_2$, ♂: X_1X_2y	$\Gamma_{\mathcal{X}\mathcal{X}} = (0, \gamma, \gamma, 2\gamma, (1+3D)\frac{\gamma}{2})$

Table A.1: **Epistasis vectors Γ for the recessive model.** Epistasis terms in female and male hybrids are given without ($D = 0$) and with dosage compensation ($D = 1$).

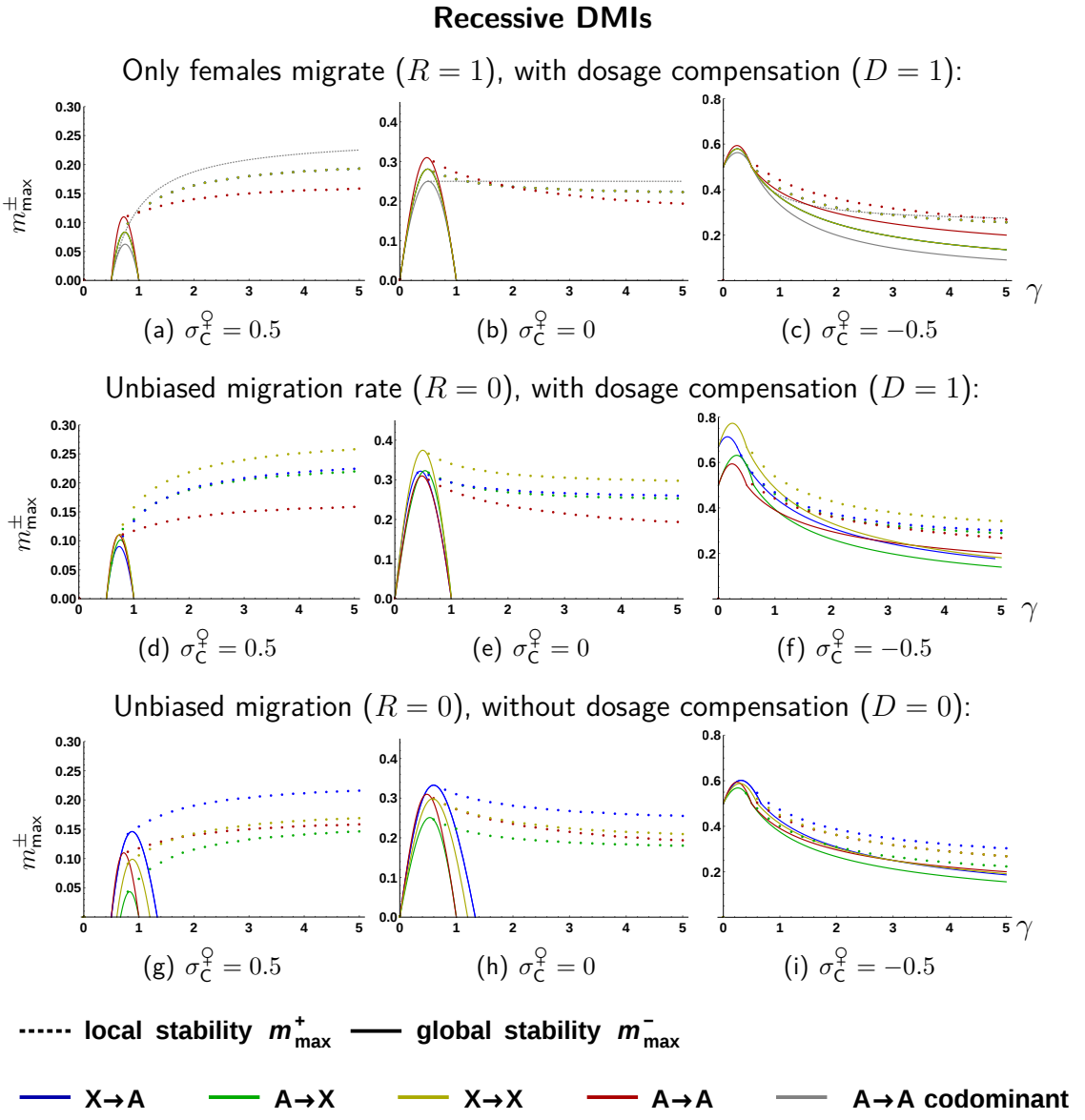

Figure A.1: **Recessive DMIs and the effect of dosage compensation and sex-biased migration.** The dynamics of the recessive models for m^{+}_{max} are determined by numerical calculations and given by dots. The solid lines denote analytical results for m^{-}_{max}, see also Eqs. (B.19),(B.20). In (a)-(c) $m^{\pm}_{\text{max}}$ overlaps for all X-linked DMIs. The gray lines show the migration bounds of the codominant model (where all four architectures coincide). The results for A→A are unchanged in the three columns, as this model is neither affected by dosage compensation nor by sex-biased migration. For all autosomal alleles we obtain $\sigma_*^{\male} = \sigma_*^{\female}$, whereas we obtain $\sigma_*^{\male} = (1 + D)\sigma_*^{\female}$ with $D = 0$ without dosage compensation and $D = 1$ with dosage compensation for all X-linked alleles. Also refer to Fig. 2.2 for further explanations.

Migration bounds for recessive DMIs

The results for recessive DMIs are shown in Fig. A.1. The largest difference relative to the codominant model occurs for A→A incompatibilities. (This can also be seen from

the first row in Fig. A.1, comparing the red and gray lines. The recessive model shows a significantly larger region for global stability and a relatively smaller bistable regime. This can be seen in Bank et al. (2012), Figure 3B, C. They also obtained strong differences for tightly linked loci, which is not studied here. The differences for m^{-}_{max} result since epistatic selection on the incompatible island locus is strongly reduced for a recessive DMI. It is therefore maintained even for higher gene flow rates.

If we compare these results with X-linked DMIs, we see that this difference in size of the regions for global and local stability to the codominant models becomes smaller. The reason is that the DMI is no longer fully recessive in the sense that it is not expressed in F1 hybrids. Indeed, epistasis is now effective in hemizygous F1 males in $\mathcal{A}$-$\mathcal{X}$ DMIs. Similarly, selection against the incompatible alleles is also stronger in the recessive X$\rightarrow$X model, relative to the autosomal case, since all male hybrids with X_1X_2y genotype are affected (see the migration bound for X-linked DMIs in Fig. A.1(a)-(c)).

The effects of dosage compensation and sex-biased migration are all similar related to the codominant model (Fig. A.1(d)-(i)). Qualitatively, the results show that the migration bounds do not change significantly relative to the codominant DMIs. As we show in the next section, this holds as long as epistasis is not very strong.

A.2 Effects of linkage disequilibrium and strong epistasis

For our analytical derivations and all previous results, we have assumed weak evolutionary forces and linkage equilibrium (LE) between the two DMI loci (on the island). However, DMIs found in natural populations can also cause strong effects, such as hybrid inviability or hybrid sterility, which in turn can create strong linkage disequilibrium (LD). Therefore we now investigate how robust our model is against a violation of the assumptions of LE between the DMI loci.

We consider a deterministic model with non-overlapping generations in discrete time and follow the dynamics of all genotypes in males and females by numerical iteration. The model allows for the build-up of LD, deviations from Hardy-Weinberg proportions,

and also differences in the allele frequencies among the sexes, which can occur as a result of strong sex-specific selection.

The results are shown in Fig. A.2. For weak and moderate epistasis the numerical results fully coincide with the analytical approximation. However, for strong epistasis ($\gamma > 10$, corresponding to a homozygote selection coefficient of the incompatibility of $> 18\%$), the numerical results start to deviate. This is due to the build-up of elevated levels of LD, which results in a reduction of effective gene flow at the DMI loci. Consequently, the migration bounds increase beyond the values predicted for LE. Qualitatively, this agrees with the results of Bank et al. (2012), who find higher migration bounds for reduced recombination rates (and thus increased LD) among the DMI loci (Figure U3 in their SI).

The magnitude of the deviation due to LD depends strongly on the genetic architecture of the DMI. For codominant DMIs, we get particularly strong increases for A→A and X→X architectures. For $\gamma > 150$ (corresponding to a selection coefficient of $> 77\%$ for the incompatibility) we even obtain a change in the qualitative result since now A→A and X→X DMI lead to the highest migration bounds. We can understand this effect as follows. For codominant A→A DMIs and very large γ all F1 hybrids are practically inviable or infertile. Thus, (almost) all gene flow among the continental and island population is blocked and speciation is completed with a single DMI. For X→X DMIs, all male F1 hybrids are viable. However, since there is no recombination among X loci in males, no new haplotypes are produced, LD remains high, and gene flow among continental and island types is once again blocked. This is different for A→X DMIs where Aaxy males are viable and can produce ax gametes, which are compatible with both incompatibility alleles.

The results are different for recessive DMIs, where gene flow via F1 females (and half of the males) is always possible. As a consequence, the deviations from the LE estimates are much smaller and we do not obtain any re-ordering of the migration bounds among the four architectures. In fact, the only scenario with a sizable LD effect is the X→A

type, which increases the precited asymmetry between the X→A and A→X cases. (The reason for the increase of $m^{\pm}_{\mathsf{max}}$ for X→A is that the incompatible A allele occurs in two haplotypes Ax and Ay on the island with strongly diverging fitness in hybrids: while all Ay haplotypes, which are found in male hybrids with genotype AaXy in the F1 generation are affected by the incompatibility, all Ax haplotypes in the F1 are unaffected. We thus obtain a sex-dependence in the frequency of the A allele on the island that is ignored in the analytical model. This is decisive since swamping at the A locus defines the m^{+}_{max} bound in this case.)

Empirical studies mostly observe that strong DMIs (conferring complete sterility or inviability) are recessive (Presgraves, 2010; Cattani and Presgraves, 2012; Matsubara et al., 2015) with effects in F1 hybrids mostly for the heterogametic sex, as predicted by Haldane's rule. We note that codominant DMIs exhibit something like a inverse Haldane's rule in this case, since part of the males remain viable, while all F1 females are affected by the incompatibility. This points to recessive DMIs as the prevalent type for an incompatibility if epistasis is strong.

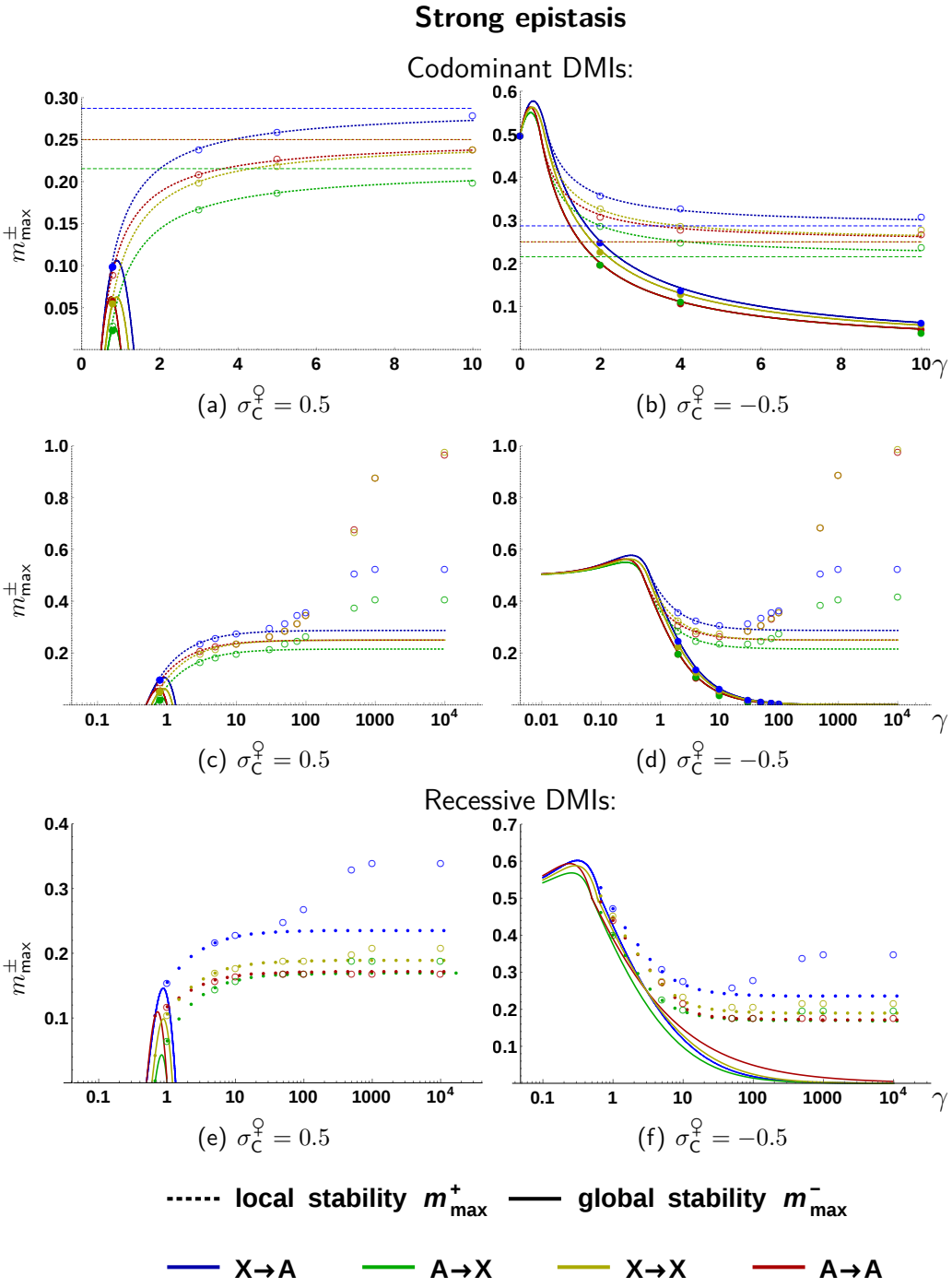

Figure A.2: **Effects of LD and strong epistasis.** Results are shown for unbiased migration ($R = 0$) without dosage compensation ($D = 0$). Lines give the results for the continuous codominant model (see Fig. (2.3)), dots show numerical results for the recessive model and open circles show migration bounds for the discrete codominant and recessive models. Thin, dashed lines give the analytical limits of convergence for m^{+}_{max} in the continuous time model. The x-axis expresses epistasis of the discrete model s_γ as a growth rate for better comparison with the continuous time model, $\gamma = -\log[1 - s_\gamma]$. Figures (c)-(f) are given in log-scale. Also refer to Fig. 2.2 for further explanations.

A.3 Finite populations and the effect of genetic drift

Our analytical model is based on the assumption of infinite population size, neglecting any effect of genetic drift. However, in nature not every population is big enough, such that drift can be ignored. In this section, we analyze how our results on maximum permissible migration rates $m^{\pm}_{\mathsf{max}}$ change due to drift a finite island population. We use simulations of the two-locus Wright-Fisher model with discrete generations.

Simulations are implemented as described for the analysis of LD in the previous section, but with an additional sampling step every generation to account for genetic drift. The life cycle is as follows: Viability selection acts on zygotes, followed by male and female migration from the continent to the island. From an infinite zygote pool, we then sample $\frac{N}{2}$ females and $\frac{N}{2}$ males to form a finite adult population on the island. Adults reproduce and contribute to an infinite gamete pool. These gametes are subsequently subject to random mating, forming a new generation of zygotes and completing the cycle.

Representative for the different models, we show results for the X→A model without dosage compensation ($D = 0$) and without sex-biased migration ($R = 0$) below. We use a population size of 10000 (5000 males and females). We start simulations in secondary contact and let them run for 100 000 generations ($10N$). For each parameter combination, we record the percentage of replicate runs that maintain both alleles at both loci (i.e. which maintain the DMI).

Fig. A.3 shows DMI survival rates for scenarios with selection against hybrids only (a), selection against immigrants (b), and combined selection against hybrids and immigrants (c,d). We use 200 replicate runs per parameter combination. Dashed lines represent the analytical values for m^{+}_{max} in an infinite population.

As expected, we find that values for m^{+}_{max} in an infinite population provide strict upper bounds for the maximum migration rates under which a DMI can be maintained in the presence of drift.

We can estimate the effective reduction in m^{+}_{max} as follows: A beneficial allele A with

selection coefficient s_A is protected against stochastic loss (drift) in a population for an exponential time, if the number of copies N_A of this allele exceeds

$$N_A = 2N \cdot p_A \geq \frac{1}{s_A}. \tag{A.1}$$

For a single allele in a panmictic population, this follows from the establishment probability, $p_{est} = \frac{1-\exp(-4Np_A s_A)}{1-\exp(-4Ns_A)}$ (Kimura, 1957).

We can use this condition to estimate a maximum migration rate m^N_{max} for the maintenance of a DMI in our model. First we estimate the effective selection coefficient s_A by the leading eigenvalue λ_{max} of the Jacobian Matrix at the DMI, following previous work by Yeaman and Otto (2011).

Second, we need a measure for the distance of the DMI equilibrium to the margin where the DMI will be lost from the population. In our case, this is not necessarily the copy number N_A of an allele, but more precisely the distance between the deterministic DMI and the basin of attraction of any other stable equilibrium (since any starting condition in this basin is doomed for deterministic extinction). If the DMI is globally stable, this distance is captured by the closest distance to the boundary (which corresponds to the copy number N_A), where we either loose the island variant or fix the continental allele. In case of a locally stable DMI, however, we estimate this distance by the distance of the DMI equilibrium to the other internal equilibrium, which is an unstable saddle point. Consult SI Section B.2 for more details on the unstable internal equilibrium and Fig. B.3 for illustrations of bifurcation patterns.

We obtain m^N_{max}, by solving the following equation for m for the different cases.

$$2N \cdot p = \frac{1}{\lambda_{max}} \tag{A.2a}$$

Case 1: locally stable DMI

$$\Rightarrow \sqrt{N_C^2\left(p_C^{DMI} - p_C^{I_0}\right)^2 + N_I^2\left(p_I^{DMI} - p_I^{I_0}\right)^2} = \frac{1}{\lambda_{max}} \tag{A.2b}$$

Case 2: globally stable DMI, lost by fixation of continental allele

$$\Rightarrow N_{\mathsf{C}}(1 - p_{\mathsf{C}}^{\mathsf{DMI}}) = \frac{1}{\lambda_{\mathsf{max}}} \tag{A.2c}$$

Case 3: globally stable DMI, lost by swamping of island allele

$$\Rightarrow N_{\mathsf{I}} \cdot p_{\mathsf{I}}^{\mathsf{DMI}} = \frac{1}{\lambda_{\mathsf{max}}} \tag{A.2d}$$

Here, $p_{\mathsf{C}}^{\mathsf{DMI}}$ and $p_{\mathsf{I}}^{\mathsf{DMI}}$ are the frequencies of the continental and the island allele at the stable DMI, and $p_{\mathsf{C}}^{\mathsf{I}_0}$ and $p_{\mathsf{I}}^{\mathsf{I}_0}$ are the allele frequencies at the unstable equilibrium (I_0), respectively. N_{C} and N_{I} correspond to the number of chromosomes for both alleles. It differs for autosomes ($N_{\mathcal{A}} = 2N$) and X-chromosomes ($N_{\mathcal{X}} = \frac{3}{4} \cdot 2N = \frac{3}{2}N$). We note that our criterion deviates from the one by Yeaman and Otto (2011), who use the condition $2N = \frac{1}{\lambda_{\mathsf{max}}}$, which is independent of the location of the deterministic equilibrium. We find that this choice is much less precise for our model.

As can be seen in Fig. A.3, m_{max}^{N} and the simulation results match well. Especially for the case of $\gamma = 0$, where simulations suggest that finite populations with 10 000 individuals have a harder time to resist swamping, effective migration rates are also lower, when compared to the deterministic case.

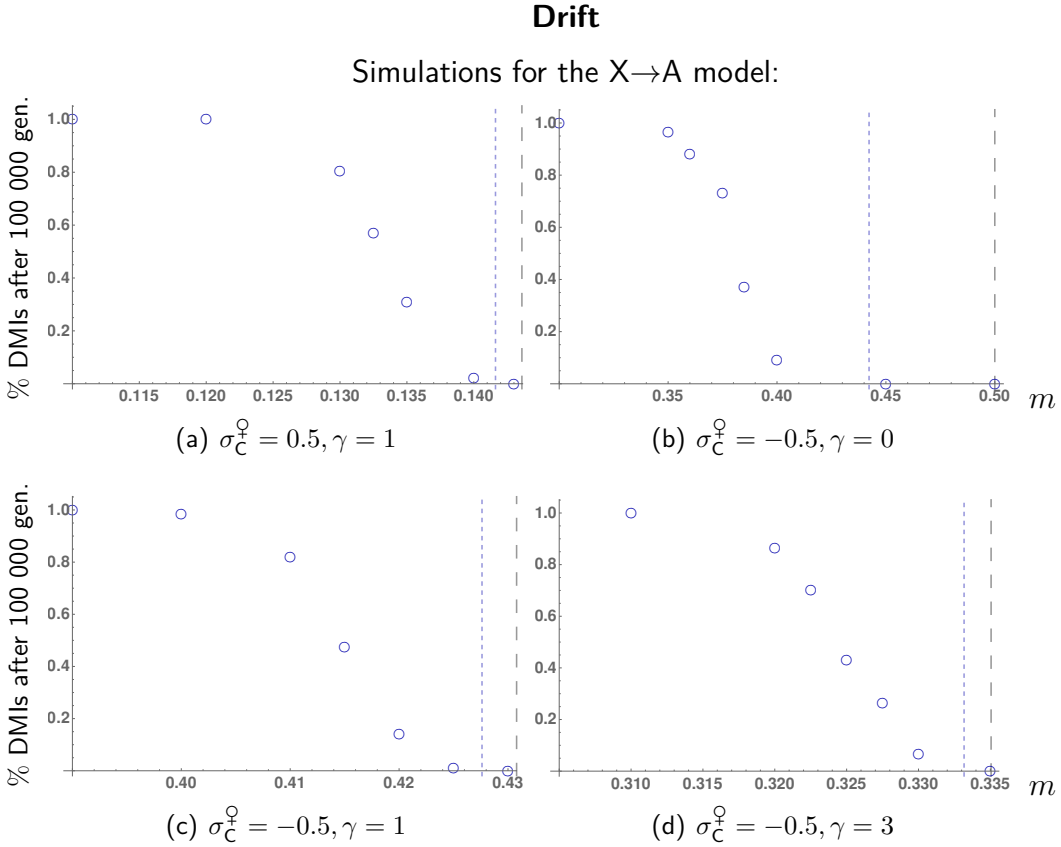

Figure A.3: **Effects of finite population size and drift.** Results are shown for unbiased migration ($R = 0$) without dosage compensation ($D = 0$) for the X→A model. Each point represents 200 replicates, run for 100 000 generations each. Finite population size is fixed to 5000 female and 5000 male individuals. The dashed, gray line gives the analytical m^{+}_{max} and the dashed blue line gives m^{N}_{max}.

A.4 Substitution rates and *faster X-effect*

In order to compare rates of adaptive substitution on autosomes and X chromosomes in our model, it is sufficient to consider a single locus on either chromosome. For an island population of size N, new mutations occur on an autosome at rate $2Nu$ and at an X chromosome at rate $\frac{3}{2}Nu$, respectively (where u is the mutation rate per haploid locus and generation). Assume that a new, locally beneficial mutation with selection coefficient $2s$ and dominance coefficient h occurs. This mutation needs to establish in the face of gene flow at rate m from the continent. On the autosome, the marginal

fitness (see definition in SI Eq. (B.1)) of a mutant relative to the wild type is

$$2hs(1-p)+2sp-2hsp-m \;\; = \;\; 2s(h+p(1-2h))-m. \tag{A.3a}$$

As long as the mutant is rare, ($p \approx 0$) this expression reduces to

$$2hs-m. \tag{A.3b}$$

We obtain the establishment probability as twice this value $2(2hs-m)$. On the X chromosome, establishment depends on dosage compensation D and sex-bias in migration R. We have fitnesses (xx,xX,XX)= $(0, 2hs, 2s)$ in females and (xy,Xy) = $(0, 2hs + D(2s-2hs))$ in males. Averaging the marginal rate of increase over both sexes we obtain

$$\frac{1}{3}\Big(2s\Big(3h+\mathsf{D}(1-h)+\mathsf{p}(2-4h)\Big)-3(1+\frac{R}{3})m\Big). \tag{A.4}$$

The establishment probability of a rare X mutant follows as

$$\frac{2}{3}\Big(2s\Big(3h+D(1-h)\Big)-3(1+\frac{R}{3})m\Big). \tag{A.5}$$

We thus obtain the substitution rates

$$K_{\mathcal{A}} = 4Nu(2hs-m) \quad ; \quad K_{\mathcal{X}} = Nu\Big(2s\Big(3h+D(1-h)\Big)-3(1+\frac{R}{3})m\Big) \tag{A.6}$$

for autosomes and X chromosomes, respectively. For unbiased migration ($R=0$), and full dosage compensation ($D=1$), we obtain

$$K_{\mathcal{X}} = Nu(2s(2h+1)-3m). \tag{A.7}$$

In this case, we obtain a *faster X-effect*, $K_{\mathcal{X}} > K_{\mathcal{A}}$, for

$$h < \frac{1}{2} + \frac{m}{4s}. \tag{A.8}$$

The effect is increased by male-biased migration ($R < 0$). In a panmictic model ($m = 0$), we have $K_{\mathcal{A}} = K_{\mathcal{X}}$ for a codominant adaptation and $D = 1$. As observed by Charlesworth et al. (1987), *faster X* substitution requires recessive adaptations in this case. With gene flow ($m > 0$), the effect is enhanced and occurs also for codominant (or slightly dominant) adaptations.

B. Supporting Information: Mathematical Model

In the Supporting Information Section on the Mathematical Model we give a comprehensive analytical investigation of the dynamical system in **Box 1** of the main text for the general fitness scheme (see Section B.1) and the special case of the codominant fitness scheme (see Section B.2). The 8 different genomic architectures we study are shown in Fig. B.1.

B.1 The general model

We investigate a two-locus DMI model, with two alleles each. The ploidy depends on the locus position: Autosomes are diploid, X-chromosomes haploid in males and organelles (mitochondria) are haploid everywhere.

We start our analysis with the general model, where we assign an arbitrary epistasis term $0 \leq \gamma_1 < \gamma$ to the double heterozygote female F1-hybrid, while all other hybrids are affected additively by epistasis. The resulting epistasis vectors are given in Table 2.2 and the detailed general fitness scheme for the different genotypes is given in Table B.1, B.2.

Later we derive comprehensive analytical and numerical results for the codominant model. Both, the codominant and the recessive model, are special cases of the general

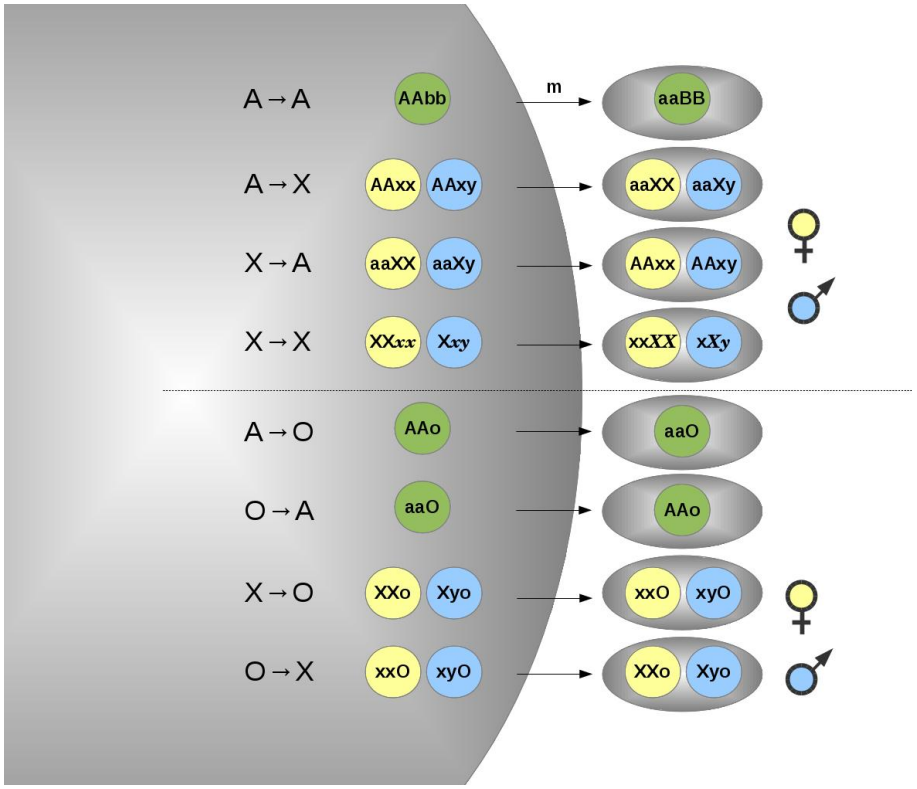

Figure B.1: **Different genomic architectures of two-locus DMIs.** The four upper cases are nuclear DMIs between autosomes (A) and X chromosomes (X), the four lower cases also include mitochondrial loci (O, organelle). Upper case letters denote incompatible alleles. The models uses a continent-island framework with unidirectional gene flow from the continent to an island.

model and we obtain them by setting γ_1 to two specific values:

- In the **codominant model** with $\gamma_1 = \frac{\gamma}{2}$ the strength of epistasis is directly proportional to the number of incompatibilities in male and female hybrids.
- In the **recessive model** with $\gamma_1 = 0$ the double heterozygote female is not affected by the DMI since it still carries a compatible allele at each locus. All other hybrids suffer according to the number of incompatibilities they are carrying.

Genotype, marginal and mean fitness of the general model

In the following Tables B.1, B.2 we give the fitness values for all different genotypes of the different genomic architectures.

.

Fitness of the general model: nuclear DMIs

A→A-model by Bank et al. (2012):

	aa	aA	AA
bb	0	σ_{I}	$2\sigma_{\mathsf{I}}$
bB	σ_{C}	$\sigma_{\mathsf{I}} + \sigma_{\mathsf{C}} - \gamma_1$	$2\sigma_{\mathsf{I}} + \sigma_{\mathsf{C}} - \gamma$
BB	$2\sigma_{\mathsf{C}}$	$\sigma_{\mathsf{I}} + 2\sigma_{\mathsf{C}} - \gamma$	$2\sigma_{\mathsf{I}} + 2\sigma_{\mathsf{C}} - 2\gamma$

In the A→A-model we average over male and female effects for $\sigma_{\mathsf{C}}, \sigma_{\mathsf{I}}, \gamma_1, \gamma$

X→A-model:

Females:

	aa	aA	AA
xx	0	$\sigma_{\mathsf{I}}^{\female}$	$2\sigma_{\mathsf{I}}^{\female}$
xX	$\sigma_{\mathsf{C}}^{\female}$	$\sigma_{\mathsf{I}}^{\female} + \sigma_{\mathsf{C}}^{\female} - \gamma_1$	$2\sigma_{\mathsf{I}}^{\female} + \sigma_{\mathsf{C}}^{\female} - \gamma$
XX	$2\sigma_{\mathsf{C}}^{\female}$	$\sigma_{\mathsf{I}}^{\female} + 2\sigma_{\mathsf{C}}^{\female} - \gamma$	$2\sigma_{\mathsf{I}}^{\female} + 2\sigma_{\mathsf{C}}^{\female} - 2\gamma$

Males:

	aa	aA	AA
x	0	$\sigma_{\mathsf{I}}^{\male}$	$2\sigma_{\mathsf{I}}^{\male}$
X	$\sigma_{\mathsf{C}}^{\male}$	$\sigma_{\mathsf{I}}^{\male} + \sigma_{\mathsf{C}}^{\male} - \epsilon$	$2\sigma_{\mathsf{I}}^{\male} + \sigma_{\mathsf{C}}^{\male} - 2\epsilon$

A→X-model:

Females:

	xx	xX	XX
aa	0	$\sigma_{\mathsf{I}}^{\female}$	$2\sigma_{\mathsf{I}}^{\female}$
aA	$\sigma_{\mathsf{C}}^{\female}$	$\sigma_{\mathsf{I}}^{\female} + \sigma_{\mathsf{C}}^{\female} - \gamma_1$	$2\sigma_{\mathsf{I}}^{\female} + \sigma_{\mathsf{C}}^{\female} - \gamma$
AA	$2\sigma_{\mathsf{C}}^{\female}$	$\sigma_{\mathsf{I}}^{\female} + 2\sigma_{\mathsf{C}}^{\female} - \gamma$	$2\sigma_{\mathsf{I}}^{\female} + 2\sigma_{\mathsf{C}}^{\female} - 2\gamma$

Males:

	x	X
aa	0	$\sigma_{\mathsf{I}}^{\male}$
aA	$\sigma_{\mathsf{C}}^{\male}$	$\sigma_{\mathsf{I}}^{\male} + \sigma_{\mathsf{C}}^{\male} - \gamma_1$
AA	$2\sigma_{\mathsf{C}}^{\male}$	$\sigma_{\mathsf{I}}^{\male} + 2\sigma_{\mathsf{C}}^{\male} - 2\gamma$

X→X-model:

Females:

	x_1x_1	x_1X_1	X_1X_1
x_2x_2	0	$\sigma_{\mathsf{I}}^{\female}$	$2\sigma_{\mathsf{I}}^{\female}$
x_2X_2	$\sigma_{\mathsf{C}}^{\female}$	$\sigma_{\mathsf{I}}^{\female} + \sigma_{\mathsf{C}}^{\female} - \gamma_1$	$2\sigma_{\mathsf{I}}^{\female} + \sigma_{\mathsf{C}}^{\female} - \gamma$
X_2X_2	$2\sigma_{\mathsf{C}}^{\female}$	$\sigma_{\mathsf{I}}^{\female} + 2\sigma_{\mathsf{C}}^{\female} - \gamma$	$2\sigma_{\mathsf{I}}^{\female} + 2\sigma_{\mathsf{C}}^{\female} - 2\gamma$

Males:

	x_1	X_1
x_2	0	$\sigma_{\mathsf{I}}^{\male}$
X_2	$\sigma_{\mathsf{C}}^{\male}$	$\sigma_{\mathsf{I}}^{\male} + \sigma_{\mathsf{C}}^{\male} - \epsilon$

Table B.1: **Fitness of the general model: Nuclear DMIs.** The genotypic fitness of hybrids for all different genomic architectures are composed of an allelic ($\sigma_{\mathsf{C}}, \sigma_{\mathsf{I}}$) and an epistatic term ($\gamma_1, \gamma, \epsilon$). Epistatic interactions are quantified by γ_1, γ in female and ϵ in male hybrids. Only double heterozygous female F1-hybrids are assigned an independent epistasis term γ_1, which is set to $\gamma_1 = 0$ for recessive models and to $\gamma_1 = \frac{\gamma}{2}$ for codominant models. Dosage compensation can be modeled as a special case of sex-specific allelic and epistatic fitness. With dosage compensation a single X-linked alleles in males has the same strengthend impact as two homozygous X-linked alleles in females concerning allelic and epistatic fitness. Therefore we can implement dosage compensation D as follows:

- without or with dosage compensation $D = 0$ or 1
- $\sigma_{\mathsf{C}}^{\male} = (1 + D)\sigma_{\mathsf{C}}^{\female}$ and $\sigma_{\mathsf{I}}^{\male} = (1 + D)\sigma_{\mathsf{I}}^{\female}$
- $\epsilon = (1 + D)\frac{\gamma}{2}$, except for $X \to X$ where $\epsilon = (1 + 3D)\frac{\gamma}{2}$.

Fitness of the general model: Cyto-nuclear DMIs.

O→A-model:

	aa	aA	AA
o	0	σ_{I}	$2\sigma_{\mathsf{I}}$
O	$2\sigma_{\mathsf{C}}$	$\sigma_{\mathsf{I}} + 2\sigma_{\mathsf{C}} - \gamma$	$2\sigma_{\mathsf{I}} + 2\sigma_{\mathsf{C}} - 2\gamma$

A→O-model:

	o	O
aa	0	σ_{C}
aA	σ_{C}	$2\sigma_{\mathsf{I}} + \sigma_{\mathsf{C}} + \gamma$
AA	$2\sigma_{\mathsf{C}}$	$2\sigma_{\mathsf{I}} + \sigma_{\mathsf{C}} + 2\gamma$

O→X-model:

Females:

	xx	xX	XX
o	0	$\sigma_{\mathsf{I}}^{\mathsf{Q}}$	$2\sigma_{\mathsf{I}}^{\mathsf{Q}}$
O	$2\sigma_{\mathsf{C}}^{\mathsf{Q}}$	$\sigma_{\mathsf{I}}^{\mathsf{Q}} + 2\sigma_{\mathsf{C}}^{\mathsf{Q}} - \gamma$	$2\sigma_{\mathsf{I}}^{\mathsf{Q}} + 2\sigma_{\mathsf{C}}^{\mathsf{Q}} - 2\gamma$

Males:

	x	X
o	0	$\sigma_{\mathsf{I}}^{\mathsf{♂}}$
O	$2\sigma_{\mathsf{C}}^{\mathsf{♂}}$	$\sigma_{\mathsf{I}}^{\mathsf{♂}} + 2\sigma_{\mathsf{C}}^{\mathsf{♂}} - \epsilon$

X→O-model:

Females:

	o	O
x	0	$2\sigma_{\mathsf{I}}^{\mathsf{Q}}$
xX	$\sigma_{\mathsf{C}}^{\mathsf{Q}}$	$2\sigma_{\mathsf{I}}^{\mathsf{Q}} + \sigma_{\mathsf{C}}^{\mathsf{Q}} - \gamma$
XX	$2\sigma_{\mathsf{C}}^{\mathsf{Q}}$	$2\sigma_{\mathsf{I}}^{\mathsf{Q}} + 2\sigma_{\mathsf{C}}^{\mathsf{Q}} - 2\gamma$

Males:

	o	O
x	0	$\sigma_{\mathsf{I}}^{\mathsf{♂}}$
X	$\sigma_{\mathsf{C}}^{\mathsf{♂}}$	$2\sigma_{\mathsf{I}}^{\mathsf{♂}} + \sigma_{\mathsf{C}}^{\mathsf{♂}} - \epsilon$

Table B.2: **Fitness of the general model: Cyto-nuclear DMIs.** Allelic and epistatic fitness are quantified as in the Table B.1. For cyto-nuclear DMIs no recessive DMIs are investigated as the haploid cytoplasmic locus cannot be heterozygous, i.e. there is never a compatible wild type allele that could rescue the phenotype of a mutant- no double heterozygotes with epistatic term γ_1 exist. As in the nuclear DMI case dosage compensation of a single X-linked alleles in males leads to strengthened allelic and epistatic effects, as two homozygous X-linked alleles in females. Dosage compensation D of X-linked alleles is modeled as follows:

- without or with dosage compensation $D = 0$ or 1
- $\sigma_{\mathsf{C}}^{\mathsf{♂}} = (1 + D)\sigma_{\mathsf{C}}^{\mathsf{Q}}$ and $\sigma_{\mathsf{I}}^{\mathsf{♂}} = (1 + D)\sigma_{\mathsf{I}}^{\mathsf{Q}}$
- $\epsilon = (1 + D)\gamma$.

For the dynamics we use the explicit expressions for the marginal fitness

$$\omega_j^{*S} = \frac{1}{p_j} \sum_{j \in G^S} \omega(G^S) P(G^S), \tag{B.1}$$

the mean fitness $\bar{\omega}^S$

$$\bar{\omega}^S = \sum_{\text{all } G^S} \omega(G^S) P(G^S) \tag{B.2}$$

where G^S denotes the genotype of sex $S \in (\female, \male)$, p_j denotes the allele frequency of allele j, and $P(G^S)$ denotes the genotype frequency, and finally $\omega(G^S)$ denotes the genotype fitness as given in Table B.1, B.2.

Dynamics of the general model

We use the equations in **Box 1** in the main text and insert the fitness terms above for the time derivative of the continental allele frequency ($\dot{p_\mathsf{C}}$) and island allele frequency ($\dot{p_\mathsf{I}}$):

$$\begin{aligned}
\dot{p_\mathsf{C}} &= c_\mathsf{C} m + p_\mathsf{C} \Bigg[\underbrace{(1-p_\mathsf{C}) s_\mathsf{C}}_{\text{selection}} \\
&\quad + k_1 p_\mathsf{I} (1-p_\mathsf{C}) \Bigg(\underbrace{\Big(t_1^\mathsf{C} p_\mathsf{C} (-1 + t_2^\mathsf{C} p_\mathsf{I}) - t_2^\mathsf{C} p_\mathsf{I} \Big)(\gamma - 2\gamma_1)}_{\text{dominance epistasis}} - \underbrace{t_3^\mathsf{C} \gamma_1 - k_2^\mathsf{C} \epsilon}_{\text{average epistasis in } \female \text{ and } \male} \Bigg) - c_\mathsf{C} m \Bigg] \\
\dot{p_\mathsf{I}} &= p_\mathsf{I} \Bigg[(1-p_\mathsf{I}) s_\mathsf{I} \\
&\quad + k_3 p_\mathsf{C} (1-p_\mathsf{I}) \Bigg(\Big(t_1^\mathsf{I} p_\mathsf{I} (-1 + t_2^\mathsf{I} p_\mathsf{C}) - t_2^\mathsf{I} p_\mathsf{C} \Big)(\gamma - 2\gamma_1) - t_3^\mathsf{I} \gamma_1 - k_2^\mathsf{I} \epsilon \Bigg) - c_\mathsf{I} m \Bigg]
\end{aligned} \tag{B.3}$$

Below we will analyse the three components of these equations:

- Selection ($s_\mathsf{C}, s_\mathsf{I}$)
- Epistasis ($\gamma_1, \gamma, \epsilon, k_i, t_j$)

General Model: Parameter combinations for the different genomic architectures.

Model	G_C[1]	G_I[2]	s_C	s_I	c_C	c_I
A→A[3]	aaBB	AAbb	$\frac{\sigma_C^{♀}+\sigma_C^{♂}}{2}$	$\frac{\sigma_I^{♀}+\sigma_I^{♂}}{2}$	1	1
X→A	aaXX, aaXy	AAxx, AAxy	$\frac{2\sigma_C^{♀}+\sigma_C^{♂}}{3}$	$\frac{\sigma_I^{♀}+\sigma_I^{♂}}{2}$	$1+\frac{R}{3}$	1
A→X	AAxx, AAxy	aaXX, aaXy	$\frac{\sigma_C^{♀}+\sigma_C^{♂}}{2}$	$\frac{2\sigma_I^{♀}+\sigma_I^{♂}}{3}$	1	$1+\frac{R}{3}$
X→X	XX*xx*[4], X*x*	xx*XX*, x*X*	$\frac{2\sigma_C^{♀}+\sigma_C^{♂}}{3}$	$\frac{2\sigma_I^{♀}+\sigma_I^{♂}}{3}$	$1+\frac{R}{3}$	$1+\frac{R}{3}$
A→O	AAo	aaO	$\frac{\sigma_C^{♀}+\sigma_C^{♂}}{2}$	$2\sigma_I^{♀}$	1	$1+R$
O→A	aaO	AAo	$2\sigma_C^{♀}$	$\frac{\sigma_I^{♀}+\sigma_I^{♂}}{2}$	$1+R$	1
X→O	XXo,Xo	xxO,xO	$\frac{2\sigma_C^{♀}+\sigma_C^{♂}}{3}$	$2\sigma_I^{♀}$	$1+\frac{R}{3}$	$1+R$
O→X	xxO,xO	XXo,Xo	$2\sigma_C^{♀}$	$\frac{2\sigma_I^{♀}+\sigma_I^{♂}}{3}$	$1+R$	$1+\frac{R}{3}$

Table B.3: The equation terms s_C, s_I and c_C, c_I are functions of allelic fitness $\sigma_{C/I}^{♀}, \sigma_{C/I}^{♂}$ and of $R \in [-1,1]$ for male to female biased migration, respectively. They differ for each architecture.

- Migration (m, c_C, c_I)

1. Selection: Allelic fitness

The sex-averaged allelic fitness effect s_C, s_I are functions of allelic fitness in females and males, $\sigma_C^{♀,♂}, \sigma_I^{♀,♂}$, and their respective value can be found in the Table B.3 for each genomic architecture. As discussed before in this study the relation of allelic fitness in females and males is determined by dosage compensation.

2. Epistasis

Epistasis is described by γ_1 and γ in females and ϵ in males. Details for their parametrization in each model by parameters k_i, t_j are given in Table B.4.

The epistatic term in the dynamics of the general model (B.3) can be decomposed into two parts:

- A sex-averaged part: This part reflects the average epistasis over all female and

[1] Immigrating genotypes from the continent
[2] Resident genotypes on the island
[3] model by Bank et al. (2012)
[4] Short for $X_1X_1x_2x_2$

Parameters in Eq. (B.3)

Model	k_1	$k_2^{C/I}$	k_3	$t_1^{C/I}$	$t_2^{C/I}$	$t_3^{C/I}$
A→A	1	0	1	2	1	2
A→X	$\frac{1}{2}$	1	$\frac{2}{3}$	2	1	2
X→A	$\frac{2}{3}$	1	$\frac{1}{2}$	2	1	2
X→X	$\frac{2}{3}$	$\frac{1}{2}$	$\frac{2}{3}$	2	1	2
A→O	1	0	1	$1/0$	$0/1$	$1/2$
O→A	1	0	1	$0/1$	$1/0$	$2/1$
X→O	$\frac{1}{3}$	$1/0$	1	$2/0$	$0/1$	2
O→X	1	$0/1$	$\frac{1}{3}$	$0/2$	$1/0$	2

Table B.4: Values for the parameters in Eq. (B.3) for the different genomic architectures of the DMI.

male F1 hybrids.

- A dominance-epistasis part: For models with non-vanishing dominance / recessivity of the DMI ($\gamma_1 \neq \frac{\gamma}{2}$) a second, frequency dependent part of epistasis exists.

If we consider the general model for nuclear DMIs, we notice a twofold departure of symmetry from the original symmetrical A→A-model by Bank et al. (2012). First, we distinguish between the two sexes, males and females, which is realized by $k_2^{C/I} \neq 0$. Second, while we still maintain codominant epistasis in males, higher order epistasis in females is asymmetrical between the autosome and the X chromosome, such that $k_1 \neq k_3$.

3. Migration

Finally for migration, we have defined a parameter R for sex-biased migration in the main text (see "Population structure and migration"). We can link R to the coefficients for sex-biased migration c_{C} and c_{I} given in Table B.3. We fix the individual migration rate m for all models and write female and male migration rate $m^{\female}, m^{\male}$ in terms of m.

$$m^{\female} = m(1+R) \quad \text{and} \quad m^{\male} = m(1-R) \tag{B.4}$$

The different **effective migration rates**, $c_{\mathsf{C}}m$ and $c_{\mathsf{I}}m$ respectively, are given for the continental and island incompatible allele as follows:

- if the incompatible allele is situated on an **autosome**:

$$m_{\mathcal{A}} = \frac{m^{\female} + m^{\male}}{2} = m \Rightarrow c_{\mathsf{C}}, c_{\mathsf{I}} = 1 \tag{B.5}$$

- if the incompatible allele is situated on an **X chromosome**:

$$m_{\mathcal{X}} = \frac{2m^{\female} + m^{\male}}{3} = m(1+\frac{R}{3}) \Rightarrow c_{\mathsf{C}}, c_{\mathsf{I}} = (1+\frac{R}{3}) \tag{B.6}$$

- if the incompatible allele is situated in the **mitochondrial genome**:

$$m_{\mathcal{O}} = m^{\female} = m(1+R) \Rightarrow c_{\mathsf{C}}, c_{\mathsf{I}} = (1+R) \tag{B.7}$$

This implies that for

- $R = 0$: equal individual migration rates for males and females $\Rightarrow m = m_{\mathcal{A}} = m_{\mathcal{X}} = m_{\mathcal{O}}$
- $-1 \leq R < 0$: excess of males migrating $\Rightarrow m_{\mathcal{A}} > m_{\mathcal{X}} > m_{\mathcal{O}}$
- $0 < R \leq 1$: excess of females migrating $\Rightarrow m_{\mathcal{A}} < m_{\mathcal{X}} < m_{\mathcal{O}}$

We thus get a uniform system of differential equations for all different architectures. Unfortunately, it is not possible to fully solve the system analytically to obtain any internal equilibria, such that we have to resort to numerical analysis eventually for the analysis of the internal dynamics. However, we can investigate the dynamics on the boundaries of the frequency space and give necessary conditions of the existence of a stable DMI.

Below, we investigate the cases of nuclear DMIs in more detail. They all share the values for the parameters $t_1^{C,I}$ to $t_3^{C,I}$, which we will set to their values for nuclear DMIs in the following.

Equilibria without migration

We calculate the nullclines to investigate the dynamics without migration. All equilibria lie at the intersection of two nullclines, $\dot{p}_\mathsf{C} = 0$ and $\dot{p}_\mathsf{I} = 0$.

The three nullcline for $\dot{p}_\mathsf{C} = 0$ are given by:

$$\left\{\{p_\mathsf{C} \to 0\}, \{p_\mathsf{C} \to 1\}, \left\{p_\mathsf{C} \to \frac{-s_\mathsf{C} + k_1 p_\mathsf{I}(p_\mathsf{I}(\gamma - 2\gamma_1) + 2\gamma_1 + k_2^\mathsf{C}\epsilon)}{2k_1(-1 + p_\mathsf{I})p_\mathsf{I}(\gamma - 2\gamma_1)}\right\}\right\} \tag{B.8}$$

Second, we find three nullclines for $\dot{p}_\mathsf{I} = 0$:

$$\left\{\{p_\mathsf{I} \to 0\}, \{p_\mathsf{I} \to 1\}, \left\{p_\mathsf{I} \to \frac{-s_\mathsf{I} + k_3 p_\mathsf{C}(p_\mathsf{C}(\gamma - 2\gamma_1) + 2\gamma_1 + k_2^\mathsf{I}\epsilon)}{2k_3(-1 + p_\mathsf{C})p_\mathsf{C}(\gamma - 2\gamma_1)}\right\}\right\} \tag{B.9}$$

With these nullclines, we find all four monomorphic equilibria to be admissible. They have the following eigenvalues.

equilibrium:$(p_\mathsf{C}, p_\mathsf{I})$	eigenvalue to $\binom{p_\mathsf{C}}{p_\mathsf{I}} = \binom{1}{0}$	eigenvalue to $\binom{p_\mathsf{C}}{p_\mathsf{I}} = \binom{0}{1}$
$(0,1)$	$s_\mathsf{C} - k_1(\gamma + k_2^\mathsf{C}\epsilon)$	$-s_\mathsf{I}$
$(1,1)$	$-s_\mathsf{C} + k_1(\gamma + k_2^\mathsf{C}\epsilon)$	$-s_\mathsf{I} + k_3(\gamma + k_2^\mathsf{I}\epsilon)$
$(1,0)$	$-s_\mathsf{C}$	$s_\mathsf{I} - k_3(\gamma + k_2^\mathsf{I}\epsilon)$
$(0,0)$	s_C	s_I

(B.10)

The third nullcline in Eq. (B.8) is never internal for

$$s_{\mathsf{C}} < k_1 p_{\mathsf{I}}(p_{\mathsf{I}}(\gamma - 2\gamma_1) + 2\gamma_1 + k_2^{\mathsf{C}}\epsilon) \qquad \text{especially} \qquad s_{\mathsf{C}} < 0.$$

Biologically this condition can be translated, such that the immigrating allele cannot to take over the population unless its advantage outweighs the effect of epistasis for $m = 0$. This is never the case if the continental allele is deleterious.

For positive s_{C}, with $s_{\mathsf{C}} > k_1 p_{\mathsf{I}}(p_{\mathsf{I}}(\gamma - 2\gamma_1) + 2\gamma_1 + k_2^{\mathsf{C}}\epsilon)$ we find that the third nullclines in Eq. (B.8) and (B.9) are both monotonically decreasing for $\gamma_1 \leq \frac{\gamma}{2}$. Furthermore, extensive numerical investigations show, that for $\gamma_1 < \gamma$ these nullclines only cross once inside the state space, to give rise to an unstable internal equilibrium, a saddle point.

In summary, we find that there is at most one unstable internal equilibrium at $m = 0$ for nuclear DMIs. Any stable DMI for small positive migration rates has to correspond to a perturbed boundary equilibrium.

Equilibria with migration

As for the codominant case discussed below, we find three boundary equilibria

$$\begin{aligned} \mathsf{SLP_C} &= (p_{\mathsf{C}} \to -\tfrac{c_{\mathsf{C}} m}{s_{\mathsf{C}}},\ p_{\mathsf{I}} \to 0) \\ \mathsf{SLP_I} &= (p_{\mathsf{C}} \to 1,\ p_{\mathsf{I}} \to 1 + \tfrac{c_{\mathsf{I}} m}{-s_{\mathsf{I}} + k_3(\gamma + k_2^{\mathsf{I}}\epsilon)}) \\ \mathsf{FIX} &= (p_{\mathsf{C}} \to 1,\ p_{\mathsf{I}} \to 0) \end{aligned} \tag{B.11}$$

We note, that the single locus polymorphism on the island locus, $\mathsf{SLP_I}$, is independent of γ_1, i.e. epistasis in the double heterozygous hybrid. This is of course understandable, as with the fixed continental allele these hybrids are missing in the population.

We find the following eigenvalues for these equilibria:

equil.	along boundary	into state space
SLP_C	$c_\text{C} m + s_\text{C}$	$-c_\text{I} m + s_\text{I} + \frac{-c_\text{C}^2 k_3 m^2(\gamma - 2\gamma_1) + c_\text{C} k_3 m s_\text{C}(2\gamma_1 + k_2^\text{I}\epsilon)}{s_\text{C}^2}$
SLP_I	$c_\text{I} m - s_\text{I} + k_3(\gamma + k_2^\text{I}\epsilon)$	$-c_\text{C} m - s_\text{C} - \frac{k_1(c_\text{I} m - s_\text{I} + k_3(\gamma + k_2^\text{I}\epsilon))(c_\text{I} m(\gamma - 2\gamma_1) + (\gamma + k_2^\text{C}\epsilon)(s_\text{I} - k_3(\gamma + k_2^\text{I}\epsilon)))}{(s_\text{I} - k_3(\gamma + k_2^\text{I}\epsilon))^2}$
FIX	$\leftrightarrow$: $-c_\text{C} m - s_\text{C}$	$\updownarrow$: $-c_\text{I} m + s_\text{I} - k_3(\gamma + k_2^\text{I}\epsilon)$

(B.12)

For the equilibrium FIX, where the continental genotype has swamped the island '$\leftrightarrow$' denotes the eigenvalue along the continental boundary ($p_\text{I} = 0$) and '$\updownarrow$' denotes the eigenvalue along the island boundary ($p_\text{C} = 1$) in the frequency phase space.

From these eigenvalues, we can deduce stability conditions and link them to conditions found in Bank et al. (2012):

Whenever SLP_I or SLP_C are admissible, the eigenvalues along the boundary are negative, hence we always evolve towards the equilibrium along the boundary.

If SLP_C is admissible, it is stable whenever:

$$\begin{aligned} &\frac{-c_\text{I} s_\text{C}^2 + c_\text{C} k_3 s_\text{C}(2\gamma_1 + k_2\epsilon) + \sqrt{s_\text{C}^2\left(4c_\text{C}^2 k_3 s_\text{I}(\gamma - 2\gamma_1) + (c_\text{I} s_\text{C} - c_\text{C} k_3(2\gamma_1 + k_2^\text{I}\epsilon))^2\right)}}{2c_\text{C}^2 k_3(\gamma - 2\gamma_1)} \\ &< m < -\frac{s_\text{C}}{c_\text{C}} \end{aligned} \tag{B.13}$$

If SLP_I is admissible, it is stable whenever:

$$\frac{(-s_{\mathsf{I}}+k_3(\gamma+k_2^{\mathsf{I}}\epsilon))}{2c_{\mathsf{I}}^2k_1(\gamma-2\gamma_1)}[(c_{\mathsf{I}}k_1(2\gamma_1+k_2^{\mathsf{C}}\epsilon)+c_{\mathsf{C}}(s_{\mathsf{I}}-k_3(\gamma+k_2^{\mathsf{I}}\epsilon))$$
$$-\{2c_{\mathsf{C}}c_{\mathsf{I}}k_1(2\gamma_1+k_2^{\mathsf{C}}\epsilon)(s_{\mathsf{I}}-k_3(\gamma+k_2^{\mathsf{I}}\epsilon))$$
$$+c_{\mathsf{C}}^2(s_{\mathsf{I}}-k_3(\gamma+k_2^{\mathsf{I}}\epsilon))^2+c_{\mathsf{I}}^2k_1(-4s_{\mathsf{C}}(\gamma-2\gamma_1)+k_1(2\gamma-2\gamma_1+k_2^{\mathsf{C}}\epsilon)^2)\}^{\frac{1}{2}})]$$
$$<m<\frac{s_{\mathsf{I}}-k_3(\gamma-k_2^{\mathsf{I}}\epsilon)}{c_{\mathsf{I}}} \tag{B.14}$$

We also observe that the two boundary equilibria cannot be stable simultaneously. If both are admissible, $c_{\mathsf{C}}m+s_{\mathsf{C}}<0$ hence $\mathsf{SLP_I}$ can never be stable, as its eigenvalue into the state space is positive.

The monomorphism FIX is stable iff

$$m>\max\left[-\frac{s_{\mathsf{C}}}{c_{\mathsf{C}}},\frac{s_{\mathsf{I}}-k_3(\gamma+k_2^{\mathsf{I}}\epsilon)}{c_{\mathsf{I}}}\right] \tag{B.15}$$

The conditions (B.13),(B.14),(B.15) correspond to the condition (T.31c), (T.31b) and (T.31a) in the Appendix of Bank et al. (2012).

For strong enough migration the island is always swamped by the immigrating genotype and FIX is becomes stable.

Although we cannot solve the dynamics in the interior of the state space, some information can be gained from the nullclines. We find 3 nullclines for $\dot{p}_{\mathsf{C}}=0$ for the general model:

- $\mathcal{N}_{1,2}: p_{\mathsf{I}}=$
$$\frac{k_1p_{\mathsf{C}}(2p_{\mathsf{C}}(\gamma-2\gamma_1)+2\gamma_1+k_2^{\mathsf{C}}\epsilon)\pm\sqrt{k_1p_{\mathsf{C}}\left(-4(-1+2p_{\mathsf{C}})(c_{\mathsf{C}}m+p_{\mathsf{C}}s_{\mathsf{C}})(\gamma-2\gamma_1)+k_1p_{\mathsf{C}}(2p_{\mathsf{C}}(\gamma-2\gamma_1)+2\gamma_1+k_2^{\mathsf{C}}\epsilon)^2\right)}}{2k_1p_{\mathsf{C}}(-1+2p_{\mathsf{C}})(\gamma-2\gamma_1)}$$
- $\mathcal{N}_3: p_{\mathsf{C}}=1$

(B.16)

With *Wolfram Mathematica* we can show that for $0 \leq \gamma_1 \leq \frac{\gamma}{2}$, $m \geq 0$, $s_\mathsf{I} > 0$, arbitrary s_C and $k_1, k_2^\mathsf{C}, k_3 > 0$ and $c_\mathsf{C}, c_\mathsf{I} > 0$ the nullcline $\mathcal{N}_1$ (with plus sign) is never internal. Furthermore, under the conditions above, we find that $\frac{d\mathcal{N}_2}{dp_\mathsf{C}} < 0$ for $0 < p_\mathsf{C} < 1$, hence the nullcline $\mathcal{N}_2$ is monotonically decreasing.

Furthermore, we find 3 nullclines for $\dot{p}_\mathsf{I} = 0$:

- $\mathcal{N}_{4,5} : p_\mathsf{I} =$

$$\frac{-s_\mathsf{I}+k_3 p_\mathsf{C}((-2+3p_\mathsf{C})\gamma-6(-1+p_\mathsf{C})\gamma_1+k_2^\mathsf{I}\epsilon)}{4k_3(-1+p_\mathsf{C})p_\mathsf{C}(\gamma-2\gamma_1)} \pm \frac{\sqrt{(s_\mathsf{I}-k_3 p_\mathsf{C}((-2+3p_\mathsf{C})\gamma+6\gamma_1-6p_\mathsf{C}\gamma_1+k_2^\mathsf{I}\epsilon))^2-8k_3(-1+p_\mathsf{C})p_\mathsf{C}(\gamma-2\gamma_1)(c_\mathsf{I}m-s_\mathsf{I}+k_3 p_\mathsf{C}(p_\mathsf{C}\gamma+2\gamma_1-2p_\mathsf{C}\gamma_1+k_2^\mathsf{I}\epsilon))}}{4k_3(-1+p_\mathsf{C})p_\mathsf{C}(\gamma-2\gamma_1)}$$

- $\mathcal{N}_6 : p_\mathsf{I} = 0$

(B.17)

Again we can show that for $0 \leq \gamma_1 \leq \frac{\gamma}{2}$, $m \geq 0$, $s_\mathsf{I} > 0$, arbitrary s_C and $k_1, k_2^\mathsf{I}, k_3 > 0$ and $c_\mathsf{C}, c_\mathsf{I} > 0$ the nullcline $\mathcal{N}_5$ (with minus sign) is never internal. Furthermore, we can show that under these conditions $\mathcal{N}_4$ is monotonically decreasing in p_C.

In summary:

- $\mathcal{N}_1, \mathcal{N}_5$ are not internal for $\gamma_1 \leq \frac{\gamma}{2}$
- $\mathcal{N}_2, \mathcal{N}_4$ decrease monotonically

Additionally, extensive numerical investigations indicate that the nullclines for the parameter space in question ($0 \leq \gamma_1 < \gamma$) cross at most twice to form a stable DMI and an unstable internal equilibrium (saddle point). However, we did not succeed to show this analytically. With large $\gamma_1 > \gamma$ the dynamics become increasingly complicated and more than two internal equilibria are admissible.

From our analysis without migration, we deduce that for small migration rates a two-locus polymorphism, a stable DMI, will only evolve as a perturbed boundary equilibrium. Thus it seems that the internal dynamics of the general model for $0 \leq \gamma_1 < \gamma$ are quite similar to the codominant model $\gamma_1 = \frac{\gamma}{2}$. Compare Fig. B.3 for bifurcation patterns.

Migration bounds for global stability

For the case of $0 \leq \gamma_1 \leq \frac{\gamma}{2}$ we obtain a protected two-locus polymorphism if all boundary equilibria are unstable. In analogy to the codominant model, we derive the migration bounds for the general model, where a transcritical bifurcation of the unstable boundary equilibria occurs, as follows:

$$m^{-}_{\mathsf{max}} \in \begin{cases} 0 & \text{no globally stable DMI admissible} \\ m^{\mathsf{C}}_{\mathsf{max}} & \text{bifurcation at SLP}_{\mathsf{C}} \\ m^{\mathsf{I}}_{\mathsf{max}} & \text{bifurcation at SLP}_{\mathsf{I}} \end{cases} \tag{B.18}$$

The migration bound $m^{\mathsf{C}}_{\mathsf{max}}$, where the SLP$_{\mathsf{C}}$ changes stability is given by:

$$m^{\mathsf{C}}_{\mathsf{max}} = \frac{-c_{\mathsf{I}} s_{\mathsf{C}}^2 + c_{\mathsf{C}} k_3 s_{\mathsf{C}} (2\gamma_1 + k_2^{\mathsf{I}} \epsilon) + \sqrt{s_{\mathsf{C}}^2 \left(4 c_{\mathsf{C}}^2 k_3 s_{\mathsf{I}} (\gamma - 2\gamma_1) + (c_{\mathsf{I}} s_{\mathsf{C}} - c_{\mathsf{C}} k_3 (2\gamma_1 + k_2^{\mathsf{I}} \epsilon))^2\right)}}{2 c_{\mathsf{C}}^2 k_3 (\gamma - 2\gamma_1)} \tag{B.19}$$

The migration bound $m^{\mathsf{I}}_{\mathsf{max}}$, where the SLP$_{\mathsf{I}}$ changes stability is given by:

$$\begin{aligned} m^{\mathsf{I}}_{\mathsf{max}} = {} & \frac{(-s_{\mathsf{I}} + k_3(\gamma + k_2^{\mathsf{I}} \epsilon)) \cdot (c_{\mathsf{I}} k_1 (2\gamma_1 + k_2^{\mathsf{C}} \epsilon) + c_{\mathsf{C}} (s_{\mathsf{I}} - k_3 (\gamma + k_2^{\mathsf{I}} \epsilon))}{2 c_{\mathsf{I}}^2 k_1 (\gamma - 2\gamma_1)} \\ & - \frac{(-s_{\mathsf{I}} + k_3(\gamma + k_2^{\mathsf{I}} \epsilon)) \sqrt{2 c_{\mathsf{C}} c_{\mathsf{I}} k_1 (2\gamma_1 + k_2^{\mathsf{C}} \epsilon)(s_{\mathsf{I}} - k_3(\gamma + k_2^{\mathsf{I}} \epsilon)) + c_{\mathsf{C}}^2 (s_{\mathsf{I}} - k_3(\gamma + k_2^{\mathsf{I}} \epsilon))^2 + c_{\mathsf{I}}^2 k_1 \left(-4 s_{\mathsf{C}} (\gamma - 2\gamma_1) + k_1 (2\gamma - 2\gamma_1 + k_2^{\mathsf{C}} \epsilon)^2\right)}}{2 c_{\mathsf{I}}^2 k_1 (\gamma - 2\gamma_1)} \end{aligned} \tag{B.20}$$

Necessary and sufficient conditions for the existence of a DMI

With perturbation analysis we finally prove that if $(p_{\mathsf{C}}, p_{\mathsf{I}}) = (0, 1)$ is stable at $m = 0$, it will move into the state space with positive migration rates ($\Delta \approx 0 \Rightarrow \Delta m$), and hence form a stable DMI. We show this for *nuclear* and *cytonuclear DMIs*. All other vertex

equilibria lie on invariant boundaries, and cannot enter the state space. We write the dynamics of of the continental allele of the general model in the following way:

$$\dot{p}_{\mathsf{C}} \;=\; 0 \;=\; p_{\mathsf{C}}(\Delta m)(\omega_{\mathsf{C}}(\Delta m) - \bar{\omega}(\Delta m)) + (1 - p_{\mathsf{C}}(\Delta m))\Delta m$$

We convert the equation to get an approximation of the continental allele frequency of the stable DMI

$$p_{\mathsf{C}}(\Delta m) \;=\; -\Delta \cdot \underbrace{\frac{(1 - p_{\mathsf{C}}(\Delta m))m}{\omega_{\mathsf{C}}(\Delta m) - \bar{\omega}(\Delta m)}}_{\text{expand around } \Delta = 0} \;\approx\; -\Delta \tfrac{m}{\omega_{\mathsf{C}} - \bar{\omega}} + \mathcal{O}(\Delta^2)$$

From $\omega_{\mathsf{C}}(\Delta = 0) - \bar{\omega}(\Delta = 0) = s_{\mathsf{C}} - k_1(t_2^{\mathsf{C}}(\gamma - 2\gamma_1) + t_3^{\mathsf{C}}\gamma_1 + k_2^{\mathsf{C}}\epsilon)$ we deduce that $p_{\mathsf{C}}(\Delta m) > 0$, i.e. that with increasing migration the frequency of the continental allele of the equilibrium will increase and be permissible for the general model including the cytonuclear DMIs, iff

$$s_{\mathsf{C}} < k_1(t_2^{\mathsf{C}}(\gamma - 2\gamma_1) + t_3^{\mathsf{C}}\gamma_1 + k_2^{\mathsf{C}}\epsilon) \quad \text{and} \quad m < |s_{\mathsf{C}} - k_1(t_2^{\mathsf{C}}(\gamma - 2\gamma_1) + t_3^{\mathsf{C}}\gamma_1 + k_2^{\mathsf{C}}\epsilon)| \tag{B.21}$$

This simplifies to

$$s_{\mathsf{C}} < k_1(\gamma + k_2^{\mathsf{C}}\epsilon) \quad \text{and} \quad m < |s_{\mathsf{C}} - k_1(\gamma + k_2^{\mathsf{C}}\epsilon)| \tag{B.22}$$

for nuclear DMIs and is independent of γ_1.

For $\dot{p}_{\mathsf{I}}$ we cannot apply the same technique as $\omega_{\mathsf{I}}(\Delta = 0) - \bar{\omega}(\Delta = 0) = 0$, so we write

$$
\begin{aligned}
\dot{p}_{\mathsf{I}} = 0 \qquad &= p_{\mathsf{I}}(\Delta m)(\omega_{\mathsf{I}}(\Delta m) - \bar{\omega}(\Delta m)) - p_{\mathsf{I}}(\Delta m)\Delta m \\
&= (\omega_{\mathsf{I}}(\Delta m) - \bar{\omega}(\Delta m)) - \Delta m \\
&= (1 - p_{\mathsf{I}}(\Delta m)) \underbrace{s_{\mathsf{I}}}_{\text{selection}} - p_{\mathsf{C}}(\Delta m)(1 - p_{\mathsf{I}}(\Delta m)) \underbrace{\Gamma^*}_{\text{epistasis term}} - \Delta m \\
&= (1 - p_{\mathsf{I}}(\Delta m))(s_{\mathsf{I}} - p_{\mathsf{C}}(\Delta m)\Gamma^*) - \Delta m
\end{aligned}
$$

$$
\begin{aligned}
\Rightarrow \qquad p_{\mathsf{I}}(\Delta m) &= 1 - \Delta \tfrac{m}{s_{\mathsf{I}} - p_{\mathsf{C}}(\Delta m)\Gamma^*}, \text{ where } p_{\mathsf{C}}(\Delta m) = 0 \\
p_{\mathsf{I}}(\Delta m) &\approx 1 - \Delta \tfrac{m}{s_{\mathsf{I}}}
\end{aligned}
$$

Hence for small migration rates and iff

$$
0 < m < s_{\mathsf{I}} \tag{B.23}
$$

the frequency of the island allele of the equilibrium will decrease with increasing migration.

Taken together, the calculations yield the perturbed, approximated coordinates of a stable DMI:

$$
\mathsf{I}_{\mathsf{DMI}}|_{\Delta m} = \left(-\Delta \frac{m}{s_{\mathsf{C}} - k_1(t_2^{\mathsf{C}}(\gamma - 2\gamma_1) + t_3^{\mathsf{C}}\gamma_1 + k_2^{\mathsf{C}}\epsilon)}, 1 - \Delta \frac{m}{s_{\mathsf{I}}} \right) \tag{B.24}
$$

If (B.21),(B.23) hold, the perturbed equilibrium (B.24) will be internal. These conditions coincide with the conditions of stability of the boundary equilibrium $(p_{\mathsf{C}}, p_{\mathsf{I}}) = (0, 1)$. Hence the island allele has to be beneficial and the continental allele has to be weak enough compared to epistasis in order to obtain a stable internal equilibrium.

Finally, these conditions are also sufficient for the existence of a single stable DMI, because any other stable equilibrium with small migration rates would already have to be present at $m = 0$. However, as we have shown in the Section B.1 'Equilibria without migration', there exists no other stable internal equilibrium at $m = 0$.

B.2 Codominant model

As discussed above the general model cannot be fully solved analytically. However, solvable models can be obtained for special parameter combinations. The model we discuss here is the codominant model, where the epistatic effect of each genotype is directly proportional to the number of incompatible pairs. The full fitness scheme can be found in Tables B.1, B.2, where we simply set $\gamma_1 = \frac{\gamma}{2}$ and obtain our unified codominant model (see Eq. (B.25)).

Dynamics of the unified codominant model

As for the general model, we follow the frequency changes in time of the continental allele p_C and the island allele p_I.

$$\begin{aligned} \dot{p}_C &= (1-p_C)(p_C(s_C - g_C p_I) + c_C m) \\ \dot{p}_I &= p_I((1-p_I)(s_I - g_I p_C) - c_I m) \end{aligned} \tag{B.25}$$

Parameters: **as in the general model**

s_C/s_I ... allelic fitness function of the continental/island allele
depending on the model, $\sigma^{\female}_{C/I}, \sigma^{\male}_{C/I}$ and dosage compensation (D)

m ... migration rate

c_C/c_I ... function for effective migration of the continental/island allele
see Eqs. (B.5),(B.6),(B.7)

unified parameters in the codominant model

g_C/g_I ... epistasis function of continental/island allele
depending on the model and γ, ϵ or γ and D, respectively

Table B.5: **Unified codominant model: Parameter combinations for the different genomic architectures**

Model	G_C[a]	G_I[b]	s_C	s_I	g_C	g_I	c_C	c_I
A→A[c]	aaBB	AAbb	$\frac{\sigma_C^{\female}+\sigma_C^{\male}}{2} \Rightarrow \sigma_C^{\female}$	$\frac{\sigma_I^{\female}+\sigma_I^{\male}}{2} \Rightarrow \sigma_I^{\female}$	$\frac{\gamma+\epsilon}{2} \Rightarrow \gamma$	$\frac{\gamma+\epsilon}{2} \Rightarrow \gamma$	1	1
X→A	aaXX, aaXy	AAxx, AAxy	$\frac{2\sigma_C^{\female}+\sigma_C^{\male}}{3} \Rightarrow \frac{(3+D)\sigma_C^{\female}}{3}$	$\frac{\sigma_I^{\female}+\sigma_I^{\male}}{2} \Rightarrow \sigma_I^{\female}$	$2\frac{\gamma+\epsilon}{3} \Rightarrow \frac{(3+D)\gamma}{3}$	$\frac{\gamma+\epsilon}{2} \Rightarrow \frac{(3+D)\gamma}{4}$	$1+\frac{R}{3}$	1
A→X	AAxx, AAxy	aaXX, aaXy	$\frac{\sigma_C^{\female}+\sigma_C^{\male}}{2} \Rightarrow \sigma_C^{\female}$	$\frac{2\sigma_I^{\female}+\sigma_I^{\male}}{3} \Rightarrow \frac{(3+D)\sigma_I^{\female}}{3}$	$\frac{\gamma+\epsilon}{2} \Rightarrow \frac{(3+D)\gamma}{4}$	$2\frac{\gamma+\epsilon}{3} \Rightarrow \frac{(3+D)\gamma}{3}$	1	$1+\frac{R}{3}$
X→X	XX*xx*[d], X*x*	xx*XX*, x*X*	$\frac{2\sigma_C^{\female}+\sigma_C^{\male}}{3} \Rightarrow \frac{(3+D)\sigma_C^{\female}}{3}$	$\frac{2\sigma_I^{\female}+\sigma_I^{\male}}{3} \Rightarrow \frac{(3+D)\sigma_I^{\female}}{3}$	$\frac{2\gamma+\epsilon}{3} \Rightarrow \frac{(5+3D)\gamma}{6}$	$\frac{2\gamma+\epsilon}{3} \Rightarrow \frac{(5+3D)\gamma}{6}$	$1+\frac{R}{3}$	$1+\frac{R}{3}$
A→O	AAo	aaO	$\frac{\sigma_C^{\female}+\sigma_C^{\male}}{2} \Rightarrow \sigma_C^{\female}$	$2\sigma_I^{\female}$	$\frac{\gamma+\epsilon}{2} \Rightarrow \gamma$	2γ	1	$1+R$
O→A	aaO	AAo	$2\sigma_C^{\female}$	$\frac{\sigma_I^{\female}+\sigma_I^{\male}}{2} \Rightarrow \sigma_I^{\female}$	2γ	$\frac{\gamma+\epsilon}{2} \Rightarrow \gamma$	$1+R$	1
X→O	XXo,Xo	xxO,xO	$\frac{2\sigma_C^{\female}+\sigma_C^{\male}}{3} \Rightarrow \frac{(3+D)\sigma_C^{\female}}{3}$	$2\sigma_I^{\female}$	$\frac{2\gamma+\epsilon}{3} \Rightarrow \frac{(5+D)\gamma}{6}$	2γ	$1+\frac{R}{3}$	$1+R$
O→X	xxO,xO	XXo,Xo	$2\sigma_C^{\female}$	$\frac{2\sigma_I^{\female}+\sigma_I^{\male}}{3} \Rightarrow \frac{(3+D)\sigma_I^{\female}}{3}$	2γ	$\frac{2\gamma+\epsilon}{3} \Rightarrow \frac{(5+D)\gamma}{6}$	$1+R$	$1+\frac{R}{3}$

Table B.6: **Parameters of the unified codominant model.** Each genomic architecture is given by a unique set of parameters for selection, epistasis and migration. We give the general and the simplified term for selection and epistasis. For X-linked alleles with dosage compensation $D = 1$, whereas $D = 0$ without dosage compensation.

[a] Immigrating genotypes from the continent
[b] Resident genotypes on the island
[c] model by Bank et al. (2012)
[d] Short for $X_1X_1x_2x_2$

Individual dynamics for the different models

As before each genomic architecture is given by a different parametrization of selection, epistasis and migration. In Table B.6 we dissect all these terms. Furthermore, we give the individual dynamical systems for each genomic architecture in Eqs. (B.26) to illustrate how the different DMI-models deviate from the reference model by Bank et al. (2012).

Since the A→A-model is symmetric, i.e. a DMI between two autosomes, we obtain symmetric epistasis and migration is not affected by sex-bias. For X→X, the symmetry between the island and the continental allele is maintained. However, the evolutionary forces are rescaled compared to A→A. For all further DMIs including one X chromosome and/or one mitochondrial locus, the original symmetry of epistasis, allelic selection and migration of the A→A-model is broken. Also, dosage compensation of the X chromosome results in a rescaling of selection and epistasis via the dosage compensation factor D ($D \in \{0, 1\}$). For $D = 0$ there is no dosage compensation in males and for $D = 1$ one X-linked allele in males has the same effect as two X-linked alleles in females. Sex-biased migration rates is scaled by $R \in [-1, 1]$, where with $R = 1$ all migrants are female and for $R = -1$ migration is purely male biased.

Any constant factors for all terms of a differential equation only modulate the velocity of the dynamics, whereas the equilibria (at $\dot{p}_\mathsf{C} = \dot{p}_\mathsf{I} = 0$) remain unchanged. For models including mitochondrial loci, only the selection coefficient of females $\sigma^{\female}$ is relevant for the dynamics on the mitochondrial locus. To keep the intra locus effect constant for the haploid mitochondrial locus, we obtain a factor of two for the selective forces of all cytoplasmic alleles.

The dynamics directly show the effect of the inclusion of X chromosomes and mitochondria. If we compare the A→A-model to all other nuclear DMI models, we see that for dosage compensation $D = 1$ in combination with female biased migration rate $R = 1$ all other models correspond simply to a rescaled A→A-model. As any constant factors are canceled out, all equilibria are the same. If we increase the ratio of male migrants $R < 1$, the models start to behave differently. While the A→A-model is unaffected by

the change, any X-linked model experiences an effectively lowered migration rate on the X chromosome. Furthermore, omitting dosage compensation changes selection pressure and epistasis on the X chromosome, and only epistasis on the incompatible partner.

General model

$$\begin{aligned} \dot{p}_{\mathsf{C}} &= (1-p_{\mathsf{C}})(p_{\mathsf{C}}(s_{\mathsf{C}} - g_{\mathsf{C}}p_{\mathsf{I}}) + c_{\mathsf{C}}m) \\ \dot{p}_{\mathsf{I}} &= p_{\mathsf{I}}((1-p_{\mathsf{I}})(s_{\mathsf{I}} - g_{\mathsf{I}}p_{\mathsf{C}}) - c_{\mathsf{I}}m) \end{aligned} \tag{B.26a}$$

Nuclear DMIs

A→A :

$$\begin{aligned} \dot{p}_{\mathsf{C}} &= (1-p_{\mathsf{C}})(p_{\mathsf{C}}(\sigma_{\mathsf{C}}^{\female} - \gamma p_{\mathsf{I}}) + m) \\ \dot{p}_{\mathsf{I}} &= p_{\mathsf{I}}((1-p_{\mathsf{I}})(\sigma_{\mathsf{I}}^{\female} - \gamma p_{\mathsf{C}}) - m) \end{aligned}$$

X→X :

$$\begin{aligned} \dot{p}_{\mathsf{C}} &= (1-p_{\mathsf{C}})(p_{\mathsf{C}}(\tfrac{3+D}{3}\sigma_{\mathsf{C}}^{\female} - \tfrac{5+3D}{6}\gamma p_{\mathsf{I}}) + (1+\tfrac{R}{3})m) \\ \dot{p}_{\mathsf{I}} &= p_{\mathsf{I}}((1-p_{\mathsf{I}})(\tfrac{3+D}{3}\sigma_{\mathsf{I}}^{\female} - \tfrac{5+3D}{6}\gamma p_{\mathsf{C}}) - (1+\tfrac{R}{3})m) \end{aligned} \tag{B.26b}$$

A→X :

$$\begin{aligned} \dot{p}_{\mathsf{C}} &= (1-p_{\mathsf{C}})(p_{\mathsf{C}}(\sigma_{\mathsf{C}}^{\female} - \tfrac{(3+D)}{4}\gamma p_{\mathsf{I}}) + m) \\ \dot{p}_{\mathsf{I}} &= p_{\mathsf{I}}(\tfrac{3+D}{3}(1-p_{\mathsf{I}})(\sigma_{\mathsf{I}}^{\female} - \gamma p_{\mathsf{C}}) - (1+\tfrac{R}{3})m) \end{aligned}$$

X→A :

$$\begin{aligned} \dot{p}_{\mathsf{C}} &= (1-p_{\mathsf{C}})(\tfrac{3+D}{3}p_{\mathsf{C}}(\sigma_{\mathsf{C}}^{\female} - \gamma p_{\mathsf{I}}) + (1+\tfrac{R}{3})m) \\ \dot{p}_{\mathsf{I}} &= p_{\mathsf{I}}((1-p_{\mathsf{I}})(\sigma_{\mathsf{I}}^{\female} - \tfrac{(3+D)}{4}\gamma p_{\mathsf{C}}) - m) \end{aligned}$$

Cytonuclear DMIs

A→O :

$$\begin{aligned}\dot{p}_{\mathsf{C}} &= (1-p_{\mathsf{C}})(p_{\mathsf{C}}(\sigma_{\mathsf{C}}^{\mathsf{Q}}-\gamma p_{\mathsf{I}})+m)\\ \dot{p}_{\mathsf{I}} &= p_{\mathsf{I}}((1-p_{\mathsf{I}})(2\sigma_{\mathsf{I}}^{\mathsf{Q}}-2\gamma p_{\mathsf{C}})-(1+R)m)\end{aligned}$$

O→A :

$$\begin{aligned}\dot{p}_{\mathsf{C}} &= (1-p_{\mathsf{C}})(p_{\mathsf{C}}(2\sigma_{\mathsf{C}}^{\mathsf{Q}}-2\gamma p_{\mathsf{I}})+(1+R)m)\\ \dot{p}_{\mathsf{I}} &= p_{\mathsf{I}}((1-p_{\mathsf{I}})(\sigma_{\mathsf{I}}^{\mathsf{Q}}-\gamma p_{\mathsf{C}})-m)\end{aligned} \tag{B.26c}$$

X→O :

$$\begin{aligned}\dot{p}_{\mathsf{C}} &= (1-p_{\mathsf{C}})(p_{\mathsf{C}}(\tfrac{3+D}{3}\sigma_{\mathsf{C}}^{\mathsf{Q}}-\tfrac{5+D}{6}\gamma p_{\mathsf{I}})+(1+\tfrac{R}{3})m)\\ \dot{p}_{\mathsf{I}} &= p_{\mathsf{I}}((1-p_{\mathsf{I}})(2\sigma_{\mathsf{I}}^{\mathsf{Q}}-2\gamma p_{\mathsf{C}})-(1+R)m)\end{aligned}$$

O→X :

$$\begin{aligned}\dot{p}_{\mathsf{C}} &= (1-p_{\mathsf{C}})(p_{\mathsf{C}}(2\sigma_{\mathsf{C}}^{\mathsf{Q}}-2\gamma p_{\mathsf{I}})+(1+R)m)\\ \dot{p}_{\mathsf{I}} &= p_{\mathsf{I}}((1-p_{\mathsf{I}})(\tfrac{3+D}{3}\sigma_{\mathsf{I}}^{\mathsf{Q}}-\tfrac{5+D}{6}\gamma p_{\mathsf{C}})-(1+\tfrac{R}{3})m)\end{aligned}$$

Equilibria of the unified codominant model

For the unified codominant model in Eq. (B.25) we find three boundary equilibria, two single locus polymorphisms (SLP), and a monomorphic equilibrium (FIX). We also calculate the eigenvalues for the different boundary equilibria, to determine their stability.

SLP$_{\mathsf{I}}$ $= (p_{\mathsf{C}} \to 1, p_{\mathsf{I}} \to 1+\frac{c_{\mathsf{I}}m}{g_{\mathsf{I}}-s_{\mathsf{I}}})$

We find the following eigenvalues corresponding to eigenvectors pointing into the state space and along the boundary:

$$\left\{ g_{\mathsf{C}} - c_{\mathsf{C}} m - s_{\mathsf{C}} + \frac{c_{\mathsf{I}} g_{\mathsf{C}} m}{g_{\mathsf{I}} - s_{\mathsf{I}}},\ \underbrace{g_{\mathsf{I}} + m c_{\mathsf{I}} - s_{\mathsf{I}}}_{<0 \text{ if } \mathsf{SLP_I} \text{ admissible}} \right\} \tag{B.27}$$

This equilibrium corresponds to a SLP on the island allele, after fixation of the continental allele. The first eigenvalue governs the dynamics into the state space and can be rewritten as

$$-c_{\mathsf{C}} m - s_{\mathsf{C}} + g_{\mathsf{C}} \cdot \underbrace{\mathsf{SLP}_{\mathsf{I}}^{p_{\mathsf{I}}}}_{p_{\mathsf{I}} \text{ of } \mathsf{SLP_I}} . \tag{B.28}$$

We see that increasing migration pressure on the continental allele and increasing advantage of the continental allele stabilize the SLP. Moreover, increasing epistasis on the continental allele, destabilizes the SLP. The second eigenvalue governs dynamics along the boundary. It is always negative, if the equilibrium is admissible, such that the dynamics evolve towards the equilibrium along the boundary.

$\mathsf{SLP_C}$ $= (p_{\mathsf{C}} \to -\frac{c_{\mathsf{C}} m}{s_{\mathsf{C}}}, p_{\mathsf{I}} \to 0)$

We find the following eigenvalues corresponding to eigenvectors pointing into the state space and along the boundary:

$$\left\{ g_{\mathsf{I}} \frac{c_{\mathsf{C}} m}{s_{\mathsf{C}}} - c_{\mathsf{I}} m + s_{\mathsf{I}},\ \underbrace{c_{\mathsf{C}} m + s_{\mathsf{C}}}_{<0 \text{ if } \mathsf{SLP_C} \text{ admissible}} \right\} \tag{B.29}$$

This equilibrium corresponds to a SLP on the continental allele, after loss of the island allele. The first eigenvalue governs the dynamics into the state space and can be rewritten in the continental allele frequency of the single locus polymorphism:

$$g_{\mathsf{I}} \cdot \underbrace{\mathsf{SLP}_{\mathsf{C}}(p_{\mathsf{C}})}_{p_{\mathsf{C}} \text{ of } \mathsf{SLP}_{\mathsf{C}}} - c_{\mathsf{I}} m + s_{\mathsf{I}}$$

This equilibrium is stabilized by increasing migration pressure on the incompatible island allele and decreasing advantage of the island allele. Furthermore increasing epistasis on the island allele, destabilizes the $\mathsf{SLP}_{\mathsf{C}}$. Again the second eigenvalue governs dynamics along the boundary. It is always negative, if the equilibrium is admissible, such that the dynamics evolve towards the equilibrium along the boundary.

FIX $= (p_{\mathsf{C}} \to 1, p_{\mathsf{I}} \to 0)$

We find the following eigenvalues along the continental boundary ($p_{\mathsf{I}} = 0$) and along the island boundary ($p_{\mathsf{C}} = 1$).

$$\{-c_{\mathsf{C}} m - s_{\mathsf{C}}, -g_{\mathsf{I}} - c_{\mathsf{I}} m + s_{\mathsf{I}}\}$$

This equilibrium corresponds to fixation of the continental genotype, such that the island genotype is completely lost from the population. This equilibrium lies at the crossing of two invariant boundaries and is always admissible. For large enough migration it always becomes stable. Moreover, increasing advantage of the immigrating variant and decreasing positive effect of the residential allele further strengthen the stability at this equilibrium.

Furthermore, we find two potentially internal equilibria, which are conjugates:

$$\begin{aligned} &\mathsf{I}_{\mathsf{DMI}} = \\ &(p_{\mathsf{C}} \to \quad \frac{-c_{\mathsf{I}} g_{\mathsf{C}} m + c_{\mathsf{C}} g_{\mathsf{I}} m + g_{\mathsf{C}} s_{\mathsf{I}} - s_{\mathsf{C}} s_{\mathsf{I}} - \sqrt{4 c_{\mathsf{C}} g_{\mathsf{I}} m(-g_{\mathsf{C}} + s_{\mathsf{C}}) s_{\mathsf{I}} + (c_{\mathsf{I}} g_{\mathsf{C}} m - c_{\mathsf{C}} g_{\mathsf{I}} m + (-g_{\mathsf{C}} + s_{\mathsf{C}}) s_{\mathsf{I}})^2}}{2 g_{\mathsf{I}} (g_{\mathsf{C}} - s_{\mathsf{C}})} \\ &p_{\mathsf{I}} \to \quad \frac{-c_{\mathsf{I}} g_{\mathsf{C}} m + c_{\mathsf{C}} g_{\mathsf{I}} m + g_{\mathsf{C}} s_{\mathsf{I}} + s_{\mathsf{C}} s_{\mathsf{I}} + \sqrt{4 c_{\mathsf{C}} g_{\mathsf{I}} m(-g_{\mathsf{C}} + s_{\mathsf{C}}) s_{\mathsf{I}} + (c_{\mathsf{I}} g_{\mathsf{C}} m - c_{\mathsf{C}} g_{\mathsf{I}} m + (-g_{\mathsf{C}} + s_{\mathsf{C}}) s_{\mathsf{I}})^2}}{2 g_{\mathsf{C}} s_{\mathsf{I}}}) \end{aligned} \tag{B.30}$$

$$
\begin{aligned}
&\mathsf{I_0} = \\
&(p_\mathsf{C} \to \quad \tfrac{-c_\mathsf{I} g_\mathsf{C} m + c_\mathsf{C} g_\mathsf{I} m + g_\mathsf{C} s_\mathsf{I} - s_\mathsf{C} s_\mathsf{I} + \sqrt{4 c_\mathsf{C} g_\mathsf{I} m(-g_\mathsf{C}+s_\mathsf{C}) s_\mathsf{I} + (c_\mathsf{I} g_\mathsf{C} m - c_\mathsf{C} g_\mathsf{I} m + (-g_\mathsf{C}+s_\mathsf{C}) s_\mathsf{I})^2}}{2 g_\mathsf{I}(g_\mathsf{C} - s_\mathsf{C})} \\
&p_\mathsf{I} \to \quad \tfrac{-c_\mathsf{I} g_\mathsf{C} m + c_\mathsf{C} g_\mathsf{I} m + g_\mathsf{C} s_\mathsf{I} + s_\mathsf{C} s_\mathsf{I} - \sqrt{4 c_\mathsf{C} g_\mathsf{I} m(-g_\mathsf{C}+s_\mathsf{C}) s_\mathsf{I} + (c_\mathsf{I} g_\mathsf{C} m - c_\mathsf{C} g_\mathsf{I} m + (-g_\mathsf{C}+s_\mathsf{C}) s_\mathsf{I})^2}}{2 g_\mathsf{C} s_\mathsf{I}})
\end{aligned}
\tag{B.31}
$$

With the nullclines for $\dot{p}_\mathsf{C} = 0$ and $\dot{p}_\mathsf{I} = 0$ we can investigate the stability of the two internal equilibria. If possible, the nullclines of the unified codominant model are given as functions of the allele frequency of the continental variant p_C on the frequency simplex:

- $\dot{p}_\mathsf{C} = 0$:

$$
\begin{aligned}
N_1 = \hat{p}_\mathsf{I}(p_\mathsf{C}) &= \tfrac{c_\mathsf{C} m + p_\mathsf{C} s_\mathsf{C}}{g_\mathsf{C} p_\mathsf{C}} & \tfrac{\mathrm{d}\hat{p}_\mathsf{I}}{\mathrm{d}p_\mathsf{C}} &= -\tfrac{c_\mathsf{C} m}{g_\mathsf{C} p_\mathsf{C}^2} < 0 & &\Rightarrow \text{monot.} \downarrow \\
& & \tfrac{\mathrm{d}^2\hat{p}_\mathsf{I}}{\mathrm{d}p_\mathsf{C}^2} &= \tfrac{2 c_\mathsf{C} m}{g_\mathsf{C} p_\mathsf{C}^3} > 0 & &\Rightarrow \text{convex} \cup
\end{aligned}
$$

$$
N_2 = p_\mathsf{C} \qquad = 1
$$

- $\dot{p}_\mathsf{I} = 0$:

$$
\begin{aligned}
N_3 = \hat{p}_\mathsf{I}(p_\mathsf{C}) &= 1 + \tfrac{c_\mathsf{I} m}{g_\mathsf{I} p_\mathsf{C} - s_\mathsf{I}} & \tfrac{\mathrm{d}\hat{p}_\mathsf{I}}{\mathrm{d}p_\mathsf{C}} &= -\tfrac{c_\mathsf{I} g_\mathsf{I} m}{(s_\mathsf{I} - g_\mathsf{I} p_\mathsf{C})^2} < 0 &&\Rightarrow \text{monot.} \downarrow \\
\text{admissible} &\Rightarrow g_\mathsf{I} p_\mathsf{C} - s_\mathsf{I} < 0 & \tfrac{\mathrm{d}^2\hat{p}_\mathsf{I}}{\mathrm{d}p_\mathsf{C}^2} &= \tfrac{2 c_\mathsf{I} g_\mathsf{I}^2 m}{(g_\mathsf{I} p_\mathsf{C} - s_\mathsf{I})^3} < 0 &&\Rightarrow \text{concave} \cap
\end{aligned}
$$

$$
N_4 = \hat{p}_\mathsf{I} \qquad = 0
$$

The nullclines are illustrated in Fig. B.2. At the intersection of the nullclines inside the state space, we find the admissible internal equilibria. From the monotony and curvature of the nullclines, we can deduce that we either obtain only the stable equilibrium, i.e.

I_{DMI} or both internal equilibria, the stable and the unstable equilibrium, I_{DMI} and I_0, respectively. We note, that the I_{DMI} is always stable, whenever it is admissible, and hence we refer to it as "stable DMI".

The necessary and sufficient conditions for the existence of a stable DMI are covered by our investigations for the general model and simplify to $-g_C + s_C < 0$ and $s_I > 0$ for the codominant model. They also follow directly from the eigenvalue of the vertex equilibrium $(p_C = 0, p_I = 1)$ at $m = 0$ (not shown).

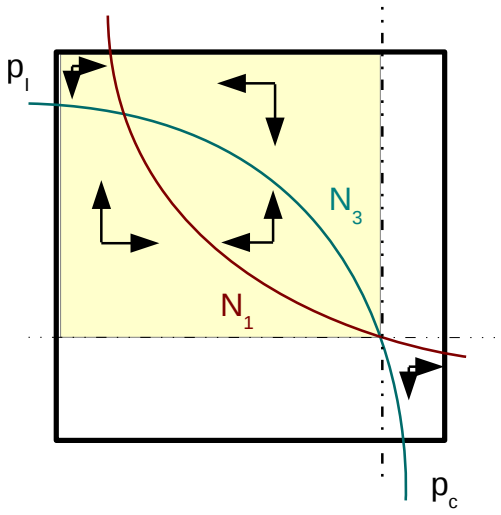

Figure B.2: **Nullclines inside the frequency phase space for a bistable scenario.** The internal equilibria lie at the crossing of the schematic nullclines N_1 and N_3. The upper left cross corresponds to the stable DMI, I_{DMI} and the lower right intersection corresponds to the unstable DMI, I_0. The yellow area covers the minimal basin of attraction of the locally stable equilibrium. See Lemma 1 for proof and link to evolutionary histories. Arrows indicate dynamics inside the phase space and show that no limits cycles can exists.

Maximum permissible migration rates

We determine the full internal dynamics of the system analytically. For illustration of the possible bifurcation patterns see Fig. B.3. We differentiate into global stability and local stability of the stable DMI or I_{DMI}.

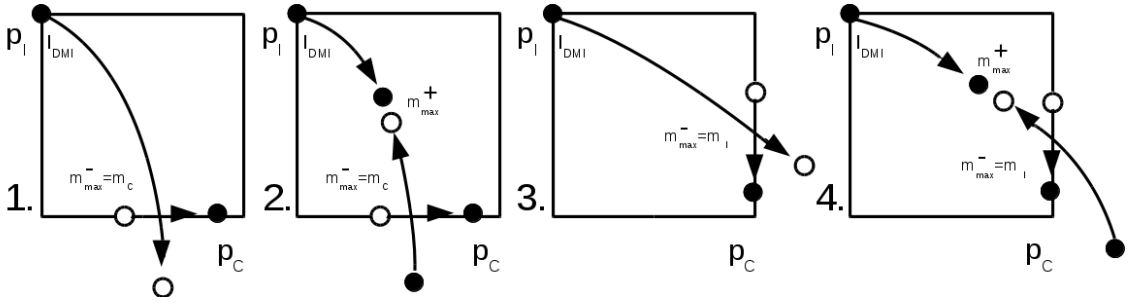

Figure B.3: **Bifurcation patterns on the phase space.** If the vertex-equilibrium $(p_C = 0, p_I = 1)$ is stable without migration, I_{DMI} will move into the state space for $m > 0$, see Section B.1. Furthermore, internal equilibria leave and enter the phase space under exchange of stability with boundary equilibria with increasing migration. The upper bounds for the migration rate permitting a globally stable DMI, $m^-_{max} = m_C$ and $m^-_{max} = m_I$, denote the SLP through which the internal equilibrium leaves the state space or through which a new, unstable internal equilibrium enters the phase space. At m^+_{max} the two internal equilibria annihilate each other via a saddle node bifurcation. Legend: frequency of the island allele (p_I), continental derived (p_C), stable equilibria $(\bullet)$, unstable equilibria $(\circ)$, arrows denote movement of equilibria with increasing migration.

- For migration rates $0 \leq m \leq m^-_{max}$, the internal equilibrium I_{DMI} is globally stable. In this case the DMI will always evolve, irrespective of the evolutionary scenario, which in mathematical terms translates to all possible starting conditions in the frequency phase space.

- For migration rates $0 \leq m^-_{max} \leq m \leq m^+_{max}$ the dynamics yield a bistable scenario and I_{DMI} is only locally stable. In this case, we always obtain a second stable equilibrium at the boundary and the second internal, unstable equilibrium I_0. Hence, only certain evolutionary scenarios will allow the evolution of a DMI. However, it is always possible to maintain a locally stable DMI.

- For $m > m^+_{max}$ there is no stable DMI, as I_{DMI} cannot exist.

In the codominant model we obtain the following analytical expressions for the migration bounds for global stability:

$$m^-_{\mathsf{max}} \in \begin{cases} 0 & \\ m^{\mathsf{C}}_{\mathsf{max}} = \frac{s_{\mathsf{C}} s_{\mathsf{I}}}{-c_{\mathsf{C}} g_{\mathsf{I}} + c_{\mathsf{I}} s_{\mathsf{C}}} & \text{bifurcation at SLP}_{\mathsf{C}} \\ m^{\mathsf{I}}_{\mathsf{max}} = \frac{(s_{\mathsf{C}} - g_{\mathsf{C}})(g_{\mathsf{I}} - s_{\mathsf{I}})}{c_{\mathsf{I}} g_{\mathsf{C}} + c_{\mathsf{C}} (s_{\mathsf{I}} - g_{\mathsf{I}})} & \text{bifurcation at SLP}_{\mathsf{island}} \end{cases} \tag{B.32}$$

If we have only selection against immigrants, but no epistasis and thus no selection against hybrids, the migration bounds for global stability of the stable DMI reduce to

$$m^{\mathsf{C}}_{\mathsf{max}} = \frac{s_{\mathsf{I}}}{c_{\mathsf{I}}} \quad \text{and} \quad m^{\mathsf{I}}_{\mathsf{max}} = -\frac{s_{\mathsf{C}}}{c_{\mathsf{C}}}. \tag{B.33}$$

We also get full analytical expressions for the migration bounds of local stability:

$$m^+_{\mathsf{max}} \in \begin{cases} 0 & \\ \frac{(\sqrt{c_{\mathsf{I}} g_{\mathsf{C}}} - \sqrt{c_{\mathsf{C}} g_{\mathsf{I}}})^2 (g_{\mathsf{C}} - s_{\mathsf{C}}) s_{\mathsf{I}}}{(c_{\mathsf{I}} g_{\mathsf{C}} - c_{\mathsf{C}} g_{\mathsf{I}})^2} & \text{iff } c_{\mathsf{C}} g_{\mathsf{I}} \neq c_{\mathsf{I}} g_{\mathsf{C}} \\ \quad \mathsf{OR} & \\ \frac{(g_{\mathsf{C}} - s_{\mathsf{C}}) s_{\mathsf{I}}}{4 g_{\mathsf{C}}} & \text{iff } c_{\mathsf{C}} g_{\mathsf{I}} = c_{\mathsf{I}} g_{\mathsf{C}} \end{cases} \tag{B.34}$$

The last, easier expression for m^+_{max} holds for the symmetric model A→A and the X→X, whereas skewed migration rates or unequal effective epistasis for the two incompatible alleles, yields the former, more complicated expression.

We now investigate bounds for the maximum permissible migration rates in the different investigated scenarios. Compare Figures 2.2, 2.3 and 2.4 for graphical representations of the migration bounds for the codominant model.

- First, in the case of an beneficial migrant $s_{\mathsf{C}} > 0$, where a stable DMI is maintained solely by unfit hybrids, the lower bound on epistasis, beyond which no DMI can be maintained is given by the necessary and sufficient conditions for the existence of a DMI. We hence need $g_{\mathsf{C}} > s_{\mathsf{C}}$. Therefore, we can only obtain an internal stable DMI, if epistasis is sufficiently strong to outweigh the selective advantage of the migrant.

- Second, for a neutral migrant ($s_C = 0$) m^+_{max} is independent of epistasis. This is due to the symmetry in the expression of m^+_{max}, which emerges with a neutral migrant and codominant fitness; all epistasis terms simply cancel each other. This independence is fitness-scheme specific, as recessive DMIs are not independent of epistasis, even if the immigrating allele behaves neutrally. See Fig. A.1, middle column.

- Third, depending on the fitness loss of the maladaptive immigrating allele we either get the maximum of m^+_{max} with only selection against immigrants (without any epistasis $\gamma = \epsilon = 0$) or with a combination of selection against epistasis and immigrants (intermediate levels of epistasis). By comparison of the eigenvalues without epistasis of the two SLP we obtain the following bound: For

$$\frac{c_C}{c_I} s_I > -s_C \tag{B.35}$$

intermediate levels of epistasis yield the maximum of m^+_{max}. If s_C exceeds that bound, i.e. the migrant becomes too strongly maladaptive, no epistasis ($= 0$) permits the highest m^+_{max}.

Evolutionary histories

As briefly discussed before and in agreement with Bank et al. (2012), we distinguish the two categories in the substitution history of a DMI. On the one hand we categorize into derived-derived (one substitution in each deme) and derived-ancestral DMIs (two substitution in the same deme) and on the other hand we differentiate into evolutionary histories, such as secondary contact or mutation-order-scenarios such as continent-island or island-island scenario, etc. See Fig. B.4 for illustration.

Mathematically, we can map the latter different scenarios to starting points in the phase space. Therefore we investigate the minimal bounds of the basin of attraction of I_{DMI} and thus we will be able to decide which evolutionary histories, i.e. starting

conditions are permissible for the evolution of a stable DMI. These minimal bounds are illustrated as dashed dotted lines in Fig. B.2. In case of a locally stable DMI, i.e. $m^-_{\mathsf{max}} < m < m^+_{\mathsf{max}}$ any starting point within these bounds will always permit the evolution of a stable DMI, if it is admissible. However, starting conditions outside the minimal bounds of the basin of attraction might only permit a stable DMI to evolve if it is globally stable.

Lemma 1: The basin of attraction of the locally stable the internal equilibrium $\mathsf{I}_{\mathsf{DMI}}$, the stable DMI, includes at least all points $P = (p^*_{\mathsf{C}}, p^*_{\mathsf{I}})$ in the phase space, which fulfill the following criterion (yellow area in Fig. B.2):

$$0 \leq p^*_{\mathsf{C}} < \mathsf{I}_0^{p_{\mathsf{C}}} \text{ and } \mathsf{I}_0^{p_{\mathsf{I}}} < p^*_{\mathsf{I}} \leq 1 \tag{B.36}$$

Proof:

1. The frequency of the island allele of any admissible point S, $p_{\mathsf{I}}(S)$, smaller than the frequency of the island allele of the nullcline N_3, $p_{\mathsf{I}}(N_3)$, given by

$$p_{\mathsf{I}}(N_4) = 0 \leq p_{\mathsf{I}}(S) < 1 + \frac{c_{\mathsf{I}} m}{g_{\mathsf{I}} p_{\mathsf{C}} - s_{\mathsf{I}}} = p_{\mathsf{I}}(N_3)$$

   is increasing.

   Proof: The leading term of $\dot{p}_{\mathsf{I}}$ in Eq. (B.25), a quadratic polynomial in p_{I} yields:

$$-p_{\mathsf{I}}^2 \underbrace{(s_{\mathsf{I}} - g_{\mathsf{I}} p_{\mathsf{C}})}_{>0 \text{ if } N_3 \text{ admissible}}$$

   Its two roots are the Nullclines N_3 and N_4. As the leading term of the polynomial is negative, $\dot{p}_{\mathsf{I}}(S) > 0$ for all $S : p_{\mathsf{I}}(N_4) < p_{\mathsf{I}}(S) < p_{\mathsf{I}}(N_3)$.

2. The frequency of the continental allele of any point T above $p_{\mathsf{C}}(N_1)$, given by

$$p_{\mathsf{C}}(N_2) = 1 \geq p_{\mathsf{I}}(T) > \frac{c_{\mathsf{C}} m + p_{\mathsf{C}} s_{\mathsf{C}}}{g_{\mathsf{C}} p_{\mathsf{C}}} = p_{\mathsf{C}}(N_1)$$

is decreasing.

Proof: We rewrite the nullcline $N_1 = \hat{p}_\mathsf{I}(p_\mathsf{C}) = \frac{c_\mathsf{C} m + p_\mathsf{C} s_\mathsf{C}}{g_\mathsf{C} p_\mathsf{C}}$ into $p_\mathsf{C} = \frac{c_\mathsf{C} m}{g_\mathsf{C} p_\mathsf{I} - s_\mathsf{C}}$. As before the nullcline N_1 is only admissible for sufficiently low migration rate $g_\mathsf{C} p_\mathsf{I} - s_\mathsf{C} > m > 0$. The first expression is also the leading term of the quadratic polynomial $\dot{p}_\mathsf{C}$ in p_C in Eq. (B.25). Hence the values between the two roots, i.e. the nullclines are negative. Therefore we obtain $\dot{p}_\mathsf{C}(T) < 0$

If we combine these two statements, we see that trajectories that enter the set

$$M = \{(p_\mathsf{C}^*, p_\mathsf{I}^*) |\ 0 \leq p_\mathsf{C}^* < \mathsf{I}_0^{p_\mathsf{C}} \text{ and } \mathsf{I}_0^{p_\mathsf{I}} < p_\mathsf{I}^* \leq 1\}$$

will never leave M forward in time. We can also exclude the existence of limit cycles, as the direction of the trajectories in M in the four areas depicted by Fig. B.2 are clear as shown above. Hence we will always converge to the locally stable DMI.

□

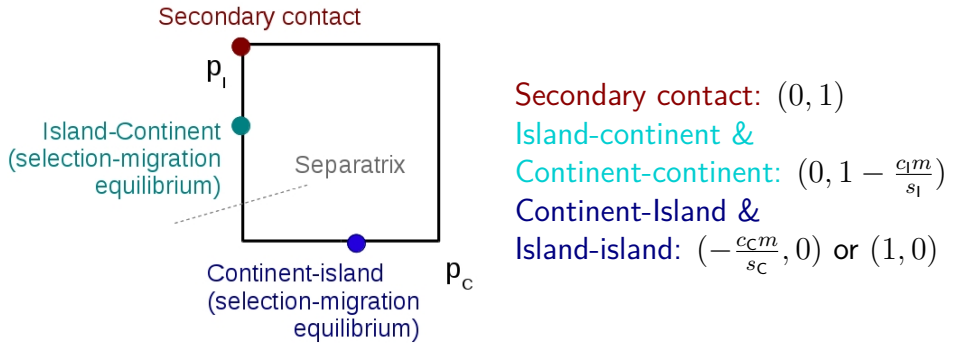

Figure B.4: **Evolutionary history:** Starting conditions in the phase space are mapped to the evolutionary history of the DMI. The starting condition in turquoise holds whenever the second substitution occurs on the continent, whereas the starting condition denoted by a blue dot is valid, whenever the second substitution evolves on the island. The schematic representation of the Separatrix divides the basin of attraction of a locally stable DMI above it and another locally stable equilibrium below.

With Lemma 1, we can decide which evolutionary histories are most permissive to the evolution of a stable DMI:

1. Secondary contact: Both mutations arise and fix during an allopatric phase. Afterwards migration to the island resumes. It hence maps to $\mapsto (p_C = 0, p_I = 1)$ which always lies within the basin of attraction of the stable DMI, as shown by Lemma 1.

2. Continent-island: First a continental substitution establishes at migration-selection balance on the island. This is followed by the second mutation at the other locus on the island.

   It hence maps to $\mapsto \begin{cases} (p_C = -\frac{c_C m}{s_C}, p_I = 0) & \text{if } s_C < 0 \\ (p_C = 1, p_I = 0) & \text{if } s_C \geq 0 \end{cases}$

   The second substitution on the island can only invade, if the stable DMI is globally stable:

   Case 1: $(p_C = -\frac{c_C m}{s_C}, p_I = 0)$ for $s_C < 0$: This scenario never allows evolution of the DMI for local stability of I_{DMI}.

   Proof: If I_{DMI} is locally stable, the saddle point I_0 needs to be inside the state space at the lower intersection of the two nullclines N_1 and N_3. The SLP_C ($p_C = -\frac{c_C m}{s_C}, p_I = 0$) is situated at the intersection of N_1 and the boundary $p_I = 0$. As N_1 is convex and N_3 is concave, the continental allele frequency of SLP_C is higher than $p_I(N_3)$ and therefore, the frequency of the island allele in its neighborhood will decrease and a DMI cannot evolve (similar argument as in proof of Lemma 1).

   Case 2: If the first substitution evolves on the continent, migrates to the island and is beneficial there ($s_C > 0$), it will sweep to fixation. It hence maps to $p_C = 1, p_I = 0$: This scenario never allows evolution of the DMI for a locally stable I_{DMI}.

   Proof: If I_{DMI} is locally stable, there exists at least another locally stable equilibrium. This can only be situated at one of the boundaries in our case. If $s_C \geq 0$, then SLP_C is not admissible, hence SLP_I or FIX itself is the second stable equilibrium and we can never evolve a DMI.

3. Island-continent: The first mutation arises on the island and sweeps to migration-selection equilibrium against constant influx of the ancestral genotype. This is followed by the substitution of the continental allele on the continent, which subsequently migrates to the island.

   Statement: It maps to $\mapsto (p_{\mathsf{C}} = 0, p_{\mathsf{I}} = 1 - \frac{c_{\mathsf{I}} m}{s_{\mathsf{I}}})$ and will always evolve towards the stable DMI.

   Proof: The starting point $(p_{\mathsf{C}} = 0, p_{\mathsf{I}} = 1 - \frac{c_{\mathsf{I}} m}{s_{\mathsf{I}}})$ lies on the intersection of the nullcline N_3 with the boundary $p_{\mathsf{C}} = 0$. As the nullcline N_3 is monotone decreasing, the starting point lies within the minimal bounds of the basin of attraction of a stable DMI and therefore a DMI will always evolve.

4. Island-island: Both substitutions occur subsequently on the island. The second substitution is incompatible with the ancestral variant at the other locus. Both ancestral alleles are still introduced to the island by migration as the continent remains monomorphic for the ancestral genotype. This evolutionary history maps to $\mapsto (p_{\mathsf{C}} = -\frac{c_{\mathsf{C}} m}{s_{\mathsf{C}}}, p_{\mathsf{I}} = 0)$ and permits evolution only of a globally stable DMI, see continent-island substitution scenario for proof.

5. Continent-continent: Both substitutions occur subsequently on the continent. The first substitution is maladaptive on the island and establishes there at selection-migration balance. This is followed by the invasion of the second substitution. This evolutionary history maps to $\mapsto (p_{\mathsf{C}} = 0, p_{\mathsf{I}} = 1 - \frac{c_{\mathsf{I}} m}{s_{\mathsf{I}}})$ and always permits evolution of stable DMI, see island-continent substitution scenario for proof.

Special cases of the codominant cytonuclear DMIs

Male-biased fitness effects in cytonuclear DMIs without epistasis in females: If we omit any epistasis effects in females, we loose the epistasis terms in the dynamics for the mitochondrial allele completely. We thus obtain dynamical systems which have only four fixed points. This entails that the bifurcation patterns we see here are different to what

we observe in the full codominant model. They are easier, as we never obtain a locally stable internal equilibrium and hence $m^{+}_{\mathsf{max}} = m^{-}_{\mathsf{max}}$.

First, we investigate the case, where the continental allele is linked to the mitochondrium.

$$\begin{aligned} \dot{p}_{\mathsf{C}} &= p_{\mathsf{C}}(s_{\mathsf{C}}(1-p_{\mathsf{C}}) - c_{\mathsf{C}}m) + c_{\mathsf{C}}m \\ \dot{p}_{\mathsf{I}} &= p_{\mathsf{I}}(s_{\mathsf{I}}(1-p_{\mathsf{I}}) - g_{\mathsf{I}}(1-p_{\mathsf{I}})p_{\mathsf{C}} - c_{\mathsf{I}}m) \end{aligned} \tag{B.37}$$

We obtain the three boundary equilibria and only one stable internal equilibrium:

$$\mathsf{I}_{\mathsf{DMI}} = (p_{\mathsf{C}}, p_{\mathsf{I}}) = \left(\frac{-c_{\mathsf{C}}m}{s_{\mathsf{C}}}, 1 - \frac{c_{\mathsf{I}}ms_{\mathsf{C}}}{c_{\mathsf{C}}g_{\mathsf{I}}m + s_{\mathsf{C}}s_{\mathsf{I}}}\right) \tag{B.38}$$

The frequency of the continental allele is equal to the expression of the frequency of the continental allele in the $\mathsf{SLP}_{\mathsf{C}}$. Hence we only obtain a stable DMI with selection against immigrants $s_{\mathsf{C}} < 0$ and if migration permits. The maximum migration bounds are a shorter expression for $m^{\mathsf{I}}_{\mathsf{max}} = -\frac{s_{\mathsf{C}}}{c_{\mathsf{C}}}$ and $m^{\mathsf{C}}_{\mathsf{max}} = \frac{s_{\mathsf{C}}s_{\mathsf{I}}}{-c_{\mathsf{C}}g_{\mathsf{I}}+c_{\mathsf{I}}s_{\mathsf{C}}}$ as for the full codominant model. The stable DMI is globally stable, whenever it exists.

Second, we study the case, where the island allele is linked to the mitochondria.

$$\begin{aligned} \dot{p}_{\mathsf{C}} &= p_{\mathsf{C}}(s_{\mathsf{C}}(1-p_{\mathsf{C}}) - g_{\mathsf{C}}(1-p_{\mathsf{C}})p_{\mathsf{I}} - c_{\mathsf{C}}m)) + c_{\mathsf{C}}m \\ \dot{p}_{\mathsf{I}} &= p_{\mathsf{I}}((1-p_{\mathsf{I}})s_{\mathsf{I}} - c_{\mathsf{I}}m) \end{aligned} \tag{B.39}$$

We also obtain the three boundary equilibria and one stable internal equilibrium:

$$\mathsf{I}_{\mathsf{DMI}} = (p_{\mathsf{C}}, p_{\mathsf{I}}) = \left(\frac{-c_{\mathsf{C}}ms_{\mathsf{I}}}{g_{\mathsf{C}}(c_{\mathsf{I}}m - s_{\mathsf{I}}) + s_{\mathsf{C}}s_{\mathsf{I}}}, 1 - \frac{c_{\mathsf{I}}m}{s_{\mathsf{I}}}\right) \tag{B.40}$$

Here the frequency of the island allele is equal to the expression of the frequency of the island allele in the $\mathsf{SLP}_{\mathsf{I}}$. Hence a stable DMI can only be admissible if the selective advantage of the island allele outweighs the effective migration pressure at the island locus, i.e. $s_{\mathsf{I}} > c_{\mathsf{I}}m$. The maximum migration bounds are for $m^{\mathsf{C}}_{\mathsf{max}} = \frac{s_{\mathsf{I}}}{c_{\mathsf{I}}}$ and

$m^{\mathsf{I}}_{\mathsf{max}} = \frac{g_{\mathsf{C}} s_{\mathsf{I}} - s_{\mathsf{C}} s_{\mathsf{I}}}{c_{\mathsf{I}} g_{\mathsf{C}} + c_{\mathsf{C}} s_{\mathsf{I}}}$. The stable DMI is globally stable, whenever it exists.

Cytonuclear DMIs without any fitness effect (direct or epistatic) in females: The dynamical systems which describe this special case are simpler, as the dynamics of the mitochondrial locus are governed only by the effects in females. This translates to two types of dynamical systems, depending on whether the continental or the island locus is cytoplasmic. In both cases we never obtain a stable DMI.

Data Archiving

Höllinger I, Hermisson J (2017) Data from: Bounds to parapatric speciation: A Dobzhansky-Muller incompatibility model involving autosomes, X chromosomes and mitochondria. Dryad Digital Repository. https://doi.org/10.5061/dryad.6kd25

Acknowledgments

We thank Andrea Betancourt, Alexandre Blanckaert, Reinhard Bürger, Brian Charlesworth, Andy Clark, Sebastian Matuszewsky, Sylvain Mousset, Mohamed Noor, Sally Otto, Christian Schlötterer, Maria Servedio, Derek Setter, Claus Vogl and three referees for helpful discussions, suggestions and comments on the manuscript. This work was made possible with financial support by the Austrian Science Fund (FWF) via funding for the Vienna Graduate School for Population Genetics.

Funding

This work has been funded by the Austrian Science Fund.

3 Polygenic adaptation:

From sweeps to subtle frequency shifts

Reference:

Hoellinger, I., Pennings, P., & Hermisson, J. (2018). Polygenic Adaptation: From sweeps to subtle frequency shifts. bioRxiv, 450759.

Abstract

Evolutionary theory has produced two conflicting paradigms for the adaptation of a polygenic trait. While population genetics views adaptation as a sequence of selective sweeps at single loci underlying the trait, quantitative genetics posits a collective response, where phenotypic adaptation results from subtle allele frequency shifts at many loci. Yet, a synthesis of these views is largely missing and the population genetic factors that favor each scenario are not well understood. Here, we study the architecture of adaptation of a binary polygenic trait (such as resistance) with negative epistasis among the loci of its basis. The genetic structure of this trait allows for a full range of potential architectures of adaptation, ranging from sweeps to small frequency shifts. By combining computer simulations and a newly devised analytical framework based on Yule branching processes, we gain a detailed understanding of the adaptation dynamics for this trait. Our key analytical result is an expression for the joint distribution of mutant alleles at the end of the adaptive phase. This distribution characterizes the polygenic pattern of adaptation at the underlying genotype when phenotypic adaptation has been accomplished. We find that a single compound parameter, the population-scaled background mutation rate Θ_{bg}, explains the main differences among these patterns. For a focal locus, Θ_{bg} measures the mutation rate at all redundant loci in its genetic background that offer alternative ways for adaptation. For adaptation starting from mutation-selection-drift balance, we observe different patterns in three parameter regions. Adaptation proceeds by sweeps for small $\Theta_{bg} \lesssim 0.1$, while small polygenic allele frequency shifts require large $\Theta_{bg} \gtrsim 100$. In the large

intermediate regime, we observe a heterogeneous pattern of partial sweeps at several interacting loci.

3.1 Author summary

It is still an open question how complex traits adapt to new selection pressures. While population genetics champions the search for selective sweeps, quantitative genetics proclaims adaptation via small concerted frequency shifts. To date the empirical evidence of clear sweep signals is more scarce than expected, while subtle shifts remain notoriously hard to detect. In the current study we develop a theoretical framework to predict the expected adaptive architecture of a trait, depending on parameters such as mutation rate, effective population size, size of the trait basis, and the available genetic variability at the onset of selection. For a population in mutation-selection-drift balance we find that adaptation proceeds via complete or partial sweeps for a large set of parameter values. We predict adaptation by small frequency shifts for two main cases. First, for traits with a large mutational target size and high levels of genetic redundancy among loci, and second if the starting frequencies of mutant alleles are more homogeneous than expected in mutation-selection-drift equilibrium, *e.g.* due to population structure or balancing selection.

3.2 Introduction

Rapid phenotypic adaptation of organisms to all kinds of novel environments is ubiquitous and has been described and studied for decades (Barton and Keightley, 2002; Messer et al., 2016). However, while the macroscopic changes of phenotypic traits are frequently evident, their genetic and genomic underpinnings are much more difficult to resolve. Two independent research traditions, molecular population genetics and quantitative genetics, have coined two opposite views of the adaptive process on the molecular level: adaptation either by selective sweeps or by subtle allele frequency shifts (*sweeps* or *shifts* from here on).

On the one hand, population genetics works bottom-up from the dynamics at single loci, without much focus on the phenotype. The implicit assumption of the sweep scenario is that selection on the trait results in sustained directional selection also on the level of single underlying loci. Consequently, we can observe phenotypic adaptation at the genotypic level, where selection drives allele frequencies at one or several loci from low values to high values. Large allele frequency changes are the hallmark of the sweep scenario. If these frequency changes occur in a short time interval, conspicuous diversity patterns in linked genomic regions emerge: the footprints of hard or soft selective sweeps (Maynard-Smith and Haigh, 1974; Kaplan et al., 1989; Barton, 1998; Hermisson and Pennings, 2017).

On the other hand, quantitative genetics envisions phenotypic adaptation top-down, from the vantage point of the trait. At the genetic level, it is perceived as a collective phenomenon that cannot easily be broken down to the contribution of single loci. Indeed, adaptation of a highly polygenic trait can result in a myriad of ways through "infinitesimally" small, correlated changes at the interacting loci of its basis (*e.g.* Boyle et al., 2017). Conceptually, this view rests on the infinitesimal model by Fisher (1918) and its extensions (*e.g.* Barton et al., 2017). Until a decade ago, the available moderate sample sizes for polymorphism data had strongly limited the statistical detectability of small frequency shifts. Therefore, the detection of sweeps with clear footprints was the major objective for many years. Since recently, however, huge sample sizes (primarily of human data) enable powerful genome-wide association studies (GWAS) to resolve the genomic basis of polygenic traits. Consequently, following conceptual work by Pritchard and Di Rienzo (2010); Pritchard et al. (2010), there has been a shift in focus to the detection of polygenic adaptation from subtle genomic signals (*e.g.* Hancock et al., 2010; Berg and Coop, 2014; Field et al., 2016) (reviewed in Csilléry et al., 2018). Very recently, however, some of the most prominent findings of polygenic adaptation in human height have been challenged (Berg et al., 2018; Sohail et al., 2018). As it turned out, the methods are highly sensitive to confounding effects in GWAS data due to population

stratification.

While discussion of the empirical evidence is ongoing, the key objective for theoretical population genetics is to clarify the conditions (mutation rates, selection pressures, genetic architecture) under which each adaptive scenario, sweeps, shifts – or any intermediate type – should be expected in the first place. Yet, the number of models in the literature that allow for a comparison of alternative adaptive scenarios at all is surprisingly limited (see also Stephan, 2016). Indeed, quantitative genetic studies based on the infinitesimal model or on summaries (moments, cumulants) of the breeding values do not resolve allele frequency changes at individual loci (*e.g.* Turelli and Barton, 1990, 1994; Bürger and Lynch, 1995; Bürger, 2000). In contrast, sweep models with a single locus under selection in the tradition of Maynard-Smith and Haigh (1974), or models based on adaptive walks or the adaptive dynamics framework (*e.g.* Geritz et al., 1998; Orr, 2005; Matuszewski et al., 2015) only allow for adaptive substitutions or sweeps. A notable exception is the pioneering study by Chevin and Hospital (2008). Following Lande (1983), these authors model adaptation at a single major quantitative trait locus (QTL) that interacts with an "infinitesimal background" of minor loci, which evolves with fixed genetic variance. Subsequent models by Pavlidis et al. (2012); Wollstein and Stephan (2014) trace the allele frequency change at a single QTL in models with 2-8 loci. Still, these articles do not discuss polygenic adaptation patterns. Most recently, Jain and Stephan (2015, 2017) studied the adaptive process for a quantitative trait under stabilizing selection with explicit genetic basis. Their analytical approach allows for a detailed view of allele frequency changes at all loci without constraining the genetic variance. However, the model is deterministic and thus ignores the effects of genetic drift. Below, we study a polygenic trait that can adapt via sweeps or shifts under the action of the evolutionary forces, mutation, selection, recombination and drift. Our model allows for comprehensive analytical treatment, leading to a multi-locus, non-equilibrium extension of Wright's formula (Wright, 1931) for the joint distribution of allele frequencies at the end of the adaptive phase. This way, we obtain predictions concerning the

adaptive architecture of polygenic traits and the population genetic variables that delimit the corresponding modes of adaptation.

The article is organized as follows. The Model section motivates our modeling decisions and describes the simulation method. We also give a brief intuitive account of our analytical approach. In the Results part, we describe our findings for a haploid trait with linkage equilibrium among loci. All our main conclusions in the Discussion part are based on the results displayed here. Further model extensions and complications (diploids, linkage, and alternative starting conditions) are relegated to appendices. Finally, we describe our analytical approach and derive all results in a comprehensive Mathematical Appendix. For the ease of reading, we have tried to keep both the main text and the Mathematical Appendix independent and largely self-contained.

3.3 Model

In the current study, we aim for a "minimal model" of a trait that allows us to clarify which evolutionary forces favor sweeps over shifts and vice versa (as well as any intermediate patterns). For shifts, alleles need to be able to hamper the rise of alleles at other loci via negative epistasis for fitness, *e.g.* diminishing returns epistasis. Indeed, otherwise one would only observe parallel sweeps. Negative fitness epistasis is frequently found in empirical studies (*e.g.* Kryazhimskiy et al., 2014) and implicit to the Gaussian selection scheme used by (*e.g.* Chevin and Hospital, 2008; Jain and Stephan, 2015, 2017). More fundamentally, diminishing returns are a consequence of partial or complete redundancy of genetic effects across loci or gene pathways. Adaptive phenotypes (such as pathogen resistance or a beneficial body coloration) can often be produced in many alternative ways, such that redundancy is a common characteristic of beneficial mutations.

As our basic model, we focus on a haploid population and study adaptation for a polygenic, binary trait with full redundancy of effects at all loci. Any single mutation switches the phenotype from its ancestral state (*e.g.* "non-resistant") to the adaptive state ("resistant"), further mutations have no additional effect. On the population level,

adaptation can be produced by a single locus where the beneficial allele sweeps to fixation, or by small frequency shifts of alleles at many different loci in different individuals – or any combination. The symmetry among loci (no build-in advantage of any particular locus) and complete redundancy of locus effects provides us with a trait architecture that is most favorable for collective adaptation via small shifts – and with a modeling framework that allows for analytical treatment. The same model has been used in a preliminary simulation study (Hermisson and Pennings, 2017). In the context of parallel adaptation in a spatially structured population, analogous model assumptions with redundant loci have been used (Ralph and Coop, 2010, 2015; Paulose et al., 2018). In a second step, we extend our basic model to relax the redundancy condition, as described below.

3.3.1 Basic model

Consider a panmictic population of N_e haploids, with a binary trait Z (with phenotypic states Z_0 "non-resistant" and Z_1 "resistant", see Fig. 3.1). The trait is governed by a polygenic basis of L bi-allelic loci with arbitrary linkage (we treat the case of linkage equilibrium in the main text and analyze the effects of linkage in Appendix C.1). Only the genotype with the ancestral alleles at all loci produces phenotype Z_0, all other genotypes produce Z_1, irrespective of the number of mutations they carry. Loci mutate at rate μ_i, $1 \leq i \leq L$, per generation (population mutation rate at the ith locus: $2N_e\mu_i = \Theta_i$) from the ancestral to the derived allele. We ignore back mutation. The mutant phenotype Z_1 is deleterious before time $t = 0$, when the population experiences a sudden change in the environment (*e.g.* arrival of a pathogen). Z_1 is beneficial for time $t > 0$. The Malthusian (logarithmic) fitness function of an individual with phenotype Z reads

$$W(Z) = \begin{cases} s_d Z & \text{for } t < 0 \\ s_b Z & \text{for } t \geq 0. \end{cases} \tag{3.1}$$

Without restriction, we can assume $Z_0 = 0$ and $Z_1 = 1$. Then $W(Z_0) = 0$ and $W(Z_1) = s_d < 0$, respectively $W(Z_1) = s_b > 0$, measure the strength of directional selection on Z (*e.g.* cost and benefit of resistance) before and after the environmental change. For the basic model, we assume that the population is in mutation-selection-drift equilibrium at time $t = 0$.

3.3.2 Model extensions

We extend the basic model in several directions. This includes linkage (Appendix C.1), alternative starting conditions at time $t = 0$ (Appendix C.2), diploids (Appendix C.3), and arbitrary time-dependent selection $s(t)$ (Mathematical Appendix D.1). Here, we describe how we relax the assumption of complete redundancy of all loci. Diminishing returns epistasis, *e.g.* due to Michaelis-Menten enzyme kinetics, will frequently not lead to complete adaptation in a single step, but may require multiple steps before the trait optimum is approached. In a model of incomplete redundancy, we thus assume that a first beneficial mutation only leads to partial adaptation. We thus have three states of the trait, the ancestral state for the genotype without mutations, $Z_0 = 0$ (non-resistant), a phenotype $Z_\delta = \delta$ (partially resistant) for genotypes with a single mutation, and the mutant state $Z_1 = 1$ (fully resistant) for all genotypes with at least two mutations, see Fig. 3.1(b). For diminishing returns epistasis, we require $\frac{1}{2} \leq \delta < 1$. The fitness function is as in Eq. (3.1).

3.3.3 Simulation model

For the models described above, we use Wright-Fisher simulations for a haploid, panmictic population of size N_e, assuming linkage equilibrium between all L loci in discrete time. Selection and drift are implemented by independent weighted sampling based on the marginal fitnesses of the ancestral and mutant alleles at each locus. Due to linkage equilibrium, the marginal fitnesses only depend on the allele frequencies. Ancestral alleles mutate with probability μ_i per generation at locus i. We start our simulations with

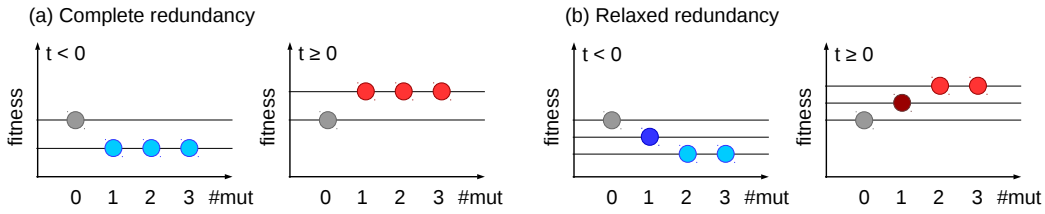

Figure 3.1: **Fitness schemes.** The fitness for individuals carrying $0, 1, 2, 3 \ldots$ mutations (y-axis) are given for the complete redundancy (a) and relaxed redundancy (b) model of fitness effects, respectively. Grey balls show the fitness of ancestral wild-type individuals (without mutations). Colored balls represent individuals carrying at least one mutation, for time points $t < 0$ before the environmental change in blue and for $t \geq 0$ in red.

a population that is monomorphic for the ancestral allele at all loci. The population evolves for $8N_e$ generations under mutation and deleterious selection to reach (approximate) mutation-selection-drift equilibrium. Following Hermisson and Pennings (2005, 2017), we condition on adaptation from the ancestral state and discard all runs where the deleterious mutant allele (at any locus) reaches fixation during this time. (We do not show results for cases with very high mutation rates and weak deleterious selection when most runs are discarded). At the time of environmental change, selection switches from negative to positive and simulation runs are continued until a prescribed stopping condition is reached.

We are interested in the genetic architecture of adaptation – the joint distribution of mutant frequencies across all loci – at the end of the rapid adaptive phase. Following Jain and Stephan (2017), we define this phase as "the time until the phenotypic mean reaches a value close to the new optimum". Specifically, we stop simulations when the mean fitness $\bar{W}$ in the population has increased up to a proportion f_w of the maximal attainable increase from the ancestral to the derived state,

$$\frac{W(Z_1) - \bar{W}}{W(Z_1) - W(Z_0)} = f_w \,. \tag{3.2}$$

For the basic model with complete redundancy, this simply corresponds to a residual proportion f_w of individuals with ancestral phenotype in the population. Extensions of the simulation scheme to include linkage or diploid individuals are described in Appendices C.1 and C.3.

Parameter choices: Unless explicitly stated otherwise, we simulate $N_e = 10\,000$ individuals, with beneficial selection coefficients $s_b = 0.1$ and 0.01, combined with deleterious selection coefficients $s_d = -0.1$ and $s_d = -0.001$ for low and high levels of SGV, respectively. (The corresponding Wrightian fitness values used as sampling weights in discrete time are $1 + s_b$ and $1 + s_d$.) We investigate $L = 2$ to 100 loci. We usually assume equal mutation rates at all loci, $\mu_i = \mu$ and define $\Theta_l = 2N_e\mu$ as the locus mutation parameter. Mutation rates are chosen such that the background mutation rates $\Theta_{bg} := 2N_e\mu(L-1)$ (detailed below in Eq. (3.10)) takes values from 0.01 to 100. We typically simulate $10\,000$ replicates per mutation rate and stop simulations when the population has reached the new fitness optimum up to $f_w = 0.05$. In the model with complete redundancy, we thus stop simulations when the frequency of individuals with mutant phenotype Z_1 has increased to 95%.

3.3.4 Analytical analysis

We partition the adaptive process into two phases (see Fig. 3.2 for illustration). An initial *stochastic phase*, governed by selection, drift, and mutation describes the establishment of mutant alleles at all loci. The subsequent *deterministic phase* governs the further evolution of established alleles until the end of the rapid adaptive phase as defined above. While mutation and drift can be ignored during the deterministic phase, interaction effects due to epistasis and linkage become important (in our model, they enter, in particular, through the stopping condition). We give a brief overview of our analytical approach below. A detailed account with the derivation of all results is provided in the Mathematical Appendix.

During the *stochastic phase*, we model the origin and spread of mutant copies as a

so-called *Yule pure birth process* following Etheridge et al. (2006) and Hermisson and Pfaffelhuber (2008). The idea of this approach is that we only need to keep track of mutations that found "immortal lineages", *i.e.* derived alleles that still have surviving offspring at the time of observation (see Fig. 3.2 for the case of $L = 2$ loci). Forward in time, new immortal lineages can be created by two types of events: new mutations at all loci start new lineages, while birth events lead to splits of existing lineages into two immortal lineages. For $t > 0$ (after the environmental change), in particular, new mutations at the ith locus arise at rate $N_e\mu_i$ per generation and are destined to become established in the population with probability $\approx 2s_b$. Simultaneously, existing beneficial mutant alleles at all loci spread at rate s_b (due to positive selection, via birth events exceeding death events). For the origin of new immortal lineages in the Yule process and their subsequent splitting we thus obtain the rates

$$p_{\mathsf{mut},i} \approx N_e\mu_i \cdot 2s_b = \Theta_i s_b \quad ; \quad p_{\mathsf{split}} \approx s_b. \tag{3.3}$$

Extended results including standing genetic variation and time-dependent fitness are given in the Appendix. Assume now that there are currently $\{k_1, \dots k_L\}$, $0 \le k_j \ll N_e$ mutant lineages at the L loci. Then the probability that the next event in the Yule process is either a birth (split) or a new mutation at locus i is

$$\frac{k_i \cdot p_{\mathsf{split}} + p_{\mathsf{mut},i}}{\sum_{j=1}^{L}(k_j \cdot p_{\mathsf{split}} + p_{\mathsf{mut},j})} = \frac{k_i + \Theta_i}{\sum_{j=1}^{L}(k_j + \Theta_j)}. \tag{3.4}$$

Importantly, all these transition probabilities among states of the Yule process are constant in time and independent of the mutant fitness s_b, which cancels in the ratio of the rates. As the number of lineages at all loci increases, their joint distribution (across replicate realizations of the Yule process) approaches a limit. In particular, as shown in the Appendix, the joint distribution of frequency ratios $x_i := k_i/k_1$ in the limit $k_1 \to \infty$

is given by an *inverted Dirichlet distribution*

$$\mathsf{P}_{\mathsf{inDir}}[\mathbf{x}|\mathbf{\Theta}] = \frac{1}{B[\mathbf{\Theta}]} \prod_{j=2}^{L} x_j^{\Theta_j - 1} \Big(1 + \sum_{i=2}^{L} x_i\Big)^{-\sum_{i=1}^{L} \Theta_i} \tag{3.5}$$

where $\mathbf{x} = (x_2, \ldots, x_L)$ and $\mathbf{\Theta} = (\Theta_1, \ldots, \Theta_L)$ are vectors of frequency ratios and locus mutation rates, respectively, and where $B[\mathbf{\Theta}] = \frac{\prod_{j=1}^{L} \Gamma(\Theta_j)}{\sum_{j=1}^{L} \Gamma(\Theta_j)}$ is the generalized Beta function and $\Gamma(z)$ is the Gamma function. Note that Eq. (3.5) depends only on the locus mutation rates, but not on selection strength.

After the initial stochastic phase, when mutant lineages have established and evaded stochastic loss, the dynamics can be adequately described by deterministic selection equations. For allele frequencies p_i at locus i, assuming linkage equilibrium, we obtain (consult the Mathematical Appendix D.1 for detailed derivations)

$$\dot{p}_i = p_i(W(Z_1) - \bar{W}) = s_b p_i (Z_1 - \bar{Z}), \tag{3.6}$$

where $\bar{W}$ and $\bar{Z}$ are population mean fitness and mean trait value. For the mutant frequency ratios $x_i = p_i/p_1$, we obtain

$$\dot{x}_i = \frac{d}{dt}\Big(\frac{p_i}{p_1}\Big) = \frac{\dot{p}_i p_1 - p_i \dot{p}_1}{p_1^2} = 0\,. \tag{3.7}$$

We thus conclude that the frequency ratios x_i do not change during the deterministic phase. In particular, this means that Eq. (3.5) still holds at our time of observation at the end of the rapid adaptive phase. As shown in the Appendix, this is even true with linked loci. Finally, derivation of the joint distribution of mutant frequencies p_i (instead of frequency ratios x_i) at the time of observation requires a transformation of the density. In general, this transformation depends on the stopping condition f_w and on other factors such as linkage. Assuming linkage equilibrium among all selected loci,

we obtain (see the Mathematical Appendix, Theorem 2, Eq. (D.20))

$$\mathsf{P}_{f_w}[\mathbf{p}|\boldsymbol{\Theta}] = \frac{\delta_{\prod_{j=1}^{L}(1-p_j)-f_w}}{B[\boldsymbol{\Theta}]} \prod_{j=1}^{L} p_j^{\Theta_j-1} \Big(\sum_{i=1}^{L} p_i\Big)^{-\sum_{i=1}^{L}\Theta_i} \Big(\sum_{j=1}^{L} \frac{f_w p_j}{1-p_j}\Big) \tag{3.8}$$

for $\mathbf{p} = (p_1, \ldots, p_L)$ in the L-dimensional hypercube of allele frequencies. The delta function δ_X restricts the distribution to the $L-1$ dimensional manifold defined via the stopping condition $f_w = \prod_{j=1}^{L}(1-p_j)$. Further expressions, also including linkage, are given in the Mathematical Appendix and in Appendix C.1. In general, the joint distribution corresponds to a family of generalized Dirichlet distributions depending on the stopping condition. In the special case $f_w \to 0$ (*i.e.* complete adaptation, enforcing fixation at at least one locus), the distribution Eq. (3.8) is restricted to a boundary face of the allele frequency hypercube and reduces to the inverted Dirichlet distribution given above in Eq. (3.5). In the results section below, we assess our analytical approximations for the joint distributions of adaptive alleles, Eq. (3.5) and Eq. (3.8), and discuss their implications in the context of scenarios of polygenic adaptation, ranging from sweeps to small frequency shifts.

L	...	size of polygenic basis (no. of loci)
s_d, s_b	...	selection coefficient before/after the environment changes
$p_i := \frac{k_i}{N}$	...	mutant allele frequency at locus i
$x_i := \frac{k_i}{k_1} = \frac{p_i}{p_1}$	...	mutant allele frequency ratio: locus i / locus 1
f_w	...	frequency of ancestral phenotype
μ_i	...	allelic mutation rate at locus i
$\Theta_i = 2N_e\mu_i$	...	haploid population mutation rate at locus i
$\boldsymbol{\Theta} = \{\Theta_1, \ldots, \Theta_L\}$	...	vector of all locus population mutation rates
Θ_l	...	locus pop. mut. rate, for model with equal mutation rates
Θ_{bg}	...	background mutation rate, Eq. (3.10)
$B[\boldsymbol{\Theta}] = \frac{\prod_{i\geq 1}\Gamma(\Theta_i)}{\sum_{i\geq 1}\Gamma(\Theta_i)}$	...	Beta function, where $\Gamma(\Theta_i)$ is the Gamma function

Table 3.1: Glossary

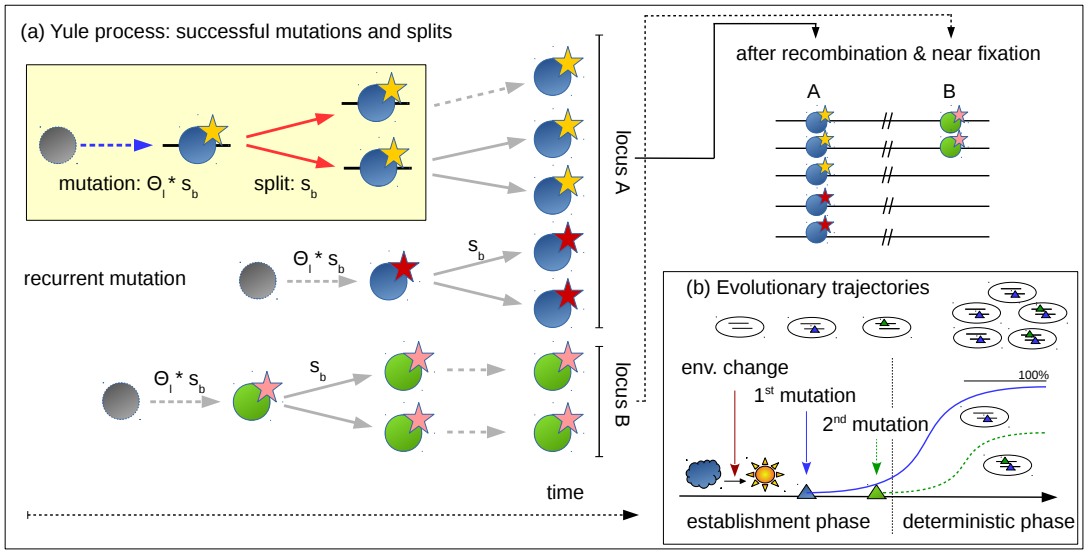

Figure 3.2: **Phases of polygenic adaptation.** The adaptive process is partitioned into two phases. The initial, stochastic phase describes the establishment of mutant alleles. Ignoring epistasis during this phase, it can be described by a *Yule* process (panel a), with two types of events (yellow box). Either a new mutation occurs and establishes with rate $\Theta_l \cdot s_b$ or an existing mutant line splits into two daughter lines at rate s_b. Mutations and splits can occur in parallel at all loci of the polygenic basis, (here 2 loci, shown in green and blue). Yellow and red stars at the blue locus indicate establishment of two recurrent mutations at this locus. When mutants have grown to larger frequencies, the adaptive process enters its second, deterministic phase, where drift can be ignored (panel b). During the deterministic phase, the trajectories of mutations at different loci constrain each other due to epistasis. We refer to the locus ending up at the highest frequency as the *major* locus (here in blue) and to all others as *minor* loci (here one in green).

3.4 Results

While the joint distribution of allele frequencies provides comprehensive information of the adaptive architecture, low-dimensional summary statistics of this distribution are needed to describe and classify distinct types of polygenic adaptation. To this end, we order loci according to their contribution to the adaptive response. In particular, we call the locus with the largest allele frequency at the stopping condition the *major locus* and all other loci *minor loci*. Minor loci are further ordered according to their frequency (first minor, second minor, etc.). The marginal distributions of the major locus or kth minor locus are 1-dim summaries of the joint distribution. Importantly, these summaries are still *collective* because the role of any specific locus (its order) is defined through the allele frequency changes at *all* loci. This is different for the marginal distribution at a fixed focal locus, which is chosen irrespective of its role in the adaptive process, (*e.g.* Chevin and Hospital, 2008; Pavlidis et al., 2012; Wollstein and Stephan, 2014).

Concerning our nomenclature, note, that the *major* and *minor* loci do not differ in their effect size, as they are completely redundant. Still, the major locus is the one with the largest contribution to the adaptive response and would yield the strongest association in a GWAS case-control study.

In the following, we analyze adaptive trait architectures in three steps. In Section 3.4.1 we use the expected allele frequency ratio of minor and major loci as a one-dimensional summary statistic. Subsequently, in Section 3.4.2, we analyze the marginal distributions of major and minor loci for a fully redundant trait with 2 to 100 loci. Finally, in Section 3.4.3 we investigate the robustness of our results under conditions of relaxed redundancy. Further results devoted to diploids, linkage, and alternative starting conditions are provided in the Appendices.

3.4.1 Expected allele frequency ratio

For our biological question concerning the type of polygenic adaptation, the ratio of allele frequency changes of minor over major loci is particularly useful. With "sweeps at few loci", we expect large differences among loci, resulting in ratios that deviate strongly from 1. In contrast, with "subtle shifts at many loci", allele frequency shifts across loci should be similar, and ratios should range close to 1. Our theory (explained above) predicts that these ratios are the outcome of the stochastic phase, yet their distribution is preserved during the deterministic phase. They are thus independent of the precise time of observation. For our results in this section, we assume that the mutation rate at all L loci is equal, $\Theta_i \equiv \Theta_l$, for all $1 \leq i \leq L$. This corresponds to the symmetric case that is most favorable for a "small shift" scenario.

Consider first the case of $L = 2$ loci. There is then a single allele frequency ratio "minor over major locus", which we denote by x. For two loci, the joint distribution of frequency ratios from Eq. (3.5) reduces to a *beta-prime* distribution. Conditioning on the case that the first locus is the major locus (probability $1/2$ for the symmetric model), we obtain for $0 \leq x \leq 1$,

$$P_{\beta'}[x|\Theta_l] = \frac{2\Gamma(2\Theta_l)}{(\Gamma(\Theta_l))^2}\, x^{\Theta_l - 1}(1+x)^{-2\Theta_l}, \tag{3.9}$$

Fig. 3.3 compares the expectation of this analytical prediction with simulation results for a range of parameters for the strength of beneficial selection s_b and for the level of standing genetic variation (implicitly given by the strength of deleterious selection s_d before the environmental change). There are two main observations. First, the simulation results demonstrate the importance of the scaled mutation rate $\Theta_{bg} \equiv \Theta_l$ (for two loci). Low Θ_{bg} leads to sweep-like adaptation (heterogeneous adaptation response among loci, $E[x] << 1$), whereas high Θ_{bg} leads to shift-like adaptation (homogeneous response, $E[x]$ near 1). Second, the panels show that the selection intensity given by s_d and s_b has virtually no effect. Both results are predicted by the analytical theory

(Eq. (3.9)). In Appendix C.1, we further show that these results hold for arbitrary degrees of linkage (including complete linkage), see Fig. C.1.

For more than two loci, $L > 2$, one-dimensional marginal distributions of the joint distribution, Eq. (3.5), generally require $(L-1)$-fold integration, which can be complicated. However, it turns out that the key phenomena to characterize the adaptive architecture can still be captured by the 2-locus formalism, with appropriate rescaling of the mutation rate. For the general L-locus model, we broaden our definition of the summary statistic x above to describe the allele frequency ratio of the *first minor* locus and the major locus. To relate the distribution of x in the L-locus model to the one in the 2-locus model, we reason as follows: For small locus mutation rates Θ_l, the order of the loci is largely determined by the order at which mutations establish at these loci. *I.e.*, the locus where the first mutation establishes ends up as the major locus and the first minor locus is usually the second locus where a mutation establishes. The distribution of the allele frequency ratio x is primarily determined by the distribution of the waiting time for this second mutation after establishment of the first mutation at the major locus. In the 2-locus model, this time will be exponentially distributed, with parameter $1/\Theta_l$. In the L-locus model, however, where $L-1$ loci with total mutation rate $\Theta_l(L-1)$ compete for being the "first minor", the parameter for the waiting-time distribution reduces to $1/(\Theta_l(L-1))$. We thus see from this argument that the decisive parameter is the cumulative *background mutation rate*

$$\Theta_{bg} = (L-1)\Theta_l \tag{3.10}$$

at all minor loci in the background of the major locus. In Fig. 3.3 (orange dots) we show simulations of a $L = 10$ locus model with an appropriately rescaled locus mutation rate $\Theta_l \to \Theta_l/9$, such that the background rate Θ_{bg} is the same as for the 2-locus model. We see that the analytical prediction based on the 2-locus model provides a good fit for the 10-locus model. A more detailed discussion of this type of approximation is given in

Appendix C.4.

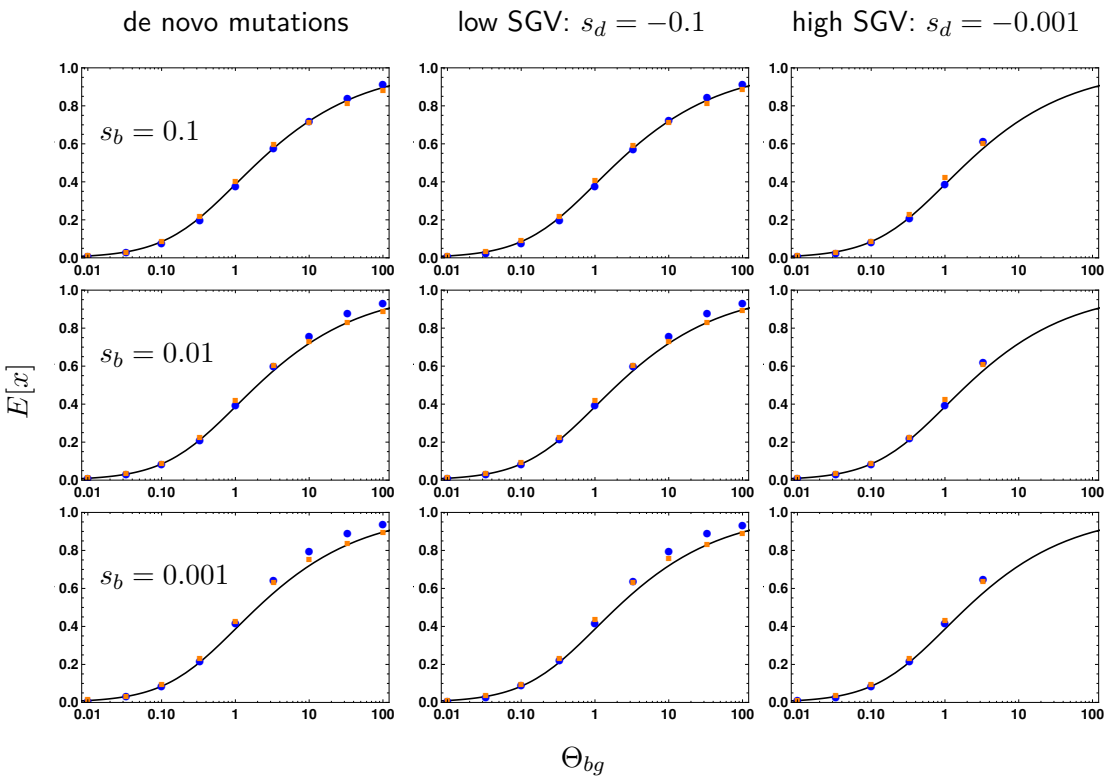

Figure 3.3: **Effect of selection strength and SGV on the frequency ratio E$[x]$.** We contrast the expected allele frequency ratios of the first minor locus (with the second largest frequency) over the major locus (with the largest frequency) for 2 loci (blue dots) and for 10 loci (orange dots) with analytical predictions (Appendix, Eq. D.16, black curve). $E[x]$ is shown as a function of Θ_{bg} ($= \Theta_l$ for the 2-locus case). Panels correspond to different strengths of positive selection (s_b, rows) and levels of SGV (no SGV, strongly deleterious $s_d = 0.1$, weakly deleterious $s_d = 0.001$, columns). We find that neither factor alters the expected ratio. We do not obtain results for all parameters, as we condition on adaptation from ancestral alleles, such that simulation runs are discarded if sampling conditions are met before the environmental change. Results for $10\,000$ replicates, standard errors < 0.005 (smaller than symbols).

3.4.2 Genomic architecture of polygenic adaptation

While the distribution of allele frequency ratios, Eqs. (3.5) and (3.9), offers a coarse (but robust) descriptor of the adaptive scenario, the joint distribution of allele frequencies at the end of the adaptive phase, Eq. (3.8), allows for a more refined view. In contrast to the distribution of ratios, the results now depend explicitly on the stopping condition (the time of observation) and on linkage among loci. We assume linkage equilibrium in

this section and assess the mutant allele frequencies when the frequency of the remaining wild-type individuals in the population is f_w ($= 0.05$ in our figures).

Fig. 3.4 displays the main result of this section. It shows the marginal distributions of all loci, ordered according to their allele frequency at the time of observation (major locus, 1st, 2nd, 3rd minor locus, *etc.*) for traits with $L = 2$, 10, 50, and 100 loci. Panels in the same row correspond to equal background mutation rates $\Theta_{bg} = (L-1)\Theta_l$, but note that the locus mutation rates Θ_l are not equal. The figure reveals a striking level of uniformity of adaptive architectures with the same Θ_{bg}, but vastly different number of loci. For $\Theta_{bg} \leq 1$ (the first three rows), the marginal distributions for loci of the same order (same color in the Figure) across traits with different L is almost invariant. For large Θ_{bg}, they converge for sufficiently large L (e.g. for $\Theta_{bg} = 10$, going from $L = 10$ to $L = 50$ and to $L = 100$). In particular, the background mutation rate Θ_{bg} determines the shape of the major-locus distribution (red in the Figure) for large $p \to 1 - f_w = 0.95$ (the maximum possible frequency, given the stopping condition). For $\Theta_{bg} < 1$, this distribution is sharply peaked with a singularity at $p = 1 - f_w$, whereas it drops to zero for large p if $\Theta_{bg} > 1$ (see also the analytical results below).

As predicted by the theory, Eq. (3.8) and below, simulations (not shown) confirm that selection parameters do not affect the adaptive architecture. As discussed in Appendix C.1, sufficiently tight linkage does change the shape of the distributions. Importantly, however, it does not affect the role of Θ_{bg} in determining the singularity of the major-locus distribution. This confirms the key role of the background mutation rate as a single parameter to determine the adaptive scenario in our model. While $\Theta_{bg} = 1$ separates architectures that are dominated by a single major locus ($\Theta_{bg} < 1$) from collective scenarios (with $\Theta_{bg} > 1$), the classical sweep or shift scenarios are only obtained if Θ_{bg} deviates strongly from 1. We therefore distinguish three adaptive scenarios.

- $\Theta_{bg} \lesssim 0.1$, *single completed sweeps*. For $\Theta_{bg} \ll 1$ (first two rows of Fig. 3.4), the distribution of the major locus is concentrated at the maximum of its range, while all other distributions are concentrated around 0. Adaptation thus occurs at

a single locus, via a selective sweep from low to high mutant frequency. Contributions by further loci are rare. If they occur at all they are usually due to a single runner-up locus (the largest minor locus).

- $0.1 < \Theta_{bg} < 100$, *heterogeneous partial sweeps*. With intermediate background mutation rates (third and forth row of Fig. 3.4), we still observe a strong asymmetry in the frequency spectrum. Even for values of Θ_{bg} slightly larger than 1, there is a clear major locus discernible, with most of its distribution for $p > 0.5$. However, there is also a significant contribution of several minor loci that rise to intermediate frequencies. We thus obtain a heterogeneous pattern of partial sweeps at a limited number of loci.

- $\Theta_{bg} \gtrsim 100$, *homogeneous frequency shifts*. Only for high background mutations rates $\Theta_{bg} \gg 1$ (last row of Fig. 3.4 with $\Theta_{bg} = 100$), the heterogeneity in the locus contributions to the adaptive response vanishes. There is then no dominating major locus. For only 2 loci, these shifts are necessarily still quite large, but for traits with a large genetic basis (large L; the only realistic case for high values of Θ_{bg}), adaptation occurs via subtle frequency shifts at many loci.

Analytical predictions

To gain deeper understanding of the polygenic architecture – and for quantitative predictions – we dissect our analytical result for the joint frequency spectrum in Eq. (3.8). We start with the case of $L = 2$ loci, allowing for different locus mutation rates Θ_1 and Θ_2. The marginal distribution at the first locus reads (from Eq. (3.8), after integration over p_2),

$$\mathsf{P}_{f_w}[p_1|\Theta_1,\Theta_2] = \frac{p_1^{\Theta_1-1}(1-p_1-f_w)^{\Theta_2-1}(1-p_1)^{\Theta_1+1}}{B[\Theta_1,\Theta_2]\,(1-p_1^2-f_w)^{\Theta_1+\Theta_2}}\left(1-\frac{f_w(1-2p_1)}{(1-p_1)^2}\right), \quad (3.11)$$

for $0 \leq p_1 \leq 1 - f_w$ (see also Appendix C.4.1). The distribution has a singularity at $p_1 = 0$ if the corresponding *locus* mutation rate is smaller than one, $\Theta_1 < 1$. It has a

singularity at $p_1 = 1 - f_w$ if the corresponding *background* mutation rate (which is just the mutation rate at the other locus for $L = 2$) is smaller than one, $\Theta_2 < 1$. The marginal distributions at the major locus, $\mathsf{P}^+_{f_w}[p|\Theta_1, \Theta_2]$, and the minor locus, $\mathsf{P}^-_{f_w}[p|\Theta_1, \Theta_2]$, follow from Eq. (3.11) as

$$\mathsf{P}^{\pm}_{f_w}[p|\Theta_1, \Theta_2] = \mathsf{P}_{f_w}[p|\Theta_1, \Theta_2] + \mathsf{P}_{f_w}[p|\Theta_2, \Theta_1], \tag{3.12}$$

where $\mathsf{P}^+_{f_w}[p|\Theta_1, \Theta_2]$ is defined for $1 - \sqrt{f_w} \leq p \leq 1 - f_w$ and $\mathsf{P}^-_{f_w}[p|\Theta_1, \Theta_2]$ is defined for $0 \leq p \leq 1 - \sqrt{f_w}$. The sum in Eq. (3.12) accounts for the alternative events that either the first locus or the second may end up as the major (or minor) locus. Consequently, $\mathsf{P}^-_{f_w}[p|\Theta_1, \Theta_2]$ has a singularity at $p = 0$ if the *minimal locus mutation rate* $\Theta_l = \min[\Theta_1, \Theta_2] < 1$. Analogously, $\mathsf{P}^+_{f_w}[p|\Theta_1, \Theta_2]$ has a singularity at $p = 1 - f_w$ if the *minimal background mutation rate* $\Theta_{bg} = \min[\Theta_1, \Theta_2] < 1$. The left column of Fig. 3.4 shows the distributions at the major and minor locus for $L = 2$ in the symmetric case $\Theta_1 = \Theta_2 = \Theta_l = \Theta_{bg}$ and $f_w = 0.05$. Simulations for a population of size $N_e = 10\,000$ and analytical predictions match well.

How do these results generalize for $L > 2$? We again allow for unequal locus mutation rates Θ_i. It is easy to see from Eq. (3.8) that the marginal distribution at the ith locus has a singularity at $p_i = 0$ for $\Theta_i < 1$. In the Mathematical Appendix D.3, we further show that it has a second singularity at $p_i = 1 - f_w$ if the corresponding background mutation rate $\sum_{j\neq i}^{d} \Theta_j$ is smaller than 1. As a first step, we split the joint distribution, Eq. (3.8), into the marginal distribution at the major locus $\mathsf{P}^+_{f_w}[p|\boldsymbol{\Theta}]$ (defined for $1 - \sqrt[L]{f_w} \leq p \leq 1 - f_w$) and a cumulative distribution at all other (minor) loci, $\mathsf{P}^-_{f_w}[p|\boldsymbol{\Theta}]$ (defined for $0 \leq p \leq 1 - \sqrt{f_w}$). Since any locus can end up as the major locus (with probability > 0), $\mathsf{P}^+_{f_w}[p|\boldsymbol{\Theta}]$ has a singularity at $p = 1 - f_w$ for

$$\Theta_{bg} := \min_{1\leq i\leq L} \left[\sum_{j=1}^{L} \Theta_j - \Theta_i \right] < 1\,. \tag{3.13}$$

This equation generalizes the definition of the background mutation rate, Eq. (3.10), to

the case of unequal locus mutation rates. Similarly, $\mathsf{P}^{-}_{f_w}[p|\mathbf{\Theta}]$ has a singularity at $p = 0$ if

$$\Theta_l := \min_{1 \le i \le L} \left[\Theta_i\right] < 1\,. \tag{3.14}$$

As long as $\Theta_{bg} \le 1$, we can approximate both the major-locus distribution $\mathsf{P}^{+}_{f_w}[p|\mathbf{\Theta}]$ and the cumulative minor locus distribution $\mathsf{P}^{-}_{f_w}[p|\mathbf{\Theta}]$ for arbitrary L by formulas for a 2-locus model with locus mutation rates matching Θ_l and Θ_{bg} of the multi-locus model, Eq. (3.12). Similarly, we can use results from a k-locus model to match the marginal distributions of the largest k loci (i.e., up to the $(k-1)$th minor) in models with $L > k$ loci, upon rescaling of the mutation rates. As explained for the ratio of the first minor and major locus in the previous section, rescaling rules match the expected waiting time for establishment of a mutation at the kth locus after establishment of a first mutation. Details are given in the Appendix C.4. In Fig. 3.4, we use formulas derived from a k-locus model $(k \le 4)$ to approximate the $(k-1)$st minor locus distribution of models with $L = 10; 50; 100$ loci and $\Theta_{bg} \le 1$. These approximations work well as long as these leading loci dominate the adaptive architecture of the trait, which is the case for $\Theta_{bg} \le 1$.

3.4.3 Relaxing complete redundancy

To complete our picture of adaptive architectures, we investigate the robustness of our model assumption against relaxation of redundancy. As explained above (*Model extensions* and Fig. 3.1), we implement diminishing returns epistasis, such that an individual with a single mutation has fitness $\delta s_{b/d}$, while individuals carrying more than one mutation have fitness $s_{b/d}$. With small deviations from complete redundancy (*e.g.* $\delta = 0.9$, stopping at 5% ancestral phenotypes, data not shown) we obtain basically no differences in the genomic patterns of adaptation. With larger deviations (*e.g.* $\delta = 0.5$) quantitative differences appear. However, the qualitative picture concerning the scenario of polygenic adaptation remains the same.

Fig. 3.5 shows the marginal frequency distributions of major and minor loci for a

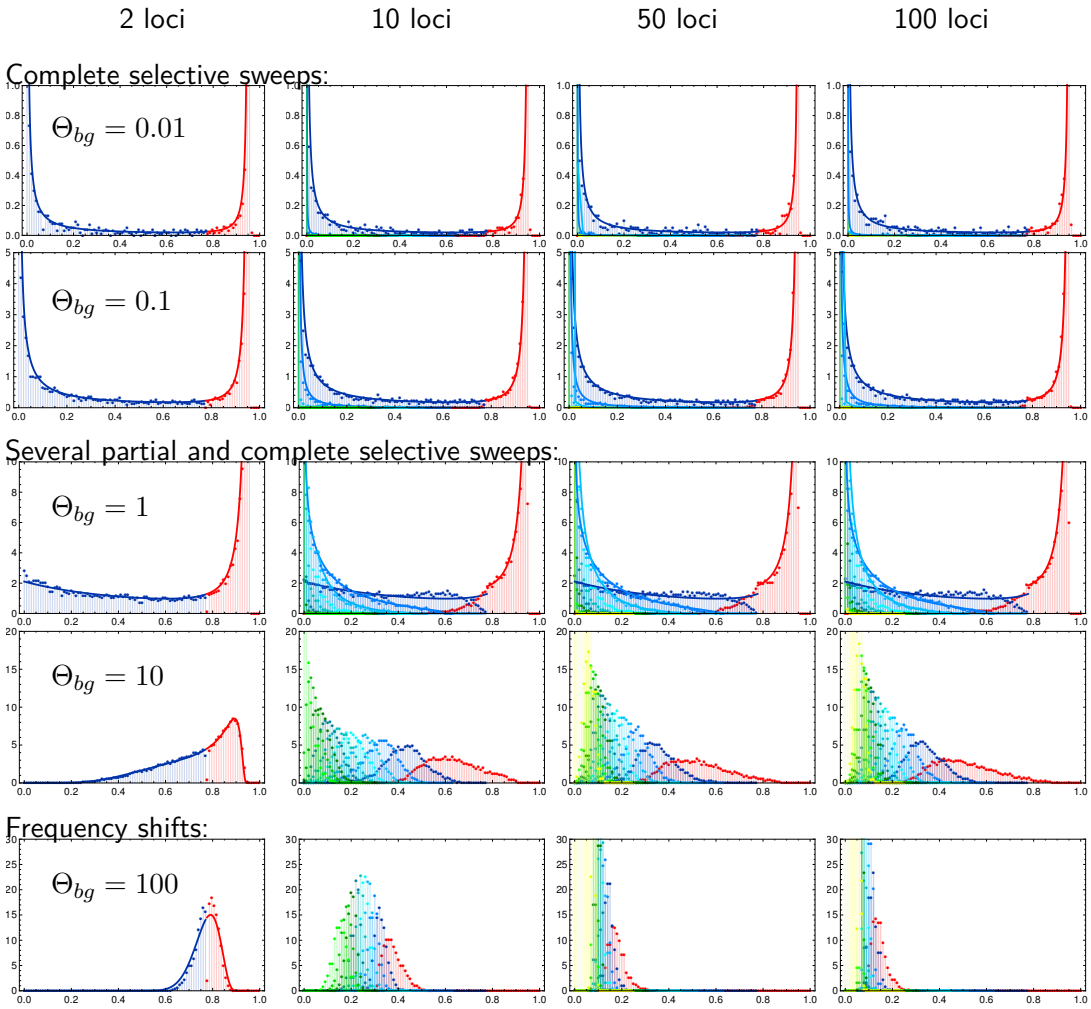

Figure 3.4: **Genomic architecture of polygenic adaptation.** We distinguish three patterns of architectures with increasing genomic background mutation rate Θ_{bg}: complete sweeps, for $\Theta_{bg} \lesssim 0.1$, heterogeneous partial sweeps at several loci for $0.1 < \Theta_{bg} < 100$, and polygenic frequency shifts for $\Theta_{bg} \gtrsim 100$. The plots show the marginal distributions of all loci, ordered according to their allele frequency, *i.e.* the major locus in red and all following (first, second, third, etc. minors) in blue to yellow. Lines in respective colors show analytical predictions, Appendix C.4. Simulations were stopped once the populations have adapted to 95% of the maximum mean fitness in each of $10\,000$ replicates, resulting in an the upper bound for the major locus distribution at, $p_1 = 0.95$. Simulations for $s_b = -s_d = 0.1$. Note the different scaling of the y-axis for different mutation rates.

trait with relaxed redundancy with $\delta = 0.5$ that is sampled when the population has accomplished 95% of the fitness increase on its way to the new optimum, Eq. (3.2). Given the fitness function, this is not possible with adaptation at only a single locus.

At least two loci are needed. The Figure compares the simulation data for the relaxed redundancy model (colored dots) and the full redundancy model (dots in back and gray). As in Fig. 3.4, traits in the same row have the same background mutation rate Θ_{bg}. However, the background rate for the model with relaxed redundancy is redefined as

$$\Theta_{bg}^{\text{relax}} = (L-2)\Theta_l \tag{3.15}$$

where Θ_l is the locus mutation rate (equal at all loci). We thus define the background rate, more precisely, as the combined population-scaled mutation rate of all loci *that are not essential* to accomplish adaptation of the phenotype and, thus, are truly redundant. With this choice, the adaptive architecture of the relaxed redundancy model reproduces the one of the model with full redundancy – up to a shift in the number of the loci due to an extra locus that is needed for adaptation with relaxed redundancy. The Figure captures this by comparing traits with relaxed redundancy with $L = 3, 4, 11,$ and 101 loci to fully redundant traits with one fewer locus. The inset figures in the column for $L = 4$ loci show the same scenario, but with an *averaged* marginal distribution for the two largest loci with relaxed redundancy (in green).

- For mutation rates, $\Theta_{bg} \ll 1$, we still find adaptation by sweeps. Relative to the full redundancy model, we now observe two "major" sweep loci instead of only a single sweep. The inset (for $L = 4$) shows that their averaged distributions matches the major locus distribution of the full redundancy model. The distribution at the third largest locus (the "first minor" locus with relaxed redundancy) resembles the corresponding distribution of the first minor locus of the trait with full redundancy.

- For intermediate mutation rates, $0.1 < \Theta_{bg} < 100$, the pattern is dominated by partial sweeps. We clearly see the similarity in the marginal distributions of the kth largest locus with full redundancy and the $k+1$st largest locus of the relaxed redundancy trait. For the two major loci with relaxed redundancy, we again see (inset) that the averaged distribution matches the major-locus distribution of the

full redundancy model.

- Finally, for strong mutation, $\Theta_{bg} \gtrsim 100$, adaptation again occurs by small frequency shifts at many loci.

In summary, our results show that relaxing redundancy leads to qualitatively similar results, but with a reduced "effective" background mutation rate that only accounts for "truly redundant" loci.

3.5 Discussion

Traits with a polygenic basis can adapt in different ways. Few or many loci can contribute to the adaptive response. The changes in the allele frequencies at these loci can be large or small. They can be homogeneous or heterogeneous. While molecular population genetics posits large frequency changes – selective sweeps – at few loci, quantitative genetics views polygenic adaptation as a collective response, with small, homogeneous allele frequency shifts at many loci. Here, we have explored the conditions under which each adaptive scenario should be expected, analyzing a polygenic trait with redundancy among loci that allows for a full range of adaptive architectures: from sweeps to subtle frequency shifts.

3.5.1 Polygenic architectures of adaptation

For any polygenic trait, the multitude of possible adaptive architectures is fully captured by the joint distribution of mutant alleles across the loci in its basis. Different adaptive scenarios (such as sweeps or shifts) correspond to characteristic differences in the shape of this distribution, at the end of the adaptive phase. For a single locus, the stationary distribution under mutation, selection and drift can be derived from diffusion theory and has been known since the early days of population genetics (Wright, 1931). For multiple interacting loci, however, this is usually not possible. To address this problem for our model, we dissect the adaptive process into two phases. The early stochastic

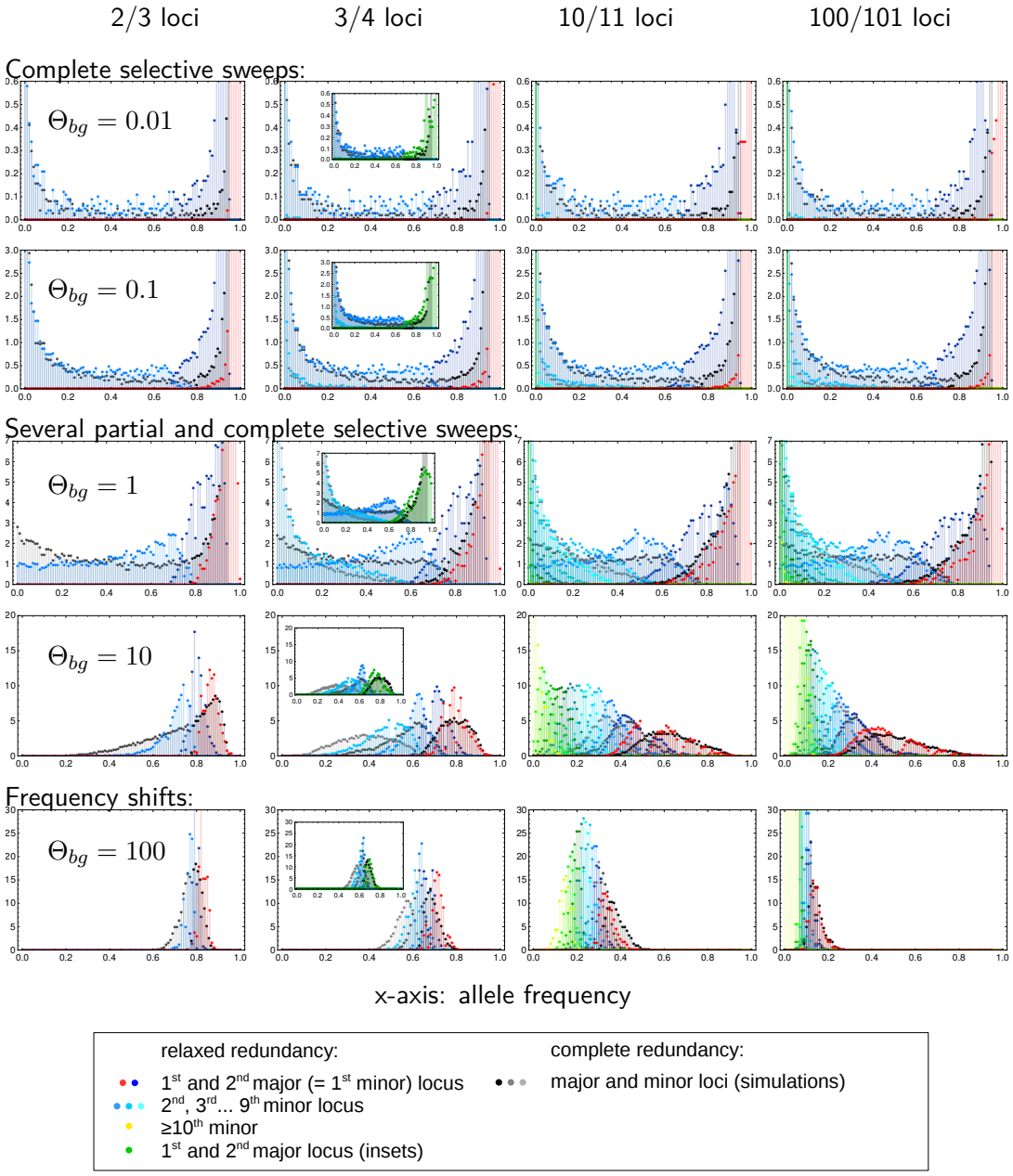

Figure 3.5: **Relaxed redundancy.** Relaxing redundancy such that a single mutant has fitness $1 + 0.5s_{b/d}$ and only two mutations or more confer the full fitness effect $(1 + s_{b/d})$ demonstrates the robustness of our model. As in Fig. 3.4, allele frequency distributions of derived alleles are displayed once the population has reached 95% of maximum attainable mean population fitness. Genomic patterns of adaptation show similar characteristics as with complete redundancy. Due to relaxed redundancy, an additional "major locus" is required to reach the adaptive optimum. As explained in the main text, the distribution of the kth largest locus with complete redundancy therefore corresponds to the distribution of the $k + 1$st largest locus with relaxed redundancy. Insets in the second column show the same data with the distributions of the two major loci for relaxed redundancy combined (in green).

phase describes the establishment of all mutants that contribute to the adaptive response under the influence of mutation and drift. We use that loci can be treated as independent during this phase to derive a joint distribution for ratios of allele frequencies at different loci, Eq. (3.5). During the second, deterministic phase, epistasis and linkage become noticeable, but mutation and drift can be ignored. Allele frequency changes during this phase can be described as a density transformation of the joint distribution. For the simple model with fully redundant loci, and assuming either LE or complete linkage, this transformation can be worked out explicitly. Our main result Eq. (3.8) can thus be understood as a multi-locus extension of Wright's stationary distribution. For a neutral locus with multiple alleles, Wright's distribution is a Dirichlet distribution, which is reproduced in our model for the case of complete linkage, see Appendix C.1. For the opposite case of linkage equilibrium, we obtain a family of inverted Dirichlet distributions, depending on the stopping condition – our time of observation.

Note that the distribution of adaptive architectures is *not* a stationary distribution, but necessarily transient. It describes the pattern of mutant alleles at the end of the "rapid adaptive phase" (Jain and Stephan, 2015, 2017), because this is the time scale that the opposite narratives of population genetics and quantitative genetics refer to. In particular, the quantitative genetic "small shifts" view of adaptation does not talk about a stationary distribution: it does not imply that alleles will never fix over much longer time scales, due to drift and weak selection. On a technical level, the transient nature of our result means that it reflects the effects of genetic drift only during the early phase of adaptation. These early effects are crucial because they are magnified by the action of positive selection. In contrast, our result ignores drift after phenotypic adaptation has been accomplished – which is also a reason why it can be derived at all.

To capture the key characteristics of the adaptive architecture, we dissect the joint distribution in Eq. (3.8) into marginal distributions of single loci. As explained at the start of the results section, these loci do not refer to a fixed genome position, but are defined *a posteriori* via their role in the adaptive process. For example, the *major*

locus is defined as the locus with the largest mutant allele frequency at the end of the adaptive phase. (Since all loci have equal effects in our model, this is also the locus with the largest contribution to the adaptive response.) This is a different way to summarize the joint distribution than used in some of the previous literature (Chevin and Hospital, 2008; Pavlidis et al., 2012; Wollstein and Stephan, 2014), which rely on a gene-centered view to study the pattern at a focal locus, irrespective of its role in trait adaptation. In contrast, we use a trait-centered view, which is better suited to describe and distinguish adaptive scenarios. For example, "adaptation by sweeps" refers to a scenario where sweeps happen at some loci, rather than at a specific locus. This point is further discussed in Appendix C.4.1, where we also display marginal distributions of Eq. (3.8) for fixed loci.

The role of the background mutation rate

Our results show that the qualitative pattern of polygenic adaptation is predicted by a single compound parameter: the background mutation rate Θ_{bg} (see Eqs. (3.10), (3.13), (3.15)), *i.e.* the population mutation rate for the background of a focal locus within the trait basis. For a large basis, Θ_{bg} is closely related to the trait mutation rate. We can understand the key role of this parameter as follows. As detailed in the Section 3.3.4, the early stochastic phase of adaptation is governed by two processes: New successful mutations (destined for establishment) enter the population at rate $\Theta_l s_b$ per locus (where Θ_l is the locus mutation rate and s_b the selection coefficient), while existing mutants spread with an exponential rate s_b. Consider the locus that carries the first successful mutant. For $\Theta_{bg} < 1$, the expected spread from this first mutant exceeds the creation of new mutant lineages at all other loci. Therefore, the locus will likely maintain its lead, with an exponentially growing gap to the second largest locus. Vice versa, for $\Theta_{bg} > 1$, most likely one of the competing loci will catch up. We can thus think of Θ_{bg} as a measure of competition experienced by the major locus due to adaptation at redundant loci in its genetic background. The argument does not depend on the

strength of selection, which affects both rates in the same way. The same can be shown for adaptation from standing genetic variation at mutation-selection-drift balance. As a consequence of low mutant frequencies during the stochastic phase, the result is also independent of interaction effects due to epistasis or linkage.

Since the order of loci is not affected by the deterministic phase of the adaptive process, Θ_{bg} maintains its key role for the adaptive architecture. In the joint frequency distribution, Eq. (3.5) and Eq. (3.8), it governs the singular behavior of the marginal distribution at the major locus. For $\Theta_{bg} < 1$, this distribution has a singularity at the maximum of its range. Adaptation is therefore dominated by the major locus, leading to heterogeneous architectures. For $\Theta_{bg} \lesssim 0.1$, adaptation occurs almost always due to a completed sweep at this locus. For $\Theta_{bg} > 1$, in contrast, no single dominating locus exists: adaptation is collective and supported by multiple loci. For a polygenic trait with $\Theta_{bg} \gtrsim 100$, we obtain homogeneous small shifts at many loci, as predicted by quantitative genetics.

The result also shows that the adaptive scenario does not depend directly on the number of loci in the genetic basis of the trait, but rather on their combined mutation rate (the mutational target size, *sensu* Pritchard et al., 2010). For redundant loci and fixed Θ_{bg}, the predicted architecture at the loci with the largest contribution to the adaptive response is almost independent of the number of loci, see Fig. 3.4. Qualitatively, the same still holds true when the assumption of complete redundancy is dropped (Fig. 3.5). In this case, only loci in the genetic background that are not required to reach the new trait optimum, but offer redundant routes for adaptation, are included in Θ_{bg}. Note that the same reasoning holds for a quantitative trait that is composed of several modules of mutually redundant genes, but where interactions among genes in different modules can be ignored. In this case, the adaptive architecture for each module depends only on the module-specific Θ_{bg}, but not on the mutation rates at genes in the basis of the trait outside of the module.

Polygenic adaptation and soft sweeps

In our analysis of polygenic adaptation, we have not studied the probability that adaptation at single loci could involve more than a single mutational origin and thus produces a so-called *soft selective sweep from recurrent mutation*. As explained in Pennings and Hermisson (2006); Hermisson and Pennings (2017), however, the answer is simple and only depends on the locus mutation rate – independently of adaptation at other loci. Soft sweeps become relevant for $\Theta_l \gtrsim 0.1$. For much larger values $\Theta_l \gg 1$, they become "super-soft" in the sense that single sweep haplotypes do not reach high frequencies because there are so many independent origins of the mutant allele. The role of Θ_{bg} for polygenic adaptation is essentially parallel to the one of Θ_l for soft sweeps. In both cases, the population mutation rate is the only relevant parameter, with a lower threshold of $\Theta \sim 0.1$ for a signal involving multiple alleles and much higher values for a "super-soft" scenario with only subtle frequency shifts. Nevertheless, the mathematical methods to analyze both cases are different, essentially because the polygenic scenario does not lend itself to a coalescent approach.

3.5.2 Alternative approaches to polygenic adaptation

The theme of "competition of a single locus with its background" relates to previous findings by Chevin and Hospital (2008) in one of the first studies to address polygenic footprints. These authors rely on a deterministic model to describe the adaptive trajectory at a single target QTL in the presence of background variation. The background is modeled as a normal distribution with a mean that can respond to selection, but with constant variance. Obviously, a drift-related parameter, such as Θ_{bg}, has no place in such a framework. Still, there are several correspondences to our result on a qualitative level. Specifically, a sweep at the focal locus is prohibited under two conditions. First, the background variation (generated by recurrent mutation in our model, constant in Chevin and Hospital, 2008) is large. Second, the fitness function must exhibit strong negative epistasis that allows for alternative ways to reach the trait optimum – and thus

produces redundancy (Gaussian stabilizing selection in Chevin and Hospital, 2008). Finally, while the adaptive trajectory depends on the *shape* of the fitness function, Chevin and Hospital note that it does not depend on the *strength* of selection on the trait, as also found for our model.

A major difference of the approach used in Chevin and Hospital (2008) is the gene-centered view that is applied there. Consider a scenario where the genetic background "wins" against the focal QTL and precludes it from sweeping. For a generic polygenic trait (and for our model) this still leaves the possibility of a sweep at one of the background loci. However, this is not possible in Chevin and Hospital (2008), where all background loci are summarized as a sea of small-effect loci with constant genetic variance.

This constraint is avoided in the approach by de Vladar and Barton (2014) and Jain and Stephan (2017), who study an additive quantitative trait under stabilizing selection with binary loci (see also Jain and Devi, 2018, for an extension to adaptation to a moving optimum). These models allow for different locus effects, but ignore genetic drift. Before the environmental change, all allele frequencies are assumed to be in mutation-selection balance, with equilibrium values derived in de Vladar and Barton (2014). At the environmental change, the trait optimum jumps to a new value and alleles at all loci respond by large or small changes in the allele frequencies. Overall, de Vladar and Barton (2014) and Jain and Stephan (2017) predict adaptation by small frequency shifts in large parts of the biological parameter space. In particular, sweeps are prevented in these models if most loci have a small effect and are therefore under weak selection prior to to the environmental change. This contrasts to our model, where the predicted architecture of adaptation is independent of the selection strength. The reason for this difference is that effects of drift on the starting allele frequencies are neglected in the deterministic models. Indeed, loci under weak selection start out from frequency $x_0 = 0.5$ (de Vladar and Barton, 2014). In finite populations, however, almost all of these alleles start from very low (or very high) frequencies – unless the population mutation

parameter is large (many alleles at intermediate frequencies at competing background loci are expected only if $\Theta_{bg} \gg 1$, in accordance with our criterion for *shifts*). To test this further, we have analyzed our model for the case of starting allele frequencies set to the deterministic values of mutation-selection balance, μ/s_d. Indeed, we observe adaptation due to small frequency shifts in a much larger parameter range (Appendix C.2).

Generally, adaptation by sweeps in a polygenic model requires a mechanism to create heterogeneity among loci. This mechanism is entirely different in both modeling frameworks. While heterogeneity is (only) produced by unequal locus effects for the deterministic quantitative trait, it is (solely) due to genetic drift for the redundant trait model. Since both approaches ignore one of these factors, both results should rather underestimate the prevalence of sweeps.

Both drift and unequal locus effects are included in the simulation studies by Pavlidis et al. (2012) and Wollstein and Stephan (2014). These authors assess patterns of adaptation for a quantitative trait under stabilizing selection with up to eight diploid loci. However, due to differences in concepts and definitions there are few comparable results. In contrast to Jain and Stephan (2017) and to our approach, they study long-term adaptation (they simulate N_e generations). In Pavlidis et al. (2012); Wollstein and Stephan (2014), *sweeps* are defined as fixation of the mutant allele at a focal locus, whereas *frequency shifts* correspond to long-term stable polymorphic equilibria (Wollstein and Stephan, 2014). With this definition, a *shift* scenario is no longer a transient pattern, but depends entirely on the existence (and range of attraction) of polymorphic equilibria. A polymorphic outcome is likely for a two-locus model with full symmetry, where the double heterozygote has the highest fitness. For more than two loci, the probability of shifts *decreases* (because polymorphic equilibria become less likely, see Bürger and Gimelfarb, 1999). However, also the probability of a sweep decreases. This is largely due to the gene-centered view in Pavlidis et al. (2012), where potential sweeps at background loci are not recorded (see also Appendix C.4.1).

3.5.3 Scope of the model and the analytical approach

We have described scenarios of adaptation for a simple model of a polygenic trait. This model allows for an arbitrary number of loci with variable mutation rates, haploids and diploids, linkage, time-dependent selection, new mutations and standing genetic variation, and alternative starting conditions for the mutant alleles. Its genetic architecture, however, is strongly restricted by our assumption of (full or relaxed) redundancy among loci. In the haploid, fully redundant version, the phenotype is binary and only allows for two states, *ancestral wild-type* and *mutant*. Biologically, this may be thought of as a simple model for traits like pathogen or antibiotic resistance, body color, or the ability to use a certain substrate (Coffman et al., 2005; Novembre and Han, 2012).

Our main motivation, however, has been to construct a minimal model with a polygenic architecture that allows for both sweep and shifts scenarios – and for comprehensive analytical treatment. One may wonder how our methods and results generalize if we move beyond our model assumptions.

Key to our analytical method is the dissection of the adaptive process into a stochastic phase that explains the origin and establishment of beneficial variants and a deterministic phase that describes the allele frequency changes of the established mutant copies. This framework can be applied to a much broader class of models. Indeed, in many cases, the fate of beneficial alleles, establishment or loss, is decided while these alleles are rare. Excluding complex scenarios such as passage through a fitness valley, the initial stochastic phase is relatively insensitive to interactions via epistasis or linkage. We can therefore describe the dynamics of traits with a different architecture (*e.g.* an additive quantitative trait with equal-effect loci under stabilizing selection) within the same framework by coupling the same stochastic dynamics to a different set of differential equations describing the dynamics during the deterministic phase.

This is important because, as described above, the key *qualitative* results to distinguish broad categories of adaptive scenarios are due to the initial stochastic phase. This holds true, in particular, for the role of the background mutation rate Θ_{bg}. We therefore

expect that these results generalize beyond our basic model. Indeed, we have already seen this for our model extensions to include diploids, linkage, and relaxed redundancy. Vice-versa, we have seen that other factors, such as alternative starting conditions for the mutant alleles, directly affect the early stochastic phase and lead to larger changes in the results. As shown in Appendix C.2, however, they can be captured by an appropriate extension of the stochastic Yule process framework.

Several factors of biological importance are not covered by our current approach. Most importantly, this includes loci with different effect sizes and spatial population structure. Both require a further extension of our framework for the early stochastic phase of adaptation. While variable locus effects (both directly on the trait or on fitness due to pleiotropy) are expected to enhance the heterogeneity in the adaptive response among loci, the opposite is true for spatial structure, as further discussed below.

3.5.4 When to expect sweeps or shifts

Although our assumptions on the genetic architecture of the trait (complete redundancy and equal loci) are favorable for a collective, shift-type adaptation scenario, we observe large changes in mutant allele frequencies (completed or partial sweeps) for major parts of the parameter range. A homogeneous pattern of *subtle frequency shifts* at many loci is only observed for large mutation rates. This contrasts with experience gained from breeding and modern findings from genome-wide association studies, which are strongly suggestive of an important role for small shifts with contributions from very many loci (reviewed in Falconer et al., 1996; Barton and Keightley, 2002; Hill, 2014; Visscher et al., 2017; Csilléry et al., 2018) (see Hancock et al., 2010; Laporte et al., 2016; Zan and Carlborg, 2018, for recent empirical examples). For traits such as human height, there has even been a case made for *omnigenic* adaptation (Boyle et al., 2017), setting up a "mechanistic narrative" for Fisher's (conceptual) infinitesimal model. Clearly, body height may be an extreme case and the adaptive scenario will strongly depend on the type of trait under consideration. Still, the question arises whether and how wide-spread

shift-type adaptation can be reconciled with our predictions. We will first discuss this question within the scope of our model and then turn to factors beyond our model assumptions.

The size of the background mutation rate

The decisive parameter to predict the adaptive scenario in our model, the background mutation rate, is not easily amenable to measurement. $\Theta_{\text{bg}} = (L-1)\Theta_l$ compounds two factors, the locus mutation parameter Θ_l and the number of loci L, which are both complex themselves and require interpretation. To assess the plausibility of values of the order of $\Theta_{bg} \gtrsim 100$, required for homogeneous polygenic shifts in our model, we consider both factors separately.

Large locus mutation rates $\Theta_l = 4N_e\mu$ (for diploids, $2N_e\mu$ for haploids) are possible if either the allelic mutation rate μ or the effective population size N_e is large. Both cases are discussed in detail (for the case of soft sweeps) in Hermisson and Pennings (2017). Basically, μ can be large if the mutational target *at the locus* is large. Examples are loss-of-function mutations or cis-regulatory mutations. N_e is the *short-term effective population size* (Pennings and Hermisson, 2006; Karasov et al., 2010; Barton, 2010) during the stochastic phase of adaptation. This *short-term* size is unaffected by demographic events, such as bottlenecks, prior to adaptation and is therefore often larger than the *long-term* effective size that is estimated from nucleotide diversity. (Strong changes in population size *during* the adaptive period can have more subtle effects (Wilson et al., 2014).) For recent adaptations due to gain-of-function mutations, plausible values are $\Theta_l \lesssim 0.1$ for *Drosophila* and $\Theta_l \lesssim 0.01$ for humans (Hermisson and Pennings, 2017).

If $10\,000$ loci or more contribute to the basis of a polygenic trait (Boyle et al., 2017), large values of Θ_{bg} could, in principle, easily be obtained. However, the parameter L in our model counts only loci that actually can respond to the selection pressure: mutant alleles must change the trait in the right direction and should not be constrained by pleiotropic effects. Omnigenic genetics, in particular, also implies ubiquitous pleiotropy

and so the size of the basis *that is potentially available for adaptation* is probably strongly restricted. For a given trait, the number of available loci L may well differ, depending on the selection pressure and pleiotropic constraints. Furthermore, our results for the model with relaxed redundancy show that Θ_{bg} only accounts for loci that are truly redundant and offer alternative routes to the optimal phenotype. With this in mind, values of L in the hundreds or thousands (required for $\Theta_{bg} \geq 100$) seem to be quite large. While some highly polygenic traits such as body size could still fulfill this condition, this appears questionable for the generic case.

Balancing selection and spatial structure

In our model, characteristic patterns in the adaptive architecture result from heterogeneities among loci that are created by mutation and drift during the initial stochastic phase of adaptation. As initial condition, we have mostly assumed that mutant alleles segregate in the population in the balance of mutation, purifying selection and genetic drift. Since this typically results in a broad allele frequency distribution (unless mutation is very strong), it favors heterogeneity among loci and thus adaptation by (partial) sweeps. However, even after decades of research, the mechanisms to maintain genetic variation in natural populations remain elusive (Barton and Keightley, 2002). As discussed in Appendix C.2, more homogeneous starting conditions for the mutant alleles can be strongly favorable of a shift scenario. Such conditions can be created either by balancing selection or by neutral population structure.

Balancing selection (due to overdominance or negative frequency dependence) typically maintains genetic variation at intermediate frequencies. If a major part of the genetic variance for the trait is due to balancing selection, adaptation could naturally occur by small shifts. However, the flexibility of alleles at single loci, and thus the potential for smaller or larger shifts, will depend on the strength of the fitness trade-off (*e.g.* due to pleiotropy) at each locus. If these trade-offs are heterogeneous, the adaptive architecture will reflect this. Also, adaptation against a trade-off necessarily involves a

fitness cost. Therefore, if the trait can also adapt at loci that are free of a trade-off, these will be preferred, possibly leading to sweeps.

As discussed in a series of papers by Ralph and Coop (2010, 2015), spatial population structure is a potent force to increase the number of alternative alleles that contribute to the adaptive response. If adaptation proceeds independently, but in parallel, in spatially separated subpopulations, different alleles may be picked up in different regions. Depending on details of the migration pattern (Paulose et al., 2018), we then expect architectures that are globally polygenic with small shifts, but locally still show sweeps or dominating variants.

Furthermore, population structure and gene flow *before* the start of the selective phase can have a strong effect on the starting frequencies. In particular, if the base population is admixed, mutant alleles could often start from intermediate frequencies and naturally produce small shifts. This applies, in particular, to adaptation in modern human populations, which have experienced major admixture events in their history (Pickrell and Reich, 2014; Lazaridis et al., 2016) and only show few clear signals of selective sweeps (Pritchard et al., 2010).

Finally, gene flow and drift will continue to change the architecture of adaptation after the rapid adaptive phase that has been our focus here. This can work in both directions. On the one hand, subsequent gene flow can erase any *local* sweep signals by mixing variants that have been picked up in different regions (Ralph and Coop, 2010, 2015). On the other hand, local adaptation, in particular, may favor adaptation by large-effect alleles at few loci, favoring sweeps over longer time-scales. Indeed, as argued by Yeaman (2015), initial rapid adaptation due to small shifts at many alleles of mostly small effect may be followed by a phase of allelic turnover, during which alleles with small effect are swamped and few large-effect alleles eventually take over. This type of allele sorting over longer time-scales is also observed in simulations studies for a quantitative trait under stabilizing selection that adapt to a new optimum after an environmental change (Franssen et al., 2017; Jain and Stephan, 2017).

Between sweeps and shifts: adaptation by partial sweeps

Previous research has almost entirely focused on either of the two extreme scenarios for adaptation: sweeps in a single-locus setting or (infinitesimal) shifts in the tradition of Fisher's infinitesimal model. This leaves considerable room for intermediate patterns. Our results for the redundant trait model show that such transitional patterns should be expected in a large and biologically relevant parameter range (values of Θ_{bg} between 0.1 and 100). Patterns between sweeps and shifts are *polygenic* in the sense that they result from the *concerted* change in the allele frequency at multiple loci. They can only be understood in the context of interactions among these loci. However, they usually do not show subtle shifts, but much larger changes (partial sweeps) at several loci. If adaptation occurs from mutation-selection-drift balance, the polygenic patterns are typically strongly heterogeneous, even across loci with identical effects on the trait. Such patterns may be difficult to detect with classical sweep scans, in particular if partial sweeps are "soft" because they originate from standing genetic variation or involve multiple mutational origins. However, they should be visible in time-series data and may also leave detectable signals in local haplotype blocks.

Indeed there is empirical evidence for partial sweeps from time series data in experimental *evolve and resequence* experiments on recombining species such as fruit flies. For example, Burke et al. (2010) observe predominantly partial sweeps (from SGV) in their long-term selection experiments with *Drosophila melanogaster* for accelerated development – a rather unspecific trait with a presumably large genomic basis. A similar pattern of "plateauing", where allele frequencies at several loci increase quickly over several generations, but then stop at intermediate levels, was recently observed by Barghi et al. (2018) for adaptation of 10 *Drosophila simulans* replicates to a hot temperature environment. Complementing the genotypic time-series data with measurements of several phenotypes, these authors found convergent evolution for several high-level traits (such as fecundity and metabolic rate), indicating that rapid phenotypic adaptation had reached a new optimum. This high-level convergence contrasts a strong heterogeneity

in the adaptation response among loci and also between replicates (Barghi et al., 2018). Based on their data, the authors reject both a selective sweep model and adaptation by subtle shifts. Instead, the observed patterns are most consistent with the intermediate adaptive scenario in our framework, featuring heterogeneous partial sweeps at interacting loci with a high level of genetic redundancy.

C. Supporting Information: Results

C.1 Linked loci

Negative epistasis for fitness causes negative linkage disequilibrium (LD) among the selected loci. While LD can usually be ignored as long as loci are unlinked, this changes once recombination rates drop below the selection coefficient $r < s_b$ (data not shown). For tight linkage $r \to 0$, in particular, individuals carrying multiple mutations can no longer be formed by recombination, but require multiple mutational hits on the same haplotype. This is unlikely while mutant allele frequencies are low, which is when the relevant mutations of the adaptive process arise. By the end of the adaptive phase, the excess of single-mutant haplotypes produces strong negative LD. Nevertheless, our theory predicts that the distribution of allele frequency ratios that emerges from the early stochastic phase of the adaptive process is unaffected Eq.(3.9). This prediction is confirmed by simulations, see Fig. C.1. If anything, the match even improves for strong linkage. (Deviations for high Θ_l values result since the rate of recurrent mutation $\sim \Theta_l(1-p)$ is smaller than assumed in the Yule process approximation, $\sim \Theta_l$, when the mutant frequency p gets large. This affects the major locus stronger than any other locus and leads to overshooting of the minor/major ratio seen in the Figure. The bias is reduced for strong linkage since 95% phenotypic adaptation corresponds to smaller allele frequencies in this case.)

Fig. C.2 shows the joint distribution of the major and the minor locus of a trait with $L = 2$ loci for different degrees of linkage. In all cases, the process is stopped when the proportion of remaining non-mutant individuals drops below $f_w = 0.05$. The results show that the linkage equilibrium assumption (red and blue lines) provides a good approximation as long as $r \geq s_b$. For $r < s_b$, the distributions are shifted to lower values and clear deviations become visible. The constraint on the allele frequencies at the stopping condition changes from $(1-p_1)(1-p_2) = f_w$ for linkage equilibrium to

$p_1+p_2 = 1-f_w$ for complete linkage. As a consequence, the boundary between the major and minor locus distributions (red and blue) drops from $1-\sqrt{f_w}$ to $(1-f_w)/2$. As shown in the Mathematical Appendix, Eq. (D.29), we can derive an analytical approximation for the distributions for complete linkage $r = 0$. For $L = 2$, we obtain a modified Beta-distribution (black lines in the Figure)

$$\mathsf{P}^{\pm}_{f_w,\mathsf{tl}}[p|\Theta] = \frac{2(1-f_w)^{-1}}{B[\Theta]} \left(\frac{p}{1-f_w}\right)^{\Theta-1} \left(1-\frac{p}{1-f_w}\right)^{\Theta-1} \tag{C.1}$$

with $p \geq (1-f_w)/2$ (resp. $p \leq (1-f_w)/2$) for the major (minor) locus. The simulation results show that this prediction is accurate for $r \ll s_b$ (deviations for $\Theta_{bg} = 100$ are due to overshooting of the stopping condition in the last generation of our Wright-Fisher simulations).

While linkage affects the shape of the joint distribution, it does not alter its key qualitative characteristics that distinguish adaptive scenarios. In particular, the same conditions on Θ_{bg} and Θ_l apply for singularities at the boundaries of marginal distributions. We still observe sweep-like adaptation for $\Theta_{bg} \ll 1$, adaptation by small shifts for $\Theta_{bg} \gg 1$, and a heterogeneous pattern of partial sweeps in a transition range of Θ_{bg} around 1.

C.2 Alternative starting allele frequencies

So far we have assumed that adaptation starts from mutation-selection-drift balance. This includes variable amounts of standing genetic variation (weak or strong s_d) and even cases where this balance is not represented by a stable equilibrium distribution (time-dependent selection, see the Mathematical Appendix). There are, however, other scenarios of biological relevance. Given the right (possibly complex) selection scheme, balancing selection can maintain mutant alleles, prior to the environmental change, at arbitrary frequencies. The same holds true if the base population is admixed, either due to natural processes or due to human activity (e.g. breeding from hybrids). For these

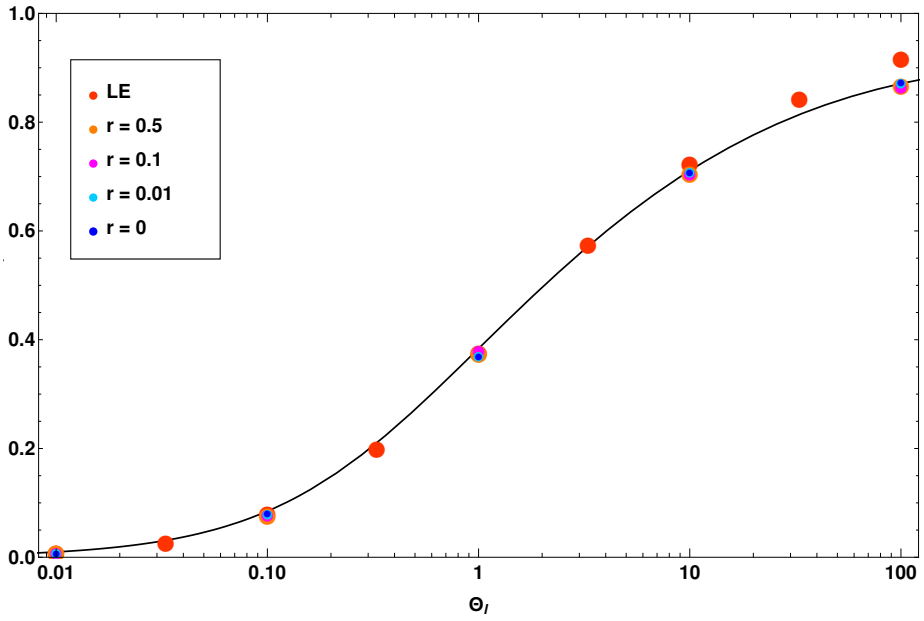

Figure C.1: **$\mathbf{E}[x]$ for redundant fitness effects with two linked loci.** Simulation results (colored dots) for the mean allele frequency ratio are plotted in dependence of the locus population mutation rate Θ_l and compared with the analytical prediction (black line). Simulations are stopped when fitness has reached 95% of its maximum. Linkage does not change the results for the ratio of allele frequencies, despite significant build up of linkage disequilibrium with low recombination rates (data not shown). Results for $10\,000$ replicates standard errors < 0.005 (smaller than symbols).

scenarios, our theoretical formalism to describe the establishment of mutants during the stochastic phase (Fig. 3.2) does not apply. In this section, we describe how the formalism can be extended to cover arbitrary starting frequencies of mutants at the onset of positive selection at time $t = 0$.

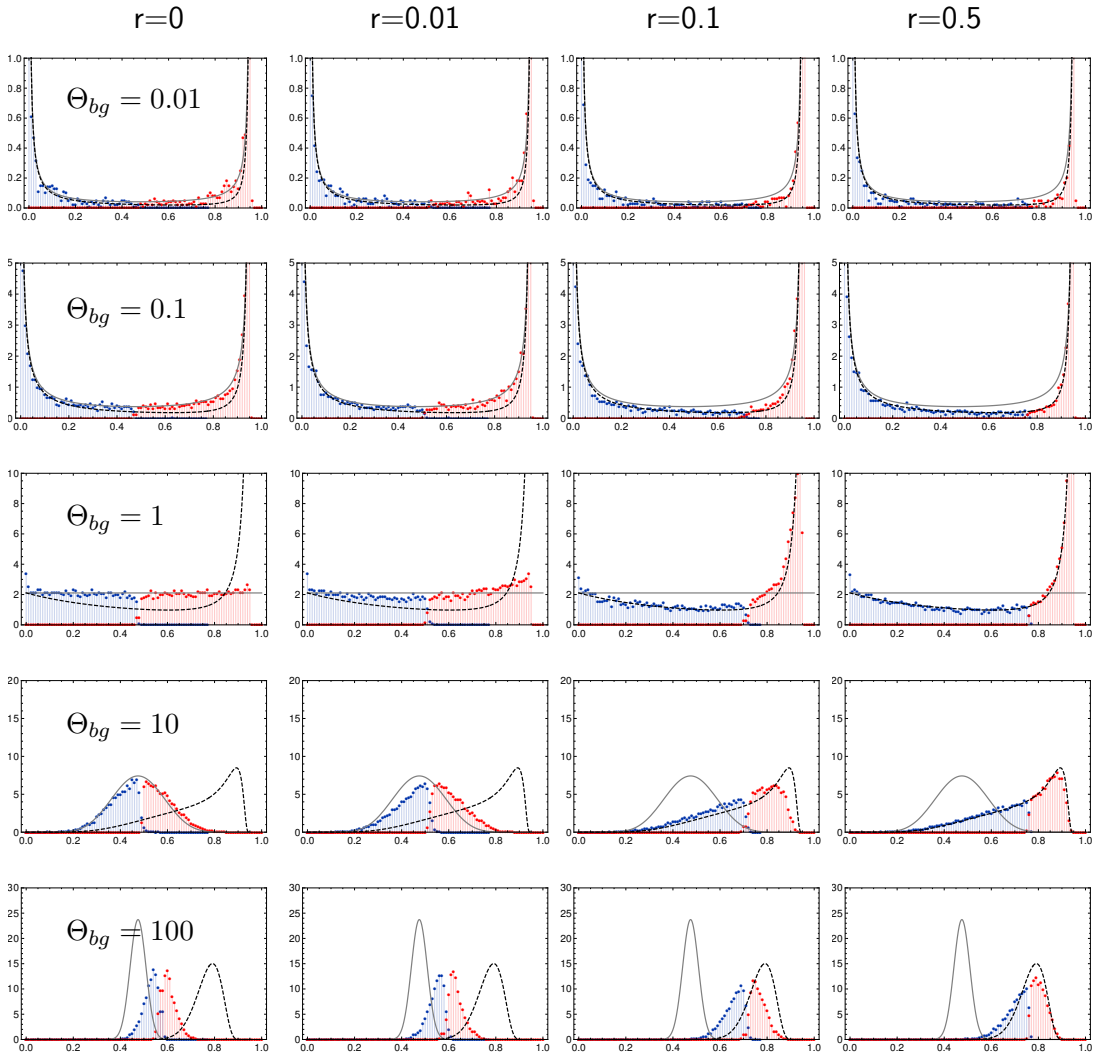

Figure C.2: **Genetic architecture of adaptation with linkage.** Marginal distributions for the major locus (red) and the minor locus (blue) of a model with $L = 2$ loci depending on Θ_{bg} (rows) and linkage among the loci (columns). Black lines show the analytical approximations for LE (dashed) and complete linkage (solid). For strong recombination $r \geq s_b = 0.1$, the deviations from the LE approximation are small. For $r \ll s_b = 0.1$, the approximation for complete linkage works well. Further parameters: $-s_d = s_b = 0.1$, $N_e = 10\,000$, $10\,000$ replicates.

C.2.1 Extended Yule framework

The Yule process that describes the stochastic phase of the adaptive process accounts for the mutant copies at all loci that are destined for establishment. In our framework so far (see the Mathematical Appendix D.2), we have started this process with zero

copies. SGV due to mutation-selection-drift balance can still be produced by such a process if it is started at some time in the past ($t < 0$). For general starting frequencies, we can alternatively start this process at time $t = 0$, but with mutant copies (immortal lineages) already present. Suppose that the mutant frequency at locus i at time $t = 0$ is p_i, corresponding to $N_e p_i$ mutant copies. Of these, only the $n_i < N_e p_i$ "immortal" mutants (destined for establishment) are included in the Yule process. Assuming an independent establishment probability p_{est} per copy, n_i is binomially distributed with parameters $N_e p_i$ and p_{est}. For the limit distribution of a multi-type Yule process that is started with a non-zero number of lines, consider that each of these initial lines can be understood as an extra source of new immortal lines (due to birth) that is entirely equivalent to the generation of new lineages by mutation. It is therefore appropriate to include these lines as *extra locus mutation rate*

$$\tilde{\Theta}_i = \Theta_i + n_i = 2N_e\mu_i + n_i\,. \tag{C.2}$$

In the absence of recurrent mutation, $\Theta_i = 0$, this procedure reproduces the well-know Polya urn scheme (*e.g.* Griffiths and Tavaré, 1998); Hoppe urn: Hoppe (1984)). Replacing Θ_i by $\tilde{\Theta}_i$ within our original Yule process formalism, and averaging over the binomial distribution, leads to the desired extension to arbitrary starting frequencies.

C.2.2 Application

Theory papers (*e.g.* Orr and Betancourt, 2001; de Vladar and Barton, 2014; Jain and Stephan, 2015, 2017) often use a deterministic framework to describe the frequency of alleles that segregate in a population in mutation-selection balance. To simplify the analysis, they do not model SGV as a distribution (due to mutation, selection, and drift), but replace this distribution by its expected value (ignoring drift). We can apply our scheme with fixed starting frequencies to this case and thus assess the effect of genetic drift in the starting allele frequency distribution. We assume equal loci and a starting

frequency $|\mu_l/s_d|$ for an (initially deleterious) mutant allele with selection coefficient s_d in the mutation-selection balance. Fig. C.3 shows the simulated marginal distributions of the loci with the largest contribution to the adaptive response (compare Fig. 3.4). We see that the type of the adaptive architecture is again constant across rows with equal background mutation rate. However, due to the more homogeneous starting conditions, adaptation involves more loci and is much more shift-like. Analytical predictions following the above scheme are shown for $L = 2$ loci. With establishment probability $p_{\text{est}} = 2s_b$, the counts n_1 and n_2 of "immortal" mutants at both loci are independent random draws from a Binomial distribution with parameters $N_e|\mu_l/s_d| = |\Theta_l/2s_d|$ and $2s_b$. For $\Theta_{bg} \geq 0.1$, we find (heuristically) that the marginal distribution for alleles starting from mutation-selection balance closely matches the one of the fully stochastic model with effective $\Theta_{bg}^{\text{eff}} = \Theta_{bg}(1 + |s_b/2s_d|) = 51\Theta_{bg}$ for the parameters in the figure (lines added in green). (Note that, from the average number of established lines, one would assume $\Theta_{bg}^{\text{eff}} = \Theta_{bg}(1 + |s_b/s_d|) = 101\Theta_{bg}$. However, this does not account for the variance in the number of immortal lines among the two loci.)

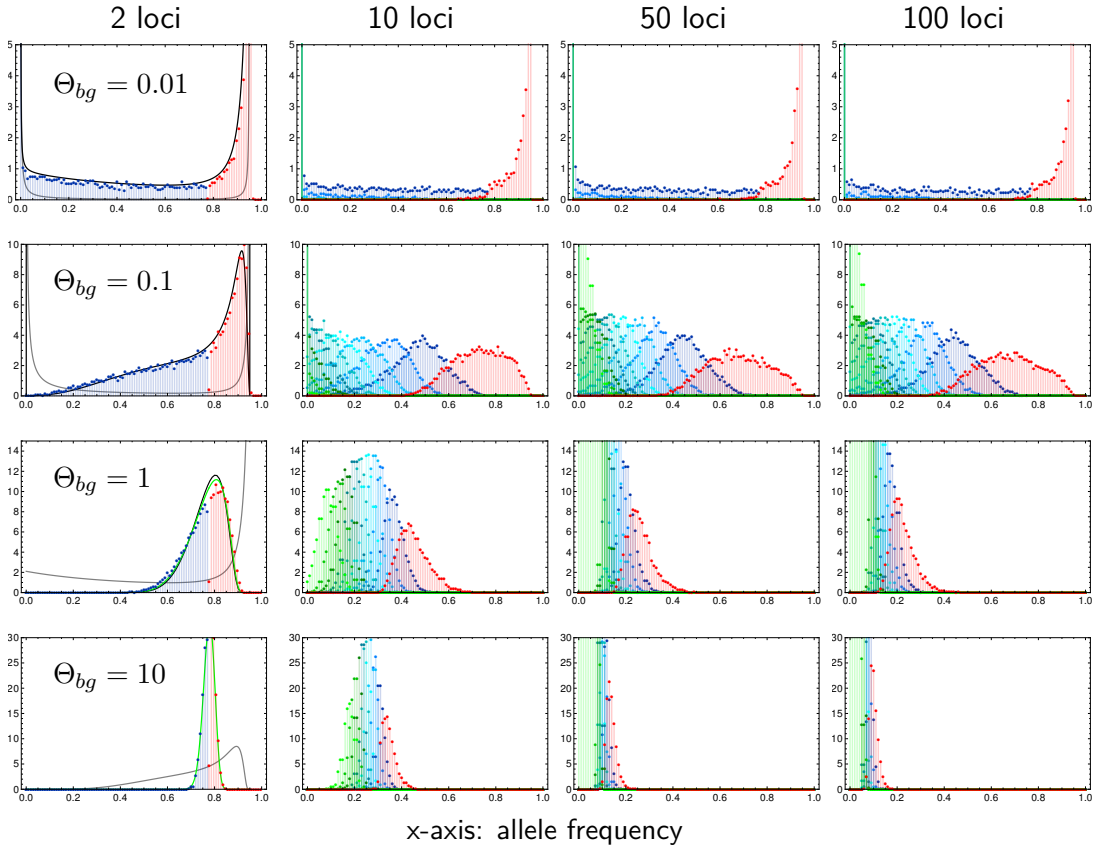

Figure C.3: **Polygenic adaptation from alternative allele starting frequencies.** The panels show the adaptive architecture when mutant alleles start from their expected value in mutation-selection balance, without drift. We distribute $L \cdot |\Theta_l/2s_d|$ mutant copies as evenly as possible across all loci. We set $-s_d = s_b/100 = 0.001$. Black lines for $L = 2$ loci show analytical predictions described in the main text (only computationally possible for $\Theta_{bg} \leq 1$), green lines for $\Theta_{bg} \geq 1$ show the heuristic prediction for $\Theta_{bg}^{\text{eff}} = 51\Theta_{bg}$. Finally, gray lines show the marginal distributions when adaptation occurs from mutation-selection-drift balance, compare Fig. 3.4.

C.3 Diploids

To extend our model to diploids, we assume that a single locus that is *homozygous* for the mutant allele is sufficient to produce the fully functional mutant phenotype, while a *heterozygous* locus produces a mutant that is functional with probability $1 - h$. We assume that mutants contribute independently. Thus, if k heterozygous loci exist, but no homozygous mutant locus, the resulting mutant phenotype will be functional with probability $1 - (1 - (1 - h))^k = 1 - h^k$. For $L = 2$ loci, in particular, the (logarithmic)

fitness of genotype G becomes

$$w(G) = \begin{cases} 0 & \text{no mutations: } G = (aabb) \\ (1-h)s & \text{1 heterozygous locus: } G = (Aabb, aaBb) \\ (1-h^2)s & \text{2 heterozygous loci: } G = (AaBb) \\ s & \geq \text{1 homozygous mutation: } G = (AA.., ..BB) \end{cases}, \tag{C.3}$$

where $s = s_b > 0$ for $t \geq 0$ and $s = s_d < 0$ for $t < 0$. Note that $h \in [0, 1]$ measures the dominance of the *ancestral* allele. We assume Hardy-Weinberg-linkage-equilibrium (HWLE). In this case, the marginal fitnesses of the mutant alleles are (for 2 loci),

$$w_A^* = s - (1-p_A)(1-p_B)\Big[1 - p_B(1-2h)\Big]hs, \tag{C.4a}$$

$$w_B^* = s - (1-p_A)(1-p_B)\Big[1 - p_A(1-2h)\Big]hs. \tag{C.4b}$$

In contrast to the haploid case, the marginal fitnesses are in general *not* equal. There are, however, two important special cases, where our fitness scheme (with redundancy on the level of loci) implies equal marginal fitnesses (and thus redundancy on the level of alleles): either if the ancestral allele is fully recessive ($h = 0$) or if the alleles are co-dominant ($h = 0.5$). As shown in the Mathematical Appendix, this holds true more generally for an arbitrary number of loci.

Simulation results

We simulated a diploid model with two loci in HWLE according to the above scheme with three different levels of dominance of the ancestral allele, $h = 0.1; 0.5;$ and 0.9. The diploid, effective population size is N_e, corresponding to $2N_e$ chromosomes. The mutation rate is μ at both loci and we define the population-scaled mutation rate for diploids as $\Theta_l^d = \Theta_{bg}^d = 4N_e\mu$. Simulations are stopped when the percentage of remaining ancestral *haplotypes* drops below $f_w = 0.05$. (This condition directly corresponds

to the stopping condition for haploids. Alternative stopping conditions, such as 95% increase in mean diploid fitness are also covered by our theoretical framework, but require a different transformation.)

The results are shown in Fig. C.4. We see that the haploid results fully carry over to diploids for co-dominance ($h = 0.5$, middle column), where the diploid fitness scheme implies redundancy on the level of alleles. As explained above, the same holds true if the ancestral allele is fully recessive. Our simulations show that the haploid result is still a good approximation for $h = 0.1$ (left column). In contrast, much larger deviations are obtained for recessive mutants (dominant ancestral allele, $h = 0.9$, right column). In this case, the locus with the larger mutant frequency experiences stronger selection. For $\Theta_l \geq 0.1$, when polymorphism at both loci is likely, this favors the major locus relative to the minor locus, increasing the heterogeneity in the adaptive architecture.

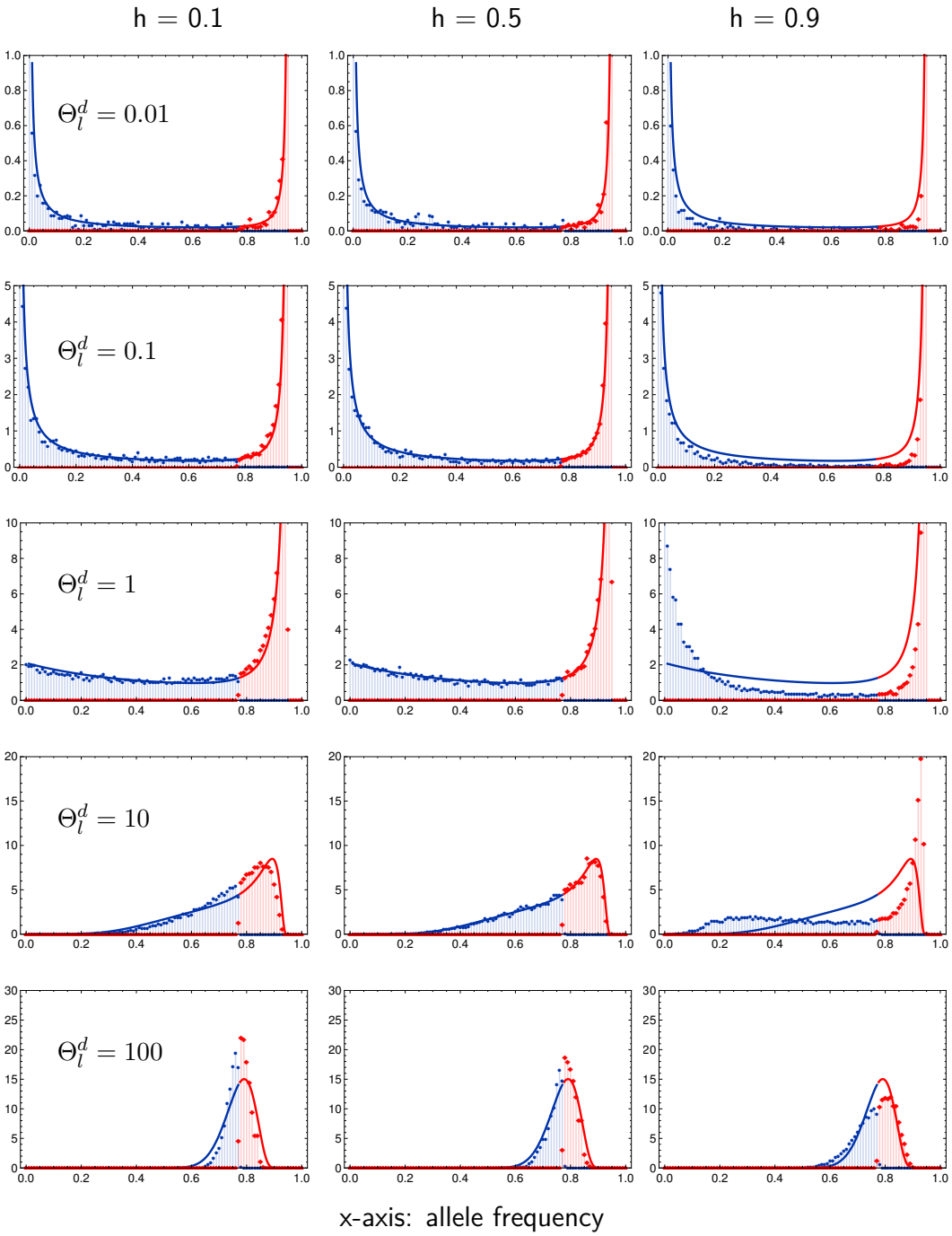

Figure C.4: **Adaptive architecture for diploids in linkage equilibrium.** Adaptation in a 2-locus model according to scheme (C.3), with recessive ($h = 0.1$), codomiant ($h = 0.5$) or dominant ($h = 0.9$) ancestral alleles. We assume Hardy-Weinberg and linkage equilibrium. Simulations are stopped when the wild type haplotypes drops below 5%. Standing genetic variation builds up for $16N_e$ generations before the change in the environment. Selection coefficients are set to $s_b = -s_d = 0.1$. Solid lines show analytical predictions using the framework developed for haploids.

C.4 Approximations for multi-locus architectures

For tight linkage, where the joint distribution of mutant alleles is given by a Dirichlet distribution, Mathematical Appendix Eq. (D.29), lower dimensional marginal distributions for single loci or groups of loci can easily be derived. For linkage equilibrium, Mathematical Appendix Eq. (D.20), however, the required integrals can only be solved numerically. For L loci, an $(L-2)$-dim integral needs to be evaluated, which becomes computationally unfeasible (with programs packages like *Mathematica*) for $L > 5$. Nevertheless, we can derive approximations for the marginal distributions of polygenic models with large L in many cases. To do so, we make use of a key property of the adaptive architecture, shown in our results: The (joint) architecture of adaptation at loci with the largest contribution to the adaptive response is primarily a function of combined mutation rates at competing loci, such as the background mutation rate Θ_{bg}. Given these values, it is largely independent of the number of loci in the genetic basis of the trait itself. We can therefore describe the adaptive architecture of a polygenic trait with L loci by a model with $k < L$ loci *given that* the total adaptive response is well captured by the contribution of the top k loci. It turns out that this is typically the case for $\Theta_{bg} < 1$, when the contributions from different loci are very heterogeneous. In the following, we describe this procedure for an L-locus model with equal mutation rates $\Theta_i = \Theta_l$ for $1 \leq i \leq L$.

Approximations using the 2-locus model

Several key properties of the L-locus architecture can already be described by the 2-locus framework. This includes the marginal distributions at the major locus and at the first minor locus. This requires that the mutation rate at the minor locus of the 2-locus model matches the background mutation rate of the L-locus model. As described in the main text, this choice matches the time lag between the first origin of a mutation destined for establishment at a locus (usually the major locus) and at a second locus

(usually the first minor locus). It also guarantees that the approximation captures the correct asymptotic shape of the major-locus distribution at $p = 1 - f_w$, and of the first-minor-locus distribution at $p = 0$. The choice of the mutation rate at the major locus itself is far less important. For the approximation of the major locus distribution, we find that setting it to the locus-mutation rate yields the best fit. We thus use a 2-locus model with unequal mutation rates, $\mathsf{P}^{1>}_{f_w}[p_1|\Theta_l, \Theta_{bg}]$, Eq. (D.28a), in Fig. 3.4. For the marginal distribution at the first minor locus, the approximation with equal mutation rates, $\mathsf{P}^{1<}_{f_w}[p_1|\Theta_{bg}, \Theta_{bg}]$, Eq. (D.28b), works slightly better. Finally, we can also approximate the distribution at an *average* minor locus (rather than the first minor locus) by $\mathsf{P}^{1<}_{f_w}[p_1|\Theta_l, \Theta_{bg}]$.

Approximations using models with $k \geq 2$ loci

The approximation of higher-order minor loci requires models with a sufficiently large genetic basis that such a locus exists at all. *I.e.* a k-locus model can approximate marginal distributions up to the $(k-1)$st minor locus. Assume that we want to approximate the marginal distribution of the jth minor locus of an L-locus model using a k-locus model, $j < k < L$. As for the case $k = 2$ discussed above, the approximation requires that the expected lag time between the establishment of a mutation at a first locus and the establishment of a mutation at a jth locus be matched. For the L-locus model, this waiting time is

$$\frac{1}{\Theta_l} \sum_{i=1}^{j} \frac{1}{L-i} \,.$$

For a k-locus model with equal mutation rate $\Theta_l^{(k)}$ at all loci, we thus obtain the matching rule

$$\Theta_l^{(k)} = \Theta_l \frac{\sum_{i=1}^{j} \frac{1}{k-i}}{\sum_{i=1}^{j} \frac{1}{L-i}}$$

for the approximation of the jth minor locus. For $j = 1$, this reproduces the matching

rule for the background mutation rate Θ_{bg}. In general, the value for Θ_l^k depends on j, but converges once $L, k \gg j$. Approximations by models with unequal locus mutation rates are also possible, but usually do not lead to a relevant improvement. In Fig. 3.4, we use formulas from 3- and 4-locus models to approximate the marginal distributions of the 2nd and 3rd minor locus, respectively. In general, the approximations for all loci can be improved by using approximation models with more loci than required, i.e. $k > j+1$. In Fig. C.5, we show this for approximations of the major locus and the first three minor loci, all derived from a 4-locus model.

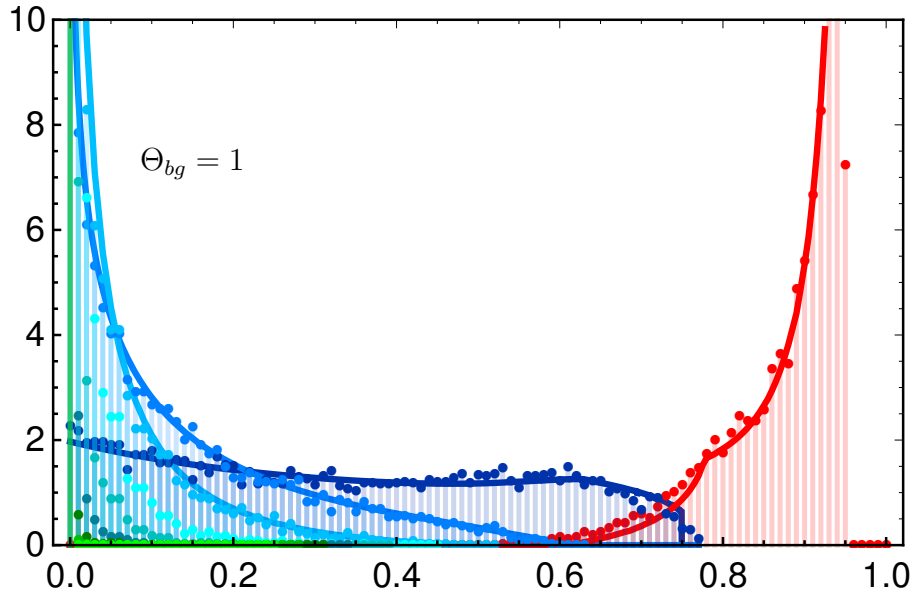

Figure C.5: **Approximating higher dimensional adaptive architectures for 10 loci, $\Theta_{bg} = 1$.** We approximate a 10 locus model with the theoretical predictions based on the four locus model for the major and the first, second and third minor locus. Compare Fig. 3.4, where we use approximations based on the minimal number of loci needed.

C.4.1 Marginal distribution of a single locus

Figure C.6 shows the marginal distribution at a single focal locus for a trait with $L = 2$ to $L = 100$ loci in its basis. Since all loci are equal, the probability that the focal locus ends up as the major locus is $1/L$. The red dots in the figure indicate the part of the marginal distribution that corresponds to this case. With an increasing number of redundant loci, the probability for each single locus to play a major role in the adaptive

process decreases. The marginal distribution of a fixed locus therefore changes strongly with an increasing number of loci L. For large L, in particular, it does not represents the key components of the adaptive architecture on the level of the trait any more. This is in contrast to Fig. 3.4, where marginal distributions of the loci with the largest contributions to the adaptive response are shown. For 2 loci, Fig. C.6 also shows the analytical approximation for the marginal distribution Eq. (3.11). As long as the adaptive architecture is dominated by only a few loci, the same 2-locus result can be used as an approximation for the marginal distribution in models with more than two loci. This is shown in the figure for $\Theta_{bg} \leq 1$. The figure also shows that the approximation fails for $\Theta_{bg} \geq 10$ when adaptation is truly collective.

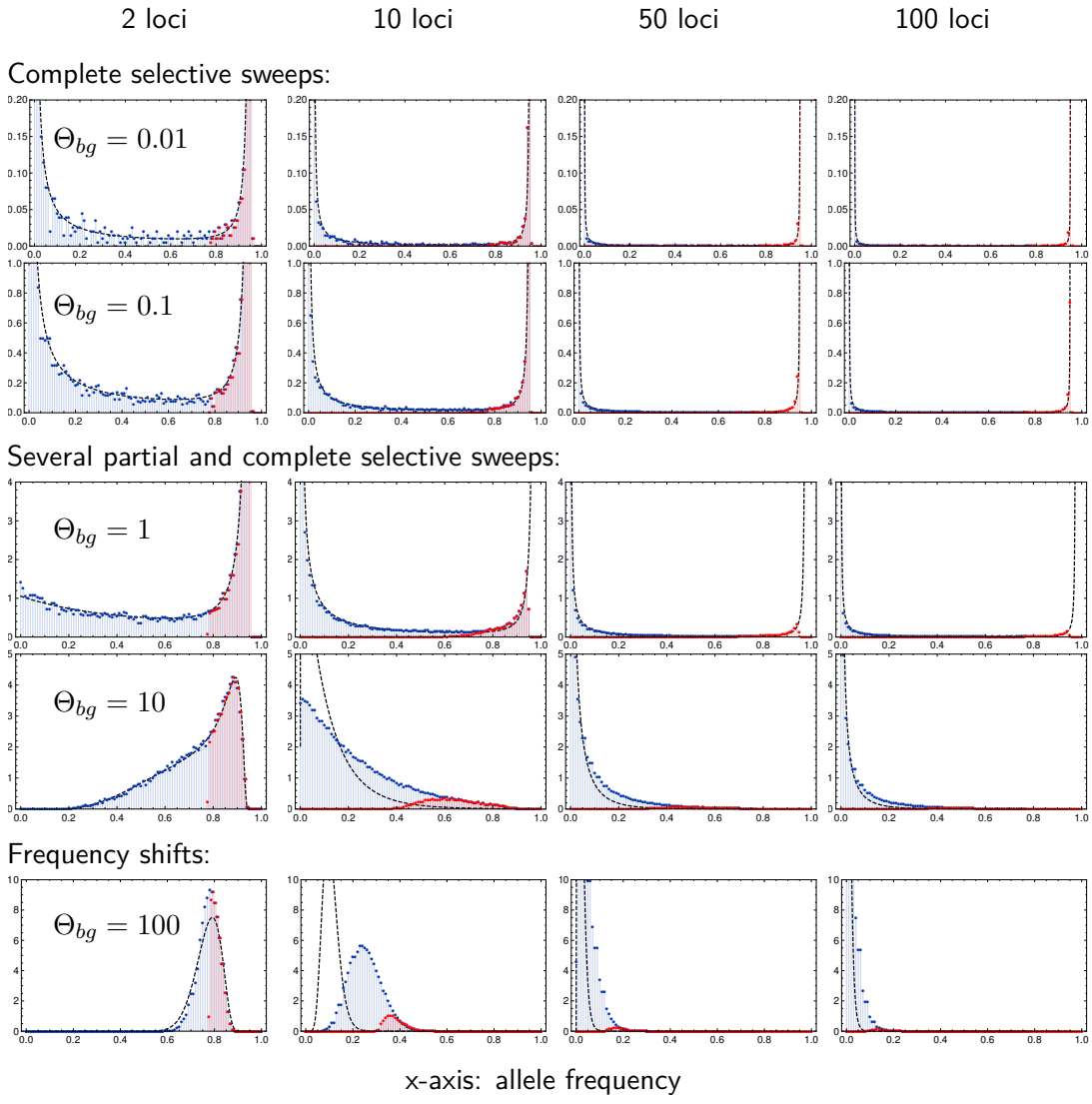

Figure C.6: **Marginal distribution at a single focal locus.** Simulation results for the marginal distribution at a single locus at the end of the adaptive phase are shown in blue. Red dots show the contribution of the major locus to this distribution (all cases, where the focal locus ends up as the major locus). Dashed lines show the analytical prediction for the 2-locus model, Eq. (3.11). Parameters and further details as in Fig. 3.4.

Acknowledgments

First, we want to thank Claus Vogl for his insightful comments and several fruitful discussions. We also thank Matthias Maschek for his help concerning programming and simulation setup. Finally, a special thank you goes to Montgomery Slatkin for his hospitality in welcoming JH and IH to his lab at UC Berkeley, where this project was started.

Data Archiving

We will provide a comprehensive *Mathematica* Inc. notebook, showing visualizations of the derived analytical predictions. The simulation code will be made available through the Dryad repository as a package upon publication.

Höllinger I, Pennings PS, Hermisson J. Data from: Polygenic adaptation: From sweeps to subtle frequency shifts. Dryad Digital Repository.

https://doi.org/10.5061/dryad.7n6vg10

Funding

IH was funded by the Austrian Science Fund (FWF): DK W-1225-B20, Vienna Graduate School of Population Genetics.

D. Supporting Information: Mathematical Appendix

This Appendix describes the details of the mathematical model and methods used to derive the analytical results of the article. Section D.1 gives an outline of the model; section D.2 introduces the branching process method used for the early stochastic phase of polygenic adaptation; section D.3 describes the derivation of the joint frequency distribution at the end of the deterministic phase.

D.1 Redundant trait model

Consider a panmictic population of N_e haploids. Selection acts on a binary trait Z (*e.g.* resistance) with just two states, a wild-type state Z_0 (not resistant) and a mutant state Z_1 (resistant). Without restriction, we can choose $Z_0 = 0$ and $Z_1 = 1$. Malthusian (logarithmic) fitness is defined by the function

$$W(Z,t) = s(t)Z \tag{D.1}$$

where the time dependent coefficient $s(t)$ defines the strength of directional selection. We assume that $s(t) < 0$ for $t < 0$, but $s(t) > 0$ for $t > 0$, such that the optimal trait value shifts from the wild-type state $Z = 0$ to the mutant state $Z = 1$ due to some change in the environment at time $t = 0$. We also assume that selection is stronger than drift, $|Ns(t)| \gg 1$ for almost all t, but is arbitrary otherwise.

We assume that Z is polygenic, with L biallelic loci (wild-type a_i and mutant allele A_i, $i = 1, \ldots, L$) constituting its genetic basis. While genotype $\mathbf{a} = (a_1, a_2, \ldots, a_L)$ produces the ancestral wild-type Z_0, all mutant genotypes are fully redundant and produce the mutant phenotype Z_1, independently of the number of mutations. New mutations from a_i to A_i occur at a rate μ_i per generation, with $\mu_i \ll |s(t)|$ for almost all t. For the purpose of our model, back mutation from A_i to a_i can be ignored. The linkage map among loci is arbitrary – unless explicitly specified otherwise. Let p_i be the frequency

of allele A_i, and let f_a be the frequency of the wild-type genotype $\mathbf{a}$. Then the mean fitness in the population is

$$\bar{W}(t) = s(t)\bar{Z}(t) = s(t)\left(f_a Z_0 + (1 - f_a)Z_1\right) \tag{D.2a}$$

where $\bar{Z}$ is the trait mean. Since $W(Z_1, t) = s(t)Z_1$ is the marginal fitness of any mutant allele, the selection dynamics at the ith locus can be expressed as

$$\dot{p}_i = p_i\Big(W(Z_1, t) - \bar{W}(t)\Big) = s(t)p_i\Big(Z_1 - \bar{Z}(t)\Big)\,. \tag{D.2b}$$

Our redundancy assumption implies strong diminishing returns epistasis on the level of fitness: the fitness of genotypes with multiple mutations is the same as the one of single mutants. Eq. D.2b shows that the epistatic effect of the genetic background on the dynamics at a particular locus is mediated by the trait mean $\bar{Z}(t)$ as single compound parameter. Allele frequencies at all loci change with the same (time and frequency-dependent) rate. We readily establish that

$$\frac{d}{dt}\left(\frac{p_i}{p_j}\right) = \frac{\dot{p}_i p_j - \dot{p}_j p_i}{p_j^2} = 0\,. \tag{D.3}$$

Thus, the ratio of allele frequencies among loci does not change under selection. Note that this holds for an arbitrary linkage map. We can conclude that any differences in (relative) allele frequencies are due to mutation and drift.

We are interested in the pattern of allele frequency changes across loci during the phase of rapid phenotypic adaptation. This phase starts with the onset of positive selection on derived alleles at time $t = 0$. It ends when mean fitness $\bar{W}(t)$ approaches its maximum $s(t)Z_1$ and further selective change in the allele frequencies is strongly decelerated. Since $(W(Z_1, t) - \bar{W}(t))/s(t) = (Z_1 - Z_0)f_a$, we can parametrize this end point by a condition $f_a(t) = f_w$ on the frequency of the wild-type Z_0 in the population. In our figures, we usually use $f_w = 0.05$. As initial state at time $t = 0$, we assume that

the population adapts from a balance of mutation, selection, and drift. We thus allow for standing genetic variation (SGV) at all loci. If selection prior to $t = 0$ is constant (which is what we generally assume in our computer simulations, see main text), SGV is given by the standard equilibrium distribution under mutation, selection, and drift, where we require that a_i is the ancestral state at each locus. I.e., each allele frequency trajectory $p_i(t)$, back in time, originates from the boundary $p_i = 0$ rather than $p_i = 1$ (see also Hermisson and Pennings, 2005, for this concept). However, our analytical results do not require a static equilibrium and, for a general $s(t) < 0$ for $t < 0$, the SGV reflects this non-equilibrium dynamics.

As described in the main text, we dissect the adaptive process into two phases. During an initial *stochastic phase* mutation, selection, and drift lead to the build-up of genetic variation, either from SGV or due to new mutation after time $t = 0$, as long as allele frequencies p_i at all loci are still low. We will describe our approach to this phase in detail in the section on Yule processes below. Once allele frequencies are sufficiently large, genetic drift and recurrent new mutation play only a minor role relative to selection until we reach the end of the rapid adaptive phase. We thus enter a *deterministic phase* where the dynamics is then well approximated by Eq. (D.2b).

D.1.1 Relaxed redundancy

To relax the stringent redundancy condition of our model, it is natural to assume that a single mutation is not sufficient to produce the full mutant phenotype $Z_1 = 1$, but only a partial phenotype $Z_q = q$ with $0 < q < 1$. This makes the marginal fitness of mutant alleles dependent on the genetic background. If genotypes with two or more mutations produce Z_1, we have

$$\dot{p}_i = \Big(W_i(t) - \bar{W}(t)\Big)p_i = s(t)p_i\left(Z_1 - \bar{Z}(t) - (Z_1 - Z_q)\frac{f_i}{p_i}\right) \tag{D.4}$$

where f_i is the frequency of the haplotype with a single mutation at locus i. Since f_i/p_i depends on i (even in linkage equilibrium), the ratio of allele frequencies at different loci is no longer invariant and the key symmetry assumption Eq. (D.3) of the fully redundant model is violated. Note that redundancy is recovered for very low mutant frequencies, such that double mutants are rare ($f_i \approx p_i$) and also late in the adaptation process, when most haplotypes carry at least one mutation and $f_i \to 0$.

D.1.2 Diploids

We can generalize the redundant trait model to diploids as follows. For a general model, the dynamical equations in continuous time read

$$\dot{p}_i = \Big(W_i(t) - \bar{W}(t)\Big)p_i \tag{D.5}$$

where $W_i(t)$ is the marginal fitness of allele A_i and $\bar{W}(t)$ the mean fitness. All fitnesses may depend on the allele frequencies and on time. Using Eq. (D.3), we see that all mutant alleles A_i are redundant in the sense that they all feel the same selection pressure if and only if their marginal fitnesses are equal at all times, $W_i(t) = W_j(t)$, $\forall\ i, j$. (The same condition can also be derived from a discrete time dynamics.) For haploids, equal marginal fitnesses, independently of the genetic composition of the population, enforces the fully redundant trait model described above. For diploids with dominance, the marginal fitness also depends on the allele frequency at the focal locus itself. An obvious solution to the condition of equal marginal fitnesses across loci is the case of complete dominance of the mutant allele. We can gain some more flexibility for the fitness scheme, if we assume that genotype frequencies are at Hardy-Weinberg equilibrium at all times. We can then distinguish three genotype classes: the wild-type without any mutations (normalized fitness 0), mutant individuals with one or more mutations on only a single haplotype (fitness $s_1(t)$) and individuals with mutations on both haplotypes (fitness

$s_2(t)$). The marginal fitness of any mutant allele then is

$$W_i(t) = s_1(t) f_a + s_2(t)(1 - f_a)\,, \tag{D.6}$$

where f_a is the frequency of the ancestral haplotype without mutations. We thus require redundancy of mutations (only) within haplotypes. Note, however, that this fitness scheme implies a position effect, i.e., the fitness of the genotype does not only depend on the number of mutations at each locus, but also on the association of mutations to one or the other haplotype. If we assume linkage equilibrium in addition to Hardy-Weinberg proportions, a position effect can be avoided if we use the following fitness scheme

1. The ancestral genotype without any mutants has normalized fitness $W(t) = 0$,
2. any genotype with at least one homozygous mutant has fitness $W(t) = s_2(t)$,
3. a genotype without a locus that is homozygous for the mutant, but with k loci that are heterozygous has fitness

$$W(t) = s_2(t) + 2^{1-k}\Big(s_1(t) - s_2(t)\Big)\,.$$

Since 2^{1-k} is the probability for any focal mutant allele to be on the same haplotype with all $k-1$ other mutant alleles, assuming linkage equilibrium, this fitness scheme leads to the same marginal fitness as Eq (D.6) above.

D.2 Yule approximation

We describe the dynamics of mutant types at the different loci during the stochastic phase by a *multi-type Yule pure birth process with immigration*. Our framework builds on established mathematical theory by Joyce and Tavaré (1987); Durrett (2010) and a previous approach to describe the genealogy of a beneficial allele during a selective

sweep in terms of a Yule process (Etheridge et al., 2006; Hermisson and Pfaffelhuber, 2008). Here, we extend this approach to the polygenic scenario.

Consider a mutation A_i that appears at some locus either prior to the environmental change (standing genetic variation) or after the change. This mutation is relevant for the joint distribution of mutant allele frequencies at the time of observation after the rapid adaptive phase if and only if descendants of this mutation still segregate in the population at this time. The idea of the Yule approach is to construct the genealogies of these mutant descendants at all loci forward in time. We start the process at some time $t_0 \ll 0$ in the past before the first mutation with surviving descendants has originated. We assume that the frequency p_i of mutant alleles is low during the entire stochastic phase. Then, new mutations at locus i appear at rate $\approx N\mu_i =: \Theta_i/2$ per generation, but only a fraction of those will survive deleterious selection prior to $t = 0$ and genetic drift to establish in the population and to contribute to the adaptation of the trait. We denote this establishment probability as $p_{\mathsf{est}}(t)$. If selection is constant and positive (as assumed in the main text), $s(t) = s_b > 0$, we can approximate $p_{\mathsf{est}} \approx 2s_b$. For general time-dependent selection, $p_{\mathsf{est}}(t)$ will depend on $s(\tilde{t})$ with $\tilde{t} \geq t$ Uecker and Hermisson (2011), and also on the mutations that were previously established at the same or at other loci. Crucially, however, since the marginal fitness of mutant copies at all loci is the same at any given time, $p_{\mathsf{est}}(t)$ does not depend on the locus. We only include mutants into our Yule process that successfully establish in the population, which are represented as "immortal lineages" in the Yule tree. We follow these lineages in continuous time. There are then two types of events:

1. First, new mutation creates new immortal lineages at rate

$$p_{\mathsf{mut},i}(t) = \frac{\Theta_i}{2}\, p_{\mathsf{est}}(t) \tag{D.7}$$

independently at each locus. This event is called "immigration" in the mathematical literature Joyce and Tavaré (1987), but it corresponds to mutation in our

model. (In a model with gene flow, where adaptation in a local deme occurs from immigration, new lines would be truly immigrants, see also Pennings and Hermisson (2006) for this analogy).

2. Second, existing immortal mutant alleles A_i can give birth to further immortal mutant copies, corresponding to a split of the immortal line in the Yule process. To derive the split rate p_{split}, imagine that we implement the evolutionary dynamics as a continuous-time Moran model, where individuals give birth (due to a binary split) at constant rate one per generation. In the corresponding Yule process, we only include this birth event if it leads to two immortal lineages. Obviously, the probability to "be immortal" for a newborn individual is the same as for a new mutation and given by $p_{\text{est}}(t)$. Conditioning on the fact that we only consider splits of immortal lineages and thus at least one of the offspring lineages must be immortal, we arrive at a split rate per immortal lineage of

$$p_{\text{split}}(t) = \frac{p_{\text{est}}^2(t)}{p_{\text{est}}^2(t) + 2p_{\text{est}}(t)(1 - p_{\text{est}}(t))} = \frac{p_{\text{est}}(t)}{2 - p_{\text{est}}(t)} \approx \frac{p_{\text{est}}(t)}{2}\,, \tag{D.8}$$

where the approximation in the last term assumes that $p_{\text{est}}(t) \ll 1$, which is usually the case unless selection is very strong.

The Yule process defines a continuous-time Markov process of a random variable $\mathbf{k} = (k_1, \ldots, k_L)$, where $k_i \in \mathbb{N}_0$ is the number of immortal mutant lineages at the ith locus. We are interested in the relative proportions in the number of lineages k_i across loci after a sufficiently long time – assuming that the distribution of these proportions reaches a limit by the end of the stochastic phase. We can generate this distribution from the transition probabilities among Yule states (the embedded jump-chain of the continuous-time process). If there are currently $(k_1, \ldots, k_L)$ lineages at the L loci, the probability that the next event is either a birth event (split) or a new mutation (immigration) at

locus i is

$$\begin{aligned}\mathsf{Pr}[(k_1,\ldots,k_L)\to(k_1,\ldots,k_i+1,\ldots,k_L)]\\ =\frac{k_i p_{\mathsf{split}}+p_{\mathsf{mut},i}}{\sum_{j=1}^{L}(k_j p_{\mathsf{split}}+p_{\mathsf{mut},j})}=\frac{k_i+\Theta_i}{\sum_{j=1}^{L}(k_j+\Theta_j)}\,.\end{aligned}\tag{D.9}$$

Crucially, these transition probabilities are constant in time and independent of the establishment probability $p_{\mathsf{est}}(t)$. As a consequence, they are also independent of the mutant fitness, which only affects the speed of the Yule process (via p_{est}), but not its sequence of events.

We start the process with no mutants and stop it whenever the number of mutants at one of the loci (e.g. locus 1) reaches some number $k_1 = n$. We are interested in the distribution of the number of mutants k_i at the other loci at this time, respectively their ratios k_i/n (remember that we already know that these ratios stay invariant during the deterministic phase of the adaptation process). We can prove the following

Theorem 1

In the limit of $n \to \infty$, the joint distribution of ratios $x_i = k_i/n$ of immortal mutant lineages across loci converges to the *inverted Dirichlet distribution*,

$$\mathsf{P}_{\mathsf{inDir}}[\{x_i\}_{i\geq 2}|\boldsymbol{\Theta}]=\frac{1}{B[\boldsymbol{\Theta}]}\prod_{j=2}^{L}x_j^{\Theta_j-1}\Big(1+\sum_{j=2}^{L}x_j\Big)^{-\sum_{j=1}^{L}\Theta_j}\tag{D.10}$$

where the vector $\boldsymbol{\Theta} = (\Theta_1,\ldots,\Theta_L)$ summarizes the mutation rates and $B[\boldsymbol{\Theta}]$ is the multivariate Beta function, which can be expressed in terms of Gamma functions as

$$B[\boldsymbol{\Theta}]=\frac{\prod_{i=1}^{L}\Gamma(\Theta_i)}{\Gamma(\sum_{i=1}^{L}\Theta_i)}\,.\tag{D.11}$$

Proof

We proceed in three steps.

Step 1 Assume that we stop the process when the first locus reaches $n > 0$ lineages. We derive the probability that the process at this time is in state $(n, k_2, \ldots, k_L)$ as follows. We need $n + k_2 + \cdots + k_L$ events (new mutations or splits) to generate all mutant individuals. The last event must occur at the first locus. All other events can occur in arbitrary order at the L loci. The probability of each realization (each order of events at the loci) is given by the corresponding product of transition probabilities (D.9). The key insight is that all realizations have the same probability. Indeed, the denominator of (D.9) does not depend on the locus where the next event occurs. Different realizations then only correspond to permutations in the factors $k_i + \Theta_i$ in the numerator of the product of transition probabilities. We can directly write down the probability for the state as

$$\mathsf{Pr}[\{k_i\}_{i\geq 2}|n, \boldsymbol{\Theta}] = \binom{n-1+k_2+\cdots+k_L}{n-1, k_2, \ldots, k_L} \frac{(\Theta_1)_{(n)} \prod_{j=2}^{L} (\Theta_j)_{(k_j)}}{(\Theta_1 + \cdots + \Theta_L)_{(n+k_2+\cdots+k_L)}}, \quad \text{(D.12)}$$

where

$$\Theta_{(k)} := \Theta(\Theta+1)\ldots(\Theta+k-1)$$

is the Pochhammer function. The leading multinomial coefficient counts the number of all permutations and the ratio of Pochhammer functions is the probability of each realization.

Step 2 We can rewrite (D.12) as a *Dirichlet-negative-multinomial* compound distribution, defined as

$$\int_0^1 \cdots \int_0^1 \binom{n-1+k_2+\cdots+k_L}{n-1, k_2, \ldots, k_L} \prod_{i=2}^{L} y_i^{k_i} \Big(1 - \sum_{i=2}^{L} y_i\Big)^n f(\{y_i\}_{i\geq 2}|\boldsymbol{\Theta})\, dy_2 \ldots dy_L\,, \quad \text{(D.13)}$$

where

$$f(\{y_i\}_{i\geq 2}|\mathbf{\Theta}) = \frac{1}{B[\mathbf{\Theta}]}\prod_{i=2}^{L} y_i^{\Theta_i-1}\Big(1-\sum_{i=2}^{L} y_i\Big)^{\Theta_1-1}$$

is the $(L-1)$-dimensional Dirichlet distribution for a L-dimensional probability vector $(y_1,\ldots,y_L)$ with constraint $y_1 = 1-\sum_{i\geq 2} y_i$. This is best shown in the reverse direction, i.e., by deriving (D.12) from (D.13). To see this, note that

$$\int_0^1 \ldots \int_0^1 \prod_{i=2}^{L} y_i^{\Theta_i+k_i-1}\Big(1-\sum_{i=2}^{L} y_i\Big)^{\Theta_1+n-1} dy_2 \ldots dy_L = \frac{\Gamma(\Theta_1+n)\prod_{i=2}^{L}\Gamma(\Theta_i+k_i)}{\Gamma\Big(\Theta_1+n+\sum_{i=2}^{L}(\Theta_i+k_i)\Big)}$$

because the integrand in this expression is just a Dirichlet density with shifted values of $\Theta_i \to \Theta_i + k_i$ and the right hand side is the corresponding normalization factor. Then using

$$\frac{\Gamma(\sum_{i=1}^{L}\Theta_i)}{\prod_{i=1}^{L}\Gamma(\Theta_i)}\frac{\Gamma(\Theta_1+n)\prod_{i=2}^{L}\Gamma(\Theta_i+k_i)}{\Gamma\Big(\Theta_1+n+\sum_{i=2}^{L}(\Theta_i+k_i)\Big)} = \frac{(\Theta_1)_{(n)}\prod_{j=2}^{L}(\Theta_j)_{(k_j)}}{(\Theta_1+\cdots+\Theta_L)_{(n+k_2+\cdots+k_L)}}$$

reduces (D.13) to (D.12).

The compound distribution Eq (D.13) can be interpreted as follows: If a random experiment can have a finite number of outcomes (here: mutant lineages at one of L loci), the negative multinomial distribution describes the probability to observe each of these events k_i times if we repeat the experiment until a focal event (here: new mutant lineage at the first locus) has occurred n times. While the negative multinomial distribution assumes that all outcomes occur with a fixed probability y_i, this probability is itself drawn from a Dirichlet distribution in the Dirichlet-negative-multinomial compound distribution. In the present context, the main advantage of (D.13) over (D.12) is that we can easily perform the limit $n \to \infty$ in this form.

Step 3 For large $n \to \infty$, the values of k_i/n, $i \geq 2$, of the negative multinomial distribution can be replaced by their expectations,

$$x_i := \mathsf{E}\left[\frac{k_i}{n}\right] = \frac{y_i}{1-\sum_{j=2}^{L} y_j} \;\Leftrightarrow\; y_i = \frac{x_i}{1+\sum_{j=2}^{L} x_j}\,.$$

We can then transform the density Eq. (D.10) from variables y_i to the x_i (representing the relative mutant frequencies). The entries of the Jacobian matrix (for $2 \leq i,j \leq L$) are

$$\mathbf{J}_{ij} = \frac{\partial y_i}{\partial x_j} = \frac{\delta_{i,j}(1+\sum_{k=2}^{L} x_k) - x_i}{(1+\sum_{k=2}^{L} x_k)^2}\,.$$

Since this is the sum of an identity matrix (times a factor) and a matrix with identical columns we can easily derive the eigenvalues and thus the determinant,

$$\mathsf{Det}[\mathbf{J}] = \frac{1}{(1+\sum_{k=2}^{d} x_k)^L}\,.$$

Applying this transformation to (D.13), we obtain Eq. (D.10).

Remarks

1. For two loci, the Dirichlet-negative-multinomial distribution (D.13) reduces to a *Beta-negative-binomial* distribution

$$\mathsf{P}_{\beta NB}[k|n] = \int_0^1 \binom{n+k-1}{k} y^k (1-y)^n \,\frac{\Gamma(\Theta_1+\Theta_2)}{\Gamma(\Theta_1)\Gamma(\Theta_2)}\, y^{\Theta_2-1}(1-y)^{\Theta_1-1}\,dy$$

   and the inverted Dirichlet distribution Eq. (D.10) simplifies to a so-called β-*prime* distribution,

$$\mathsf{P}_{\beta'}(x) = \frac{\Gamma(\Theta_1+\Theta_2)}{\Gamma(\Theta_1)\Gamma(\Theta_2)}\, x^{\Theta_2-1}\Big(1+x\Big)^{-\Theta_1-\Theta_2}\,. \tag{D.14}$$

   If we measure the ratio x always relative to the locus with the higher frequency, we obtain a conditioned distribution that is truncated at $x = 1$. For equal locus mutation rates $\Theta_1 = \Theta_2 = \Theta_l$, in particular,

$$\mathsf{P}_{\beta'}[x|\Theta_l] = \frac{2\Gamma(2\Theta_l)}{(\Gamma(\Theta_l))^2}\, x^{\Theta_l-1}(1+x)^{-2\Theta_l}. \tag{D.15}$$

with expectation

$$\mathbf{E}[x] = \int_0^1 x P_{\beta'}[x|\Theta_l]dx = \frac{2\Gamma(2\Theta_l)\,{}_2F_1[2\Theta_l, 1+\Theta_l, 2+\Theta_l, -1]}{(1+\Theta_l)(\Gamma(\Theta_l))^2}\,, \qquad \text{(D.16)}$$

where ${}_2F_1$ is the hypergeometric function.

2. The process described here is a variant of the *Polya urn* and *Hoppe urn* processes that are well-known in the mathematical literature and have been used to describe coalescent processes forward in time (Joyce and Tavaré, 1987; Durrett, 2010).

3. Our result Eq. (D.10) can also be seen as multi-locus version of Wright's formula for the stationary distribution of the Wright-Fisher diffusion (Wright, 1931). For L neutral alleles at a singe locus, and if the mutation rates Θ_i depend only on the target allele (house-of-cards condition), this is a Dirichlet distribution. Here, we see that an analogous result holds for a distribution of equivalent (mutually redundant) alleles across L loci. Although alleles at different loci cannot mutate into each other and are never identical by descent, it turns out that the genealogy in both models can be described by a Yule process with immigration. In contrast to the single-locus case, we obtain an *inverted* Dirichlet distribution for multiple loci. This difference results from a different stopping condition for the Yule process. For a single locus, the population size sets an upper bound for the total number of copies across all alleles. If we stop the process for a given total number n_{tot} of lines, we obtain the classical Dirichlet distribution in the limit $n_{\text{tot}} \to \infty$. In contrast, the population size defines a bound for mutants of a only single type in the multi-locus case, which is reflected by our choice of the stopping condition. This choice is appropriate unless all loci are tightly linked, as we will see below.

4. In our model, we did not distinguish different mutational origins of mutant alleles at the same locus. It is, in principle, possible to do so. For any single locus, the process *conditioned on* reaching some number of mutants k_i at this locus i

is entirely independent of the process at the other loci. The joint distribution of different mutational origins at this locus is therefore given by the Ewens sampling formula, as described in the theory of soft selective sweeps (Pennings and Hermisson, 2006; Hermisson and Pennings, 2017).

D.3 Allele frequency distributions

Eq. (D.10) predicts the distribution of allele frequency ratios x_i at the end of the stochastic phase of the adaptive process. Typically, the Yule process will approach convergence for $n \gtrsim 100$. In a large population, this still corresponds to a small allele frequency. However, since the allele frequency ratios remain constant also during the deterministic phase, we can use the Yule process result to derive the distribution of mutant allele frequencies also at a later stage, when (partial or complete) phenotypic adaptation has been achieved. As above, we characterize the time of observation via the frequency of the ancestral phenotypes f_w that is still found in the population. We treat the case of full adaptation, $f_w = 0$, before we turn to the case of a general f_w.

Complete phenotypic adaptation, $f_w = 0$

If selection is very strong, complete fixation of the mutant phenotype may be rapidly achieved. For any non-zero level of recombination among loci, $f_w = 0$ requires, in our model, that there is (at least) a single locus where the mutant allele has reached fixation. In the following, we will call the locus with the largest mutant frequency the *major locus* and all other loci *minor loci*. We are interested in the joint distribution of allele frequencies when the major locus has reached fixation. From Eq. (D.10), we can derive the probability that the first locus ends up being the major locus as

$$\mathsf{P}_{1>}^{(\boldsymbol{\Theta})} = \int_0^1 \dots \int_0^1 \mathsf{P}_{\mathsf{inDir}}[\{x_i\}_{i\geq 2}|\boldsymbol{\Theta}]\, dx_2 \dots dx_L\,. \tag{D.17}$$

Since allele frequencies p_i equal allele frequency ratios x_i relative to the major locus in this case, the joint distribution at all minor loci, $\{p_i\}_{i\geq 2}$, $0 \leq p_i \leq 1$, conditioned on fixation of the mutant allele at the first locus, follows as $\mathsf{P}_{\mathsf{inDir}}[\{p_i\}_{i\geq 2}|\boldsymbol{\Theta}]/\mathsf{P}_{1>}[\boldsymbol{\Theta}]$. The joint allele frequency distribution for all loci at $f_w = 0$ results as product of a Dirac point measure at the major locus and truncated inverted Dirichlet densities at the minor loci. Summing over all possible loci as major locus we obtain

$$\mathsf{P}_0[\{p_i\}_{i\geq 1}|\boldsymbol{\Theta}] = \sum_{k=1}^{L} \left(\frac{\delta_{p_k-1}}{B[\boldsymbol{\Theta}]} \prod_{j\neq k} p_j^{\Theta_j - 1} \Big(1 + \sum_{j\neq k} p_j\Big)^{-\sum_{j=1}^{L}\Theta_j} \right), \tag{D.18}$$

where the Dirac δ constrains the distribution to the boundary faces $p_k = 1$ of the L-dimensional hypercube $[0,1]^L$ of allele frequencies. Note that this formula is independent of linkage patterns as long as loci can recombine at all and are not completely linked (see below for this case).

Incomplete phenotypic adaptation, $f_w > 0$, linkage equilibrium

While the distribution of allele frequency *ratios* x_i, Eq. (D.10), holds for any time of observation during the adaptive process (once the Yule process has reached convergence), the corresponding distribution Eq. (D.18) for the *absolute* allele frequencies p_i holds only for complete phenotypic adaptation, $f_w = 0$. To derive this distribution for arbitrary $f_w \geq 0$, we need to translate the stopping condition for the ancestral phenotype to a condition on the p_i. For $f_w = 0$, this just leads to the condition $p_k = 1$ for the major locus, constraining the distribution Eq. (D.18) to the boundary faces of the allele frequency hypercube. Importantly, this constraint is independent of linkage. For $f_w > 0$, in contrast, any constraint on the distribution of the p_i due to the stopping condition will necessarily also depend on the linkage disequilibria. For further analytical progress we now assume that recombination is sufficiently strong that linkage disequilibria can be ignored. We then obtain

$$\prod_{j=1}^{L}(1-p_j) = f_w \tag{D.19}$$

and the joint allele frequency distribution is given by the following Theorem, which is our main analytical result.

Theorem 2

If the adaptive process is stopped at a frequency f_w of the ancestral phenotype in the population, and assuming linkage equilibrium among loci, the joint distribution of mutant frequencies on the L-dimensional hypercube is

$$\mathsf{P}_{f_w}[\{p_i\}_{i\geq 1}|\mathbf{\Theta}] = \frac{\delta_{\prod_{j=1}^{L}(1-p_j)-f_w}}{B[\mathbf{\Theta}]} \prod_{i=1}^{L} p_i^{\Theta_i-1} \left(\sum_{j=1}^{L} p_j\right)^{-\sum_{j=1}^{L}\Theta_j} \left(\sum_{j=1}^{L} \frac{f_w\, p_j}{1-p_j}\right), \quad \text{(D.20)}$$

where the δ-function restricts the support of $\mathsf{P}_{f_w}[\{p_i\}_{i\geq 1}|\mathbf{\Theta}]$ to the $(L-1)$-dimensional submanifold $\prod_{j=1}^{L}(1-p_j) = f_w$.

Proof

We can rewrite (D.19) as condition on the frequency p_1 at the first locus,

$$p_1 = 1 - \frac{f_w}{\prod_{j=2}^{L}(1-p_j)} \quad \text{(D.21)}$$

to obtain the transformation from frequency ratios x_i to absolute allele frequencies p_i, $i \geq 2$,

$$x_i = \frac{p_i}{p_1} = \frac{p_i \prod_{j=2}^{L}(1-p_j)}{\prod_{j=2}^{L}(1-p_j) - f_w}\,. \quad \text{(D.22)}$$

The corresponding Jacobian matrix reads $(2 \leq i,j \leq L)$

$$\begin{aligned}\tilde{\mathbf{J}}_{ij} = \frac{\partial x_i}{\partial p_j} &= \frac{p_i}{1-p_j} \frac{f_w \prod_{k=2}^{L}(1-p_k)}{(\prod_{k=2}^{L}(1-p_k) - f_w)^2} + \delta_{i,j} \frac{\prod_{k=2}^{L}(1-p_k)}{\prod_{k=2}^{L}(1-p_k) - f_w}\,. \\ &= \frac{p_i}{1-p_j} \frac{1-p_1}{p_1^2} + \frac{\delta_{i,j}}{p_1}\,.\end{aligned}$$

Thus

$$\tilde{\mathbf{J}} = \frac{1-p_1}{p_1^2}\,\mathbf{Q} + \frac{1}{p_1}\,\mathbf{I}\,,$$

where $\mathbf{I}$ is the identity matrix and $\mathbf{Q}_{i,j} = p_i/(1-p_j)$. Since $\mathbf{Q}$ has the eigenvalue $\sum_j p_j/(1-p_j)$ and a $(L-2)$-fold eigenvalue 0, we obtain the spectrum of $\tilde{\mathbf{J}}$ and thus the determinant

$$\mathsf{Det}[\tilde{\mathbf{J}}] = p_1^{1-L}\left(\sum_{j=1}^{L}\frac{p_j(1-p_1)}{(1-p_j)p_1}\right). \tag{D.23}$$

From Eq. (D.10), we then obtain the joint distribution of locus frequencies $p_2,\ldots,p_L$ at the stopping condition Eq. (D.21) as

$$\begin{aligned}\mathsf{P}_{f_w}[\{p_i\}_{i\geq 2}|\boldsymbol{\Theta}] &= \frac{\mathsf{Det}[\tilde{\mathbf{J}}]}{B[\boldsymbol{\Theta}]}\prod_{i=2}^{L}\left(\frac{p_i}{p_1}\right)^{\Theta_i-1}\left(1+\sum_{j=2}^{L}\frac{p_j}{p_1}\right)^{-\sum_{j=1}^{L}\Theta_j}\\ &= \frac{1}{B[\boldsymbol{\Theta}]}\prod_{i=1}^{L}p_i^{\Theta_i-1}\left(\sum_{j=1}^{L}p_j\right)^{-\sum_{j=1}^{L}\Theta_j}\left(\sum_{j=1}^{L}\frac{p_j(1-p_1)}{1-p_j}\right)\end{aligned} \tag{D.24}$$

where the dependence on f_w is implicit in $p_1 = p_1(f_w)$, as given in Eq. (D.21). The joint distribution over all L loci follows as

$$\mathsf{P}_{f_w}[\{p_i\}_{i\geq 1}|\boldsymbol{\Theta}] = \delta_{p_1-1+f_w/\prod_{j=2}^{L}(1-p_j)}\,\mathsf{P}_{f_w}[\{p_i\}_{i\geq 2}|\boldsymbol{\Theta}]\,. \tag{D.25}$$

Note that we do not assume that the first locus is the major locus in Eq. (D.25). Finally, the symmetrical form Eq. (D.20) results from the relation

$$\delta_{g(x)-c} = \frac{\delta_{x-x_c}}{|g'(x)|_{x_c}|} \quad ; \quad g(x_c) = c$$

for the Dirac δ-function.

Remarks

1. To obtain marginal distributions for single loci we generally need to perform a $(L-2)$-dimensional integral (after resolving the δ-function). Details for specific cases

used in the main part of the article are provided in the Mathematica notebook. For two loci, simple explicit formulas for marginal distributions can be derived. E.g., the marginal distribution at the first locus reads

$$\mathsf{P}_{f_w}[p_1|\Theta_1,\Theta_2] = \frac{p_1^{\Theta_1-1}(1-p_1-f_w)^{\Theta_2-1}(1-p_1)^{\Theta_1+1}}{B[\Theta_1,\Theta_2]\,(1-p_1^2-f_w)^{\Theta_1+\Theta_2}}\left(1-\frac{f_w(1-2p_1)}{(1-p_1)^2}\right) \tag{D.26}$$

for $0 \leq p_1 \leq f_w$. The distribution has singularities at $p_1 = 0$ for $\Theta_1 < 1$ and at $p_1 = 1 - f_w$ for $\Theta_2 < 1$. The distributions $\mathsf{P}^+_{f_w}[p|\Theta_1,\Theta_2]$ at the major locus and $\mathsf{P}^-_{f_w}[p|\Theta_1,\Theta_2]$ at the minor locus (which can either be locus 1 or locus 2) follow as

$$\mathsf{P}^\pm_{f_w}[p|\Theta_1,\Theta_2] = \Big(\mathsf{P}_{f_w}[p|\Theta_1,\Theta_2] + \mathsf{P}_{f_w}[p|\Theta_2,\Theta_1]\Big)\,H_{\pm(p-1+\sqrt{f_w})} \tag{D.27}$$

where $H(x)$ is the Heaviside function with $H_x = 1$ for $x \geq 0$ and $H_x = 0$ else. Finally, the *conditioned* distributions $\mathsf{P}^{1\gtrless}_{f_w}[p_1|\Theta_1,\Theta_2]$ at the first locus if this locus is the major/minor locus are

$$\mathsf{P}^{1>}_{f_w}[p_1|\Theta_1,\Theta_2] = \frac{\mathsf{P}_{f_w}[p_1|\Theta_1,\Theta_2]}{\mathsf{P}^{(\Theta_1,\Theta_2)}_{1>}}\,H_{p_1-1+\sqrt{f_w}}\,, \tag{D.28a}$$

$$\mathsf{P}^{1<}_{f_w}[p_1|\Theta_1,\Theta_2] = \frac{\mathsf{P}_{f_w}[p_1|\Theta_1,\Theta_2]}{1-\mathsf{P}^{(\Theta_1.\Theta_2)}_{1>}}\,H_{-(p_1-1+\sqrt{f_w})}\,, \tag{D.28b}$$

where $\mathsf{P}^{(\Theta_1,\Theta_2)}_{1>}$, defined in Eq. (D.17), evaluates to a Hypergeometric function for general $\Theta_1 \neq \Theta_2$, but reduces to $1/2$ for $\Theta_1 = \Theta_2$.

2. The marginal distribution for p_k has a singularity at $p_k = 0$ for $\Theta_k < 1$ and a singularity at $p_k = 1 - f_w$ for $\sum_{j\neq k}^L \Theta_j < 1$. To see this, consider the marginal distribution of p_L, which is obtained from Eq. D.25 after integration over $p_1, \ldots, p_{L-1}$. Dropping non-singular terms (such as the sums in Eq. D.24), and defining

$$q_k = \frac{\prod_{j=k+1}^L (1-p_j) - f_w}{\prod_{j=k+1}^L (1-p_j)}$$

the singular part can be written as

$$\begin{aligned}\mathsf{P}_{f_w}[p_L|\boldsymbol{\Theta}] &\sim \int_0^1 \int_0^1 \dots \int_0^1 \delta_{p_1-q_1} \prod_{i=1}^{L} p_i^{\Theta_i-1} dp_1 \dots dp_{L-1} \\ &= \int_0^{q_{L-1}} \int_0^{q_{L-2}} \dots \int_0^{q_2} q_1^{\Theta_1-1} \prod_{i=2}^{L} p_i^{\Theta_i-1} dp_2 \dots dp_{L-1}\,,\end{aligned}$$

after performing the p_1 integral. The upper integral limits q_k account for the constraint $q_1 > 0$. Substituting

$$\tilde{p}_2 := \frac{p_2}{q_2} \quad \Rightarrow \quad dp_2 = q_2\, d\tilde{p}_2$$

and using that $q_1 = q_2(1-\tilde{p}_2)/(1-\tilde{p}q_2)$ we obtain

$$\begin{aligned}&\mathsf{P}_{f_w}[p_L|\boldsymbol{\Theta}] \sim \int_0^{q_{L-1}} \dots \int_0^{q_3} \int_0^1 q_1^{\Theta_1-1} q_2^{\Theta_2} \tilde{p}_2^{\Theta_2-1} \prod_{i=3}^{L} p_i^{\Theta_i-1} d\tilde{p}_2 dp_3 \dots dp_{L-1} \\ &= \int_0^{q_{L-1}} \dots \int_0^{q_3} q_2^{\Theta_1+\Theta_2-1} \int_0^1 \left(\frac{1-\tilde{p}_2}{1-\tilde{p}_2 q_2}\right)^{\Theta_1-1} \tilde{p}_2^{\Theta_2-1} d\tilde{p}_2 \prod_{i=3}^{L} p_i^{\Theta_i-1} dp_3 \dots dp_{L-1}.\end{aligned}$$

Since the $\tilde{p}_2$ integral is bounded by $1/\Theta_2$ from below and by $1/\Theta_2 + 1/\Theta_1$ from above for all $0 \le q_2 \le 1$, it does not contribute to a singularity in $\mathsf{P}_{f_w}[p_L|\boldsymbol{\Theta}]$. For the singular part, we thus have

$$\mathsf{P}_{f_w}[p_L|\boldsymbol{\Theta}] \sim \int_0^{q_{L-1}} \dots \int_0^{q_3} q_2^{\Theta_1+\Theta_2-1} \prod_{i=3}^{L} p_i^{\Theta_i-1} dp_3 \dots dp_{L-1}.$$

Iterating the substitution procedure for variables p_3 to p_{L-1}, we arrive at

$$\mathsf{P}_{f_w}[p_L|\boldsymbol{\Theta}] \sim q_{L-1}^{\sum_{j=1}^{L-1}\Theta_j-1} p_L^{\Theta_L-1} = \left(\frac{1-f_w-p_L}{1-p_L}\right)^{\sum_{j=1}^{L-1}\Theta_j-1} p_L^{\Theta_L-1}\,,$$

demonstrating the singular behavior for $p_L \to 0$ and for $p_L \to 1-f_w$. Since the labeling of loci is arbitrary, the assertion follows for all loci.

Incomplete phenotypic adaptation, $f_w > 0$, tight linkage

Even if all loci are completely linked, the joint distribution of allele frequency *ratios* is still given by Eq. (D.10). However, the transformation to absolute allele frequencies at the stopping condition $f_w \neq 0$ depends on linkage. Because all mutant alleles are rare during the stochastic phase, we can ignore haplotypes with more than a single mutant during this time. Since we ignore new mutations during the deterministic phase, mutant alleles stay in maximal linkage disequilibrium in the absence of recombination. We thus have

$$\sum_{j=1}^{L} p_j = 1 - f_w \quad \Rightarrow \quad x_i = \frac{p_i}{p_1} = \frac{p_i}{1 - f_w - \sum_{j=2}^{L} p_j}$$

with corresponding Jacobian

$$\mathbf{J}_{ij} = \frac{\partial x_i}{\partial p_j} = \frac{p_i + \delta_{i,j}\, p_1}{p_1^2} \quad ; \quad \mathsf{Det}[\mathbf{J}] = \frac{1 - f_w}{p_1^L}\,.$$

Using this transformation on Eq. (D.10), the joint distribution of mutant frequencies reads

$$\mathsf{P}_{f_w,\mathsf{tl}}[\{p_i\}_{i\geq 1}|\boldsymbol{\Theta}] = \frac{\delta_{\sum_{i=1}^{L} p_i - 1 + f_w}}{B[\boldsymbol{\Theta}](1-f_w)^{L-1}} \prod_{i=1}^{L} \left(\frac{p_i}{1-f_w}\right)^{\Theta_i - 1}\,. \tag{D.29}$$

Evidently, this is just the Dirichlet distribution on the cube $[0, 1-f_w]^L$. This is expected since the problem reduces to a single-locus, L-alleles problem for tight linkage. The marginal distributions can be derived for an arbitrary number of loci and are given by transformed β-distributions,

$$\mathsf{P}_{f_w,\mathsf{tl}}[p_k|\boldsymbol{\Theta}] = \frac{(1-f_w)^{-1}}{B[\boldsymbol{\Theta}]} \left(\frac{p_k}{1-f_w}\right)^{\Theta_k - 1} \left(1 - \frac{p_k}{1-f_w}\right)^{\left(\sum_{j\neq k}^{d} \Theta_j\right) - 1}\,, \tag{D.30}$$

with singularities at the boundaries $p_k = 0$ for $\Theta_k < 1$ and at $p_k = 1 - f_w$ for $\sum_{j \neq k} \Theta_j < 1$ as in the linkage equilibrium case. For two tightly linked loci, the major locus must have frequency $p > (1 - f_w)/2$. The distribution at the major/minor locus therefore reads

$$\mathsf{P}^{\pm}_{f_w,\mathsf{tl}}[p|\Theta_1,\Theta_2] = \Big(\mathsf{P}_{f_w,\mathsf{tl}}[p|\Theta_1,\Theta_2] + \mathsf{P}_{f_w,\mathsf{tl}}[p|\Theta_2,\Theta_1]\Big)\, H_{\pm(p-(1-f_w)/2)} \tag{D.31}$$

and conditioned distributions follow as in Eq. (D.28).

4 Polygenic adaptation:

A quantitative trait under stabilizing selection

4.1 Introduction

In the previous Chapter, we explored the prevalence of different adaptive architectures, from single sweeps to concerted frequency shifts, resulting from phenotypic adaptation of a binary trait with a polygenic basis. We implemented strong redundancy within the trait basis, which yields very strong negative epistasis, a necessary requirement for the occurrence of small, frequency shifts. Due to this model choice, combined with complete uniformity of fitness effects, this model is most favorable of such a homogeneous, concerted adaptive response of the entire trait basis (*i.e.* frequency shifts) which is the expected adaptive architecture in quantitative genetics. However, it turned out that under the effect of genetic drift, the polygenic, adaptive shift pattern requires relatively large mutation rates.

In contrast to our model of a binary trait, classic models from quantitative genetics have long been used to study adaptation of complex, quantitative traits (QT) with an infinitesimal genetic basis (infinitesimal model proposed by Fisher, 1918), (reviewed and extended in *e.g.* Rice, 2004; Barton et al., 2017). Their evolution is usually described by phenotypic means and variances, however these models do not resolve individual locus dynamics. Such models normally rely on additive genotype-phenotype maps and include epistasis (if they do) by stabilizing selection, such that curvature of Gaussian fitness landscape causes negative epistasis. Yet, in contrast to the redundant trait model, epistasis depends on the distance to the trait optimum. With adaptation from a phenotypic state far away from a new optimum selection is mainly directional and epistasis is negligible, while negative epistasis is most effective close to the new optimum (including sign epistasis, when the mean overshoots the optimum).

Due the discrepancies in the modeling approach between our binary trait and previous

QT-models, as well as different, less polygenic outcomes compared to *e.g.* de Vladar and Barton (2014); Jain and Stephan (2015, 2017), it is interesting to investigate how our findings hold up. In the following section we show that our framework leads to general conclusions, in particular also covering the quantitative trait. We demonstrate that our previous results not only constitute a rich, new theoretical approach but serve as an excellent stepping stone for the extension of our investigations towards studying adaptation of a classic QT.

Still we do not abide to all traditions of quantitative genetics modeling, but we adhere to concepts of population genetics. We do this for a good reason. For example we refrain from using infinitely many loci of infinitesimal effect: clearly, these models do not allow for sweeps (or even shifts ...) in the first place, as individual contributions are by definition *infinitesimal*. Only trait-level quantities make sense in this framework. In contrast, we follow the dynamics of allele frequencies within a *finite* genetic basis and do so rather in dependence of the level of phenotypic adaptation (as customary in quantitative genetics) than in time. Moreover, we dissect the adaptive architecture according to the contribution of loci to the adaptive response of the trait. However, our model choice represent a classic QT-model, comprising an additive phenotype-genotype map of a polygenic basis and stabilizing selection. So in conclusion, although we use a population genetics model and describe (changes in) allele frequencies, we assess the adaptive process from a phenotypic perspective.

We embed this into a non-deterministic framework including the effect of genetic drift, mutation and selection and extend previous results on a deterministic QT-model investigated by de Vladar and Barton (2014); Jain and Stephan (2015, 2017). Importantly the current QT-model allows *all* possible adaptive architectures, from classic expectations in quantitative genetics to population genetic, *i.e.* frequency shifts to sweeps, as well as any intermediate patterns. We show that the newly developed analytical framework for the binary trait, as well as the qualitative classification of adaptive patterns, easily extends far beyond complete redundancy.

4.2 Model

We assume a haploid, panmictic population and model adaptation of a QT with a polygenic, genetic basis of L loci to a new phenotypic optimum Z_{opt}. Each locus i is biallelic, with an ancestral variant a_i and a derived variant A_i. Without loss of generality the ancestral allelic effect is set to 0 and each derived allele A_i obtains a locus effect γ_i. All loci contribute additively to the phenotype Z of an individual, which we hence obtain as

$$Z = \sum_{1 \leq i \leq L} \delta_{A_i} \gamma_i, \tag{4.1}$$

such that $\delta_{A_i} = 1$ if the individual carries the A_i allele and 0 otherwise. With this parametrization we obtain the ancestral phenotype (constitutes of only ancestral alleles at all loci) as $Z_0 = 0$.

We implement stabilizing selection on the phenotype Z proportional to a Gaussian fitness function, such that the fitness of a phenotype is given by

$$\omega(Z) \approx \exp[-\frac{\sigma}{2}(Z - Z_{\text{opt}})^2]. \tag{4.2}$$

We obtain the marginal fitness values of a given allele by averaging over all possible backgrounds. For that we use the fact that the marginal phenotypic effect of a given allele a_i and A_i at locus i, $< Z_{a_i} >$ and $< Z_{A_i} >$ (a phenotype containing a_i or A_i), are additive and, assuming LE, can be expressed as

$$< Z_{a_i} > + \gamma_i = < Z_{A_i} > . \tag{4.3}$$

such that the mean phenotype $\bar{Z}$ can be simply be given by the average over the ancestral allele at the given locus shifted by the individual effect of the derived allele at locus i,

$$\bar{Z} = < Z_{a_i} > + p_{A_i} \cdot \gamma_i. \tag{4.4}$$

If we assume weak selection dynamics and linkage equilibrium between the loci, we can approximate the multi-locus dynamics with the continuous, single locus allele frequency dynamics at locus i

$$\dot{p}_{A_i} = (\omega^*_{A_i} - \bar{\omega}) p_{A_i} \tag{4.5}$$

where ω^*_i and $\bar{\omega}$ are the Malthusian marginal fitness of an allele and the mean population fitness, respectively. Using $\bar{\omega} = \omega^*_{A_i} p_{A_i} + \omega^*_{a_i}(1 - p_{A_i})$, we obtain

$$\dot{p}_{A_i} = p_{A_i}(1 - p_{A_i})(\omega^*_{A_i} - \omega^*_{a_i}) \tag{4.6}$$

for the dynamics of the derived allele A_i.

We obtain the marginal fitnesses for a single allele by averaging over all possible phenotypic backgrounds ($< . >_{Z_{a_i}}$ averaging over all background of a_i)

$$\begin{aligned} \omega^*_{a_i} &=< \exp[-\frac{\sigma}{2}(Z_{a_i} - Z_{\text{opt}})^2] >_{Z_{a_i}} \\ \omega^*_{A_i} &=< \exp[-\frac{\sigma}{2}(Z_{a_i} + \gamma_i - Z_{\text{opt}})^2] >_{Z_{a_i}} . \end{aligned} \tag{4.7}$$

Given our evolutionary dynamics given in Eq. (4.6), we are interested in

$$\begin{aligned} \omega^*_{A_i} - \omega^*_{a_i} &=< \exp[-\frac{\sigma}{2}(Z_{a_i} + \gamma_i - Z_{\text{opt}})^2] >_{Z_{a_i}} - < \exp[-\frac{\sigma}{2}(Z_{a_i} - Z_{\text{opt}})^2] >_{Z_{a_i}} \\ &\overset{(\exp[x] \approx 1+x)}{\approx} - < \frac{\sigma}{2}(Z_{a_i} + \gamma_i - Z_{\text{opt}})^2 >_{Z_{a_i}} + < \frac{\sigma}{2}(Z_{a_i} - Z_{\text{opt}})^2] >_{Z_{a_i}} \\ &= -\frac{\sigma}{2}\gamma_i \Big(2(< Z_{a_i} > - Z_{\text{opt}}) + \gamma_i \Big) \\ &\overset{\text{Eq (4.4)}}{=} -\frac{\sigma}{2}\gamma_i \Big(2(\bar{Z} - \gamma_i \cdot p_{A_i} - Z_{\text{opt}}) + \gamma_i \Big) \\ &= -\sigma\gamma_i \Big((\bar{Z} - Z_{\text{opt}}) + \frac{\gamma_i}{2}(1 - 2p_{A_i}) \Big). \end{aligned} \tag{4.8}$$

Using this result in Eq. (4.6), we obtain the dynamics of a derived allele A_i as

$$\dot{p}_{A_i} = p_{A_i}(1-p_{A_i}) \cdot \underbrace{\sigma\gamma_i\Big((Z_{\text{opt}} - \bar{Z}) - \frac{\gamma_i}{2}(1-2p_{A_i})\Big)}_{=:\mathcal{A}}. \tag{4.9}$$

This model corresponds exactly to the model described by de Vladar and Barton (2014); Jain and Stephan (2015, 2017). As detailed in these studies, the first term of $\mathcal{A}$ captures the dynamics caused by directional selection towards the optimum, *i.e.* selection up the fitness slope. The second part of $\mathcal{A}$ covers the sorting of alleles, *i.e.* disruptive selection, resulting in depletion of genetic variation. The first term dominates the dynamics as long as the trait mean is far from the optimum. As also done in Jain and Stephan (2017), we investigate and contrast results for two models for the adaptive dynamics of a QT. Namely, we either approximate $\mathcal{A}$ by only the first term, which we call the "directional selection model",

$$\dot{p}_{A_i} = p_A(1-p_A)\sigma\gamma_i(Z_{\text{opt}} - \bar{Z}) \tag{4.10}$$

or we study the full dynamics, including allelic sorting, which we refer to as "full model" or "full selection model", given in (4.9).

4.2.1 Simulations

With these result, we set up Wright Fisher simulations to study the adaptation of polygenic trait under stabilizing selection and mutation, including the effect of drift (finite population size within our simulations). We simulate $10\,000$ haploid individuals in a panmictic population under the assumption of linkage equilibrium, such that we can treat every locus separately. The allele frequencies at all other loci influence the dynamics at a particular locus only via the mean trait value $\bar{Z}$, included in the marginal fitness term. Backward and forward mutation at allelic rate μ_i per individual and generation is followed by binomial sampling for selection coupled to reproduction. For the "directional selection model", we use the selective weights corresponding to the marginal fitness,

given as

$$\exp[\sigma \cdot \gamma_i \cdot (Z_{\text{opt}} - \bar{Z})]. \tag{4.11}$$

Analogously, for the "full model", we simulate using

$$\exp[\sigma \cdot \gamma_i \cdot (Z_{\text{opt}} - \bar{Z} - \frac{\gamma_i}{2} \cdot (1 - 2p_{A_i})] \tag{4.12}$$

as selective weight of the derived allele. In both cases the weight of the ancestral allele is normalized to 1. We study adaption from de novo mutation, as well as from standing genetic variation (SGV) at mutation-selection-drift equilibrium. In the current model we focus on equal locus effects, $\gamma_i = \frac{1}{L}$ and $\sigma = s \cdot L$, such that we obtain $\gamma_i \cdot \sigma = s$ for each locus.

Starting conditions

Adaptation from de novo mutations: We start from a monomorphic population with only ancestral alleles $\bar{Z} = 0$, and subsequently let the population evolve to a new optimum $Z_{opt} > 0$. We stop the simulations, once the mean trait value has reached the stopping condition $0 < \bar{Z} = \frac{c_Z}{L} \leq Z_{opt}$ or the new optimum.

Adaptation from SGV: We choose a first optimum trait value, $0 < Z_{\text{opt}}^{SGV} < 1$. In this case the distinction into "ancestral" and "derived" allele is no longer valid. Nevertheless we still assume two alleles (a_i and A_i) per locus i. We select the first $k < L$ loci and set the frequency $p_{A_i} = 1$, to match this first optimum. The optimum Z_{opt}^{SGV} is always chosen such that it can be realized with a purely monomorphic population (every locus is monomorphic for either the a_i or the A_i). We let the population equilibrate under selection, mutation and drift for a burn-in period of $8N_e$ generations. In Fig. 4.14, we show that after $8N_e$ generations, the populations have equilibrated to a stable state, where the variance of allele frequencies

$$\frac{\mathrm{d}\Big(\sum_{1 \leq i \leq L} p_i(1 - p_i)\Big)}{\mathrm{d}t} \approx \text{const.}$$

stays constant. After equilibration the optimum jumps to a new value (usually $Z_{\text{opt}}^{SGV} < Z_{opt}$) and the population evolves under mutation, selection, and drift. We stop the simulations, once the mean trait value has reached the stopping condition $Z_{\text{opt}}^{SGV} < \bar{Z} = \frac{c_Z}{L} \leq Z_{opt}$.

4.2.2 Analytical approximations

Using our theoretical framework developed in Chapter 3, we can obtain analytical predictions also for stabilizing selection. Again we separate the adaptation into two phases (Fig. 3.2). An initial *stochastic phase*, and a subsequent *deterministic phase*, covering evolution until the end of the rapid adaptive phase (until the phenotypic optimum is reached). While we ignore mutation and drift during the deterministic phase, epistasis and linkage become important during the latter phase. Dynamics in the *stochastic phase* are modeled with the stochastic *Yule pure birth process*, such that we only track the origin and establishment of immortal mutation lines. For details see Section 3.3.4. New mutations occur at rate $N_e\mu_i$ per generation and establish with probability $p_{est} \approx 2s_b$. Simultaneously, existing derived alleles at all loci propagate at rate s_b. We relegate the detailed derivations to the Appendix F. and only state the main steps and the final result here.

We start out with the *directional selection model* (4.10), as in Jain and Stephan (2017),

$$\dot{p}_i = s\gamma_i p_i(1-p_i)(Z_{\text{opt}} - \bar{Z})$$

where $\bar{Z} = \sum_i p_i\gamma_i$ (equivalent to Eq. (4.4)) is the mean of a QT under stabilizing selection. Defining new variables $u_i = p_i/(1-p_i)$, the dynamics can be written as

$$\dot{u}_i = s\gamma_i u_i(Z_{\text{opt}} - \bar{Z})$$

and

$$\frac{\partial}{\partial t}\frac{u_i}{u_j} = \frac{u_i}{u_j}(\gamma_i - \gamma_j)(Z_{\text{opt}} - \bar{Z})\,.$$

Assume equal locus effects, we set $\gamma_i = \gamma$. Like for the model with complete redundancy, we then obtain a constant ratio of $\partial/\partial t(u_i/u_j) = 0$. To include genetic drift, we set up a Yule process model for parameters u_i. Note that the u_i are unbounded variables, in contrast to the complete redundancy case, and run from 0 to ∞. According to the Yule process, the joint distribution of the ratios $u_i/\sum_i u_i$ converges to the Dirichlet distribution and the distribution of the ratios u_i/u_1 converges to the inverted Dirichlet distribution. In general, we are rather interested in the allele frequencies p_i than in the ratios u_i and in a stopping condition based on the trait mean, or of

$$\frac{\bar{Z}}{\gamma} = \sum_{i=1}^{L} p_i = \sum_{i=1}^{L} \frac{u_i}{u_i + 1} =: c_Z \,. \tag{4.13}$$

with $c_Z \in [0, L]$. We relegate the detailed derivations to the Mathematical Appendix F. Defining $\Theta \equiv \Theta_1$ and the inverse of the *Beta*-function

$$C_\Gamma := \frac{\Gamma(\Theta + \sum_i \Theta_i)}{\Gamma(\Theta) \prod_i \Gamma(\Theta_i)} \,.$$

we finally obtain the joint distribution of the p_i, $i = 2, \ldots, L$ (due to the stopping condition, we can eliminate one locus) at the stopping condition as

$$\begin{aligned} \mathsf{P}[\{p_i\}|c_Z] = C_\Gamma \prod_{i=2}^{L} \frac{p_i^{\Theta_i - 1}}{(1-p_i)^{\Theta_i + 1}} \left(1 + \frac{\sum_{i=2}^{L} p_i(1-p_i)}{(c_Z - \sum_{k=2}^{L} p_k)(1 + \sum_{k=2}^{L} p_k - c_Z)}\right) \\ \cdot \left(1 + \frac{1 + \sum_{k=2}^{L} p_k - c_Z}{c_Z - \sum_{k=2}^{L} p_k} \sum_{i=2}^{L} \frac{p_i}{1-p_i}\right)^{-\Theta} \left(\frac{c_Z - \sum_{k=2}^{L} p_k}{1 + \sum_{k=2}^{L} p_k - c_Z} + \sum_{2=1}^{L} \frac{p_i}{1-p_i}\right)^{-\sum_{2=1}^{L} \Theta_i} , \end{aligned} \tag{4.14}$$

which is the analog of the joint distribution function in the redundancy case, see

Eq. (D.20). For two loci, in particular, we obtain ($p_2 \equiv p$)

$$\mathsf{P}[p|c_Z] = \frac{\Gamma(\Theta+\Theta_2)}{\Gamma(\Theta)\Gamma(\Theta_2)} \frac{p(1-p)+(c_Z-p)(1+p-c_Z)}{(c_Z-2p(c_Z-p))^{\Theta+\Theta_2}} \cdot ((c_Z-p)(1-p))^{\Theta-1} ((1+p-c_Z)p)^{\Theta_2-1}. \tag{4.15}$$

4.3 Results

As for the redundant trait model and if not stated otherwise, we contrast results for constant $\Theta_{bg} = 2N_e\mu(L-1)$. With complete redundancy in the binary trait model, Θ_{bg} captures the level of redundancy within the trait basis. However with the QT-model *effective* redundancy depends on the distance between the mean phenotype of the population to the new optimum. As detailed in the introduction in Eq. (6), $\Theta'_{bg} = \Theta_{bg}\frac{L'}{L-1}$ captured the rescaled background mutation rates, where L' gives the number of truly redundant loci. Thereby $L' = L - d$, where d is the number of loci required to flip from $a_i \to A_i$ in order to reach the stopping condition (the point of observation of the architecture). Thus follows that the more loci are needed, the lower the degree of redundancy within the trait basis, as well as that the effective Θ_{bg} declines as adaptation proceeds.

4.3.1 Adaptive architectures for adaptation from de novo mutations

At first we investigate the adaptive architecture from a monomorphically ancestral population ($\bar{Z} = 0$ at $t = 0$). As in the complete redundancy model, we look at the marginal distributions of loci ordered according to their contribution to adaptation (major and minor loci). For adaptation from the ancestral state, we refer to the locus with the highest frequency increase as the "major locus" and all others as "minor loci". Additionally, we investigate the marginal allele frequency distributions of an arbitrary trait locus.

These two distributions capture different aspects of the collective, adaptive behavior of the entire trait basis: The ordered distributions show how many loci actually contribute to adaptation, and thus make comparisons between different trait basis sizes easier.

The marginal distribution of an arbitrary locus (also detailed in Section C.4.1 and the Discussion of Chapter 3) gives an overview of the potential destiny of a particular locus, corresponding to a more "gene centered point of view" used previously in Chevin and Hospital (2008); Pavlidis et al. (2012); Wollstein and Stephan (2014).

We start our analysis with two loci, where we try to disentangle the impact of mutation rates, selection strength, time point of sampling and model choice. We proceed by including larger trait basis and analyze the effect various degrees of redundancy. As before, we distinguish more or less polygenic responses based on how similar or different the allele frequency distribution of major and minor loci are. Alternatively, for the marginal distribution for an arbitrary locus a strongly u-shaped distribution is considered as characteristic of sweep patterns and most loci are found at the bounds with very low (no contribution to adaptation) or very high (completed sweeps) frequencies. In contrast a homogeneous response, what we consider a more polygenic adaptive pattern, is characterized by stronger weight on intermediate frequencies.

Adaptive architectures for two loci

In Fig. 4.1 ($L = 2$, where $\bar{Z} = \frac{1}{2}(p_1 + p_2)$) we contrast adaptive patterns for strong and weak selection, $s_b = 0.1$ and $s_b = 0.01$, respectively under the directional as well as under the full model. We look at three "snapshots" during the course of adaptation to a new optimum $Z_{opt} = 0.5$, namely once the population has adapted to $\frac{1}{3}$ and $\frac{2}{3} \cdot Z_{opt}$, as well as at complete phenotypic adaption. Note that complete adaption is accomplished if the sum of the derived allele frequencies $p_1 + p_2 = 2 \cdot Z_{opt} = 1$ for two loci, resulting in a symmetric marginal distribution. Any adaptive pattern lies between either one locus having completely fixed or both loci having increased their derived allele frequency by 50%. (For figures illustrating adaptation to $Z_{opt} = 0.3, 0.8$ consult Figs. E.1, E.2.)

Overall, we see a shift from u-shape for $\Theta_{bg} < 1$, to unimodal frequency distributions for $\Theta_{bg} \geq 1$ with the directional selection model, irrespective of the stopping condition. Especially at complete adaptation (distributions in blue) we see that the directional

selection model yields more polygenic adaptive signatures, than the full model. There, sweeps (u-shape) still dominate the adaptive response for $\Theta_{bg} \leq 1$ and weak selection and $\Theta_{bg} \leq 10$ with strong selection. In contrast, if we sample the population further away from the optimum, $\bar{Z} << Z_{opt}$, the directional and the full model yield much more similar results.

The different outcomes of the two models result, in dependence of the point of sampling can be understood, when looking at the dynamics, see Eq. (4.9). There we see that if the mean phenotype of the population is still quite far of the optimum the first directional selection term of the dynamics dominates. Yet, if the mean phenotype approaches the new optimum, selection in the directional model is almost zero $(Z_{opt} - \bar{Z}) \approx 0$ while the second term, sorting out allele frequencies in the full model, is still influencing selective dynamics. Hence results of the directional selection model and the full model for the early part of the rapid adaptive phase coincide, while deviations start to accumulate close to adaptation.

Furthermore, we observe an effect of selection strength only for the full model. In the full model, we obtain more polygenic responses with weak selection compared to strong selection. Again this effect is most pronounced at points closer to the optimum. For example, if we consider $\Theta_{bg} = 10$ we still observe a u-shaped distribution with strong selection, yet with weak selection the marginal distribution has become unimodal. Given that the effect is strongest for sampling close to the optimum, this hints towards an effect of allele sorting in the full model. With Malthusian fitness values increasing σ in the dynamics entails increasing the difference between the directional and the disruptive term.

Finally, including or neglecting back-mutations in this scenario does not lead to any differences in the adaptive response in any case as can be seen when comparing (Fig. 4.1, E.3 with and without back-mutations).

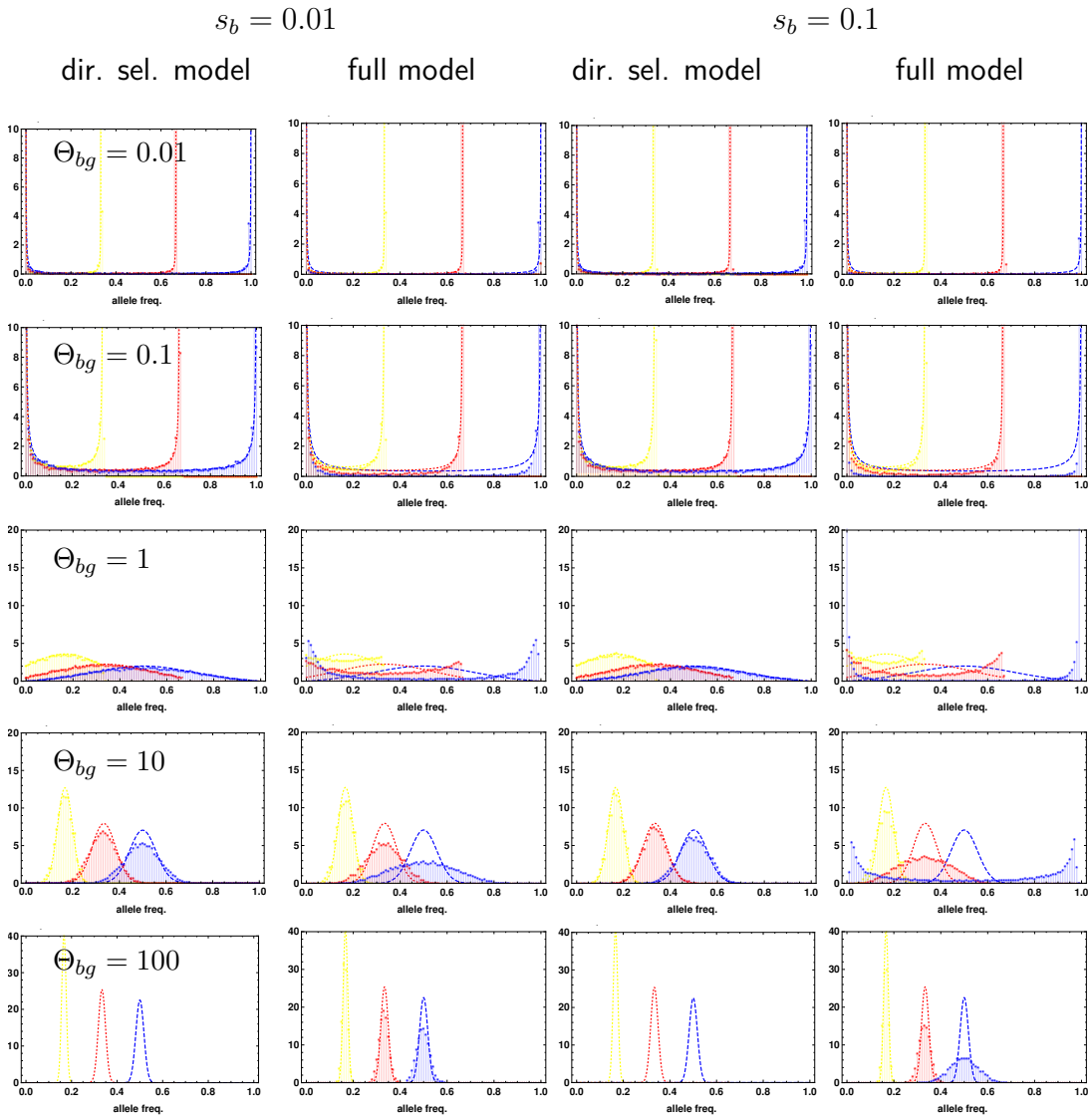

Figure 4.1: **Marginal frequency distribution at three stages of adaptation.** The marginal allele frequency distribution of a single locus ($L = 2$) upon adaptation to $Z_{opt} = 0.5$ from a completely ancestrally monomorphic population. The "snapshots" (yellow, red and blue) show the population at three stages of adaptation: When the population has adapted to $\frac{1}{3} \cdot Z_{opt}$ in yellow, $\frac{1}{3} \cdot Z_{opt}$ in red and at complete adaptation to the new optimum Z_{opt} in blue. We contrast the results for the directional selection model and the full model for weak and strong selection, $s_b = 0.01$ and 0.1 and for $10\,000$ replicates. There are no simulation results for populations evolving under the directional selection model for $\Theta_{bg} = 100$, as they never reach Z_{opt}, because mutation pressure exceeds selection close to adaptation.

Adaptive architectures for larger trait basis, $L > 2$

We proceed by investigating adaptive architectures for larger trait basis. To compare traits with a different size of the basis, we measure the distance to the new optimum in units of $\frac{1}{L}$, requiring always the same amount of loci for phenotypic adaptation irrespective of L. In Figs. 4.2 and 4.3 we set $Z_{opt} = \frac{1}{L}$ such that all are redundant (similar to binary trait model in Fig. 3.4). As a second step and in analogy to the relaxed redundancy model (Fig. 3.5), we investigate the adaptive architecture for $Z_{opt} = 2 \cdot \frac{1}{L}$. This means that for an arbitrary trait basis a single, respectively two fixations are already sufficient to reach the new optimum. In the latter case, we refer to both fixed loci as "major loci", if we find that they contributed comparably to adaptation, and the cohort of major loci is clearly distinguishable from all other loci. In both cases we sample the population upon complete phenotypic adaptation to the new optimum, where we expect the largest differences between the full and the directional selection model.

In general we see a strong uniformity within the adaptive architectures across different trait basis sizes with constant Θ_{bg} (as in the redundant trait model). This is especially true for the directional selection model. For this model it is also possible to describe multi-locus models with $L > 2$ with the two locus or three locus formalism (To obtain the desired approximations we need to integrate over Eq. (4.15) for 2 loci and Eq. (4.14) for 3 loci, respectively.) as long as mutation rates are not too high. We find the following threefold classification for adaptive patterns across different L (see Fig. 4.2 and 4.4):

1. For $\Theta_{bg} \leq 0.01$ we see mainly completed sweeps. For $Z_{opt} = \frac{1}{L}$ almost the entire phenotypic adaptation is attributable to one major locus, and similarly for $Z_{opt} = 2 \cdot \frac{1}{L}$ we obtain two major loci, which sweep to fixation. All other minor loci do not contribute.

2. For $0.1 \leq \Theta_{bg} \leq 1$ we obtain a hand full of complete and partial sweeps. In detail for $\Theta_{bg} = 0.1$ there is usually only one additional minor locus ($0 << p \lesssim 0.5$) contributing besides the one ($Z_{opt} = \frac{1}{L}$) or two ($Z_{opt} = 2 \cdot \frac{1}{L}$) major loci. For

$\Theta_{bg} = 1$ adaptation is achieved few loci, usually $\lesssim 6$ for $Z_{opt} = \frac{1}{L}$ and $\lesssim 7$ for $Z_{opt} = 2 \cdot \frac{1}{L}$. Thereby the distributions of majors to minors show a clear order over the entire range $0.01 < \Theta_{bg} \leq 1$, and still show a clear structural heterogeneity in the adaptive response across different L.

3. Finally, for $10 \leq \Theta_{bg}$ we find very similar patterns of subtle, concerted frequency shifts for both optima, $Z_{opt} = \frac{1}{L}$ and $Z_{opt} = 2 \cdot \frac{1}{L}$. For $L > 2$ major and minor distributions blur and form a homogeneous, unimodal joint distribution.

This classification of adaptive architectures in is good agreement with the redundant trait model. However, the results are more polygenic with the directional selection model.

For the full model, the classification is a bit more elaborate, as it also depends on L. Because of the analytical complexity of the full model, we cannot obtain any approximations, when the population mean phenotype has come close to the optimum. In Fig. 4.3 and 4.5 we find the following adaptive patterns for complete phenotypic adaptation, which are closely related to what we observe with the binary trait model:

1. For $\Theta_{bg} \leq 0.01$ adaptation is entirely achieved by sweeps at one major ($Z_{opt} = \frac{1}{L}$) or at two major loci ($Z_{opt} = 2 \cdot \frac{1}{L}$).

2. For $\Theta_{bg} = 0.1$ and $L \leq 10$ this adaptive pattern is preserved, in contrast to the directional model, where we locate already few partial sweeps. For $L = 100$ we also find that one minor locus performs a partial sweep in addition the major sweep (or 2 major sweeps with two required mutation steps).

3. For $\Theta_{bg} = 1$, we still find a very heterogeneous pattern, *i.e.* a major sweep and one or two minor partial sweeps with $L \leq 10$ while the major distributions is already much more flat (shifted to intermediate frequencies) in the case of $L = 100$.

4. This trend is continued for $\Theta_{bg} = 10$. For $L \leq 10$ there is still a clear distinction between one or two majors, for $Z_{opt} = \frac{1}{L}$ and $Z_{opt} = 2 \cdot \frac{1}{L}$, respectively, while for $L = 100$ we can already characterize the adaptive architecture as shift like.

5. Only for $\Theta_{bg} = 100$ we obtain homogeneous, polygenic responses for all L. These frequency shifts are still necessarily quite large in the case of $L = 2$, while the become rather small for larger basis.

In conclusion, for small L, the disruptive term is quite important and leads to stronger sweep-like architectures. For large L the full model gets closer to the directional selection model because the directional selection term dominates for a longer time during the adaptation (the disruptive term has an extra factor $\frac{1}{L}$).

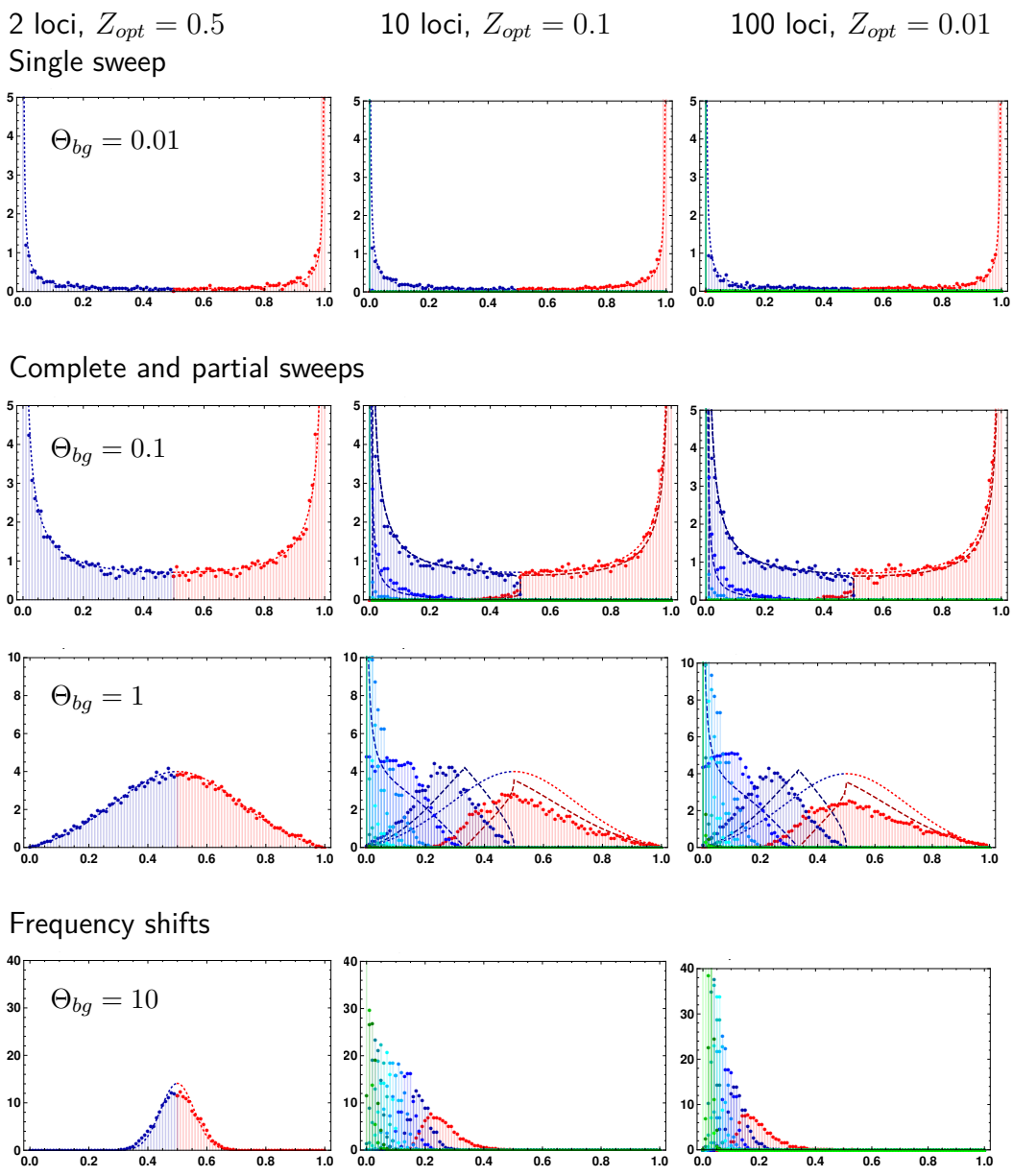

Figure 4.2: **Major and minor distributions at adaptation, $Z_{opt} = \frac{1}{L}$ with the directional selection model.** We show the distribution of the leading locus (red) and the runner ups (from blue to green) for 2 to 100 loci at complete phenotypic adaptation for evolution under the directional selection model. Adaptation occurs from de novo mutations only to a new optimum $Z_{opt} = \frac{1}{L}$, such that for each trait basis phenotypic adaptation is completed with only a single fixation event. We simulate $10\,000$ replicates for each mutation rate at a selection strength of $s_b = 0.1$. The approximations for $L = 2$ correspond to Eq. (4.15). The approximations in the $L > 2$ cases correspond to the 2 locus approximations with $\Theta_1 = \Theta_2 = \Theta_{bg}$ and the stopping condition $c_Z = Z_{opt} \cdot L$.

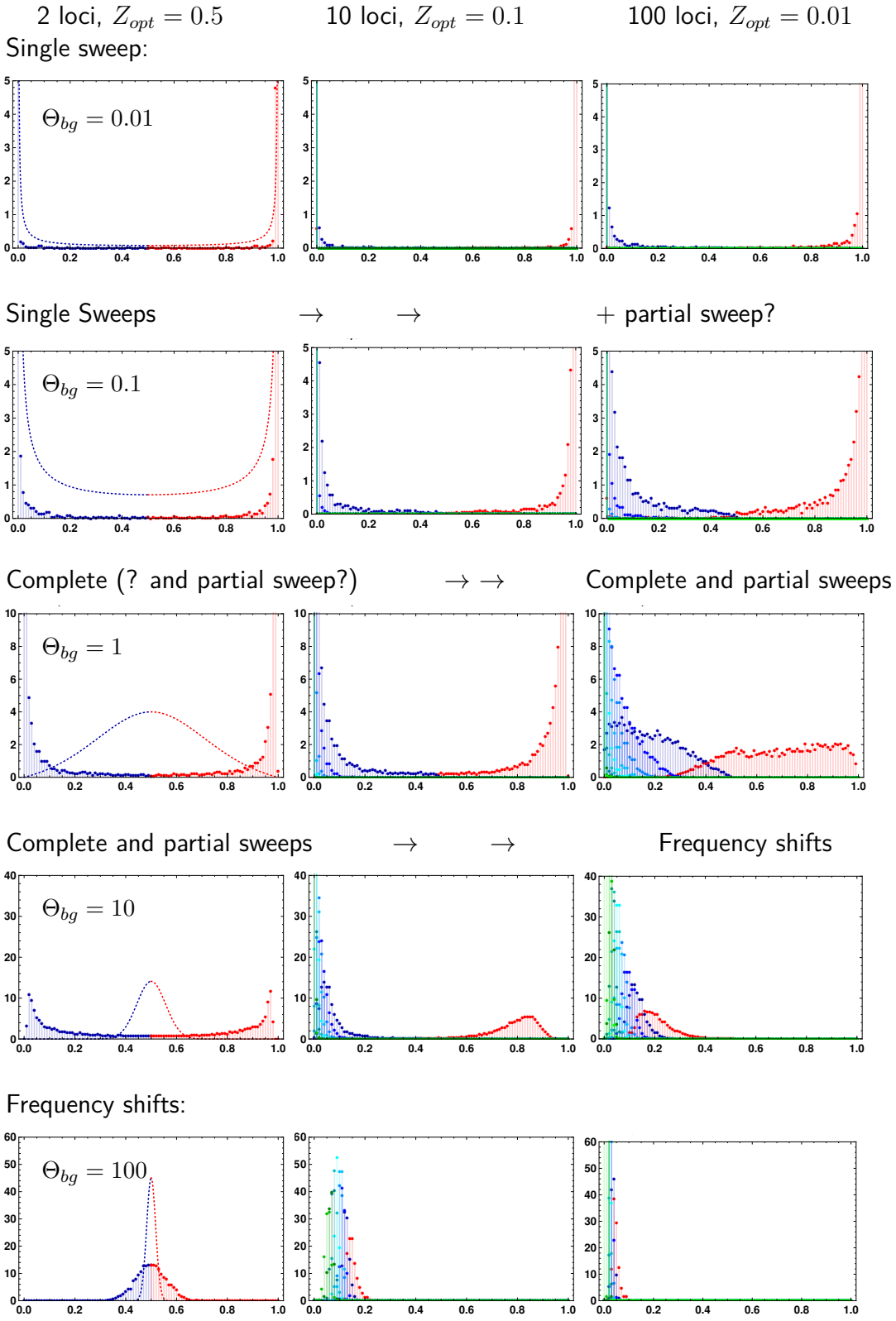

Figure 4.3: **Major and minor distributions, $Z_{opt} = \frac{1}{L}$ with the full model.** Rest as in Fig. 4.2

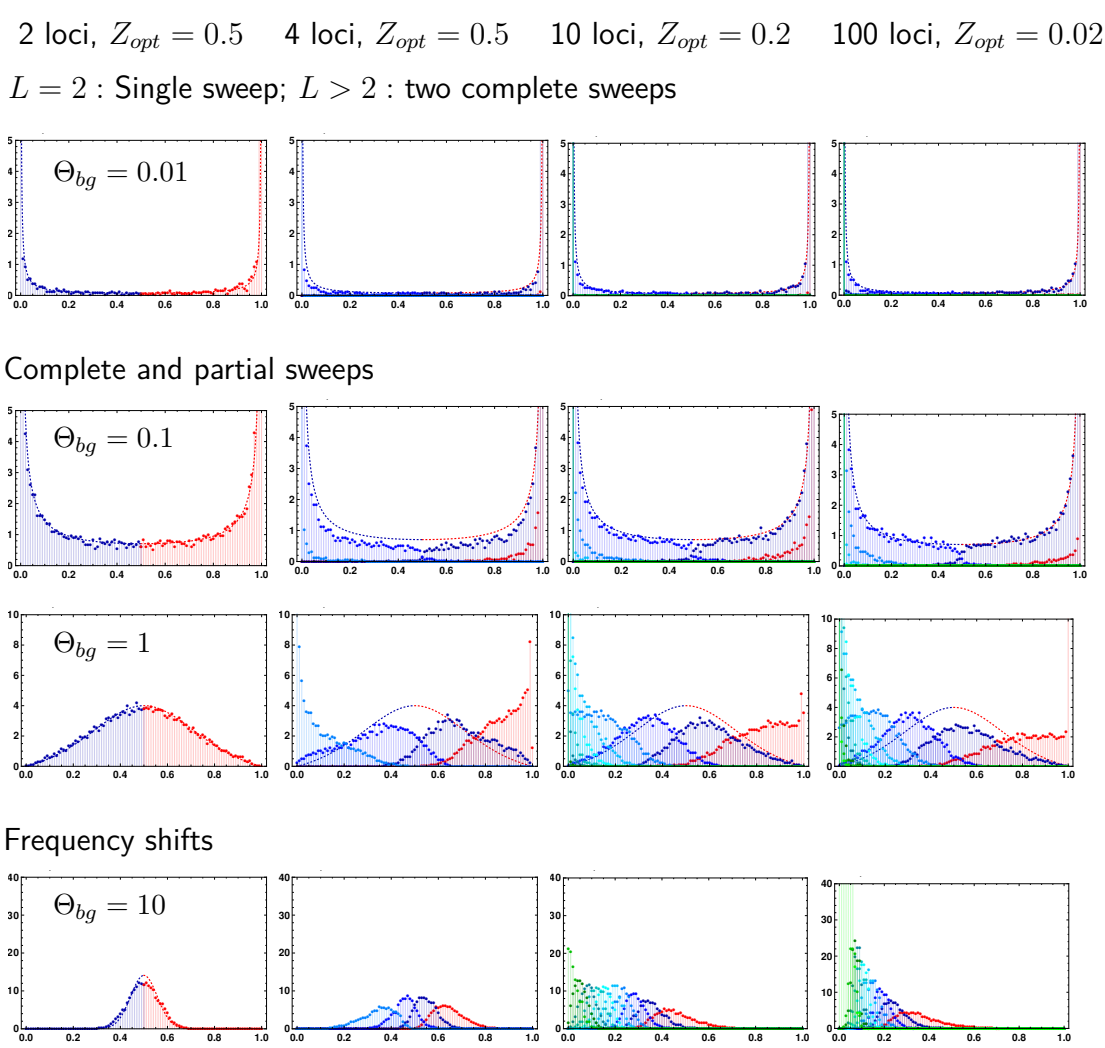

Figure 4.4: **Major and minor distributions, $Z_{opt} = \frac{2}{L}$ with the directional selection model.** We show the marginal distributions of the ordered major and minor loci at complete phenotypic adaptation for evolution under the directional selection model. Adaptation occurs from de novo mutations to a new optimum $Z_{opt} = 2 \cdot \frac{1}{L}$, for $L > 2$ such that for each trait basis phenotypic adaptation is completed with two fixation event. The first column for $L = 2$ shows adaptation to $Z_{opt} = \frac{1}{L}$ as a reference for the two locus approximations, Eq. (4.15), given in the rest of the panels, which fit well to the second major and the first minor ($3rd$ order locus). We simulate $10\,000$ replicates for each mutation rate at a selection strength of $s_b = 0.1$.

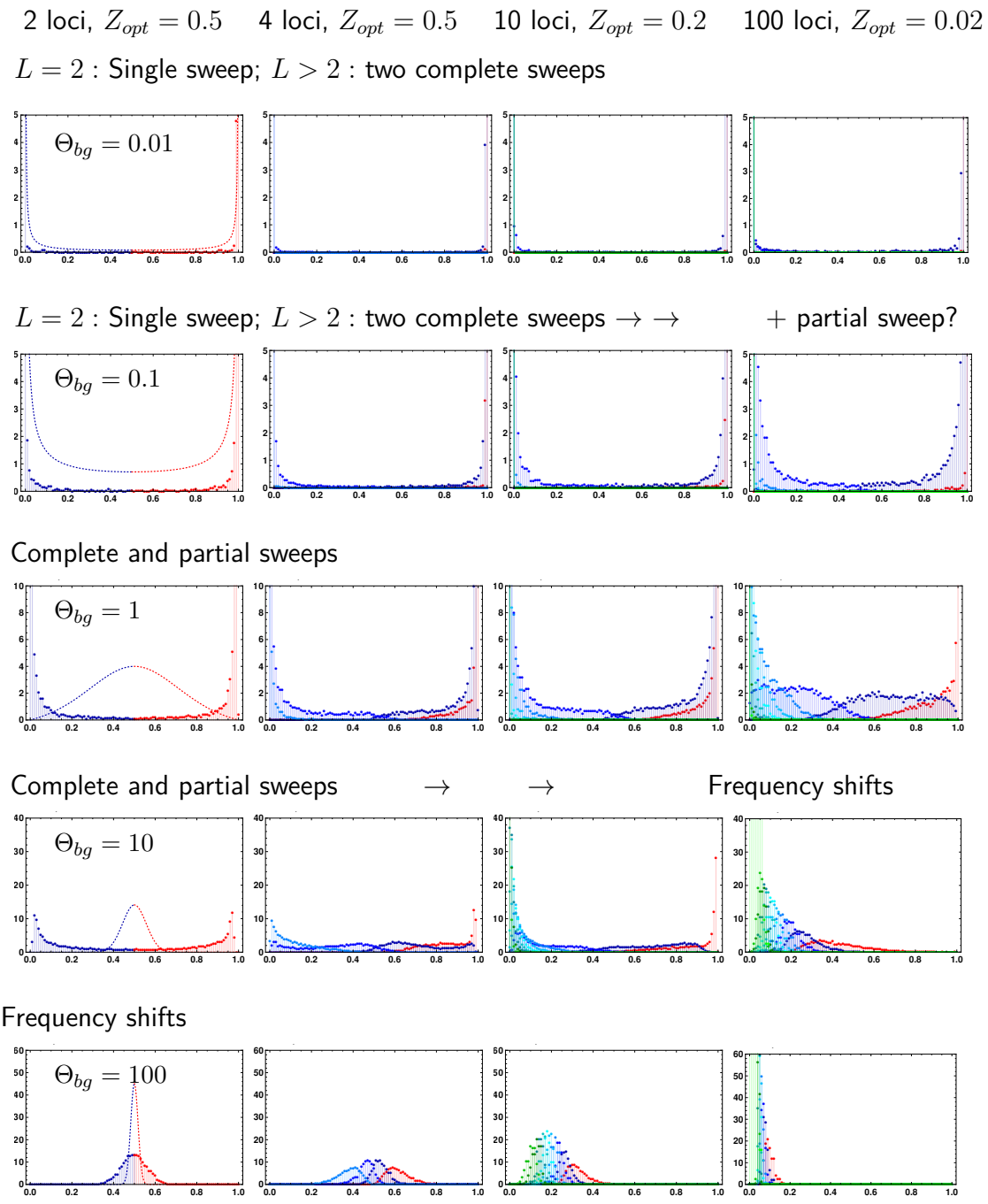

Figure 4.5: **Major and minor distributions at adaptation requiring two mutational steps with the full model.** Rest as in Fig. 4.4

4.3.2 The course of adaptation during the rapid adaptive phase

When studying the course of adaptation, we refrain from sampling points conditional on time, but rather prefer a measure of the level of phenotypic adaptation as a point of reference. This entails, that *different temporal dynamics*, caused by stochastic processes such as waiting times for new mutations, are negligible in favor of studying the *qualitative adaptive dynamics*.

As already seen in detail with the 2 locus model, the stopping condition is decisive for the differences between the directional selection model and the full model. In the Section above we sampled the population at complete adaptation for $L > 2$ to capture the initial dynamics of the rapid adaptive phase, as well as the dynamics closer to the optimum. In Fig. 4.6 and 4.7 the impact of deviating stopping conditions far away from the optimum becomes apparent, as the directional model and the full model coincide well there. Differences accumulate only closer to the optimum. As discussed for two loci, this is due to the second term in the evolutionary dynamics of the full model, the sorting of alleles, which plays an increasingly important role, if the population mean moves closer to the optimum. For the same reason the analytical approximations work well for the full model at stopping conditions far away from the optimum, while they do not reflect the later dynamics of variance depletion and hence are off once the population has (almost) adapted.

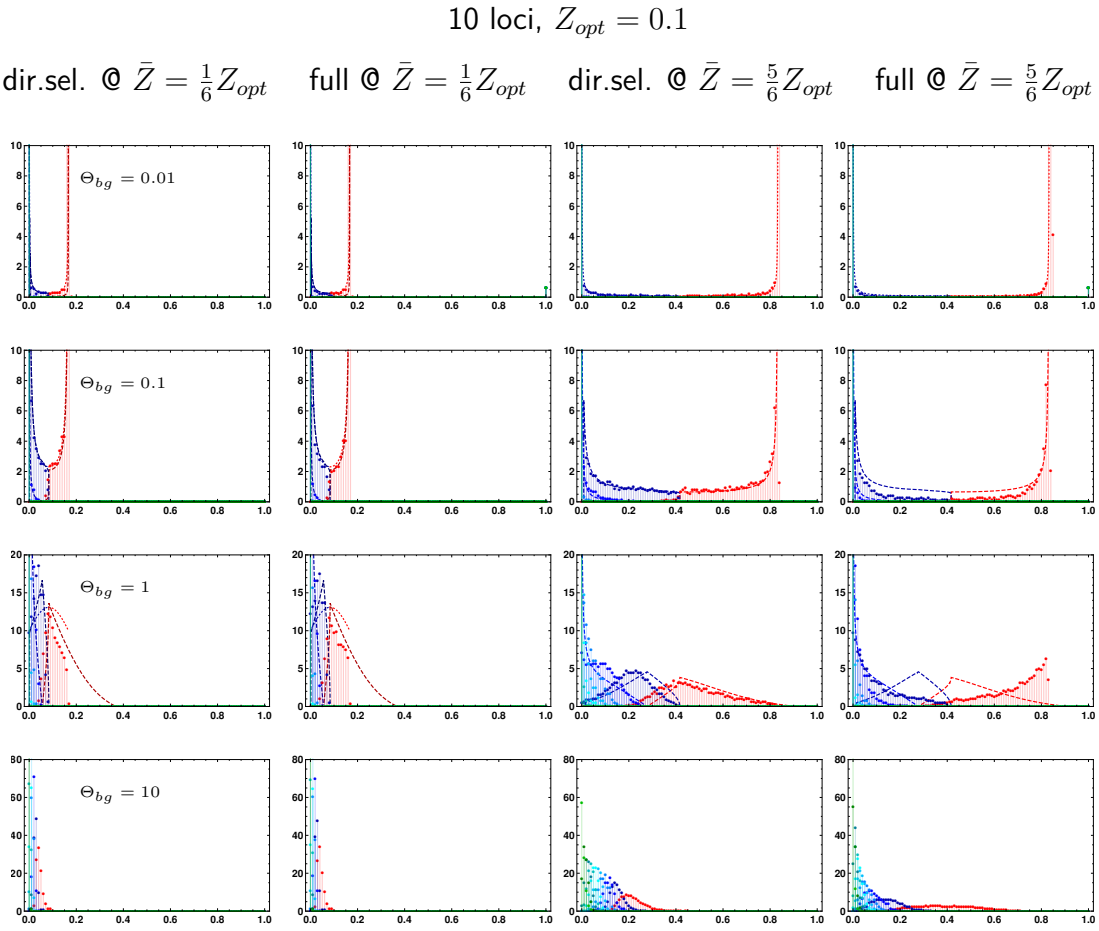

Figure 4.6: **Stopping close or far away of the optimum, $L = 10$.** The marginal distribution of the major (red) and the successive minors (first, second, third, *etc.*, from dark blue, light blue to green) show that the resulting adaptive architectures of the directional and the full model are much more similar if the population is sampled further away from the optimum, *e.g.* $\bar{Z} = \frac{1}{6}Z_{opt}$ (left two columns), than close to complete adaptation at $\bar{Z} = \frac{5}{6}Z_{opt}$ (right two columns). Simulations results are based on 10 000 replicates per mutation rate with selection strength $s_b = 0.1$. Approximations for $\Theta_{bg} = 0.01$ are based on the 2 locus formalism, while they are based on the 3 locus approximations (large dashes) for $0.1 \leq \Theta_{bg} \leq 1$. For $\bar{Z} = \frac{1}{6}Z_{opt}$ we contrast the 2 and more accurate 3 locus approximations for $0.1 \leq \Theta_{bg} \leq 1$.

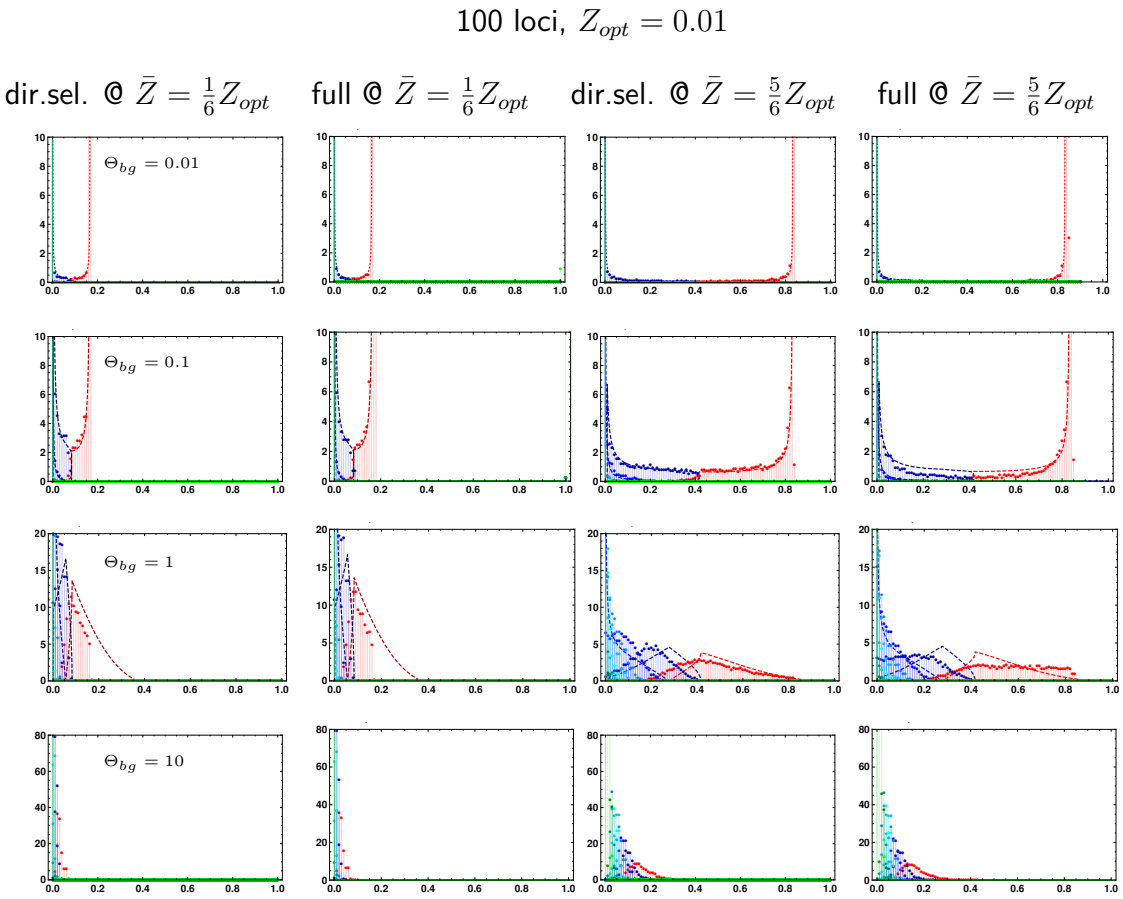

Figure 4.7: **Stopping close or far away of the optimum,** $L = 10$**.** The marginal distribution of the major (red) and the successive minors (first, second, third, *etc.*, from dark blue, light blue to green, 11th to 100th locus are given as cumulative distribution in light green) show that the resulting adaptive architectures of the directional and the full model are much more similar if the population is sampled further away from the optimum, *e.g.* $\bar{Z} = \frac{1}{6}Z_{opt}$ (left two columns), than close to complete adaptation at $\bar{Z} = \frac{5}{6}Z_{opt}$ (right two columns). Approximations are based on the 2 locus formalism for $\Theta_{bg} = 0.01$ and on the 3 locus formalism (large dashes) for $0.1 \leq \Theta_{bg} \leq 1$. Rest as in Fig. 4.6.

4.3.3 Moving the optimum further away: Relaxing redundancy

Complete or almost complete redundancy of the trait basis is a limiting assumption. Hence in the following section, we extend our considerations to strongly relaxed redundancy for 10 or 100 loci. Before we measured the distance to the optimum in units of $\frac{1}{L}$, while now we study the course of adaptation to the phenotypic optimum at 50% of its phenotypic range (evolutionary accessible range), *e.g.* $Z_{opt} = 0.5$. This results in relaxation of redundancy in two ways. First in general we need at least 50% of all loci to contribute to adaptation, to reach this optimum, when we start from a completely ancestral population. Second, the bigger the basis, the more loci we need to reach this optimum. In Fig. 4.8 and 4.9 we first show the marginal distribution of a focal locus and confirm the previously observed trend that the directional model tends to be more polygenic. Nevertheless, the differences between the models attenuate with larger basis, as well as with sampling further away from the optimum. For 100 loci they already become relatively small. All of this can be understood, when considering the selective weights. As depicted in Fig. 4.10, they become much more alike for increasing number of loci between the two the selection models for sampling before complete adaptation (at $\bar{Z} = \frac{1}{3}Z_{opt}$ or $= \frac{2}{3}Z_{opt}$). While the difference for 2 loci is apparent, it is already much smaller for 10 loci and almost negligible for 100 loci.

Of course, with a larger trait basis and a far optimum, we require the contribution of more loci (in absolute numbers) to reach phenotypic adaptation at $Z_{opt} = 0.5$. As a result we find stronger sweep patterns also for high mutation rates, with larger trait basis. In detail, we observe that for $\Theta_{bg} \leq 1$ and $L \geq 10$ and $L = 100$ and $\Theta_{bg} \leq 10$ the adaptive architecture among the contributing loci is very heterogeneous, leading to a strongly u-shaped distribution due to several sweeps.

In Fig. 4.11 we further disentangle the adaptive architecture for 10 and 100 loci given in red in Fig. 4.8 and 4.9 at $\bar{Z} = \frac{2}{3}Z_{opt}$. To do so, we bin loci according to their contribution as before and depict their marginal frequencies. For 10 loci we follow our established concept and plot the distribution for the major, first minor, second minor

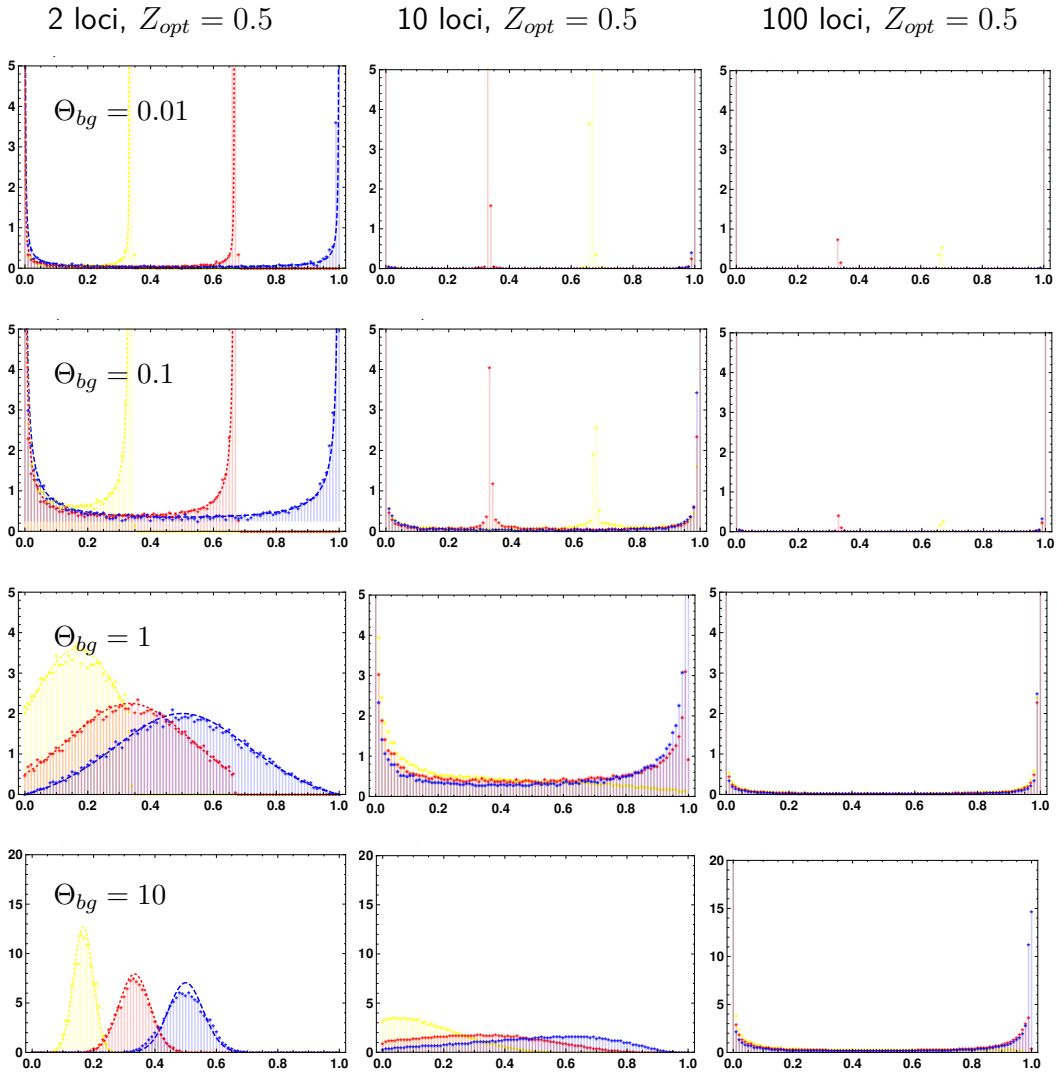

Figure 4.8: $L = 2$, 10 **and** 100**: Marginal allele frequency distribution with the directional model.** The marginal allele frequency distribution of a single locus for various trait basis sizes resulting from simulations using the directional selection model to study adaptation to a new trait optimum, $Z_{opt} = 0.5$. Adaptation occurs solely by de novo mutations from a monomorphically ancestral population with strong selection, $s_b = 0.1$. As before, we show the allele frequency distribution at three different stages towards complete phenotypic adaptation, namely when the mean phenotype of the population has reached $1/3 \cdot Z_{opt}$ in yellow, $2/3 \cdot Z_{opt}$ in red and evolved to complete phenotypic adaptation in blue. For the two first rows, the single intermediate peaks for 10 and 100 loci are single loci on their way to fixation, therefore the yellow peak appears right to the red peak. As above we use $10\,000$ replicates per mutation rate and trait basis size.

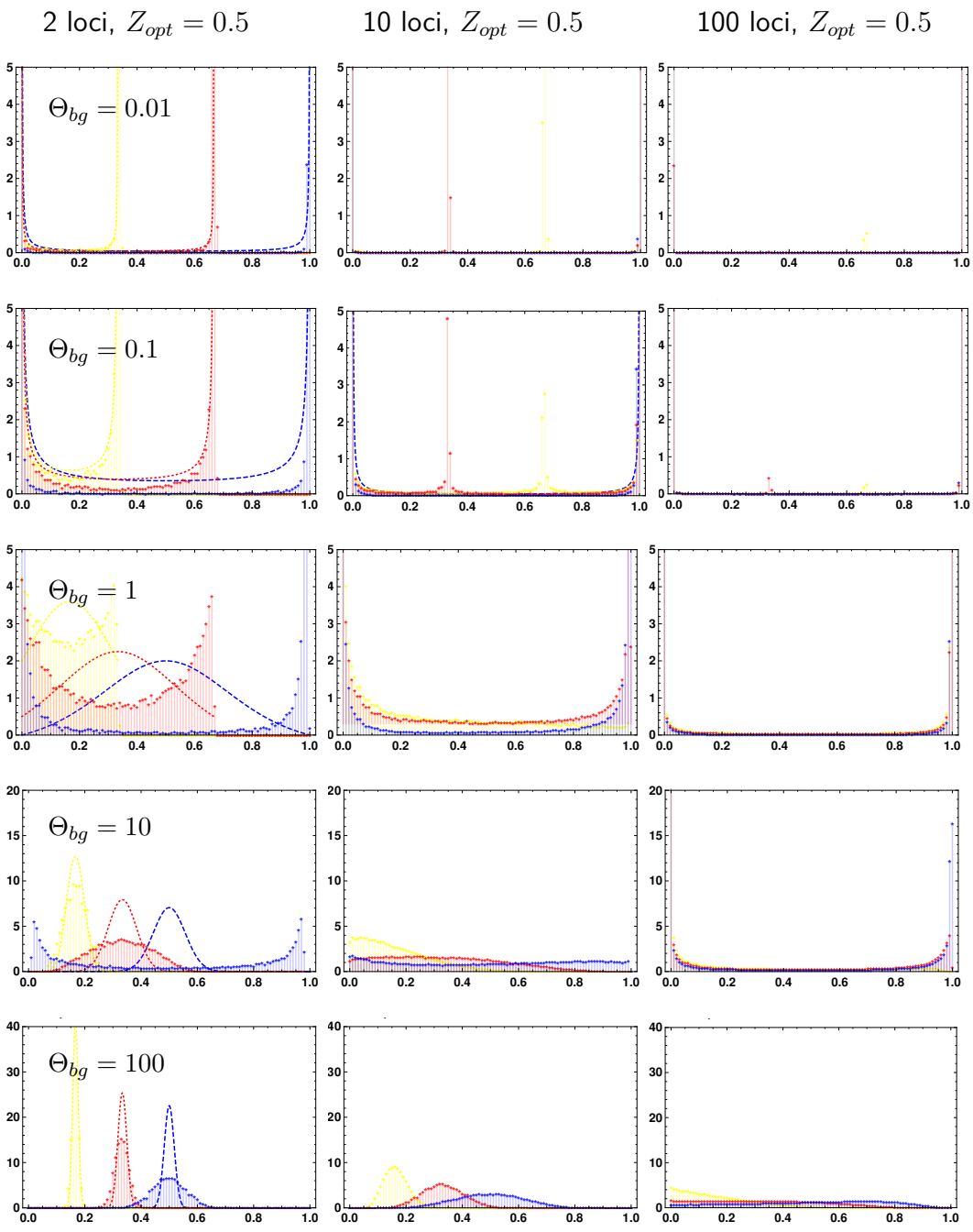

Figure 4.9: $L = 2$, 10 **and** 100**: Marginal allele frequency distribution with the full selection model.** The marginal allele frequency distribution of a single locus resulting from simulations using the full selection model. Parameters as in Fig. 4.8.

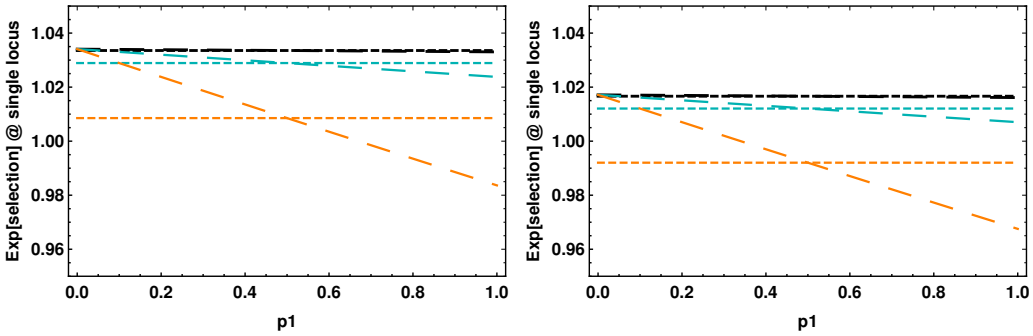

(a) $Z_{opt} = 0.5, \bar{Z} = \frac{1}{3} \cdot Z_{opt} + \frac{1}{L} p_1$ (b) $Z_{opt} = 0.5, \bar{Z} = \frac{2}{3} \cdot Z_{opt} + \frac{1}{L} p_1$

Figure 4.10: **Marginal fitness of a focal locus.** The marginal fitness of an arbitrary locus is calculated as the exponential of the selective weights as in the simulations and is depicted for 2 (in orange), 10 (in turquoise) and 100 (in black) loci in dependence of the allele frequency $0 \leq p_1 \leq 1$. We show results for the full selection model (short dashes) and the directional selection model (long dashes), respectively. While the slope of the full model is almost constant with increasing p_1, the weights in directional selection decrease. Generally, the selective weights for the two models become more and more alike for larger basis. Selection is set to $s_b = 0.1$.

etc.. For adaptation of $L = 100$ we need such a large number of non-redundant loci to fix to reach the new optimum, that the previous way of illustration is not applicable. Therefore, we bin the major and its 9 consecutive minors, followed by the 10th to the 19th minor, 20th to 29th *etc.*, and display each of their joint, marginal frequency distributions. First, we see that the full and the directional selection model are still pretty similar at this stopping condition. Secondly, we recover the analogous classification of adaptive architectures as before. To see that, we need to keep in mind, that with the chosen optimum of $Z_{opt} = 0.5$ we need a large number of loci to contribute to adaptation in a non-redundant way.

- For $\Theta_{bg} = 0.01$ we see most of the loci concentrated at the bounds, so either they have swept to fixation or they have remained in the ancestral state.

- For $\Theta_{bg} = 0.1$ we still find a clear heterogeneous pattern, between loci distributed at the two bounds (ancestral and derived state), yet for 10 loci we have about 1-3 loci at intermediate frequencies, yielding on average 1-3 partial sweeps, on top of at least 2-3 completed sweeps. For 100 loci, we see an intermediate peak also

only for one cohort (4th cohort). This cohort of 10 loci corresponds to the 30th to 39th locus, similar to the 10 locus case, where the intermediate peak belongs to 3rd minor. This analogy is also indicated by the same color of the respective intermediate peak.

- For $\Theta_{bg} = 1$ we observe many partial sweeps in the 10 locus case. In the 100 locus case the cohort of the 30-39th locus is almost uniformly distributed across the entire range of frequencies, also indicating many partial sweeps within that bin.

- For $\Theta_{bg} = 10$ and 10 loci, the distributions start to blur into each other. While given the Z_{opt} these frequency changes are still relatively large, probably best classified as partial sweeps, their homogeneous nature is already indicative of polygenic, shift-like behavior. Analogously in the 100 locus case, we find 3 cohorts of a total of 30 loci "smeared" across the frequency space.

- Finally, for $\Theta_{bg} = 100$ we obtain a clear shifts pattern for 10 loci. Similarly, for 100 loci almost the entire basis starts to contribute to adaptation.

Following the dynamics of adaptation to a far optimum

Finally, we can also adapt our approximations to reduced redundancy and manage to comprehensively predict the dynamics of the entire adaptive process. For illustrative purposes we set the phenotypic optimum to the maximum of the phenotypic range $Z_{opt} = 1$, and follow the course of adaptation for 10 loci, see Fig. 4.12 and 4.13. This choice of Z_{opt} finally means that all 10 loci will eventually have to fix to the derived state to reach complete phenotypic adaptation (of course, we can never really reach it, because of back-mutations). The closer $\bar{Z}$ moves to the optimum, the smaller the number of loci becomes that can redundantly contribute to further adaptation: Assume that the mutation rate is sufficiently small, that fixations occur one after the other. At the beginning, where the population mean is $\bar{Z} = 0$, each of the 10 loci is equally

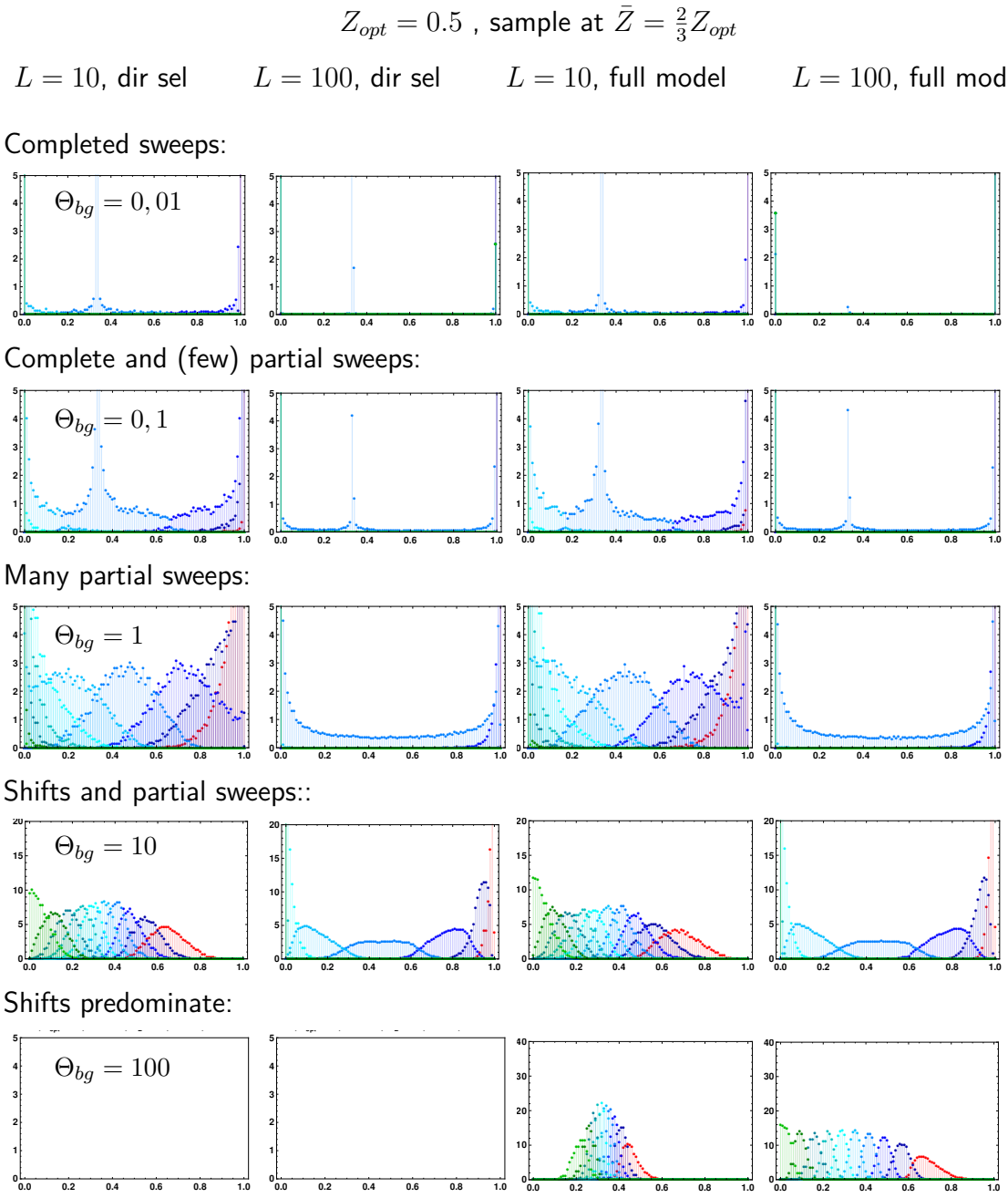

Figure 4.11: **Adaptive architectures with low redundancy.** We show the marginal, ordered allele frequencies for 10 and 100 loci. For 10 loci each color represents one locus, *e.g.* major, first minor, second minor *etc.*. In contrast for 100 loci we summarize 10 loci each, such that one color always depicts the marginal allele frequency distribution of 10 loci, *e.g.* the major, first minor, ... 9th minor, followed by 10th to 19th minor *etc.*. Populations adapt to a new optimum $Z_{opt} = 0.5$ and simulations are stopped, when populations have adapted to $\bar{Z} = \frac{2}{3} Z_{opt}$. 10 000 replicates per mutation rate, $s_b = 0.1$. We do not obtain any simulation results for the directional selection model at $\Theta_{bg} = 100$.

likely to take the first step. In this case a focal locus that rises, has to out-compete 9 redundant competitors. Yet, if the population has already traveled $i > 1$ mutational steps, a focal locus that establishes has to battle a smaller number of potential rivals, namely $L' = L - (i + 1)$. We succeed to provide well fitting approximations for the focal locus that is about to rise and its successor for sufficiently low mutation rates, by appropriately rescaling the background mutation rate $\Theta_{bg} = L' \cdot \Theta_l$, to account for reduced redundancy. As before, we see that the directional selection model and the full model coincide pretty well for earlier sampling, while differences accumulate during the later course of evolution closer to the optimum.

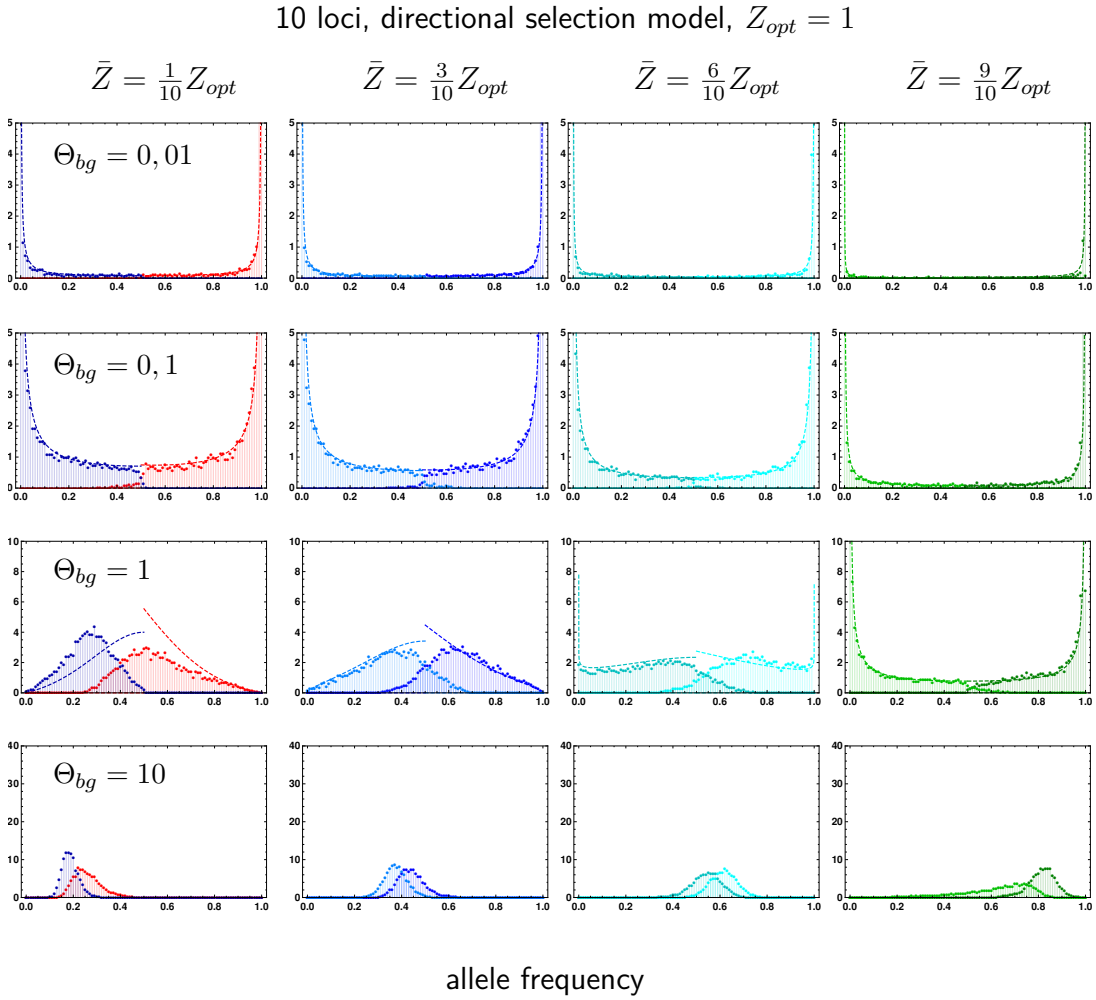

Figure 4.12: **Major and minor loci over course of adaptation.** Using the directional selection model, we always plot the two highest ranking, *redundant* loci. At $\bar{Z} = \frac{1}{10} Z_{opt}$ these correspond to the major and first minor. Once we stop at $i \cdot \frac{1}{L}$, with $i > 1$, $i - 1$ loci are not redundant anymore, as at least i loci are required to reach this optimum ($i - 1$ non redundant steps and $L - (i + 1)$ remaining, redundant loci required for the last mutational step). Hence at $\bar{Z} = \frac{i}{L} Z_{opt}$, redundancy is reduced and we need to appropriately rescale $\Theta'_{bg} = \Theta^i_{bg}$ within our two locus approximations. We use the focal mutation rate $\Theta_1 = \Theta_l$ for the larger locus in the 2 locus approximations for the major locus and the rescaled $\Theta^i_{bg} = (L - i)\Theta_{bg}$ for all other mutation rates. 10 000 replicates, $s_b = 0.1$.

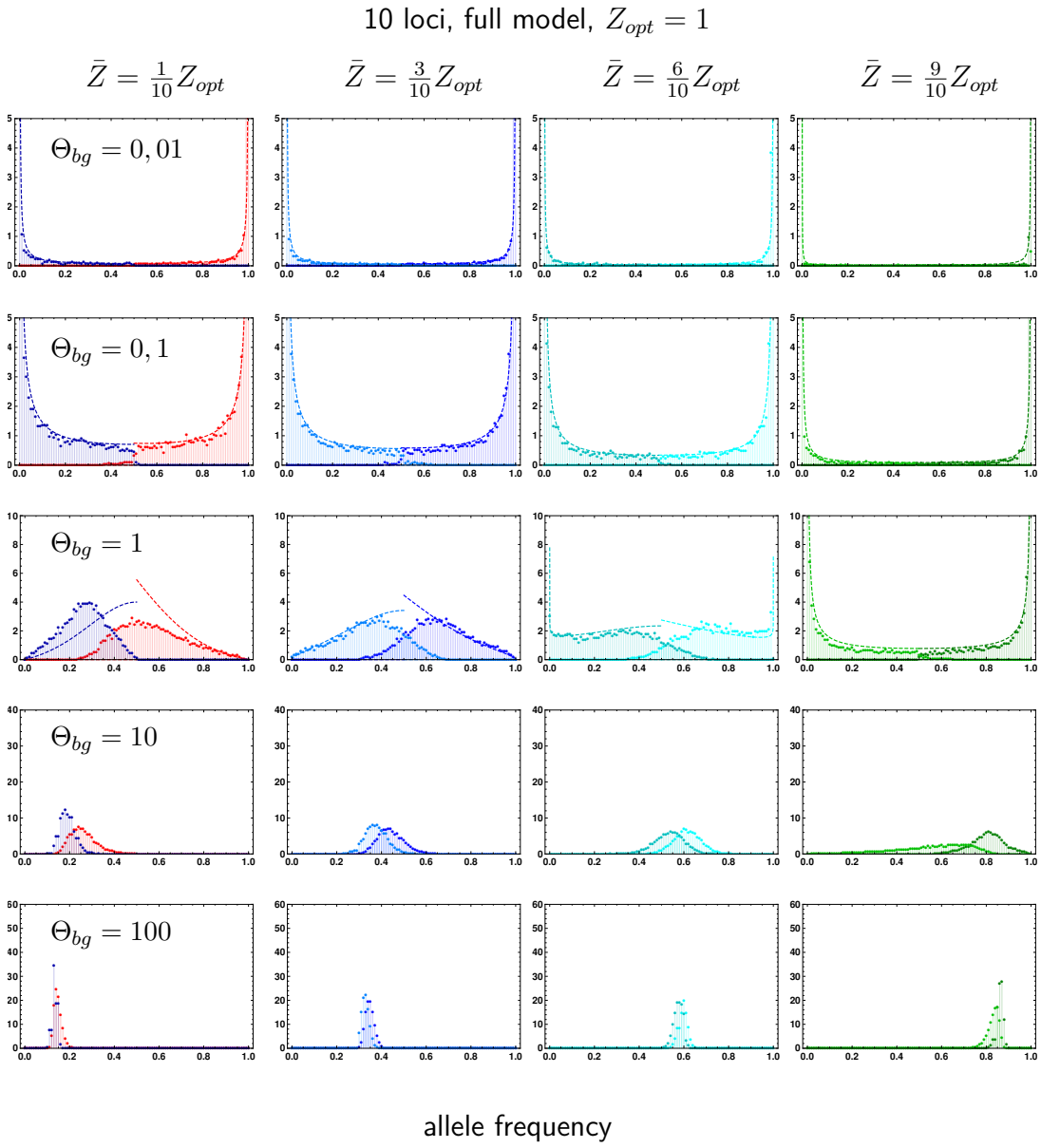

Figure 4.13: **Major and minor loci over course of adaptation.** Adaptive architecture resulting from the full selection model. All other parameters are chosen as in Fig. 4.12.

4.3.4 Adaptation from standing genetic variance

Build-up of standing genetic variance

We let populations evolve under both selection models and test when they have successfully equilibrated to an optimum $0 < Z_{opt}^{SGV} < 1$. At time $t = 0$, we fix $L \cdot Z_{opt}^{SGV}$ loci to 1 (A_i allele) and the rest to 0 (a_i allele). We choose Z_{opt}^{SGV} in a way, such that this is always possible. Then we follow the mean of the normalized variance within the population $\frac{1}{L}\sum_{i\leq L} p_i(1-p_i)$ over the course of time (see Fig. 4.14). We find that after $8N_e$ generations the mean population variance has reached a stable value. This is much lower for the full model, compared to the directional selection model, as the former purges genetic variance much more efficiently.

Adaptation from SGV

In Fig. 4.15 and 4.16 we present our results for adaptive patterns for adaptation from SGV (*i.e.* mutation-selection-drift balance) to a new, shifted optimum. As we let the population equilibrate for $8N_e$ generations at an equilibrium $0 < Z_{opt}^{SGV} < Z_{opt}$, we implement evolution under the full selection model during the equilibration phase, because the directional model is not well suited to capture this phase. Again we initiate the simulations with $L \cdot Z_{opt}^{SGV}$ loci fixed to $p_{A_i} = 1$ and the rest fixed to $p_{A_i} = 0$ at $t = 0$. With low mutation rates, and $Z_{opt}^{SGV} = 0.5$ this entails that 50% of the loci will be fixed or close to fixation for the A_i-allele also at the change of the environment. Subsequently, the new optimum is shifted to Z_{opt}, which we here set to $Z_{opt} = Z_{opt}^{SGV} + \frac{1}{L}$ in Fig. 4.15 and 4.16. This corresponds to a distance of one mutational step and hence complete redundancy within the remaining loci in state a_i. We compare allele frequencies p_{A_i} before and after adaptation, that is after the equilibration phase (gray squares) and at complete phenotypic adaptation to the new optimum for $L = 4, 10$ and 100 loci (colored circles).

Given that we do not start from an ancestral monomorphic a_i state, the locus with

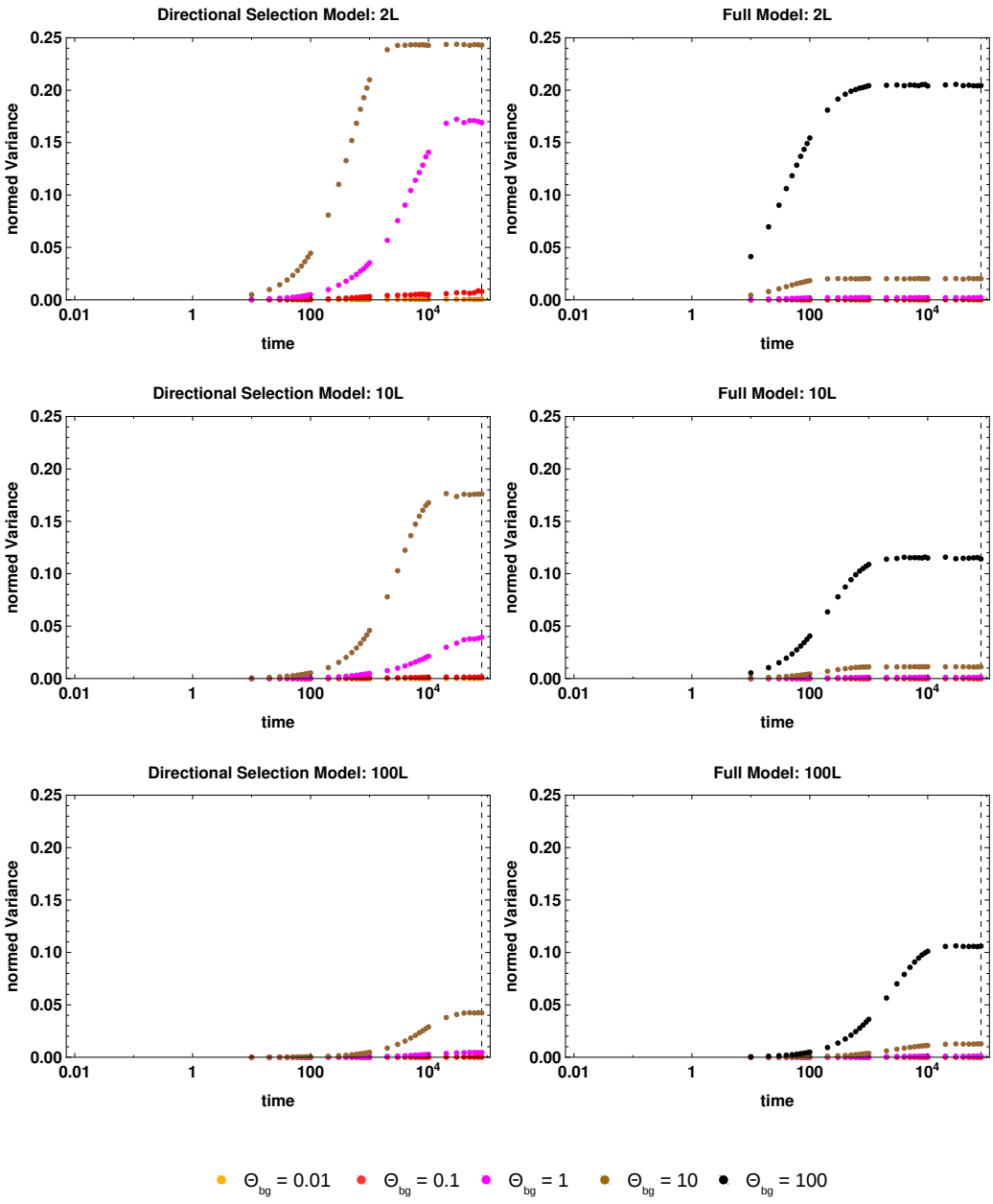

Figure 4.14: **Available SGV with directional selection and full model.** We show that the normed variance of allele frequencies, $\frac{1}{L}\sum_{i\leq L} p_i(1-p_i)$, with $Z_{opt}^{SGV} = 0.5$ has equilibrated after the burn-in-period of $t = 8N_e$ (grid line). The obtained mean in the full model is about a magnitude lower compared to the directional selection model. We simulate 1000 replicates per mutation rate, for $10\,000$ haploid individuals, and a selection coefficient of $s = 0.1$.

the highest allele frequency at the end is not necessarily the locus that contributed the most to adaptation. Hence we need to adequately redefine the terms "major" and "minor" loci in this context. If used, these will refer to the locus/loci that contributed the most (second most) to adaptation given their respective *frequency increase* during adaptation to the new optimum. In general, for low to intermediate mutation rates, we expect the largest changes for the $\frac{L}{2}$th locus and its runner-up(s). These start out at $p_{A_i} \approx 0$ for low mutation rates. For 4 and 10 loci the representation is rather straight forward, and we simply look at the marginal allele frequency of all L loci within the basis before and after phenotypic adaptation. Yet, for 100 loci, we need to find a good representation. Hence, as before, we bin 10 loci together, such that we present the locus with the highest frequency up to the 10th locus together, followed by the 11th to the 20th and so on. We do so for the distributions at the change of the environment (gray squares), as well as at complete phenotypic adaptation (colored circle). Additionally, we represent 10 individual loci, with order 46 to 55 individually (in colored stars), as these are among the most likely to change and contribute to adaptation.

As before, we find that adaptive architectures with the directional selection model are more polygenic, than they are with the full model and that these differences attenuate with sampling further away form the optimum, yet they do not vanish (data not shown). Overall, we can come to a similar classification of unified adaptive patterns. For the directional selection model, we find mostly one locus sweeping through the population for low $\Theta_{bg} \leq 0.01$. On the other hand, we observe concerted frequency shift like patterns for $\Theta_{bg} \geq 10$. For intermediate mutation rates, the adaptive patterns are best characterized by a handful of partial sweeps.

The bounds of this classification patterns are shifted upwards, that is less polygenic in the full model, such that we have mostly single sweeps for $\Theta_{bg} \leq 0.1$ and subtle frequency shifts for $\Theta_{bg} \geq 100$. For example for $L = 100$ and $\Theta_{bg} \geq 100$, we find that the 46th to 55th allele frequency distributions are all situated at intermediate frequencies, and as such all homogeneously contribute to adaptation. Intermediate patterns of completed

and partial sweeps are found for mutation rates between these bounds.

As discussed before, to obtain well fitting predictions we need to rescale Θ_{bg} in order to capture effective redundancy. With adaptation from $Z_{opt}^{SGV} = 0.5$ to a new optimum $Z_{opt} = Z_{opt}^{SGV} + \frac{1}{L}$, redundancy within the trait basis is reduced, as it takes already $\frac{L}{2}$ loci to reach Z_{opt}^{SGV}. This leaves only $\frac{L}{2}$ redundant loci to respond to selection. In Fig. 4.15 we hence show approximations based on $\Theta'_{bg} = \frac{\Theta_{bg}}{2}$. With this rescaling, we can again perfectly predict the allele frequency distribution of the mainly contributing loci (major) and its pursuer (minor). Therefore, in the four locus case there are usually only two loci at low frequency p_{A_i}, that might respond to the new selection pressure, hence described well by two locus formalism. In the ten locus case, for $\Theta_{bg} > 0.1$ we use the 3 locus case and the appropriately rescaled $\Theta'_{bg} = \frac{\Theta'_{bg}}{2}$. For $\Theta'_{bg} < 10$, the fit of these approximations is very satisfactory.

4.4 Discussion

In this Chapter, we show that the adaptive patterns of a QT-model under stabilizing selection, can be conceived as an extension to the model of a binary, complex trait presented in Chapter 3. However, as complete or strong genetic redundancy is often perceived as a limitation, we have set up this model in the tradition of quantitative genetics. This enables us to study a complex trait of arbitrary redundancy governed by a basis of biallelic loci with additive, genotypic effects under stabilizing selection.

As before, we include the whole range of possible adaptive patterns, from sweeps to concerted frequency shifts. In the QT-model the required negative epistasis for small concerted frequency shifts is accomplished by the stabilizing selection scheme, a common feature of QT-models. Second, the clear distinction of sweep versus shift patterns requires explicit tracking of allele frequencies, instead of the summaries of phenotypic means or variances. To achieve this, we start from deterministic, single locus dynamics in Eq. (4.5) and assuming linkage equilibrium, we are able to derive individual, differential equations for each of the allele frequency dynamics at each locus, Eq. (4.9) with

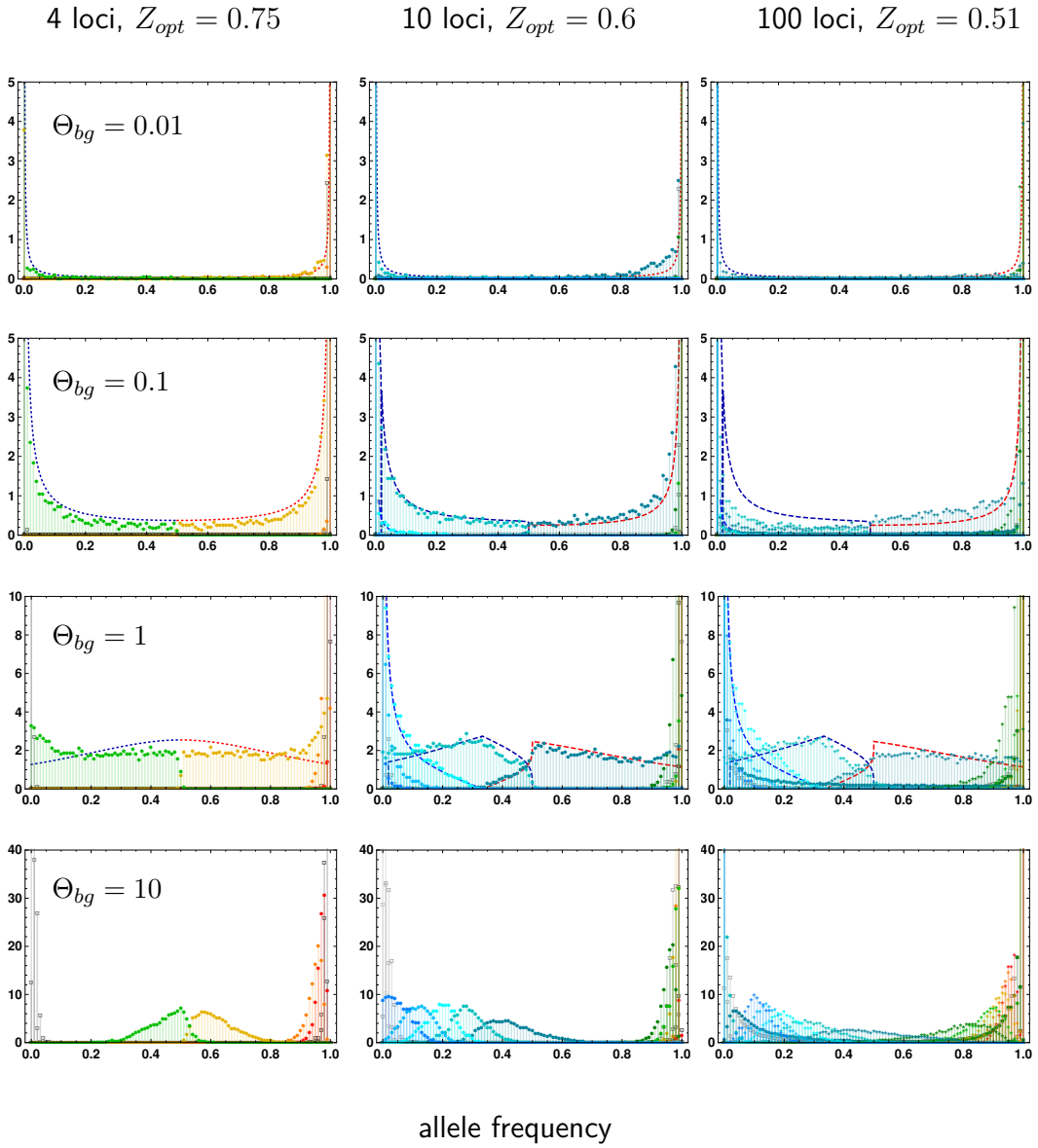

Figure 4.15: **Adaptation from SGV with the directional selection model.** Derived allele frequency distributions are given at complete phenotypic adaptation from SGV ($Z_{opt}^{SGV} = 0.5$) to a new optimum $Z_{opt} = 0.5 + \frac{1}{L}$ under the directional selection model. In simulations SGV builds up under the full model. For 4 and 10 loci we plot the marginal allele frequency distribution for loci in descending frequencies at $t = 8N_e$ in gray squares (dark to light) and at complete adaptation in colored, full circles (red to yellow to green to blue). For 100 loci, we display marginal frequency distributions of summaries of 10 binned loci (first to tenth locus, eleventh to 20th locus, etc.) in gray squares at $t = 8N_e$ and at complete adaptation in colored circles. Additionally, we show the marginal frequency of 10 individual loci, *i.e.* the 46th to the 55th locus, in colored asterisks. In the 4 locus case we show 2 locus approximations for the major (red) and minor (blue) locus, obtained for rescaled $\Theta'_{bg} = \Theta_{bg} \cdot \frac{1}{2}$. In the 10 and 100 locus case, we use the 2 locus approximations due to numerical reasons for $\Theta_{bg} = 0.01$ and rescale Θ'_{bg} accordingly. We switch to the 3 locus formalism with $\Theta_{bg} \geq 0.1$. 10 000 replicates, $s_b = 0.1$.

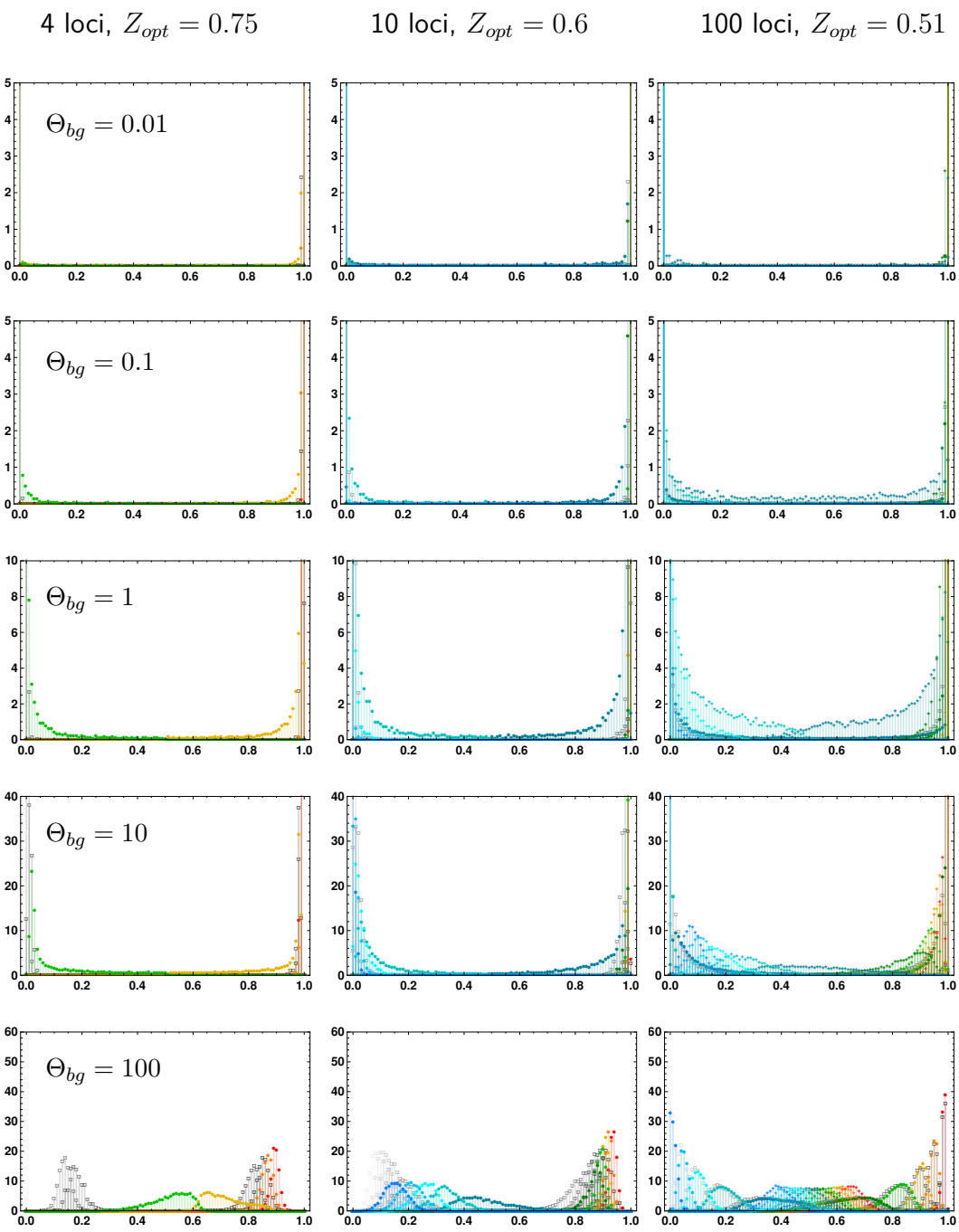

Figure 4.16: **Adaptation from SGV with the full model.** Derived allele frequency distributions are given at complete phenotypic adaptation to a new optimum $Z_{opt} = 0.5 + \frac{1}{L}$ under the full model before and after the environmental change. All other parameter settings are as given in the previous Fig. 4.15.

stabilizing fitness. The obtained dynamics coincide with the model studied by de Vladar and Barton (2014); Jain and Stephan (2015, 2017) and describe the initial phase of rapid phenotypic adaptation. As done in these previous papers, we focus either only on directional selection, or we additionally include a term capturing the depletion of genetic variance. The previous results show that the former, directional selection model is a satisfactory approximation to the latter, full model, for the initial phase of rapid adaptation.

Yet, the aforementioned studies all restrict their investigations to infinite population size, hence neglecting the effect of genetic drift. We combine their approach, and extend it to include genetic drift. Given the striking similarity between the deterministic dynamics of the redundant trait model and the QT-model, we can adapt the developed framework to capture the dynamics in the QT-model. In detail, we use the same partitioning of the adaptive process into an initial stochastic and a subsequent deterministic phase. Then, we study the outcome of the initial phase, which transmits to the final adaptive architecture upon phenotypic adaptation. We again obtain comprehensive analytical results, predicting joint and marginal allele frequency distributions upon adaptation with selection, mutation and drift. This is achieved by a simple, additional transformation of variables, such that the analytical predictions based on the Yule process derived in Chapter 3 expand to the QT-model. (However, this is only possible for the directional selection model, while it does not work for the full model, due to the mathematical complexity of the dynamical equations there.) Indeed, these new predictions yield an extremely good fit to the performed Wright-Fisher simulations. We also present a solution how to deal with a discrete, polygenic trait basis under stabilizing selection in a stochastic framework by using single locus dynamics and assuming LE.

4.4.1 Adaptive architectures

Similarly to the redundant trait model, we investigate trait bases of different sizes L and recover Θ_{bg} as the most decisive, single compound parameter. As with the binary

trait and predicted by our analytical framework, selection strength does not influence the resulting architecture, at least for the directional selection model. This also holds true for the full model, as long as the population is samples far enough from the optimum.

We study adaptation from de novo mutations, as well as from SGV to close optima (one or two mutation steps away) and recuperate a similar threefold classification of adaptive architectures as with the binary trait. Thereby, several mechanisms work against each other to shape the adaptive reponse in the QT-model. On the one hand, when looking at the dynamical equations, due to the extra term $1-p$ a focal allele hampers its own rise more effectively than in the binary trait model. On the other hand, we need to consider that for adaptation across long distances an effectively reduced Θ_{bg} enters the predictions (see next paragraph). Also, the full QT-model predicts a stronger sweep-like architecture once we are close to the optimum. So, all in all, there is at most a slight shift towards "more shifts" and the broad classification remains the same. This also holds up for reduced redundancy.

As before, we obtain well fitting predictions, if we rescale Θ'_{bg} according to the *effective* redundancy, such that $\Theta'_{bg} = 2N\mu(L'-1)$, where L' gives the number of truly redundant loci within the basis (usually $\Theta'_{bg} < \Theta_{bg}$). This number might also change over the course or adaptation, depending on the distance of the population with respect to the optimum it adapts to. In detail this means, that a trait basis of a trait adapting to an optimum, that can be reached with a single mutation, is completely redundant over the entire course of adaptation. However, a genetic basis of a trait adapting to an optimum, that requires several mutations, shows decreasing redundancy over the course of evolution. Accounting for this continuous change of redundancy, we cannot only predict the final adaptive architectures, but we develop comprehensive predictions for the entire adaptive process. This holds, for the directional and the full selection model, as long as Z_{opt} is far enough away, such that directional selection dominates the dynamics, as well as if mutation rates are sufficiently low, $\Theta_{bg} \leq 1$.

The course of adaptation

Conceptually, we choose not to analyze the dynamics in dependence of time, but we rather consider them in dependence of phenotypic adaptation. As such, we describe the stopping condition in terms of allele frequencies or analogously of the mean population phenotype. This could also be applied to evolution experiments, where often adaptation is studied across replicates at the same time (Franssen et al., 2017; Barghi et al., 2018). If the adaptive process abides to deterministic mechanisms, such that new mutations are negligible and genetic variance is homogeneous over different replicates, time might serve as an appropriate point of reference. Yet, if adaptation is more stochastic, as with small sample sizes under strong genetic drift, different replicates at the same time point, might not be well suited for comparisons. Instead, our predictions are based on the course of phenotypic adaptation, such that replicates should be compared, if they have reached similar levels of adaptation.

Gene-centered versus trait centered view of adaptation

As also discussed in the previous Chapter, there are different ways how to interpret adaptive architectures. In contrast to the trait or genome based view, that we mostly follow here, we can also look at the marginal distribution of a focal locus. This distribution conceptualizes a more gene-centered view, presented in the previous literature (*e.g.* Chevin and Hospital, 2008; Pavlidis et al., 2012; Wollstein and Stephan, 2014). In Fig. 4.8 and 4.9 we show that increasing the number of loci within the basis of a trait that adapts to the same trait optimum, *e.g.* $Z_{opt} = 0.5$, diminishes the likelihood of a polygenic response *for a focal locus*, such that sweeps become more and more abundant. Yet, this is of course not due to the increased size of the trait basis, but due to the relaxed level of redundancy, and hence in good agreement with our previous results.

4.4.2 Adaptation from SGV

When studying adaptation from SGV, we need to make several, conceptual adjustments. First, to assess the adaptive architecture we need to consider the differences in the allele frequency distributions after the built-up of SGV in comparison to the state at adaptation to the new optimum. This also entails that the major locus, now refers to the locus with the largest frequency change (rather than the largest absolute value at the end), which is again the locus with the largest contribution to adaptation. Similarly, the minor loci are ordered according to their contributions. Second, for adaptation from an intermediate optimum we obtain an effective reduction of redundancy. Yet, keeping our previous results for evolution over several mutational steps in mind, we simply use the rescaled Θ'_{bg} (proportional to the true number of redundant loci). It is quite striking that we obtain such a good fit using the two and three locus formalisms, especially considering the non-trivial shape of these distributions. Remaining deviations, especially for a larger trait basis, can be attributed to the higher degree of flexibility of which loci yield phenotypic adaptation, when adaptation occurs from SGV. At $\Theta_{bg} \geq 0.1$, when mutation rates are not too low, we start adaptation from a population containing variation at both ends of the frequency spectrum (high, $p \lesssim 1$ and low $p \gtrsim 0$ frequency polymorphisms). The high frequency polymorphisms of derived variants can quickly react to the new selection pressure, such that the strength of the sweeps at the major and minor loci are slightly dampened compared to the predictions.

The analysis of adaptation from SGV with drift is of particular interest, as previous studies have effectively neglected drift effects. This leads to a dominance of intermediate starting frequencies at the onset the environmental change. On the contrary, in our approach, we do not see this, but we rather obtain a bimodal distribution of starting frequencies, centered around ancestral and derived variants for low to intermediate background mutation rates. This also entails that the adaptive architectures we recuperate with our approach are much less polygenic that previously obtained results using the same dynamics in a deterministic framework (de Vladar and Barton, 2014; Jain and

Stephan, 2015, 2017).

4.4.3 Outlook

There are several obvious next steps, some of which are already work in progress.

- *Different locus effects*: We have so far only treated the case of equal locus effects, which has made analytical predictions possible. Nevertheless, it is a necessary to extend our approach to variable locus effects to capture the full complexity of biological reality. In general, we predict that different locus effects γ_i will result in heterogeneous, less polygenic response, because larger effect loci will dominate the dynamics, especially, for adaptation from SGV, as they sweep quicker – but they could start from lower frequencies. Indeed, the independence of selection strength in our predictions relies on the assumption of uniform locus effects.

- *Linkage*: With increasing trait basis our assumption of LE between the different loci becomes less likely. Especially with complex traits governed by hundreds or thousands of loci, some of them will necessarily fall onto the same linkage group. The implementation of linkage, however, requires substantial alterations to our simulation approach, including a switch to individual based simulations. This poses heavy constraints on the computability of such simulations.

- *Diploids and dominance*: Another possible extension concerns the treatment of diploid populations, including deviations from co-dominance.

- *Population structure and its evolution*: Finally, so far we have only considered panmictic populations. There are of course interesting questions, when thinking about structured populations. How might isolation by distance affect the obtained adaptive patterns? How will changing N_e impact the results? This is of particular interest in the case of human evolution, where signals of polygenic adaptation have been vividly discussed over the last decade (*e.g.* Pritchard et al., 2010; Berg et al., 2018; Sohail et al., 2018; Csilléry et al., 2018). The various bouts of strong

population extension since the movement "out of Africa", as well as admixture events (Pickrell and Reich, 2014; Lazaridis et al., 2016), might also have a strong impact on adaptive architectures.

E. Supporting Information: Results

De novo adaptation to different optima

In analogy to Fig. 4.1, we present snapshots of the course of adaptation of a 2 locus trait to $Z_{opt} = 0.3$ and 0.8. Qualitatively, the same classification patterns holds true, with single sweeps for low background mutation rates and shift like patterns for high background mutation rates. Again the directional selection model yields more polygenic responses, than the full model at complete adaptation. We also see that we can appropriately predict the outcome for the directional selection model at arbitrary stopping conditions.

Back mutation

In our simulations, we focus on the initial adaptive phase. Directional selection quickly brings the phenotypic mean of the population to the new optimum. As this phase is short, we do not expect many mutation events if mutation rates are reasonably low. Hence, we can understand that neglecting back-mutations during the rapid adaptive phase does not alter the results significantly, as can be seen in Fig. E.3 in comparison to analogous results with back-mutation presented before in Fig. 4.1.

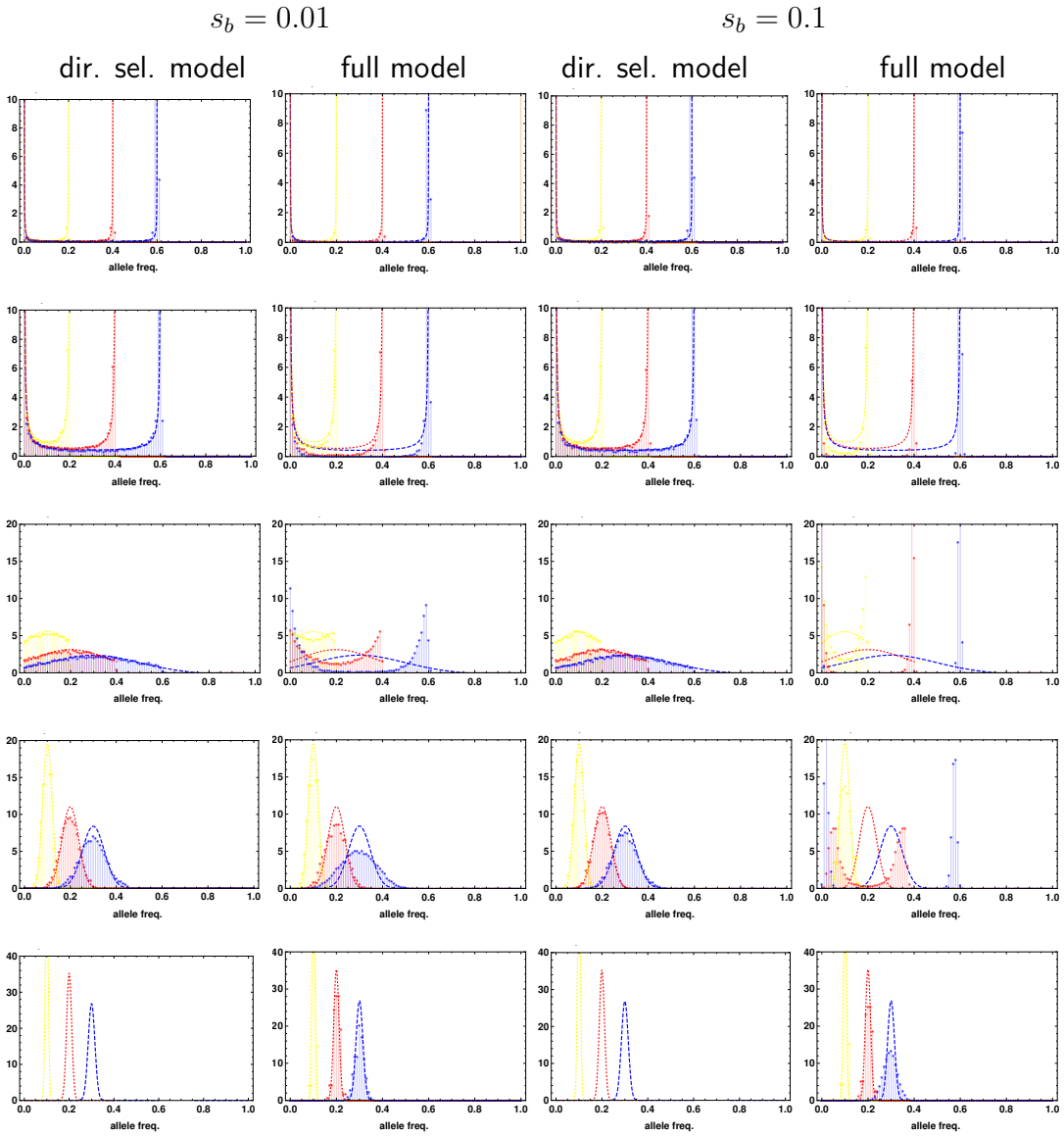

Figure E.1: **Allele frequency distribution, 2L,** $Z_{opt}^{new} = 0.3$ We capture the allele frequency distribution at three states of adaptation: When the population has adapted to $\frac{1}{3} \cdot Z_{opt}^{new}$ in yellow, $\frac{1}{3} \cdot Z_{opt}^{new}$ in red and at complete adaptation to the new optimum in blue.

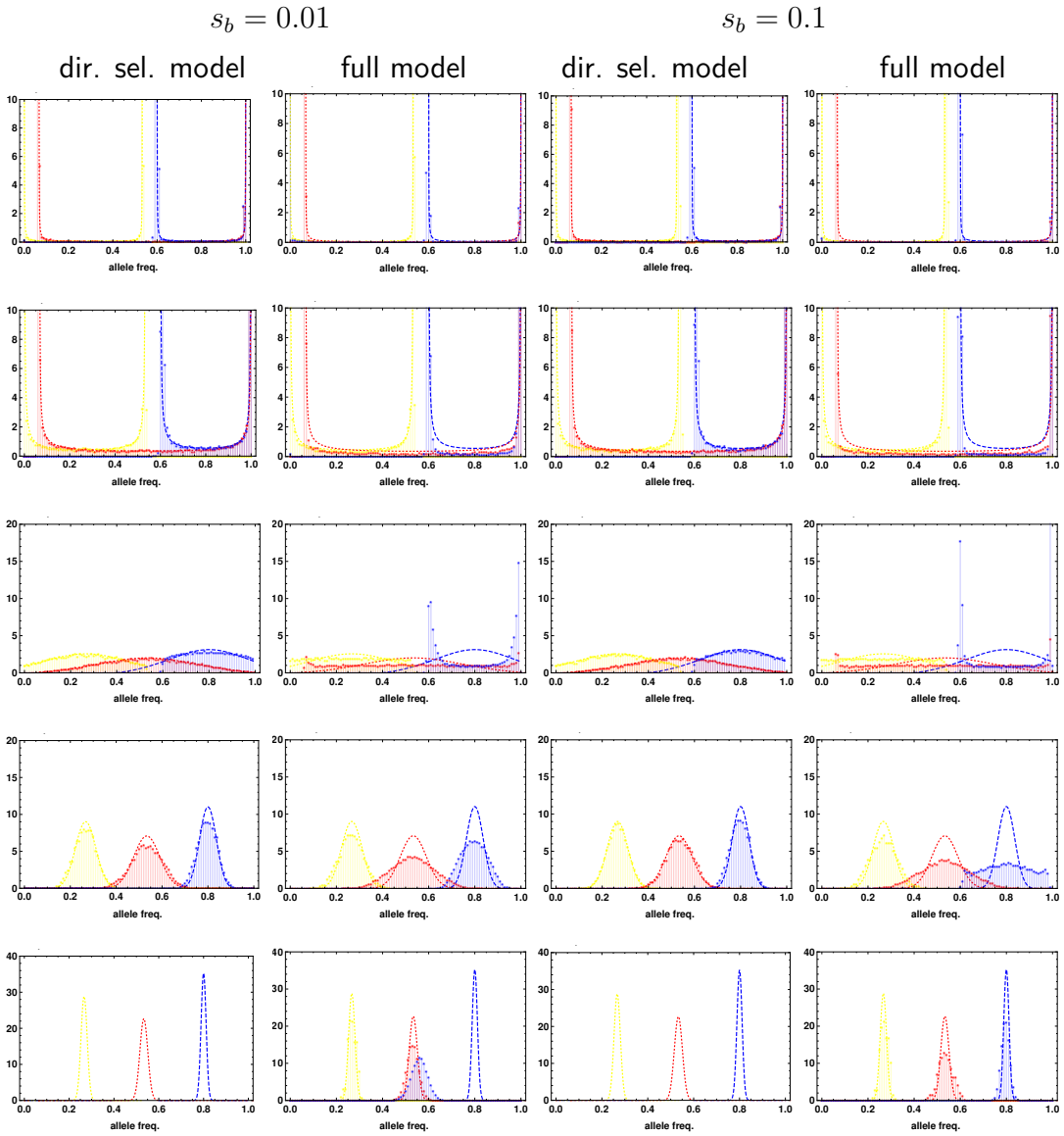

Figure E.2: **Allele frequency distribution, 2L,** $Z_{opt}^{new} = 0.8$ We capture the allele frequency distribution at three states of adaptation: When the population has adapted to $\frac{1}{3} \cdot Z_{opt}^{new}$ in yellow, $\frac{1}{3} \cdot Z_{opt}^{new}$ in red and at complete adaptation to the new optimum in blue.

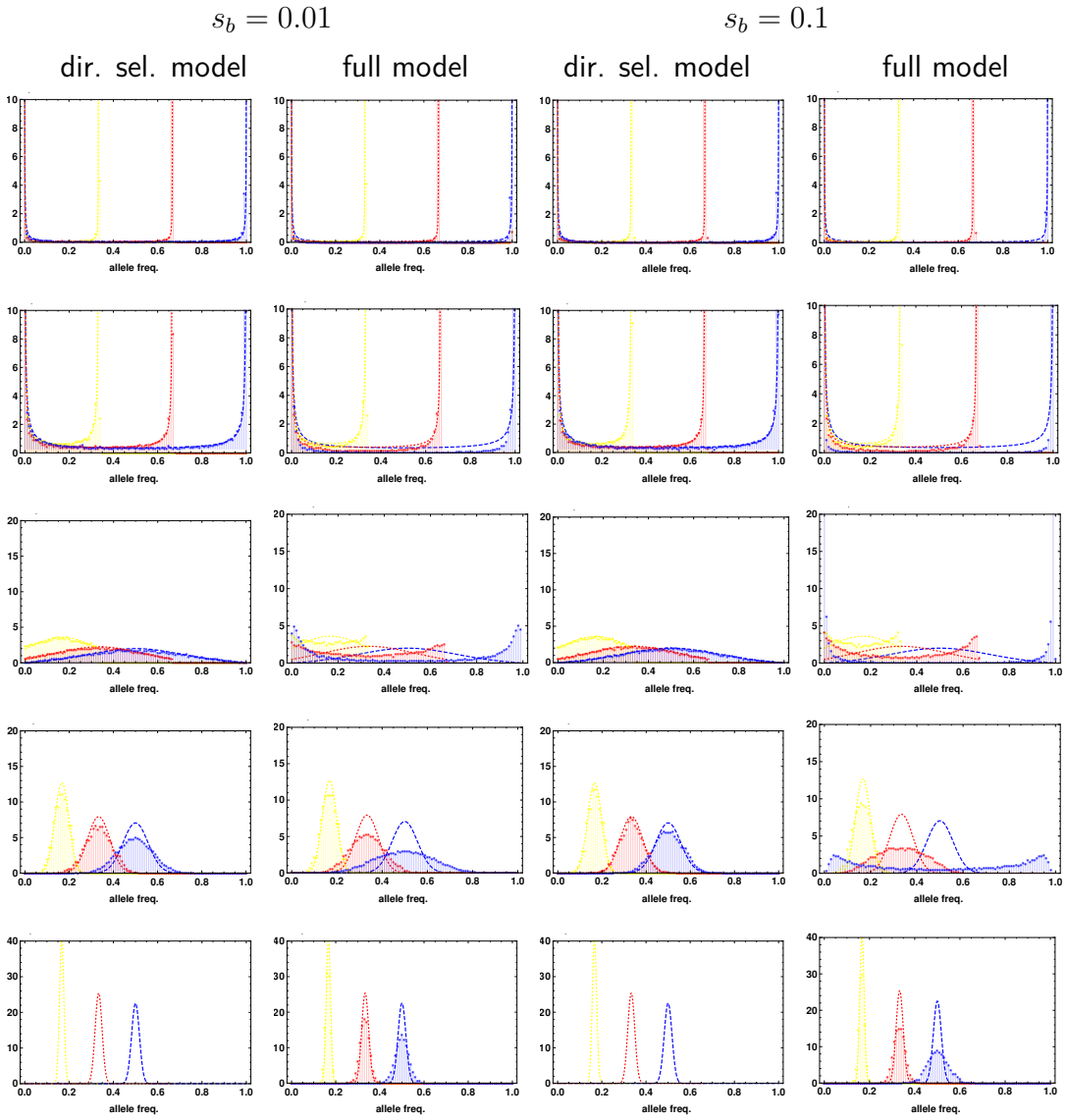

Figure E.3: **Allele frequency distribution, 2L, without backmutation,** $Z_{opt}^{new} = 0.5$**.** We capture the allele frequency distribution at three states of adaptation, similarly to Figure 4.1, however now we ignore backmutation from the derived to the acestral allele. We show data for when the population has adapted to $\frac{1}{3} \cdot Z_{opt}^{new}$ in yellow, $\frac{1}{3} \cdot Z_{opt}^{new}$ in red and at complete adaptation to the new optimum in blue and find no differences to results with backmutation.

F. Supporting Information: Mathematical Appendix

Here, we start out with the *directional selection model* of Jain and Stephan (2017),

$$\dot{p}_i = s\gamma_i p_i(1-p_i)(Z_{\text{opt}} - \bar{Z})$$

where $\bar{Z} = \sum_i p_i\gamma_i$ is the mean of a quantitative trait governed by L loci under stabilizing selection. Defining new variables $u_i = p_i/(1-p_i)$, the dynamics can be written as

$$\dot{u}_i = s\gamma_i u_i(Z_{\text{opt}} - \bar{Z})$$

and

$$\frac{\partial}{\partial t}\frac{u_i}{u_j} = \frac{u_i}{u_j}(\gamma_i - \gamma_j)(Z_{\text{opt}} - \bar{Z})\,.$$

Assume now that all loci are equal, $\gamma_i = \gamma$. Like for the model with complete redundancy, we then have $\partial/\partial t(u_i/u_j) = 0$. To include genetic drift, we can try and set up a Yule process model for parameters u_i. Note that the u_i are unbounded variables and run from 0 to ∞. According to the Yule process, the joint distribution of the ratios $u_i/\sum_i u_i$ converges to the Dirichlet distribution and the distribution of the ratios u_i/u_1 converges to the inverted Dirichlet distribution. In general, we are rather interested in the p_i than in the u_i and in a stopping condition based on the trait mean, or of

$$\frac{\bar{Z}}{\gamma} = \sum_{i=1}^{L} p_i = \sum_{i=1}^{L} \frac{u_i}{u_i+1} =: c_Z\,. \tag{F.1}$$

with $c_Z \in [0, L]$. It is easier to work with the inverted Dirichlet distribution, where the transformation of variables reads

$$x_i := \frac{u_i}{u_1} = \frac{p_i(1-p_1)}{(1-p_i)p_1} = \frac{p_i(1+\sum_{k=2}^{L} p_k - c_Z)}{(1-p_i)(c_Z - \sum_{k=2}^{L} p_k)} \tag{F.2}$$

The Jacobian follows as

$$\begin{aligned}\mathbf{J}_{ij} = \frac{\partial x_i}{\partial p_j} &= \frac{p_i}{(1-p_i)(c_Z - \sum_{k=2}^L p_k)^2} + \delta_{i,j}\frac{1+\sum_{k=2}^L p_k - c_Z}{(1-p_i)^2(c_Z - \sum_{k=2}^L p_k)} \\ &= \frac{p_i(1-p_i) + \delta_{ij}\, p_1(1-p_1)}{(1-p_i)^2 p_1^2}\end{aligned} \tag{F.3}$$

with determinant

$$\begin{aligned}\mathsf{Det}[\mathbf{J}] &= \prod_{i=2}^L \frac{1}{(1-p_i)^2}\left(\frac{1+\sum_{k=2}^L p_k - c_Z}{c_Z - \sum_{k=2}^L p_k}\right)^L \left(1 + \frac{\sum_{i=2}^L p_i(1-p_i)}{(1+\sum_{k=2}^L p_k - c_Z)(c_Z - \sum_{k=2}^L p_k)}\right) \\ &= \prod_{i=2}^L \frac{1}{(1-p_i)^2}\left(\frac{1-p_1}{p_1}\right)^L \left(1 + \frac{\sum_{i=2}^L p_i(1-p_i)}{p_1(1-p_1)}\right) \\ &= \prod_{i=1}^L \frac{1}{(1-p_i)^2}\left(\frac{1-p_1}{p_1}\right)^L \left(\sum_{i=1}^L p_i(1-p_i)\right) .\end{aligned}$$

The joint distribution of the p_i at the stopping condition follows as

$$\begin{aligned}\mathsf{P}[\{p_i\}|c_Z] &= C_\Gamma \mathsf{Det}[\mathbf{J}] \prod_{i=2}^L \left(\frac{p_i(1-p_1)}{(1-p_i)p_1}\right)^{\Theta_i - 1} \left(1 + \sum_{i=1}^L \frac{p_i(1-p_1)}{(1-p_i)p_1}\right)^{-\Theta - \sum_{i=2}^L \Theta_i} \\ &= C_\Gamma \mathsf{Det}[\mathbf{J}] \prod_{i=1}^L \left(\frac{p_i(1-p_1)}{(1-p_i)p_1}\right)^{\Theta_i - 1} \left(\sum_{i=1}^L \frac{p_i(1-p_1)}{(1-p_i)p_1}\right)^{-\sum_{i=1}^L \Theta_i} \\ &= C_\Gamma \prod_{i=1}^L \frac{p_i^{\Theta_i - 1}}{(1-p_i)^{\Theta_i + 1}} \left(\sum_{i=1}^L p_i(1-p_i)\right) \left(\sum_{i=1}^L \frac{p_i}{1-p_i}\right)^{-\sum_{i=1}^L \Theta_i}\end{aligned}$$

defining $\Theta \equiv \Theta_1$ and

$$C_\Gamma = \frac{\Gamma(\Theta + \sum_i \Theta_i)}{\Gamma(\Theta)\prod_i \Gamma(\Theta_i)} .$$

Because the stopping condition is symmetric in the p_i, $i = 1, \ldots, L$, also the joint distribution is symmetric in the locus frequencies (*i.e.*, under the exchange of p_i and corresponding mutation rates Θ_i). Due to the constraint (F.1), the distribution is $L-1$-dimensional and for a given frequency at any $L-1$ loci, the frequency at the last Lth

locus follows. Eliminating (for example) p_1, the distribution reads

$$\begin{aligned}
\mathsf{P}[\{p_i\}|c_Z] &= C_\Gamma \mathsf{Det}[\mathbf{J}] \prod_{i=2}^{L} \left(\frac{p_i(1+\sum_{k=2}^{L} p_k - c_Z)}{(1-p_i)(c_Z - \sum_{k=2}^{L} p_k)} \right)^{\Theta_i - 1} \left(1 + \frac{(1+\sum_{k=2}^{L} p_k - c_Z) \sum_i \frac{p_i}{1-p_i}}{c_Z - \sum_{k=2}^{L} p_k} \right)^{-\Theta - \sum_i \Theta_i} \\
&= C_\Gamma \prod_{i=2}^{L} \frac{p_i^{\Theta_i - 1}}{(1-p_i)^{\Theta_i + 1}} \left(1 + \frac{\sum_{i=2}^{L} p_i(1-p_i)}{(c_Z - \sum_{k=2}^{L} p_k)(1+\sum_{k=2}^{L} p_k - c_Z)} \right) \\
&\quad \cdot \left(1 + \frac{1+\sum_{k=2}^{L} p_k - c_Z}{c_Z - \sum_{k=2}^{L} p_k} \sum_{i=2}^{L} \frac{p_i}{1-p_i} \right)^{-\Theta} \left(\frac{c_Z - \sum_{k=2}^{L} p_k}{1+\sum_{k=2}^{L} p_k - c_Z} + \sum_{2=1}^{L} \frac{p_i}{1-p_i} \right)^{-\sum_{2=1}^{L} \Theta_i}
\end{aligned}$$

For two loci, in particular, we obtain ($p_2 \equiv p$)

$$\begin{aligned}
\mathsf{P}[p|c_Z] &= \frac{\Gamma(\Theta + \Theta_2)}{\Gamma(\Theta)\Gamma(\Theta_2)} \frac{p^{\Theta_2 - 1}}{(1-p)^{\Theta_2 + 1}} \left(1 + \frac{p(1-p)}{(c_Z - p)(1+p-c_Z)} \right) \\
&\quad \cdot \left(1 + \frac{1+p-c_Z}{c_Z - p} \frac{p}{1-p} \right)^{-\Theta} \left(\frac{c_Z - p}{1+p-c_Z} + \frac{p}{1-p} \right)^{-\Theta_2} \\
&= \frac{\Gamma(\Theta + \Theta_2)}{\Gamma(\Theta)\Gamma(\Theta_2)} \frac{p(1-p) + (c_Z - p)(1+p-c_Z)}{(c_Z - 2p(c_Z - p))^{\Theta + \Theta_2}} \\
&\quad \cdot ((c_Z - p)(1-p))^{\Theta - 1} ((1+p-c_Z)p)^{\Theta_2 - 1} . \qquad \text{(F.4)}
\end{aligned}$$

References

Aeschbacher, S. and Bürger, R. (2014). The effect of linkage on establishment and survival of locally beneficial mutations. *Genetics*, 197(1):317–336.

Agrawal, A., Feder, J., and Nosil, P. (2011). Ecological divergence and the origins of intrinsic postmating isolation with gene flow. *International Journal of Ecology*, 2011.

Akerman, A. and Bürger, R. (2014). The consequences of gene flow for local adaptation and differentiation: a two-locus two-deme model. *Journal of mathematical biology*, 68(5):1135–1198.

Bank, C., Bürger, R., and Hermisson, J. (2012). The limits to parapatric speciation: Dobzhansky–Muller incompatibilities in a continent–island model. *Genetics*, 191(3):845–863.

Barbash, D., Awadalla, P., and Tarone, A. (2004). Functional divergence caused by ancient positive selection of a Drosophila hybrid incompatibility locus. *PLoS biology*, 2:839–848.

Barghi, N., Tobler, R., Nolte, V., Jaksic, A. M., Mallard, F., Otte, K., Dolezal, M., Taus, T., Kofler, R., and Schloetterer, C. (2018). Polygenic adaptation fuels genetic redundancy in drosophila. *bioRxiv*, page 332122.

Barnard-Kubow, K., So, N., and Galloway, L. (2016). Cytonuclear incompatibility contributes to the early stages of speciation. *Evolution*, 70(12):2752–2766.

Barton, N. (1998). The effect of hitch-hiking on neutral genealogies. *Genetics Research*, 72(2):123–133.

Barton, N. (2010). Understanding adaptation in large populations. *PLoS genetics*, 6(6):e1000987.

Barton, N. (2013). Does hybridization influence speciation? *Journal of evolutionary biology*, 26(2):267–269.

Barton, N. and Bengtsson, B. (1986). The barrier to genetic exchange between hybridising populations. *Heredity*, 57(3):357–376.

Barton, N., Etheridge, A., and Véber, A. (2017). The infinitesimal model: Definition, derivation, and implications. *Theoretical population biology*, 118:50–73.

Barton, N. and Keightley, P. D. (2002). Multifactorial genetics: understanding quantitative genetic variation. *Nature Reviews Genetics*, 3(1):11.

Bateson, W. (1909). Heredity and variation in modern lights. *Darwin and modern science*, 85:101.

Berg, J. J. and Coop, G. (2014). A population genetic signal of polygenic adaptation. *PLoS genetics*, 10(8):e1004412.

Berg, J. J., Harpak, A., Sinnott-Armstrong, N., Joergensen, A. M., Mostafavi, H., Field, Y., Boyle, E. A., Zhang, X., Racimo, F., Pritchard, J. K., and Coop, G. (2018). Reduced signal for polygenic adaptation of height in uk biobank. *bioRxiv*.

Beukeboom, L., Koevoets, T., Morales, H. E., Ferber, S., and van de Zande, L. (2015). Hybrid incompatibilities are affected by dominance and dosage in the haplodiploid wasp Nasonia. *Frontiers in Genetics*, 6:14.

Blanckaert, A. and Bank, C. (2018). In search of the goldilocks zone for hybrid speciation. *bioRxiv*, page 266254.

Blanckaert, A. and Hermisson, J. (2018). The limits to parapatric speciation ii: Strengthening a preexisting genetic barrier to gene flow in parapatry. *Genetics*, pages genetics–300652.

Boyle, E. A., Li, Y. I., and Pritchard, J. K. (2017). An expanded view of complex traits: from polygenic to omnigenic. *Cell*, 169(7):1177–1186.

Bürger, R. (2000). *The mathematical theory of selection, recombination, and mutation*. Wiley.

Bürger, R. and Akerman, A. (2011). The effects of linkage and gene flow on local adaptation: A two-locus continent–island model. *Theoretical population biology*, 80(4):272–288.

Bürger, R. and Gimelfarb, A. (1999). Genetic variation maintained in multilocus models of additive quantitative traits under stabilizing selection. *Genetics*, 152(2):807–820.

Bürger, R. and Lynch, M. (1995). Evolution and extinction in a changing environment: a quantitative-genetic analysis. *Evolution*, 49(1):151–163.

Burke, M., Dunham, J., Shahrestani, P., Thornton, K., Rose, M., and Long, A. (2010). Genome-wide analysis of a long-term evolution experiment with drosophila. *Nature*, 467(7315):587–590.

Burton, R. and Barreto, F. (2012). A disproportionate role for mtDNA in Dobzhansky–Muller incompatibilities? *Molecular Ecology*, 21(20):4942–4957.

Butlin, R., Debelle, A., Kerth, C., Snook, R., Beukeboom, L., Castillo, C., Diao, W., Maan, M., Paolucci, S., Weissing, F., et al. (2012). What do we need to know about speciation? *Trends in Ecology & Evolution*, 27(1):27–39.

Cattani, M. and Presgraves, D. (2012). Incompatibility Between X Chromosome Factor and Pericentric Heterochromatic Region Causes Lethality in Hybrids Between Drosophila melanogaster and Its Sibling Species. *Genetics*, 191(2):549–559.

Charlesworth, B., Coyne, J., and Barton, N. (1987). The relative rates of evolution of sex chromosomes and autosomes. *American Naturalist*, pages 113–146.

Chevin, L.-M. and Hospital, F. (2008). Selective sweep at a quantitative trait locus in the presence of background genetic variation. *Genetics*.

Coffman, C. J., Doerge, R. W., Simonsen, K. L., Nichols, K. M., Duarte, C., Wolfinger, R. D., and McIntyre, L. (2005). Model selection in binary trait locus mapping. *Genetics*.

Cook, L., Grant, B., Saccheri, I., and Mallet, J. (2012). Selective bird predation on the peppered moth: the last experiment of michael majerus. *Biology Letters*, 8(4):609–612.

Corbett-Detig, R., Zhou, J., Clark, A., Hartl, D., and Ayroles, J. (2013). Genetic incompatibilities are widespread within species. *Nature*, 504(7478):135–137.

Coyne, J. and Orr, H. (1989). Two rules of speciation. *Speciation and its Consequences*, pages 180–207.

Coyne, J. and Orr, H. (2004). *Speciation*. Sinauer Associates Sunderland, MA.

Crow, J. F. (2010). On epistasis: why it is unimportant in polygenic directional selection. *Philosophical Transactions of the Royal Society of London B: Biological Sciences*, 365(1544):1241–1244.

Cruickshank, T. and Hahn, M. (2014). Reanalysis suggests that genomic islands of speciation are due to reduced diversity, not reduced gene flow. *Molecular Ecology*, 23(13):3133–3157.

Csilléry, K., Rodríguez-Verdugo, A., Rellstab, C., and Guillaume, F. (2018). Detecting the genomic signal of polygenic adaptation and the role of epistasis in evolution. *Molecular ecology*.

Darwin, C. (1859). *The origin of species*. London: Murray.

Daub, J. T., Hofer, T., Cutivet, E., Dupanloup, I., Quintana-Murci, L., Robinson-Rechavi, M., and Excoffier, L. (2013). Evidence for polygenic adaptation to pathogens in the human genome. *Molecular biology and evolution*, 30(7):1544–1558.

de Vladar, H. P. and Barton, N. (2014). Stability and response of polygenic traits to stabilizing selection and mutation. *Genetics*, 197(2):749–767.

Dettman, J., Sirjusingh, C., Kohn, L., and Anderson, J. (2007). Incipient speciation by divergent adaptation and antagonistic epistasis in yeast. *Nature*, 447(7144):585–588.

Dobzhansky, T. (1936). Studies on hybrid sterility. II. Localization of sterility factors in Drosophila pseudoobscura hybrids. *Genetics*, 21(2):113.

Durrett, R. (2010). *Probability: theory and examples*. Cambridge university press.

Ellegren, H. (2009). Genomic evidence for a large-Z effect. *Proceedings of the Royal Society B: Biological Sciences*, 276(1655):361–366.

Ellegren, H., Hultin-Rosenberg, L., Brunström, B., Dencker, L., Kultima, K., and Scholz, B. (2007). Faced with inequality: chicken do not have a general dosage compensation of sex-linked genes. *BMC biology*, 5(1):40.

Ellison, C. and Burton, R. (2008). Interpopulation hybrid breakdown maps to the mitochondrial genome. *Evolution*, 62(3):631–638.

Etheridge, A., Pfaffelhuber, P., Wakolbinger, A., et al. (2006). An approximate sampling formula under genetic hitchhiking. *The Annals of Applied Probability*, 16(2):685–729.

Falconer, D., Mackay, T., and Bulmer, M. (1996). Introduction to quantitative genetics. *Genetical Research*, 68(2):183.

Feder, J., Gejji, R. Y. S., and Nosil, P. (2012). Establishment of new mutations under divergence and genome hitchhiking. *Philosophical Transactions of the Royal Society B: Biological Sciences*, 367(1587):461–474.

Feder, J. and Nosil, P. (2009). Chromosomal inversions and species differences: when are genes affecting adaptive divergence and reproductive isolation expected to reside within inversions? *Evolution*, 63(12):3061–3075.

Felsenstein, J. (1981). Skepticism towards Santa Rosalia, or why are there so few kinds of animals? *Evolution*, pages 124–138.

Field, Y., Boyle, E. A., Telis, N., Gao, Z., Gaulton, K. J., Golan, D., Yengo, L., Rocheleau, G., Froguel, P., McCarthy, M. I., et al. (2016). Detection of human adaptation during the past 2000 years. *Science*, page aag0776.

Fisher, R. A. (1918). The correlation between relatives on the supposition of mendelian inheritance.

Fishman, L. and Sweigart, A. L. (2018). When two rights make a wrong: the evolutionary genetics of plant hybrid incompatibilities. *Annual review of plant biology*, 69.

Fontaine, M., Pease, J., Steele, A., Waterhouse, R. M., Neafsey, D., Sharakhov, I., Jiang, X., Hall, A., Catteruccia, F., Kakani, E., et al. (2015). Extensive introgression in a malaria vector species complex revealed by phylogenomics. *Science*, 347(6217):1258524.

Franssen, S., Kofler, R., and Schlötterer, C. (2017). Uncovering the genetic signature of quantitative trait evolution with replicated time series data. *Heredity*, 118(1):42.

Franssen, S., Nolte, V., Tobler, R., and Schlötterer, C. (2015). Patterns of linkage disequilibrium and long range hitchhiking in evolving experimental drosophila melanogaster populations. *Molecular biology and evolution*, 32(2):495–509.

Gavrilets, S. (1997). Hybrid zones with Dobzhansky-type epistatic selection. *Evolution*, pages 1027–1035.

Geritz, S. A., Mesze, G., Metz, J. A., et al. (1998). Evolutionarily singular strategies and the adaptive growth and branching of the evolutionary tree. *Evolutionary ecology*, 12(1):35–57.

Gerlach, G. (1990). Dispersal mechanisms in a captive wild house mouse population (Mus domesticus Rutty). *Biological Journal of the Linnean Society*, 41(1-3):271–277.

Gingerich, P. D. (2009). Rates of evolution. *Annual Review of Ecology, Evolution, and Systematics*, 40:657–675.

Good, J., Dean, M., and Nachman, M. (2008). A complex genetic basis to X-linked hybrid male sterility between two species of house mice. *Genetics*, 179(4):2213–2228.

Good, J., Giger, T., Dean, M., and Nachman, M. (2010). Widespread over-expression of the X chromosome in sterile F1 hybrid mice. *PLoS genetics*, 6(9):e1001148.

Grant, P. R. and Grant, B. R. (2008). How and why species multiply. *The Radiation of Darwin's Finches. Princeton Series in Evolutionary Biology*.

Grant, P. R. and Grant, B. R. (2011). *How and why species multiply: the radiation of Darwin's finches*. Princeton University Press.

Graves, J., Disteche, C., et al. (2007). Does gene dosage really matter. *J Biol*, 6(1):1.

Greenwood, P. (1980). Mating systems, philopatry and dispersal in birds and mammals. *Animal behaviour*, 28(4):1140–1162.

Greiner, S., Rauwolf, U., Meurer, J., and Herrmann, R. (2011). The role of plastids in plant speciation. *Molecular ecology*, 20(4):671–691.

Griffiths, R. and Tavaré, S. (1998). The age of a mutation in a general coalescent tree. *Stochastic Models*, 14(1-2):273–295.

Hairston Jr, N. G., Ellner, S. P., Geber, M. A., Yoshida, T., and Fox, J. A. (2005). Rapid evolution and the convergence of ecological and evolutionary time. *Ecology Letters*, 8(10):1114–1127.

Haldane, J. (1922). Sex ratio and unisexual sterility in hybrid animals. *Journal of genetics*, 12(2):101–109.

Hancock, A. M., Alkorta-Aranburu, G., Witonsky, D. B., and Di Rienzo, A. (2010). Adaptations to new environments in humans: the role of subtle allele frequency shifts. *Philosophical Transactions of the Royal Society of London B: Biological Sciences*, 365(1552):2459–2468.

Hansen, T. F. (2006). The evolution of genetic architecture. *Annu. Rev. Ecol. Evol. Syst.*, 37:123–157.

Hansen, T. F. (2013). Why epistasis is important for selection and adaptation. *Evolution*, 67(12):3501–3511.

Hendry, A. P., Farrugia, T. J., and Kinnison, M. T. (2008). Human influences on rates of phenotypic change in wild animal populations. *Molecular Ecology*, 17(1):20–29.

Hermisson, J. and Pennings, P. (2017). Soft sweeps and beyond: Understanding the patterns and probabilities of selection footprints under rapid adaptation. *bioRxiv*, page 114587.

Hermisson, J. and Pennings, P. S. (2005). Soft sweeps: molecular population genetics of adaptation from standing genetic variation. *Genetics*, 169(4):2335–2352.

Hermisson, J. and Pfaffelhuber, P. (2008). The pattern of genetic hitchhiking under recurrent mutation. *Electronic Journal of Probability*, 13:2069–2106.

4034 Hill, W. G. (2014). Applications of population genetics to animal breeding, from wright, fisher
4035 and lush to genomic prediction. *Genetics*, 196(1):1–16.

4036 Hill, W. G., Goddard, M. E., and Visscher, P. M. (2008). Data and theory point to mainly
4037 additive genetic variance for complex traits. *PLoS genetics*, 4(2):e1000008.

4038 Hooper, D. and Price, T. (2015). Rates of karyotypic evolution in Estrildid finches differ
4039 between island and continental clades. *bioRxiv*, page 013987.

4040 Hoppe, F. M. (1984). Pólya-like urns and the ewens' sampling formula. *Journal of Mathemat-*
4041 *ical Biology*, 20(1):91–94.

4042 Inc., W. R. Mathematica, Version 11.3. Champaign, IL, 2018.

4043 Jain, K. and Devi, A. (2018). Polygenic adaptation in changing environments. *arXiv preprint*
4044 *arXiv:1806.03454*.

4045 Jain, K. and Stephan, W. (2015). Response of polygenic traits under stabilizing selection and
4046 mutation when loci have unequal effects. *G3: Genes, Genomes, Genetics*, 5(6):1065–1074.

4047 Jain, K. and Stephan, W. (2017). Rapid adaptation of a polygenic trait after a sudden
4048 environmental shift. *Genetics*, 206(1):389–406.

4049 Josefsson, C., Dilkes, B., and Comai, L. (2006). Parent-dependent loss of gene silencing during
4050 interspecies hybridization. *Current Biology*, 16(13):1322–1328.

4051 Joyce, P. and Tavaré, S. (1987). Cycles, permutations and the structure of the yule process
4052 with immigration. *Stochastic processes and their applications*, 25:309–314.

4053 Kaplan, N. L., Hudson, R., and Langley, C. (1989). The" hitchhiking effect" revisited. *Genetics*,
4054 123(4):887–899.

4055 Karasov, T., Messer, P. W., and Petrov, D. A. (2010). Evidence that adaptation in drosophila
4056 is not limited by mutation at single sites. *PLoS genetics*, 6(6):e1000924.

4057 Khera, A. V., Chaffin, M., Aragam, K. G., Haas, M. E., Roselli, C., Choi, S. H., Natarajan, P.,
4058 Lander, E. S., Lubitz, S. A., Ellinor, P. T., et al. (2018). Genome-wide polygenic scores for

common diseases identify individuals with risk equivalent to monogenic mutations. *Nature genetics*, 50(9):1219.

Kimura, M. (1957). Some problems of stochastic processes in genetics. *The Annals of Mathematical Statistics*, pages 882–901.

Kolbe, J. J., Leal, M., Schoener, T. W., Spiller, D. A., and Losos, J. B. (2012). Founder effects persist despite adaptive differentiation: a field experiment with lizards. *Science*, 335(6072):1086–1089.

Kopp, M. and Matuszewski, S. (2014). Rapid evolution of quantitative traits: theoretical perspectives. *Evolutionary Applications*, 7(1):169–191.

Kryazhimskiy, S., Rice, D. P., Jerison, E. R., and Desai, M. M. (2014). Global epistasis makes adaptation predictable despite sequence-level stochasticity. *Science*, 344(6191):1519–1522.

Kutschera, U. and Niklas, K. J. (2004). The modern theory of biological evolution: an expanded synthesis. *Naturwissenschaften*, 91(6):255–276.

Lachance, J. and True, J. (2010). X-autosome incompatibilities in Drosophila melanogaster: tests of Haldane's rule and geographic patterns within species. *Evolution*, 64(10):3035–3046.

Lamichhaney, S., Berglund, J., Almén, M. S., Maqbool, K., Grabherr, M., Martinez-Barrio, A., Promerová, M., Rubin, C.-J., Wang, C., Zamani, N., et al. (2015). Evolution of darwin's finches and their beaks revealed by genome sequencing. *Nature*, 518(7539):371.

Lande, R. (1983). The response to selection on major and minor mutations affecting a metrical trait. *Heredity*, 50(1):47.

Laporte, M., Pavey, S. A., Rougeux, C., Pierron, F., Lauzent, M., Budzinski, H., Labadie, P., Geneste, E., Couture, P., Baudrimont, M., et al. (2016). Rad sequencing reveals within-generation polygenic selection in response to anthropogenic organic and metal contamination in north atlantic eels. *Molecular ecology*, 25(1):219–237.

Lawson Handley, L. and Perrin, N. (2007). Advances in our understanding of mammalian sex-biased dispersal. *Molecular Ecology*, 16(8):1559–1578.

Lazaridis, I., Nadel, D., Rollefson, G., Merrett, D. C., Rohland, N., Mallick, S., Fernandes, D., Novak, M., Gamarra, B., Sirak, K., et al. (2016). Genomic insights into the origin of farming in the ancient near east. *Nature*, 536(7617):419.

Lee, H., Chou, J., Cheong, L., Chang, N., Yang, S., and Leu, J. (2008). Incompatibility of nuclear and mitochondrial genomes causes hybrid sterility between two yeast species. *Cell*, 135(6):1065–1073.

Levene, H. (1953). Genetic equilibrium when more than one ecological niche is available. *American Naturalist*, pages 331–333.

Lindtke, D. and Buerkle, C. (2015). The genetic architecture of hybrid incompatibilities and their effect on barriers to introgression in secondary contact. *Evolution*.

Liu, K., Steinberg, E., Yozzo, A., Song, Y., Kohn, M., and Nakhleh, L. (2015). Interspecific introgressive origin of genomic diversity in the house mouse. *Proceedings of the National Academy of Sciences*, 112(1):196–201.

Losos, J. B. (2014). What darwin got wrong. *Chronicle of Higher Education*, 20.

Macholán, M., Munclinger, P., Šugerková, M., Dufková, P., Bímová, B., Božíková, E., Zima, J., and Piálek, J. (2007). Genetic analysis of autosomal and X-linked markers across a mouse hybrid zone. *Evolution*, 61(4):746–771.

Mackay, T. F. (2009). The genetic architecture of complex behaviors: lessons from drosophila. *Genetica*, 136(2):295–302.

Macnair, M. and Christie, P. (1983). Reproductive isolation as a pleiotropic effect of copper tolerance in Mimulus guttatus. *Heredity*, 50(3):295–302.

Maheshwari, S. and Barbash, D. (2011). The genetics of hybrid incompatibilities. *Annual review of genetics*, 45:331–355.

Mallet, J. (2008). Hybridization, ecological races and the nature of species: empirical evidence for the ease of speciation. *Philosophical Transactions of the Royal Society B: Biological Sciences*, 363(1506):2971–2986.

Malmberg, R. L. and Mauricio, R. (2005). Qtl-based evidence for the role of epistasis in evolution. *Genetics Research*, 86(2):89–95.

Mani, G. and Clarke, B. (1990). Mutational order: a major stochastic process in evolution. *Proceedings of the Royal Society of London B: Biological Sciences*, 240(1297):29–37.

Manolio, T. A., Brooks, L. D., and Collins, F. S. (2008). A hapmap harvest of insights into the genetics of common disease. *The Journal of clinical investigation*, 118(5):1590–1605.

Manolio, T. A., Collins, F. S., Cox, N. J., Goldstein, D. B., Hindorff, L. A., Hunter, D. J., McCarthy, M. I., Ramos, E. M., Cardon, L. R., Chakravarti, A., et al. (2009). Finding the missing heritability of complex diseases. *Nature*, 461(7265):747.

Masly, J. and Presgraves, D. (2007). High-resolution genome-wide dissection of the two rules of speciation in Drosophila. *PLoS Biol*, 5(9):e243.

Matsubara, K., Yamamoto, E., Mizobuchi, R., Yonemaru, J., Yamamoto, T., Kato, H., and Yano, M. (2015). Hybrid Breakdown Caused by Epistasis-Based Recessive Incompatibility in a Cross of Rice (Oryza sativa L.). *Journal of Heredity*, 106(1):113–122.

Matuszewski, S., Hermisson, J., and Kopp, M. (2015). Catch me if you can: adaptation from standing genetic variation to a moving phenotypic optimum. *Genetics*, pages genetics–115.

Maynard-Smith, J. and Haigh, J. (1974). The hitch-hiking effect of a favourable gene. *Genetics Research*, 23(1):23–35.

Messer, P. W., Ellner, S. P., and Hairston Jr, N. G. (2016). Can population genetics adapt to rapid evolution? *Trends in Genetics*, 32(7):408–418.

Muller, H. (1942). Isolating mechanisms, evolution and temperature. In *Biological Symposia*, volume 6, pages 71–125.

Nosil, P. (2012). *Ecological speciation*. Oxford University Press.

Nosil, P. and Feder, J. (2012). Genomic divergence during speciation: causes and consequences. *Philosophical Transactions of the Royal Society B: Biological Sciences*, 367(1587):332–342.

Novembre, J. and Barton, N. H. (2018). Tread lightly interpreting polygenic tests of selection. *Genetics*, 208(4):1351–1355.

Novembre, J. and Han, E. (2012). Human population structure and the adaptive response to pathogen-induced selection pressures. *Phil. Trans. R. Soc. B*, 367(1590):878–886.

Oka, A., Mita, A., Sakurai-Yamatani, N., Yamamoto, H., Takagi, N., Takano-Shimizu, T., Toshimori, K., Moriwaki, K., and Shiroishi, T. (2004). Hybrid breakdown caused by substitution of the X chromosome between two mouse subspecies. *Genetics*, 166(2):913–924.

Oka, A. and Shiroishi, T. (2013). Regulatory divergence of X-linked genes and hybrid male sterility in mice. *Genes & genetic systems*, 89(3):99–108.

O'Neill, S., Giordano, R., Colbert, A., Karr, T., and Robertson, H. (1992). 16S rRNA phylogenetic analysis of the bacterial endosymbionts associated with cytoplasmic incompatibility in insects. *Proceedings of the National Academy of Sciences*, 89(7):2699–2702.

Orr, H. (2005). The genetic theory of adaptation: a brief history. *Nature Reviews Genetics*, 6(2):119–127.

Orr, H. and Turelli, M. (2001). The evolution of postzygotic isolation: accumulating Dobzhansky-Muller incompatibilities. *Evolution*, 55(6):1085–1094.

Orr, H. A. and Betancourt, A. J. (2001). Haldane's sieve and adaptation from the standing genetic variation. *Genetics*, 157(2):875–884.

Paaby, A. B. and Rockman, M. V. (2013). The many faces of pleiotropy. *Trends in Genetics*, 29(2):66–73.

Paulose, J., Hermisson, J., and Hallatschek, O. (2018). Spatial soft sweeps: patterns of adaptation in populations with long-range dispersal. *bioRxiv*, page 299453.

Pavlidis, P., Metzler, D., and Stephan, W. (2012). Selective sweeps in multilocus models of quantitative traits. *Genetics*, 192(1):225–239.

Payer, B. and Lee, J. (2008). X chromosome dosage compensation: how mammals keep the balance. *Annual review of genetics*, 42:733–772.

Payseur, B., Krenz, J., and Nachman, M. (2004). Differential patterns of introgression across the x chromosome in a hybrid zone between two species of house mice. *Evolution*, 58(9):2064–2078.

Pennings, P. and Hermisson, J. (2006). Soft sweeps ii—molecular population genetics of adaptation from recurrent mutation or migration. *Molecular biology and evolution*, 23(5):1076–1084.

Pennisi, E. (2014). Disputed islands. *Science*, 345(6197):611–613.

Perbal, L. (2015). The case of the gene: Postgenomics between modernity and postmodernity. *EMBO reports*, 16(7):777–781.

Pickrell, J. K. and Reich, D. (2014). Toward a new history and geography of human genes informed by ancient dna. *Trends in Genetics*, 30(9):377–389.

Presgraves, D. (2008). Sex chromosomes and speciation in Drosophila. *Trends in Genetics*, 24(7):336–343.

Presgraves, D. (2010). The molecular evolutionary basis of species formation. *Nature Reviews Genetics*, 11(3):175–180.

Presgraves, D., Balagopalan, L., Abmayr, S., and Orr, H. (2003). Adaptive evolution drives divergence of a hybrid inviability gene between two species of Drosophila. *Nature*, 423(6941):715–719.

Pritchard, J., Pickrell, J., and Coop, G. (2010). The genetics of human adaptation: hard sweeps, soft sweeps, and polygenic adaptation. *Current biology*, 20(4):R208–R215.

Pritchard, J. K. and Di Rienzo, A. (2010). Adaptation–not by sweeps alone. *Nature Reviews Genetics*, 11(10):665.

Ralph, P. L. and Coop, G. (2010). Parallel adaptation: one or many waves of advance of an advantageous allele? *Genetics*.

Ralph, P. L. and Coop, G. (2015). The role of standing variation in geographic convergent adaptation. *The American Naturalist*, 186(S1):S5–S23.

Reznick, D. N. (2011). *The origin then and now: an interpretive guide to the origin of species*. Princeton University Press.

Rice, S. H. (2004). *Evolutionary theory: mathematical and conceptual foundations*. Sinauer Associates.

Rutschman, D. (1994). Dynamics of the two-locus haploid model. *Theoretical population biology*, 45(2):167–176.

Sætre, G., Borge, T., Lindroos, K., Haavie, J., Sheldon, B., Primmer, C., and Syvänen, A.-C. (2003). Sex chromosome evolution and speciation in Ficedula flycatchers. *Proceedings of the Royal Society of London B: Biological Sciences*, 270(1510):53–59.

Schluter, D. and Conte, G. (2009). Genetics and ecological speciation. *Proceedings of the National Academy of Sciences*, 106(Supplement 1):9955–9962.

Slatkin, M. (1987). Gene flow and the geographic structure of natural populations. *Science*, 236:787–792.

Snijder, R., Brown, F., and van Tuyl, J. (2007). The role of plastome-genome incompatibility and biparental plastid inheritance in interspecific hybridization in the genus Zantedeschia (Araceae). *Floriculture and Ornamental Biotechnology*, 1(2):150–157.

Sohail, M., Maier, R. M., Ganna, A., Bloemendal, A., Martin, A. R., Turchin, M. C., Chiang, C. W. K., Hirschhorn, J. N., Daly, M., Patterson, N., Neale, B., Mathieson, I., Reich, D., and Sunyaev, S. R. (2018). Signals of polygenic adaptation on height have been overestimated due to uncorrected population structure in genome-wide association studies. *bioRxiv*.

Stephan, W. (2016). Signatures of positive selection: from selective sweeps at individual loci to subtle allele frequency changes in polygenic adaptation. *Molecular ecology*, 25(1):79–88.

Storchova, R., Gregorová, S., Buckiova, D., Kyselova, V., Divina, P., and Forejt, J. (2004). Genetic analysis of X-linked hybrid sterility in the house mouse. *Mammalian Genome*, 15(7):515–524.

Strasburg, J. L., Sherman, N. A., Wright, K. M., Moyle, L. C., Willis, J. H., and Rieseberg, L. H. (2012). What can patterns of differentiation across plant genomes tell us about adaptation and speciation? *Philosophical Transactions of the Royal Society of London B: Biological Sciences*, 367(1587):364–373.

Sweigart, A. and Flagel, L. (2014). Evidence of Natural Selection Acting on a Polymorphic Hybrid Incompatibility Locus in Mimulus. *Genetics*, pages genetics–114.

Ting, C., Tsaur, S., Wu, M., and Wu, C. (1998). A rapidly evolving homeobox at the site of a hybrid sterility gene. *Science*, 282(5393):1501–1504.

Tobler, R., Franssen, S., Kofler, R., Orozco-terWengel, P., Nolte, V., Hermisson, J., and Schlötterer, C. (2014). Massive habitat-specific genomic response in d. melanogaster populations during experimental evolution in hot and cold environments. *Molecular Biology and Evolution*, 31(2):364.

Togninalli, M., Seren, Ü., Meng, D., Fitz, J., Nordborg, M., Weigel, D., Borgwardt, K., Korte, A., and Grimm, D. G. (2017). The aragwas catalog: a curated and standardized arabidopsis thaliana gwas catalog. *Nucleic acids research*, 46(D1):D1150–D1156.

Tucker, P., Sage, R., Warner, J., Wilson, A., and Eicher, E. (1992). Abrupt cline for sex chromosomes in a hybrid zone between two species of mice. *Evolution*, pages 1146–1163.

Turelli, M. and Barton, N. (1990). Dynamics of polygenic characters under selection. *Theoretical Population Biology*, 38(1):1–57.

Turelli, M. and Barton, N. (1994). Genetic and statistical analyses of strong selection on polygenic traits: what, me normal? *Genetics*, 138(3):913–941.

Turelli, M. and Orr, H. (2000). Dominance, epistasis and the genetics of postzygotic isolation. *Genetics*, 154(4):1663–1679.

Turner, T., Hahn, M., and S., N. (2005). Genomic islands of speciation in Anopheles gambiae. *PLoS biology*, 3(9):e285.

Uecker, H. and Hermisson, J. (2011). On the fixation process of a beneficial mutation in a variable environment. *Genetics*, pages genetics–110.

van't Hof, A. E., Campagne, P., Rigden, D. J., Yung, C. J., Lingley, J., Quail, M. A., Hall, N., Darby, A. C., and Saccheri, I. J. (2016). The industrial melanism mutation in british peppered moths is a transposable element. *Nature*, 534(7605):102.

Via, S. (2012). Divergence hitchhiking and the spread of genomic isolation during ecological speciation-with-gene-flow. *Philosophical Transactions of the Royal Society B: Biological Sciences*, 367(1587):451–460.

Via, S. and West, J. (2008). The genetic mosaic suggests a new role for hitchhiking in ecological speciation. *Molecular Ecology*, 17(19):4334–4345.

Visscher, P., Brown, M., McCarthy, M., and Yang, J. (2012). Five years of gwas discovery. *The American Journal of Human Genetics*, 90(1):7–24.

Visscher, P. M., Wray, N. R., Zhang, Q., Sklar, P., McCarthy, M. I., Brown, M. A., and Yang, J. (2017). 10 years of gwas discovery: biology, function, and translation. *The American Journal of Human Genetics*, 101(1):5–22.

Wagner, G. P. (2000). *The character concept in evolutionary biology*. Elsevier.

Wang, R. (2013). Gene flow across a hybrid zone maintained by a weak heterogametic incompatibility and positive selection of incompatible alleles. *Journal of Evolutionary Biology*, pages 386–396.

Wangler, M. F., Hu, Y., and Shulman, J. M. (2017). Drosophila and genome-wide association studies: a review and resource for the functional dissection of human complex traits. *Disease Models & Mechanisms*, 10(2):77–88.

Werren, J. (1997). Biology of wolbachia. *Annual review of entomology*, 42(1):587–609.

White, M., Stubbings, M., Dumont, B. L., and Payseur, B. (2012). Genetics and evolution of hybrid male sterility in house mice. *Genetics*, 191(3):917–934.

Wilson, B. A., Petrov, D. A., and Messer, P. W. (2014). Soft selective sweeps in complex demographic scenarios. *Genetics*, pages genetics–114.

Wollstein, A. and Stephan, W. (2014). Adaptive fixation in two-locus models of stabilizing selection and genetic drift. *Genetics*, pages genetics–114.

Wright, S. (1931). Evolution in mendelian populations. *Genetics*, 16(2):97.

Wu, C. (2001). The genic view of the process of speciation. *Journal of Evolutionary Biology*, 14(6):851–865.

Yeaman, S. (2013). Genomic rearrangements and the evolution of clusters of locally adaptive loci. *Proceedings of the National Academy of Sciences*, page 201219381.

Yeaman, S. (2015). Local adaptation by alleles of small effect. *The American Naturalist*, 186(S1):S74–S89.

Yeaman, S., Aeschbacher, S., and Bürger, R. (2016). The evolution of genomic islands by increased establishment probability of linked alleles. *Molecular ecology*, 25(11):2542–2558.

Yeaman, S. and Otto, S. (2011). Establishment and maintenance of adaptive genetic divergence under migration, selection, and drift. *Evolution*, 65(7):2123–2129.

Yeaman, S. and Whitlock, M. (2011). The genetic architecture of adaptation under migration–selection balance. *Evolution*, 65(7):1897–1911.

Zan, Y. and Carlborg, Ö. (2018). A multilocus association analysis method integrating phenotype and expression data reveals multiple novel associations to flowering time variation in wild-collected arabidopsis thaliana. *Molecular ecology resources*.

Zan, Y., Sheng, Z., Lillie, M., Rönnegård, L., Honaker, C. F., Siegel, P. B., and Carlborg, Ö. (2017). Artificial selection response due to polygenic adaptation from a multilocus, multiallelic genetic architecture. *Molecular biology and evolution*, 34(10):2678–2689.